Dissertation

submitted to the
Combined Faculties for the Natural Sciences and for Mathematics
of the
Ruperto-Carola University of Heidelberg, Germany,
for the degree of
Doctor of Natural Sciences

Put forward by
Julia Jäger
born in Wermelskirchen
Oral examination: 29th July 2020

Multiscale Modelling
of Malaria-Infected Red Blood Cells

Referees: Prof. Dr. Ulrich S. Schwarz
Prof. Dr. Frauke Gräter

Summary

Multiscale Modelling of Malaria-Infected Red Blood Cells

Red blood cells (RBCs) are the type of human cells that are most accessible to biophysical multiscale modelling because they feature a regular molecular cell envelope organization and lack internal organelles. Extensive previous research on how their physical properties are shaped by the actin-spectrin network and other molecular constituents provides a good basis to understand the physical consequences of becoming infected by malaria parasites, which use RBCs to hide from the immune system. After invasion, the malaria parasite rebuilds the RBC-envelope, relying on the self-assembly of parasite proteins released into the cytoplasm. Optical tweezer experiments have shown that infected RBCs (iRBCs) become stiffer. Here, the underlying mechanisms are investigated by quantitative analysis of the flickering spectrum of iRBCs. Extending the membrane Hamiltonian by anchoring points, we find that the parasite stiffens the membrane mostly by introducing more connections between the lipid bilayer and the underlying cytoskeleton. To identify the exact points of attack in the RBC-cytoskeleton, a reaction-diffusion model is developed to investigate the dynamical equilibrium of the RBC-cytoskeleton, allowing us to simulate different scenarios of parasite protein self-assembly and to compare these results with experimental data. The parasite induces protrusions to make the iRBC adhesive, thus increasing residence time in the vasculature and avoiding clearance by the spleen. The number of new transmembrane receptors incorporated into the cell membrane is estimated by quantitative analysis of fluorescence and electron microscopy data. We develop a finite element model aiming to predict the effect of these changes on the movement of iRBCs in hydrodynamic flow. Finally, as an instructive contrast to RBC-mechanics, we investigate the spreading of tissue cells onto micropatterned substrates leading to a complete change in their actin cytoskeleton. A Cellular Potts Model is used to describe this highly dynamic situation. We find that due to its focus on geometrical aspects, it predicts reliably how a family of actin stress fibres is formed, which serves as memory of the spreading process.

Zusammenfassung

Größenordnungsabhängige Modellierung von Malaria-infizierten roten Blutzellen

Die rote Blutzelle ist die am besten geeignete Zelle für die biophysikalische Modellierung, da sie eine gleichmäßige molekulare Membranstruktur besitzt und keine internen Organellen vorhanden sind. Basierend auf vorherigen Forschungsergebnissen über die Einflüsse des Aktin-Spektrin-Netzwerkes und anderer molekularer Bestandteile auf die Eigenschaften der Membran kann das Verständnis der durch die Malaria-Infektion herforgerufenen Veränderungen erweitert werden. Nach der Invasion der roten Blutzelle baut der Malaria-Parasit die Membran der roten Blutzelle um, indem er Proteinkomplexe assemblieren lässt, die aus zuvor ins Zytoplasma exportierten Proteinen bestehen. Experimente mit optischen Fallen haben gezeigt, dass die rote Blutzelle durch den Malaria-Parasiten steifer wird. In dieser Arbeit werden die zugrundeliegenden Mechanismen mithilfe der quantitativen Analyse des Undulationsspektrums untersucht. Durch die Ergänzung der Membran-Hamiltonian durch Ankerpunkte wird herausgefunden, dass der Parasit die Membran verhärtet, indem er mehr Ankerpunkte zwischen der Doppellipidschicht und dem Zytoskelett erschafft. Um die genauen Punkte zu finden, die der Parasit angreift, wird ein Reaktions-Diffusions-Modell entwickelt, durch das der dynamische Gleichgewichtszustand des Zytoskeletts modelliert werden kann. Hierdurch können sowohl verschiedene Varianten des Assemblierungsprozesses der Proteinkomplexe modelliert werden, als auch die Resultate mit experimentellen Daten verglichen werden. Der Parasit entwickelt hervorgewölbte Strukturen auf der Oberfläche der roten Blutzelle, um diese haftfähig zu machen und dadurch die Aufenthaltsdauer im Blutfluss zu erhöhen, da er ansonsten in der Milz aussortiert werden würde. Durch die quantitative Analyse von Fluoreszenz- und Elektronenmikroskopieaufnahmen wird die Anzahl der Transmembranrezeptoren pro hervorgewölbter Struktur bestimmt. Um die Effekte dieses molekularen Umbaus auf die Eigenschaften der roten Blutzelle im hydrodynamischen Fluss zu bestimmen, wird eine Finite-Elemente-Simulation verwendet. Als hilfreicher Kontrast zur Struktur der roten Blutzelle werden schlussendlich Zellen auf mikrostrukturierten Substraten simuliert, in denen das Aktin-Zytoskelett dynamisch umgebaut wird. Dafür wird ein zelluläres Potts-Modell verwendet. Wir folgern, dass das Modell durch die Spezialisierung auf geometrische Aspekte die Organisation der entstehenden Aktinfilamente vorhersagen kann. Die Struktur der Aktinfilamente agiert somit als Gedächtnis des Ausbreitungsprozesses.

Contents

Chapter 1

Introduction

1.1 Motivation

This thesis aims to shed light on the biophysics of RBCs using multiscale modelling; models of the cell's membrane, its molecular components, its shape and its dynamics on micropatterns are discussed. All these models are demonstrated to be relevant facets of a comprehensive biophysical perspective on RBCs, adding fundamentally to the foundations of malaria research.

RBCs are very attractive models for multiscale physics because their structure is relatively stable and simplistic in the way that the membrane, a quasi two-dimensional surface, determines their properties completely [1, 2]. Other types of cells cannot be accessed that easily because they possess complicated internal structures [3]. RBCs are easily accessible for biophysical modelling, so a large background of theoretical models and experiments has been built up [4, 5, 6, 7, 8]. Even more work has been done on lipid vesicles [9, 10], which are similar to RBCs but do not possess a thin polymeric network underneath the membrane. Building on this knowledge, it is possible to examine how the malaria parasite changes the RBC membrane.

During its life-cycle, discussed in Section 1.3, the malaria parasite eventually enters RBCs. It remodels the cell completely by exporting proteins which assemble to structures within the membrane and the cytosol. Particularly, the spectrin-actin network undergoes drastic changes [11, 12]. The models applied in this thesis aim to understand this remodelling process and its consequences better.

As a comparison of cytoskeletal structures in other cell types, the development of actin stress fibres is studied in human bone osteosarcoma epithelial cells spreading on micro patterns. In that case, the cell adapts its cytokeletal structure in order to move across non-adhesive areas [13, 14].

It is very important that a biophysical model is validated by experimental data. Each of the presented models were developed in close collaboration with our experimental partners as it will become clear throughout the thesis. These collaborations were very fruitful since people with different backgrounds came together to develop new interdisciplinary ideas. Now, I will explain the biophysical background required to understand the rest of this thesis.

1.2 A Physicist's Perspective on RBCs

Formation and Function of RBCs

Our blood is made up of three types of cells suspended in plasma; red blood cells (RBCs) or erythrocytes (see Figure 1.1), white blood cells or leucocytes, and platelets or thrombocytes. RBCs contain haemoglobin molecules, which bind with oxygen and carbon dioxide molecules and carry them around the body (see Figure 1.1c). This process is so significant that RBCs account for $2.6 \cdot 10^{31}$, or 84%, of the human body's cells. RBCs are formed in the bone marrow and are deformed dramatically during their lifespan of 120 days due to being squeezed through very narrow capillaries. After 120 days, a RBC becomes too stiff from being continually deformed and is destroyed within the spleen.

Figure 1.1: a) Side view of a RBC of hight 2 µm. b) Top view of a RBC of diameter 7.5 µm. c) Artistic representation of a RBC by Prof. David S. Goodsell, the Scripps Research Institute. The red structures show the haemoglobin molecules. The plasma membrane with attached structures is drawn in purple.

RBCs are shaped as biconcave disocytes (see Figure 1.1a) and have a diameter of 7.5 to 8.7 µm (see Figure 1.1b). Lacking the usual internal cell structures such as a nucleus, their shape is solely determined by their membrane. The RBC membrane is a composite structure, which is made up of a phospholipid bilayer containing various membrane proteins, also called the plasma membrane, and a cytoskeletal network attached to it from the cytosolic side. An illustration can be seen in Figure 1.1c with the cytoskeletal components in purple surrounded by the cytosol and the haemoglobin in red. The straight filaments are short actin filaments that build up the junctional points of the network. The flexible connections between these are two stranded helical spectrin filaments. The microscopic structure of the cytoskeleton is discussed in more detail in Chapter 3.

The RBC's composite structure allows for it to exhibit the properties necessary for squeezing through capillaries and yet recovering its shape. Its plasma membrane is comprised of two lipid sheets pointing their hydrocarbon chains towards each other. The membrane is kept in shape by high hydrophobic energy costs; the dense packing of the chains increases the difficulty of membrane compression. The compressibility of approximately 10^3 mN m^{-1} is necessary to prevent ion loss throughout passive transport [15]. When applying a shear, the plasma membrane behaves like a fluid within the plane as the lipids can swap places within the membrane. Here, the cytoskeleton reveals its significance, as the RBC needs to withstand shear during the frequent deformations. The spectrin filaments are elastic and are anchored to the plasma membrane mostly by band 3 and as a result the composite system gains a shear modulus of $\mu \approx 0.006$ mN m^{-1} [15].

The RBC's shape can be understood within the formalism of differential geometry by treating it as a thin shell and formulating a Hamiltonian mostly based on the energy cost of bending. Equivalent to the Brownian motion of small molecules, membranes also exhibit thermal motion, making the membrane move on the small scale (see Chapter 2).

1.3 The Malaria Infection

Although the number of deaths due to malaria has declined in recent years, around $405,000$ cases were still recorded in 2018 according to the World Health Organisation [16]. In order to fulfil the long-term goal of completely controlling this deadly disease, all stages in the life-cycle of the malaria parasite need to be understood thoroughly. This will facilitate the development of new drugs, and help to avoid problems that occur due to drug resistance.

The sickle cell disease has been found to protect carriers from severe malaria symptoms, due to a mutation of the haemoglobin within the RBC. Normal haemoglobin (HbAA) is a heterotetramer, consisting of two α- and two β-globin chains. Sickle cells contain HbS, in which the β-globin is altered at position six by a glutamate to valine substitution. This substitution causes severe anaemia and is more common in countries with many malaria cases because it protects its carriers from severe malaria symptoms. A different haemoglobin mutation that protects from malaria is HbC. Heterozygotes, featuring both genes of normal haemoglobin A and mutated haemoglobin S or C, are denoted as HbAS and HBAC. In Chapter 2, the potential explanations why the sickle cell trait protects its carriers from malaria are discussed.

The Malaria Life-Cycle

The most virulent form of human malaria is caused by the parasite *Plasmodium falciparum* (Pf) which, during a blood meal, is injected into the host skin by the female Anopheles mosquito. After the skin stage, the parasite goes through three other stages before it continues to infect new mosquitoes: the liver stage, the asexual intra-erythrocyte stage and the sexual intra-erythrocyte stage as illustrated in Figure 1.2. After injection into the skin, the sporozoites travel to the liver where they replicate asexually, producing merozoites. These are released from the liver into the blood to infect RBCs functioning as hiding places. During the asexual cycle, the parasite grows inside the cell, restructures it and finally causes rupture after 48 hours, infecting more RBCs. This development can be divided into the ring ($0 - 24$ h), trophozoite ($24 - 36$ h) and schizont stages ($40 - 48$ h) and is accompanied by changes in elasticity and morphology of the infected RBC (iRBC). In some iRBCs, the parasite does not go through this cycle but form male or female gametocytes (sexual intra-erythrocyte cycle). When a mosquito takes up such iRBCs, the life-cycle in the human host is closed.

A detailed quantitative understanding of the iRBC's remodelling in the asexual intra-erythrocyte stage is currently lacking, despite it being central to the infection and causing most of the malaria-associated pathology [17]. Therefore, this thesis will attempt to model the iRBC during this central stage. By remodeling the spectrin network and establishing nano-scale protrusions, called knobs, on the iRBC membrane, the parasite reduces the deformability of the iRBC [18] and makes the cell approach a more spherical shape [19] (see Figure 1.3). The knobs mainly comprise of the knob-associated histidine-rich protein (KAHRP) and the membrane-embedded cytoadherence protein Pf-erythrocyte membrane protein 1 (PfEMP1). The resulting alterations lead to cytoadherence and hence sequestra-

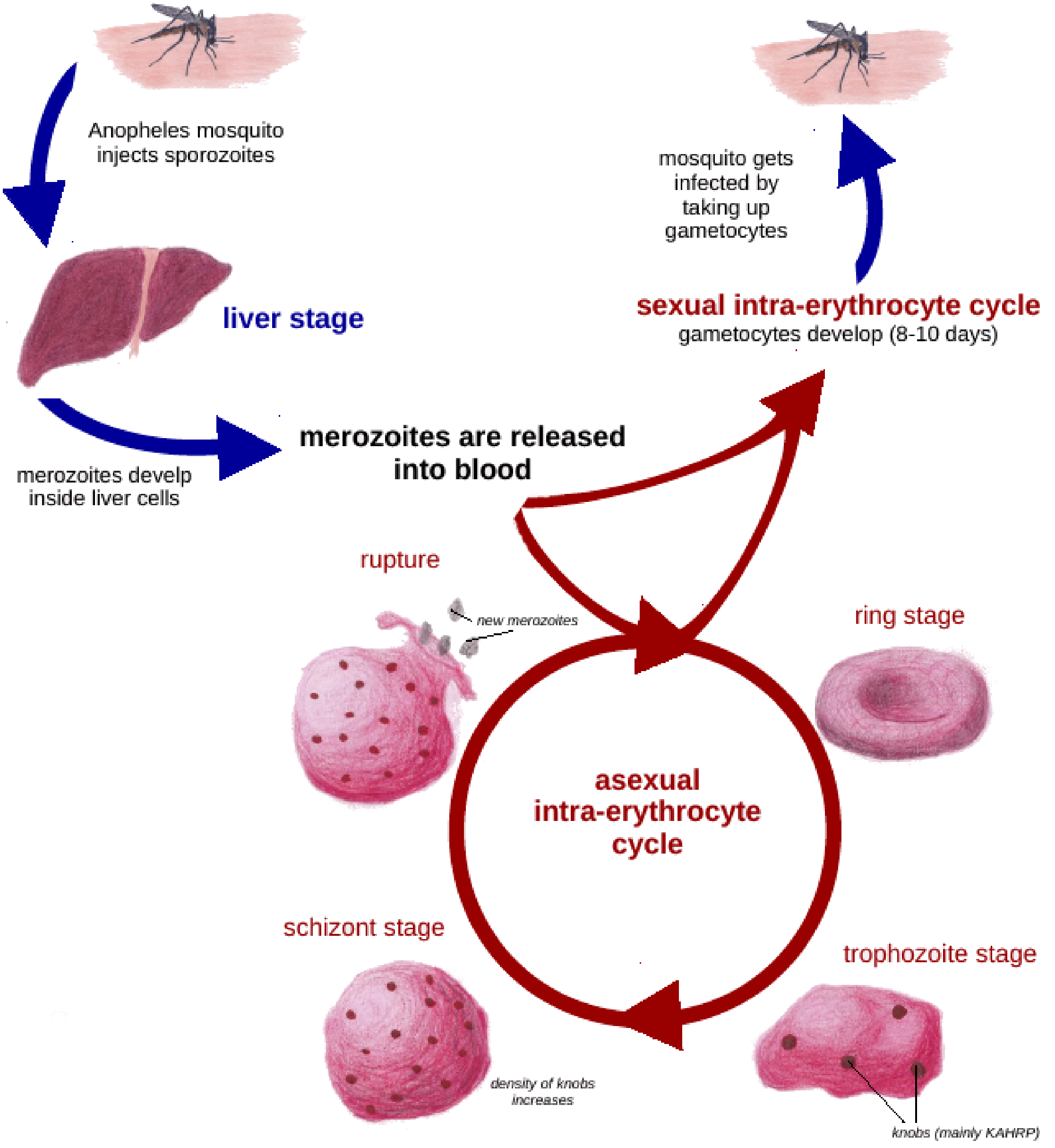

Figure 1.2: Illustration of the malaria life-cycle within the human body. The stages taking place in the blood stream are depicted with red arrows. Graphic based on personal drawings.

tion of iRBCs in the microvasculature. The parasite uses this as a strategy to avoid passage through the spleen, where iRBCs would be sorted out, but this structural alteration also leads to organ dysfunction in severe cases of malaria.

In order to remodel the iRBC, the parasite needs to export proteins to the host cell. For example, the membrane proteins RIFIN, SEVOR and PfEMP1 are synthesized within the parasite and need to be transported across the parasite plasma membrane, the parasitophorous vacuolar membrane and the cytosol of the host cell. One way of transport out of the parasite is the complex PTEX (Plasmodium Translocon of Exported proteins) [20]. Once the proteins are in the erythrocyte cytoplasm, they still need to be delivered to the membrane. Since mature human RBCs lack a secretory machinery, which usually sorts and delivers proteins to the membrane, the parasite establishes an exomembrane system called Maurer's clefts [21, 22]. It was shown that these Maurer's clefts are anchored to components of the erythrocyte cytoskeleton [23]. Many details concerning the Maurer's clefts are still unclear, but it has been found that the parasite uses them for transporting proteins to the membrane. It was further found by Cyrklaff *et al.* [23] that the parasite mines actin from the spectrin network underlying the host cell's plasma membrane in order to generate actin filaments that connect the Maurer's clefts to the developing knobs. Some proteins are thought to be transported along these actin filaments.

At the end of the 48 hour asexual intra-erythrocyte stage, which is summarised in Figure 1.3c, the iRBC ruptures [25]. This process is not well understood, but it is clear that both the increase in osmotic pressure and the disruption of the spectrin network are essential. Shi *et al.* performed AFM-based imaging of the cytoplasmic surface of the iRBC [11] and found an increase in the spectrin network mesh size, extension of the spectrin tetramers and a decrease of spectrin abundance. It is very likely that the resulting expansion of the mesh size also facilitates rupture.

How Physics Can Contribute to Understanding the Infection

As the RBC is one of the best understood cellular model systems in biophysics [26], this knowledge can be exploited as a background to study the details of a malaria infection. Since the average shape and its fluctuations can be calculated for the wild-type RBC from the mechanical properties of the plasma membrane and the spectrin network (see Chapter 2), they can be used as a macroscopic readout of the molecular changes.

In recent years, several studies addressed the relation between the molecular processes affected by the parasite and the large-scale changes in host cell mechanics, adhesion and shape. For example, Zhang *et al.* [18] developed a coarse-grained molecular dynamics model capturing the molecular structures of Pf iRBC membranes to study the origin of the changes in deformability. They found that the remodelling of the spectrin network itself contributes little to the strain-hardening properties of the iRBC, but that the knobs are responsible for the loss of deformability in several ways: not only do they act as structural strengtheners, but they also introduce strain inhomogeneities.

Waldecker *et al.* measured the iRBC's changes during the asexual intra-

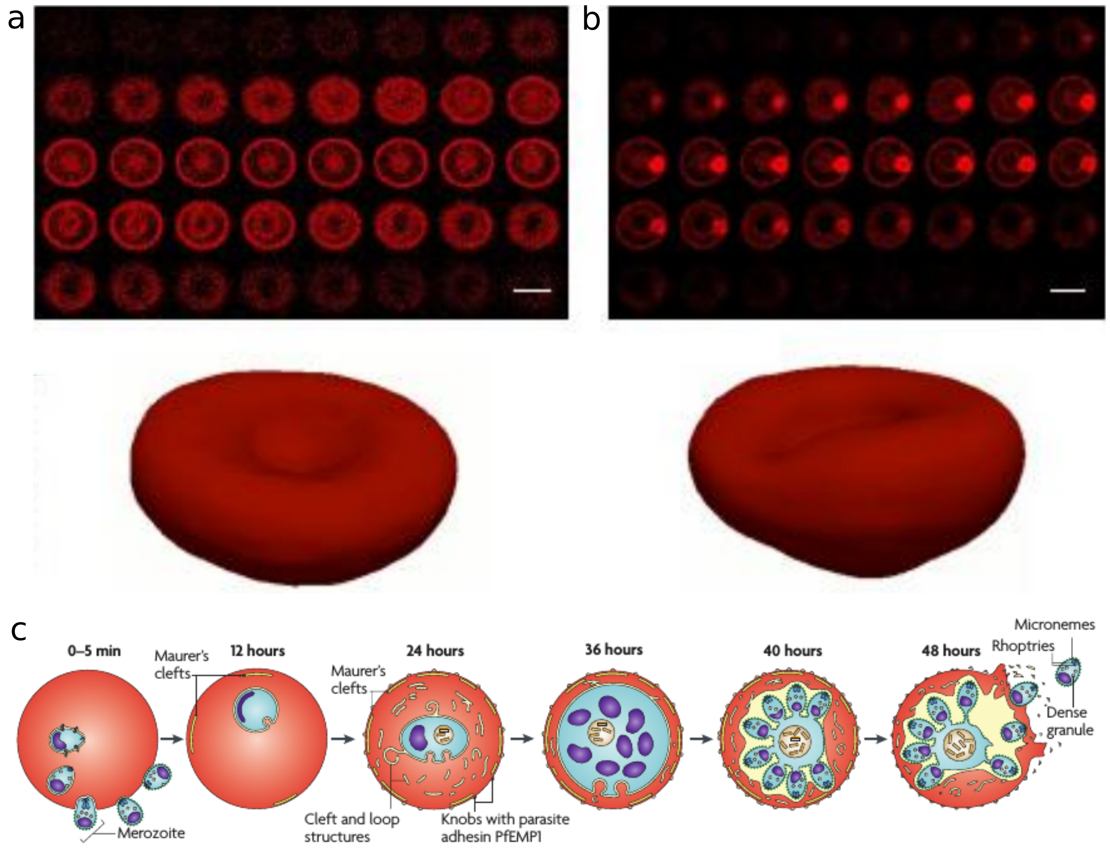

Figure 1.3: a) Confocal images of an uninfected RBC and the corresponding three-dimensional reconstruction. Images taken from Ref. [19]. b) Same as in a) but for an iRBC in ring stage. c) Illustration of the 48 hour RBC cycle of the multiplying malaria parasite. The blue and purple structures are the parasite. Taken from Ref. [24].

erythrocyte cycle in both volume and surface area [19]. Based on this data they verified that the colloid-osmotic model, which describes changes in osmotic pressure due to the new permeation pathways, can predict the iRBC approaching a spherical shape.

Furthermore, biophysical models of protein assembly are crucial to thoroughly understand the membrane changes induced by the parasite. Similar models have been applied to study the assembly of viruses or cytoskeletal filaments [27, 28]. Correspondingly, in Chapter 3, I apply a reaction-diffusion model to achieve a deeper understanding of knob assembly.

Finally, the behaviour of iRBCs in flow can also be analysed with biophysical models. The strength of biophysical models such as Multi-Partlicle Collision Dynamics, Dissapative Particle Dymanics or the Finite Element Method is their ability to test the cell parameters' magnitude and importance. I chose to apply the Finite Element Method in Chapter 4 to model the hydrodynamic behaviour of RBCs in a two-dimensional approximation.

1.4 Cell Adhesion and Migration

Forces Contributing to Cell Movement

In order for cells to move, they need to interact with the substrate through focal adhesions. The main drive of motion is actin polymerisation at the front of the cell and depolymerisation at the rear. A more detailed description of this process is given in Chapter 5. In this thesis I focus on the spreading of cells on micropatterns; this allows details of the process to be examined in a controlled manner in contrast to cells in unstructured environments. The micropattern consists of a printed two-dimensional surface of fibronectin to which the cell can adhere; an example of such a pattern is given in Figure 1.4a.

When cells spread, they need to work against the cell cortex which induces surface tension. They also need to bridge areas without adhesion possibilities (compare Figure 1.4a and b). To do so, they build up a stress fibre, made up of actin and other cross linking proteins, at the cell's front. For detailed information on the composition of different stress fibres, see Chapter 5.

Biophysical Approaches

Several biophysical models have helped to get a better understanding of cell spreading, and aim to determine the properties of cellular components and their relation to cell migration. First of all, cells can be treated in the framework of continuum mechanics as first introduced by Nelson *et al* [30]. In this approach, the cellular properties are represented by a stiffness and a stress tensor. Such a continuum approach can determine the traction forces on the extracellular environment as in Edwards *et al* [31]. In an alternative approach, the cell's internal actin fibres have been modelled using cable networks [32] which behave elastic upon extension, but cannot support compression without buckling.

The model applied in Chapter 5 is a contour based model. The advantage of such a model is the reduction of a cell to its shape which decreases the modelling

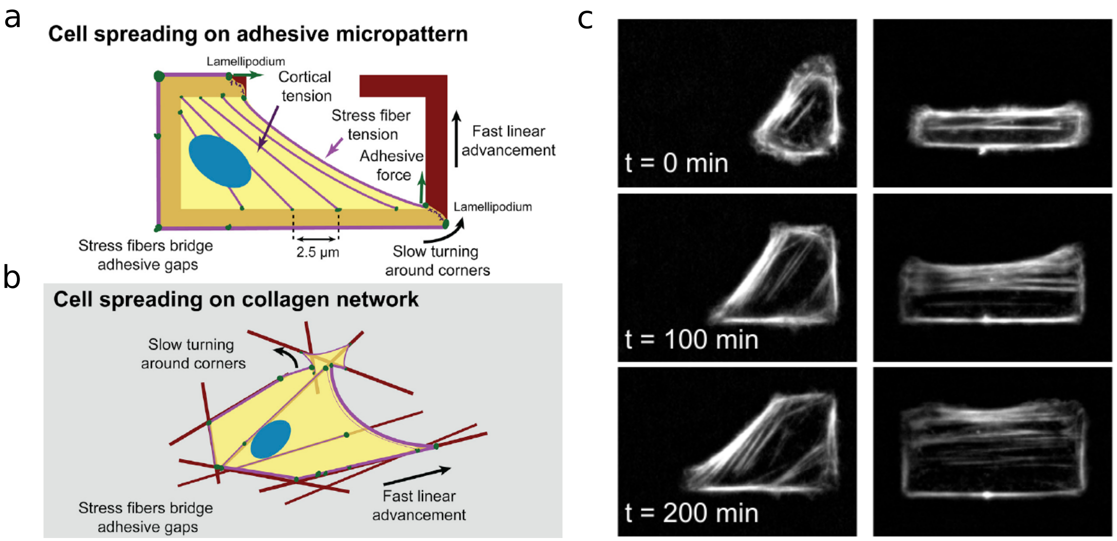

Figure 1.4: a) Illustration showing the spreading of a cell on a micropattern. In order to bridge the non-adhesive region between the pattern legs, the cell forms stress fibres spanning the non-adhesive region. The blue oval indicates the position of the cell nucleus. b) Illustration of a cell spreading on a network of collagen fibres. On this complicated network the cell has to turn corners and spread along linear elements similar to the situaiton on micropatterns. c) Six examples of U2OS cells spreading on micorpatterns. The formation of stress fibres can be clearly seen. All images are taken from Ref. [29].

cost. I apply a Cellular Potts Model (CPM) developed by Dr. Albert in the group of Prof. Schwarz which treats the cell as a collection of quadratic lattice sites and applies the Metropolis algorithm to sample the cell's phase space.

1.5 Outline of Thesis

In **Chapter 2** I treat the fluctuations of healthy and infected RBCs. After deriving the theoretical framework and extending the existing spherical harmonic approach, I explain the experimental data collected by Dr. Fröhlich. Based on these experimental observations, I apply a numerical approach to the RBC membrane, treating the discrete connections to the cytoskeleton explicitly. I make a connection between the membrane parameters and the microscopic changes induced by the parasite. I find that the increase in confinement is mostly caused by the incorporation of more connectors between the bilayer and the cytoskeleton.

I continue to examine the cytoskeleton, reducing scale by applying a reation-diffusion model to the molecular constituents of the cytoskeleton in **Chapter 3**. First, the properties of the relevant RBC and malaria associated proteins are discussed as their interactions are important for the molecular modelling approach. Second, I show experimental results from Prof. Lanzer's group which were analysed by Dr. Patra. Patra's analysis of protein colocalization proves to be an intriguing point of comparison to my molecular model. After explaining the details of the reaction-diffusion model and validating its applicability, I use the model to study KAHRP assembly within the RBC cytoskeleton. I find that KAHRP associates to the actin junctions only for a very small parameter range and that the parasite has to change binding affinities to move KAHRP away from the ankyrin junctions. Finally, the placement of PfEMP1 molecules is determined by a analytical approach, finding that the adhesion molecules are clustered towards the top of the knobs.

Next, I change to a much larger scale by considering the hydrodynamic flow behaviour of RBCs. The aim of **Chapter 4** is determining the shape of a RBC in a simplified two-dimensional environment. I explain how the mechanics of the viscoelastic RBC envelope can be coupled to the two dimensional Stokes flow and describe the implementation of this method in the FEniCS software. Since the implementation of the model used in this thesis does not seem to work in a numerically stable way, I point out potential problems in the implementation and show examples of calculated flow fields.

Finally, I add another perspective on cytoskeletal organisation in **Chapter 5** by examining the stress fibre architecture of cells spreading on micropatterns. After introducing the relevant biological structures, the Cellular Potts Model (CPM) is explained. Then, energy contributions during spreading are discussed in detail, comparing two different implementations of arc tensions. Finally, experimental data obtained by Elena Kassianidou and analysed by Dimitri Probst is compared to my simulation results. We find that the stress fibre network encodes the memory of the spreading process with a typical distance of 2.5 µm between subsequent stress fibres. The model is found to describe the experimental data very well.

Chapter 2

Flickering Analysis of Red Bood Cells

2.1 Testing Mechanical Properties of the Infected RBC Membrane

A common technique to shed light on membrane properties is the Flickering Analysis, in which the hight profile of a membrane is detected and analysed in Fourier space. The typical size of these fluctuations is approximately 30 nm and they are both of thermal and active origin.

RBCs are confined by lipid bilayers, which are two sheets of lipids being held together by hydrophobic effects. The lipids are free to flow within the membrane plane so they cannot withstand shear forces, but bending the membrane out of the plane is hindered by the lipid tails. Therefore, lipid bilayers can be understood by applying the Helfrich Hamiltonian, which takes into account curvature energy via a bending modulus κ and area conservation via the surface tension σ. The theoretical description needs to be extended in the case of RBCs, because contrary to lipid vesicles a spectrin network is anchored to the inner side of the RBC membrane and acts as an elastic layer.

One way to describe the coupled system is to introduce a harmonic confinement term to the Hamiltonian on a phenomenological level. This term is quadratic in membrane displacement and is proportional to the confinement parameter γ. Thus, the cytoskeleton is treated as a rigid shell at a fixed distance [4]. In contrast to the lipid bilayer, such a shell is mostly determined by its in-plane elasticity. Subsequently, it was found that the confinement can also be explained by the discrete attachment of the spectrin network to the phospholipid bilayer [33] which has similar effects to a continuous confining potential. Building on this idea, an approach with discrete tethers was successfully applied to describe the diffusion of proteins on RBCs over large length scales [34]. The equivalence between the discrete tether approach and the continuous approach holds within the experimentally relevant parameter range corresponding to RBCs [35, 36].

Historically, the fluctuations were described by equilibrium theories, whereas an active contribution to the flickering spectrum is commonly assumed nowadays [7]. Since the origin of the active processes is not entirely resolved, we start by looking more closely at the equilibrium theories. I focus on how an alteration of the spectrin network changes the membrane properties. Specifically, I compare healthy and malaria infected ring and trophozoite RBCs. Since the parasite restructures the spectrin network drastically and exports membrane proteins, it can be assumed that the mechanical properties of the iRBC membrane are altered equally. To determine the changes on the microscopic level, we employ a numerical model on the scale of the spectrin network attachment sites.

The outline of this chapter is as follows. First, I will introduce the theoretical background necessary to understand membrane fluctuations and derive a formula for harmonic confinement in spherical coordinates. Then the experimental data from Dr. Fröhlich (group of Prof. Tanaka) of malaria infected RBCs is discussed, which forms the basis for the application of my numerical model introduced in the section following this. Finally, implications for infected RBCs are discussed in detail.

The experimental data and the model described in this chapter have been published in Communications Biology under the title ”Hemoglobin S and C affect biomechanical membrane properties of P. falciparum-infected erythrocytes" [37].

2.2 Theoretical Analysis of Membrane Shape and Flickering

Unlike the properties of soap bubbles, which are mainly determined from their surface tension, the most important contribution to membrane behaviour is its curvature energy. A membrane is made of a very thin lipid bilayer which is only 4 nm thick. The relevant lateral extensions are a few length scales larger, so the membrane can be treated as a two-dimensional elastic sheet. The special structure of the lipid's hydrocarbon chains pointing towards each other makes it cost more energy to induce a curvature for it than for a soap film. Additionally, the area of such a bilayer stays approximately constant since the lipids remain densely packed due to their hydrophobic interactions.

2.2.1 Description via Differential Geometry

To describe surfaces in three dimensional space mathematically, some concepts from differential geometry need to be introduced. Let us denote a two dimensional surface by $\boldsymbol{R}(x,y)$, and define two tangent vectors at each point on the surface by $\boldsymbol{R}_i = \partial_i \boldsymbol{R}(x,y)$ with $i = x, y$. The unit normal to the surface at point (x,y) is defined as

$$\boldsymbol{n}(x,y) = \frac{\partial_x \boldsymbol{R} \times \partial_y \boldsymbol{R}}{|\partial_x \boldsymbol{R} \times \partial_y \boldsymbol{R}|}. \tag{2.1}$$

Using this, we can define two second rank tensors that describe the surface geometrically, the metric tensor g_{ij} and the curvature tensor h_{ij}:

$$g_{ij} = \partial_i \boldsymbol{R} \cdot \partial_j \boldsymbol{R} \tag{2.2}$$

$$h_{ij} = (\partial_i \partial_j \boldsymbol{R}) \cdot \boldsymbol{n}. \tag{2.3}$$

They are known as the first and second fundamental form respectively. Using these, we can define the mean curvature $\mathcal{H}$ and Gaussian curvature $\mathcal{K}$ of a point on the surface. To illustrate the meaning of these two curvatures more clearly, they can also be expressed in terms of the two principal radii of curvature, R_1 and R_2, which are the maximum and minimum radii of curvature respectively at the given point:

$$\mathcal{H} = -\frac{1}{2} Tr(h^i_j) = \frac{1}{2}\left(\frac{1}{R_1} + \frac{1}{R_2}\right) \tag{2.4}$$

$$\mathcal{K} = det(h^i_j) = \frac{1}{R_1 R_2}, \tag{2.5}$$

where $h^i_j = g^{ik} h_{kj}$. For example, a sphere has a mean curvature of $-1/R$ and a Gaussian curvature of $1/R^2$ at every point, where R denotes the radius. For more complex objects these values will vary in space.

An important question is which parametrization is chosen for the surface one wants to examine since this either simplifies the problem significantly or makes it intractable. In the following sections, two parametrizations will be used: the Monge parametrization and the spherical harmonic parametrization. Therefore, a brief introduction to each of these is provided below.

1. Monge parametrization for flat surfaces:
   In this parametrization the surface is described by a height function $h(x, y)$ and we assume small variations $|\nabla h(x, y)| \ll 1$:

   $$\boldsymbol{R} = \begin{pmatrix} x \\ y \\ h(x,y) \end{pmatrix}, \quad \partial_x \boldsymbol{R} = \begin{pmatrix} 1 \\ 0 \\ h_x \end{pmatrix}, \quad \partial_y \boldsymbol{R} = \begin{pmatrix} 0 \\ 1 \\ h_y \end{pmatrix}. \tag{2.6}$$

   In this parametrization $det(g) \approx 1 + (\nabla h)^2$, therefore the mean and Gaussian curvatures are $\mathcal{H} \approx \nabla^2 h$ and $\mathcal{K} \approx h_{xx} h_{yy} - h_{xy}^2$. Finally, the differential area element, $\mathrm{dA} = \sqrt{det(g)}\,\mathrm{dxdy}$, can be approximated as

   $$\mathrm{dA} \approx \left(1 + \frac{1}{2}(\nabla h)^2\right) \mathrm{dxdy}. \tag{2.7}$$

2. Spherical harmonic parametrization:
   If the object that we want to describe is close to a sphere of radius r_0, the following parametrization is useful:

   $$\boldsymbol{R}(\theta, \phi) = r_0(1 + u(\theta, \phi))\hat{\boldsymbol{r}} \quad \text{with} \quad u(\theta, \phi) = \sum_{l,m} u_{lm} Y_{lm}(\theta, \phi), \tag{2.8}$$

   where $0 \leq \theta \leq \pi$ and $0 \leq \phi \leq 2\pi$. $\hat{\boldsymbol{r}}$ is the unit vector pointing radially outward and $Y_{lm}(\theta, \phi)$ are the spherical harmonics weighted by coefficients u_{lm}.

   In this geometry, the mean curvature is $\mathcal{H} = -\frac{2}{r_0}$ and the Gaussian curvature is $\mathcal{K} = \frac{1}{r_0^2}$. The first and second fundamental forms are

   $$g = r_0^2 \begin{pmatrix} 1 & 0 \\ 0 & \sin^2\theta \end{pmatrix}, \qquad h = -r_0 \begin{pmatrix} 1 & 0 \\ 0 & \sin^2\theta \end{pmatrix}, \tag{2.9}$$

   and the area element is given by

   $$\mathrm{dA} = r_0 \sin(\theta) \mathrm{d}\theta \mathrm{d}\phi. \tag{2.10}$$

2.2.2 Energy Functional for a Membrane

Using these concepts an expression for the membrane Hamiltonian can be written down starting with only the local curvature energy, originally formulated by Canham [38] and Helfrich [39] as a surface integral:

$$\mathcal{F} = \int \mathrm{dA} \left(2\kappa \mathcal{H}^2 + \kappa_{\mathrm{G}} \mathcal{K}\right). \tag{2.11}$$

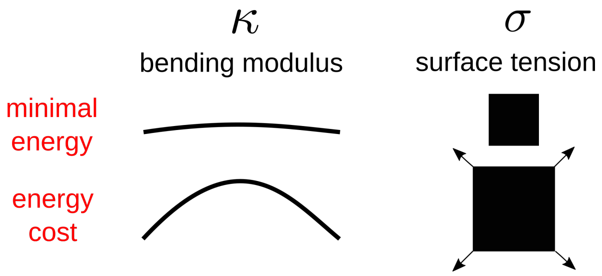

Figure 2.1: Graphical illustrations of the energy penalties introduced by the bending modulus and the surface tension.

The right hand side of (2.11) is an expansion in small curvatures and κ and κ_{G} are the bending rigidity and Gaussian bending rigidity respectively. The second term is often omitted since it is a constant if the topology of the described object does not change. By the Gauss-Bonnet theorem the integral over the Gaussian curvature is given by $4\pi(1-g)$, where g is the number of handles of the object (e.g. 0 for a vesicle and 1 for a doughnut-like object). The bending modulus κ determines how much force is required to to induce a bend membrane as depicted in Figure 2.1.

Area and volume conservation are incorporated into this expression via Lagrange multipliers, which can be identified as surface tension σ and pressure P:

$$\mathcal{F} = \int \mathrm{dA}\left(2\kappa\mathcal{H}^2 + \kappa_{\mathrm{G}}\mathcal{K} + \sigma\right) + P\int \mathrm{dV}. \tag{2.12}$$

The surface tension is not the usual surface tension known from soap bubbles because stretching or compressing the bilayer is not possible with the relevant force ranges. Instead, σ is an effective surface tension which comes from the membrane fluctuations; this will be discussed later on. The idea is that fluctuations reduce the projected area of the membrane, so stretching it out costs energy (compare Figure 2.1). For a detailed discussion of this topic see the work of Seifert [40]. He found that the description by an effective surface tension breaks down if the vesicle approaches a sphere, in which case the excess area approaches zero.

It was realized early on that this Hamiltonian was not sufficient to describe all vesicle shapes because it does not take into account that the sheet is made of two distinct layers which have a different lipid composition in most cases. In 1992 three groups came up with the area-difference-elasticity model [41, 42, 43] which accounts for the asymmetry of the two lipid layers by adding the following term to the Hamiltonian:

$$\frac{\kappa\alpha\pi}{4Ad^2}(\Delta A - \Delta A_0)^2. \tag{2.13}$$

Here, α is a dimensionless material parameter, d is the thickness of the membrane and $\Delta A = 2d\int \mathrm{d}A\ H$. Prior to this, different approaches had been taken in an attempt to describe this effect, but these could be shown to be special cases of the area-difference-elasticity model. One of these is the spontaneous curvature model introduced by Helfrich [39], which can be elegantly incorporated into the above expression by considering the deviation of the mean curvature from the spontaneous curvature $\mathcal{H}_0$:

$$\mathcal{F} = \int \mathrm{dA}\left[2\kappa(\mathcal{H}-\mathcal{H}_0)^2 + \kappa_{\mathrm{G}}\mathcal{K}\right] + \sigma\int \mathrm{dA} - P\int \mathrm{dV}. \tag{2.14}$$

The concept of spontaneous curvature is problematic in the sense that in principle it will dynamically vary in space because of the fluidity of the membrane.

Shape Equations and Fluctuations

From the Hamiltonian, information about equilibrium shapes and fluctuations around these can be extracted. To do this, the first and second variations of functional (2.14) need to be found while neglecting the Gaussian curvature term which only contributes if the topology changes (Gauss-Bonnet-Theorem):

$$\begin{aligned}
\delta\mathcal{F} = \int \big[&2\kappa\mathcal{H}^2\ \delta(\mathrm{dA}) + 4\kappa H\ \delta H\ \mathrm{dA} - 4\kappa\mathcal{H}_0 H\ \delta(\mathrm{dA}) - 4\kappa\mathcal{H}_0\ \delta H\ \mathrm{dA}\\
&+2\kappa\mathcal{H}_0^2\ \delta(\mathrm{dA})\big] + \sigma\int \delta(\mathrm{dA}) - P\int \delta(\mathrm{dV}) \qquad (2.15)\\
\delta^2\mathcal{F} = \int \big[&2\kappa\mathcal{H}^2\ \delta^2(\mathrm{dA}) + 8\kappa H\ \delta H\ \delta(\mathrm{dA}) + 4\kappa H\ \delta^2 H\ \mathrm{dA} + 4\kappa\ (\delta H)^2\ \mathrm{dA}\\
&-8\kappa\mathcal{H}_0\ \delta H\ \delta(\mathrm{dA}) - 4\kappa\mathcal{H}_0\ \delta^2 H\ \mathrm{dA} - 4\kappa\mathcal{H}_0 H\ \delta^2(\mathrm{dA}) + 2\kappa\mathcal{H}_0^2\ \delta^2(\mathrm{dA})\big]\\
&+\sigma\int \delta^2(\mathrm{dA}) - P\int \delta^2(\mathrm{dV}). \qquad (2.16)
\end{aligned}$$

In general coordinates the above variations are relatively complicated when expressed in terms of the first and second fundamental forms (see Zhong-Can and Helfrich [44]), but, using planar or spherical coordinate parametrization, they simplify dramatically.

By setting the first variation to zero, we find the shape equations (Euler-Lagrange equations) determining the equilibrium shape of the membrane. This is a fourth order differential equation that can only be solved analytically in very special cases, but more generally can be solved numerically. A common technique is to use triangulated surfaces or the finite element method for arbitrary shapes.

To study membrane fluctuation amplitudes experimentally, we need an analytical formula to fit the measured spectrum, with κ and σ acting as fit parameters. Deriving such a formula is only possible in planar or spherical geometry. Early approaches all used formulas derived from planar membranes and found these to fit reasonably well. At the length scale of the fluctuations, the vesicles can be approximated as locally flat. However, there are several studies extending the approach to nearly spherical vesicles [45, 46] and comparing the two approaches [47]. It was found that the approaches differ only for very small wave numbers. Below, we first discuss the planar approach because of its wide use. Then we do the same calculation in spherical coordinates because later an extension to the spherical harmonic approach will be made.

For the planar case, the Monge parametrization will be used. Since the mean and Gaussian curvature are zero in this case, the expression for the second variation of the Hamiltonian simplifies considerably:

$$\delta^2\mathcal{F}_{\text{Monge}} = \int \left(\frac{\kappa}{2}(\Delta h)^2 + \frac{\sigma}{2}(\nabla h)^2\right) \mathrm{dA}. \tag{2.17}$$

For more details see the expressions for the variations in Appendix B.1. As for most correlations, it is useful to Fourier transform this equation and work with the Fourier modes:

$$\begin{aligned} h_q &= \int \mathrm{d}\boldsymbol{r} h(\boldsymbol{r}) e^{-i\boldsymbol{q}\cdot\boldsymbol{r}}, \\ h(\boldsymbol{r}) &= \frac{1}{A}\sum_q h_q e^{i\boldsymbol{q}\cdot\boldsymbol{r}}, \\ \delta^2\hat{\mathcal{F}}_{\text{Monge}} &= \int \left(\kappa q^4 + \sigma q^2\right) h_q h_q^* \mathrm{d}q. \end{aligned}$$

By the equipartition theorem, each mode corresponds to an energy of $k_BT/2$ and hence we find:

$$\langle h_q h_q^* \rangle = \frac{k_BT}{\kappa q^4 + \sigma q^2}. \tag{2.18}$$

This equation shows that bending is important on the small scales, whereas surface tension contributes to the larger length scales.

Let us now do the same calculation for spherical vesicles. Usually the spontaneous curvature $\mathcal{H}_0$ is neglected in the spherical case but here I keep terms proportional to $\mathcal{H}_0$ in order to examine their effects later on. The basis of the calculation for spherical membranes is the parametrization of the equilibrium shape $\mathbf{r} = r_0(1+u)\hat{\mathbf{r}}$ with u describing deviations from the sphere. For exact expressions of the fundamental forms and curvatures see Appendix B.1. By setting the first variation to zero, we find an equation for the pressure of a spherical vesicle:

$$P = \frac{4\mathcal{H}_0\kappa + \mathcal{H}_0^2 r_0\kappa + 2r_0\sigma}{r_0^2}, \tag{2.19}$$

which will be used to eliminate the pressure from the second variation.

Taking this into account and plugging everything into the equation for the second variation, we find for deviations from the sphere:

$$\delta^2\mathcal{F} = \int \mathrm{dA} u \left(\frac{\kappa}{r_0^2}\Delta^2 + \sigma_{\text{eff}}\Delta + \gamma_{\text{eff}}\right) u, \tag{2.20}$$

where

$$\sigma_{\text{eff}} = -\sigma + \frac{2\kappa}{r_0^2} - \frac{4\mathcal{H}_0\kappa}{r_0} - \mathcal{H}_0^2\kappa/2, \tag{2.21}$$

$$\gamma_{\text{eff}} = -2\sigma - \frac{8\mathcal{H}_0\kappa}{r_0} - \mathcal{H}_0^2\kappa, \tag{2.22}$$

and Δ is the Laplace-Beltrami operator on the surface, which in this geometry reduces to the angular part of the spherical Laplacian. Since the spherical harmonics are eigenfunctions of this operator, it is useful to decompose u in spherical harmonics:

$$u(\theta, \phi) = \sum_{l,m} u_{l,m} Y_{l,m}(\theta, \phi), \tag{2.23}$$

$$\Delta Y_{l,m} = -l(l+1) Y_{l,m}. \tag{2.24}$$

One has to be careful to start the sum at $l = 2$ since $l = 0$ corresponds to the volume changes and $l = 1$ to the movement of the centre of mass.

Using these, we write

$$\delta^2 \mathcal{F} = r_0^2 \sum_{l,m} \lambda_{l,m} |u_{l,m}|^2, \tag{2.25}$$

$$\text{with } \lambda_{l,m} = l(l+1) \left[l(l+1)\kappa / r_0^2 - \sigma_{\text{eff}} \right] + \gamma_{\text{eff}}. \tag{2.26}$$

After taking the thermal average of (2.25), the equipartition theorem can be used to fix the energy in each mode,

$$\frac{k_B T}{2} = \frac{1}{2} \delta^2 \mathcal{F}_{l,m}. \tag{2.27}$$

Hence, the dimensionless mean square fluctuation amplitudes of a spherical vesicle are given by:

$$\langle |u_{l,m}|^2 \rangle = \frac{k_B T}{r_0^2 \lambda_{l,m}} = \frac{1}{r_0^2} \frac{k_B T}{l(l+1) \left[l(l+1)\kappa / r_0^2 - \sigma_{\text{eff}} \right] + \gamma_{\text{eff}}}. \tag{2.28}$$

Notice that the right hand side does not depend on m; due to the symmetry of the geometry in question, the m modes are equally excited.

One reason to use this more complicated approach is in spherical geometry, bending modes require tangential and normal movement, unlike in the planar case where bending and shear can be decoupled [48]. Using the formula for a planar membrane would miss this effect.

Relation between Tension and Excess Area

The fluctuations calculated above lead to an additional area reservoir, since the actual surface area is larger than the projected area A. In this context, the excess area is defined as:

$$\alpha = \frac{\Delta A}{A} \approx \frac{1}{2A} \int \mathrm{d}\boldsymbol{r} |\nabla h(\boldsymbol{r})|^2, \tag{2.29}$$

where the approximation comes from using the Monge parametrization. This quantity can be evaluated by inserting the previously derived expression for $\langle |h_q| \rangle^2$

from Equation (2.18):

$$\alpha = \frac{1}{2A}\sum_q q^2\langle|h_q|\rangle^2 = \frac{1}{4\pi}\int \mathrm{d}q q^3\langle|h_q|\rangle^2 = \frac{1}{4\pi}\int \mathrm{d}q q^3 \frac{k_BT}{\kappa q^4 + \sigma q^2} \tag{2.30}$$

$$= \frac{k_BT}{8\pi\kappa}\int_{q_{\min}}^{q_{\max}} \mathrm{d}q \frac{2q}{q^2+\sigma/\kappa} = \frac{k_BT}{8\pi\kappa}\frac{\ln(q_{\max}^2+\sigma/\kappa)}{\ln(q_{\min}^2+\sigma/\kappa)}. \tag{2.31}$$

We see that the excess becomes zero (indicating a completely flat membrane) if either the surface tension is much larger than the bending rigidity or the ratio of bending rigidity to temperature diverges.

2.2.3 Description of RBCs

RBC Shapes

The area-difference-elasticity model described above can predict all shapes of normal vesicles. However, some shapes observed experimentally for RBCs (e.g. echinocytes) are not predicted by this model, which implies that there is an aspect of the RBC structure missing. In 2002, Lim, Wortis and Mukhopadhyay [2] made a simple addition to the Hamiltonian which accounts for the missing effects. Their idea was to incorporate the stretch and shear elasticity of the RBC cytoskeleton in an extra contribution to the Hamiltonian. The results of their approach are shown in Figure 2.2 where they compare experimental shapes to those predicted by their model.

For their calculations they used the ADE Hamiltonian $\mathcal{F}_{\text{bending}}$ and the additional elastic contribution $\mathcal{F}_{\text{elastic}}$ to arrive at the following surface integrals:

$$\begin{aligned}\mathcal{F}_{\text{bending}} =& \frac{\kappa}{2}\int \mathrm{dA}\,[2\mathcal{H}-\mathcal{H}_0]^2 \\ &+ \frac{\alpha\kappa}{2}\frac{\pi}{Ad^2}(\Delta A - \Delta A_0)^2 \\ \mathcal{F}_{\text{elastic}} =& \frac{K_\alpha}{2}\int \mathrm{dA}(\alpha^2 + a_3\alpha^3 + a_4\alpha^4) \\ &+ \mu\int \mathrm{dA}(\beta + b_1\alpha\beta + b_2\beta^2),\end{aligned}$$

with the following constants:

K_α	linear elastic stretching modulus,
a_i, b_i	coefficients for nonlinear terms,
μ	linear elastic shear modulus,
α, β	local area and shear strain invariants.

In this approach, the membrane is treated as a hyperelastic isotropic material. In reality the cytoskeleton is a strain hardening material, but this does not seem to play an important role for the equilibrium shapes which do not require large deformations.

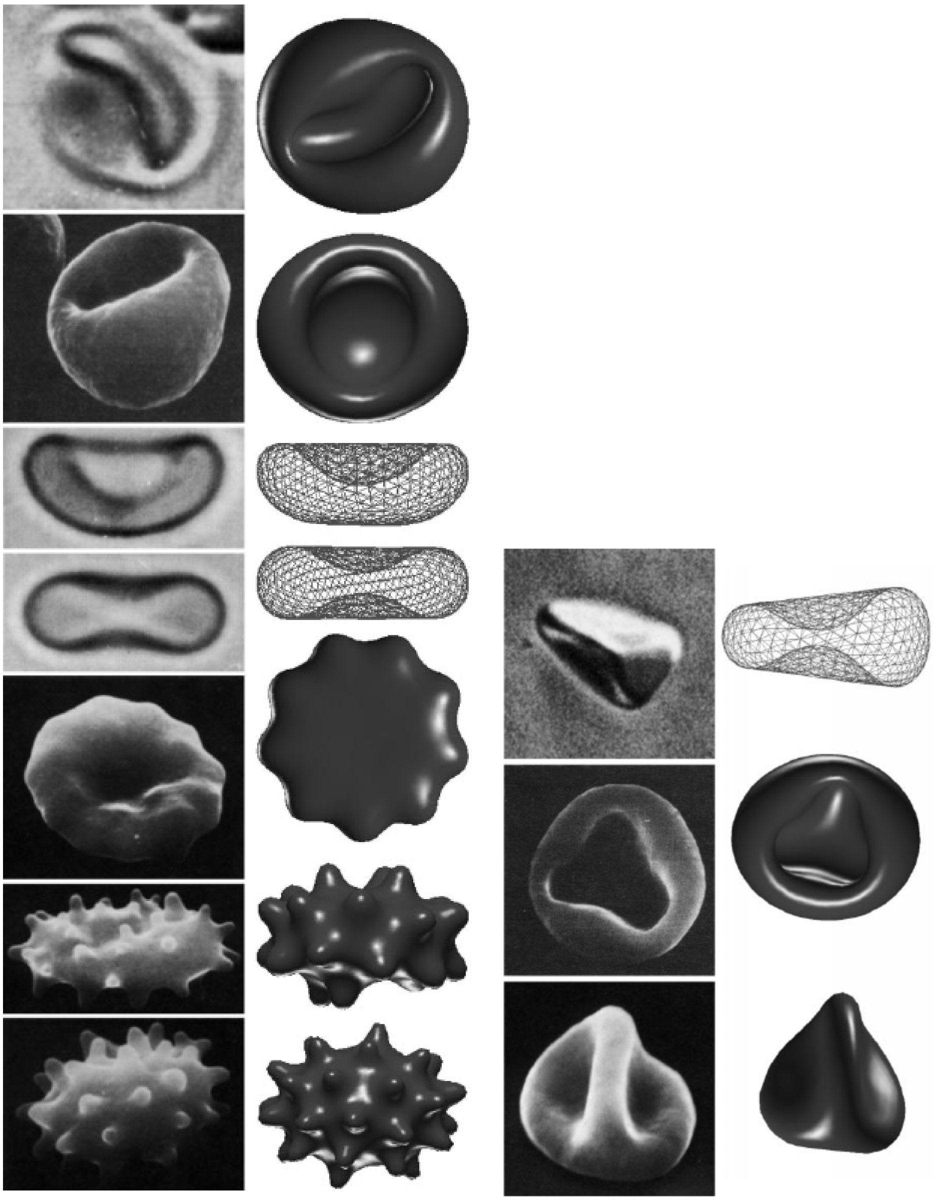

Figure 2.2: RBC shapes produced by Wortis *et al.* [2] by taking into account the elasticity of the RBC cytoskeleton. They compare experimental images (column one and three) to calculated shapes (column two and four). The experimental and modelled shapes on the left are from the main stomatocyte-discocyte-echinocyte cycle and on the right other interesting shapes (not from this main cycle) are shown.

RBC Membrane Fluctuations

To describe membrane fluctuations of RBCs, the above approach is not so useful since an expression for the second deviation of the Hamiltonian needs to be found analytically. In 1975 Brochard *et al.* [1] first applied the Helfrich Hamiltonian approach to understand the membrane undulations of RBCs. The aim of this and follow up studies was to extract membrane specific parameters from experimental data. However, some discrepancies between the data and the theoretical description were found.

Since healthy RBCs have a discocyte shape, some approaches tried looking at more complex membrane geometries, which turns out to be rather difficult because it is hard to find suitable parametrisations of the surface. In one approach Döbereiner *et al.* [49] combined Monte Carlo Simulations with Flicker Spectroscopy to determine the membrane's spontaneous curvature.

In subsequent years it was realized that contributions from the underlying elastic spectrin network were missing in the description. It was found that large wavelength undulations were smaller than expected and the coupled nature of the membrane was very likely to be important for fixing this problem. There are two main approaches that have been explored. In one of them, the composite membrane is considered to be one entity that fluctuates with contributions from the fluid bilayer and the elastic skeleton taken together. In the other approach, the bilayer is thought to fluctuate alone, constrained by either an elastic shell at some distance or by discrete pinning sites. The most realistic approach is the latter but the former has the advantage of being analytically traceable as it treats the cytoskeleton as a continuum.

The concept of confined fluctuations has been explored in other contexts besides the RBC membrane. People have looked at cases of two bilayers fluctuating next to each other at a fixed distance or onw bilayer fluctuating next to a rigid wall [50, 51, 52, 53]. A detailed discussion of this topic can be found in the work by Auth *et al.* [54], in which they consider fluid-fluid, fluid-solid and solid-solid membrane pairs being held at a constant average distance by an external pressure. They show that fluid membranes can be described by a constant bending modulus, whereas solid membranes need a wave-vector dependent modulus. When considering a fluid-solid membrane pair, they found that for small separations the system scales like a solid membrane next to a wall and for large distances the scaling of a fluid membrane next to a wall is recovered. By applying their theory to RBCs, they found that above 400 nm the membrane can be described as one effective membrane with bending and shear and below this wavelength the two layers have to be treated separately.

Based on the idea of a confined membrane, Gov *et al.* [4] introduced a harmonic confinement term to the Hamiltonian to account for the cytoskeletal network beneath the bilayer:

$$\mathcal{F} \approx \int \left(\frac{\kappa}{2}(\Delta h)^2 + \frac{\sigma}{2}(\nabla h)^2 + \frac{\gamma}{2} h^2 \right) \mathrm{dA}. \qquad (2.32)$$

This approach is very elegant, since it simplifies the description in a way that makes it trackable analytically and yields a simple formula for analysing experimental

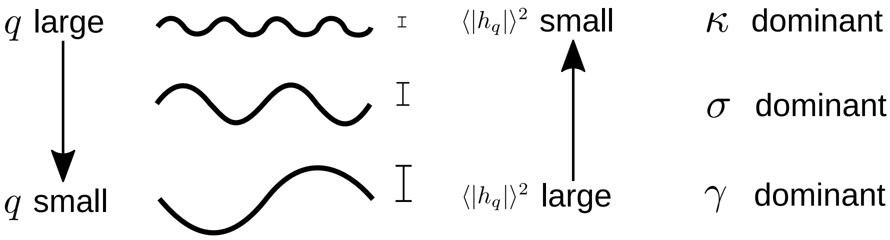

Figure 2.3: Illustration of the different mean square displacement regimes in Fourier space. For a large wavenumber q (short wavelength) the displacements are large and κ dominates. For a small wavenumber (long wavelength) the displacements are large and the confinement dominates. In the intermediate regime the surface tension becomes important.

data. They think of the cytoskeleton as a rigid shell at a fixed average distance. In later work, they show that such a confining potential can arise from sparce tethering by calculating the fluctuations of bilayers with additional sinosoidal and delta function potentials [33].

The Hamiltonian considered in the method above leads to the following mean squared displacement in Fourier modes:

$$\langle h_q^2 \rangle = \frac{k_B T}{\gamma + \sigma q^2 + \kappa q^4}. \tag{2.33}$$

Here, we see that the confinement is mostly important for the small modes, which corresponds to large wavelengths as illustrated in Figure 2.3.

Although this formula can easily be applied to experimental data, it does not give much insight into the microscopic details that lead to this confinement. There have been several approaches that have tried to better understand these details by treating the cytoskeleton explicitly by springs. This approach can be justified since spectrin is a flexible polymer which behaves like a spring in some regime (for larger extensions it has a strain hardening behaviour). One way to approach this is to treat the cytoskeleton as a two-dimensional network of springs [55] that fluctuate with the bilayer. This is similar to the approach of one composite membrane discussed above. A different approach is to only consider the attachment sites between the bilayer and the cytoskeleton, and model these by springs.

Merath *et al.* [35] have shown that this is a valid approach to calculate fluctuation amplitudes. They add a sum over the discrete springs to the Hamiltonian and use the approach of Lin *et al.* [56] to calculate the mean squared displacements. For weak springs their effects can be described by an equivalent confinement parameter γ, but for very strong pinning a negative surface tension would be necessary to describe the amplitudes.

Derivation of Confinement in Spherical Harmonics

As explained in the last section, Gov *et al.* introduced the confinement parameter γ to the Hamiltonian in Monge parameterization in order to explain the contribution of the spectrin network to the fluctuations of RBC membranes. Here, I show

how the same confinement parameter can be implemented into the spherical harmonic approach. The motivation for this comes from considering length scales; it has been shown that the planar and spherical approaches only differ for small wavenumbers [47], but this is exactly the same regime where γ contributes.

I start by adding the term $\gamma r_0^2 u^2$ to the second variation of the energy, such that deviations in u are harmonically damped. The difference to the planar case is the deviation u points in the radial direction. Using the same notation as above, we see the new term just needs to be added to γ_{eff} (compare with Equation (2.20)):

$$\delta^2 \mathcal{F} = \int \mathrm{dA} u \left(\frac{\kappa}{r_0^2} \Delta^2 + \sigma_{\text{eff}} \Delta + \gamma_{\text{eff}} \right) u, \tag{2.34}$$

where

$$\sigma_{\text{eff}} = -\sigma + \frac{2\kappa}{r_0^2} - \frac{4\mathcal{H}_0 \kappa}{r_0} - \mathcal{H}_0^2 \kappa/2, \tag{2.35}$$

$$\gamma_{\text{eff}} = \gamma r_0^2 - 2\sigma - \frac{8\mathcal{H}_0 \kappa}{r_0} - \mathcal{H}_0^2 \kappa. \tag{2.36}$$

The mean squared deviations of the spherical harmonic modes can be derived, giving

$$\langle |u_{l,m}|^2 \rangle = \frac{k_B T}{r_0^2 \lambda_{l,m}} = \frac{1}{r_0^2} \frac{k_B T}{l(l+1)\left[l(l+1)\kappa/r_0^2 - \sigma_{\text{eff}}\right] + \gamma_{\text{eff}}}. \tag{2.37}$$

For $H_0 = 0$, this reduces to

$$\langle |u_{l,m}|^2 \rangle = \frac{k_B T}{\gamma r_0^4 + (l-1)l(l+1)(l+2)\kappa + (-2 + l + l^2) r_0^2 \sigma}. \tag{2.38}$$

2.2.4 Spherical Harmonic Approach Containing γ and $\mathcal{H}_0$

Now we can examine how the spherical description differs from the planar case in the presence of the spontaneous curvature $\mathcal{H}_0$ and the confinement parameter gamma. In order to compare the two descriptions, the spherical harmonic modes $u_{l,m}$ need to be written in terms of the Fourier mode q. For a detailed description on how this is done, see Appendix B.3. The ratios of the planar mean squared amplitudes to the spherical ones are plotted in Figure 2.4.

In the case of $\gamma = \mathcal{H}_0 = 0$, the spherical approach yields slightly larger fluctuations than the planar approach for small wavenumber and slightly smaller fluctuations for high wavenumber. This means when using the planar approximation we very slightly overestimate the size of fluctuations at short wavelengths, whereas for long wavelengths we underestimate their size. The plots in Figure 2.4 show that γ and $\mathcal{H}_0$ increase the difference between the two approaches at long wavelengths but to not affect the short wavelengths. Note that for a negative spontaneous curvature the planar fluctuations are always higher than the spherical ones.

However, the differences discussed above are small enough in magnitude that they should not matter for the application to experimental data, as the experimental noise will be larger than these deviations. This is the reason why applying the planar approach has been so successful.

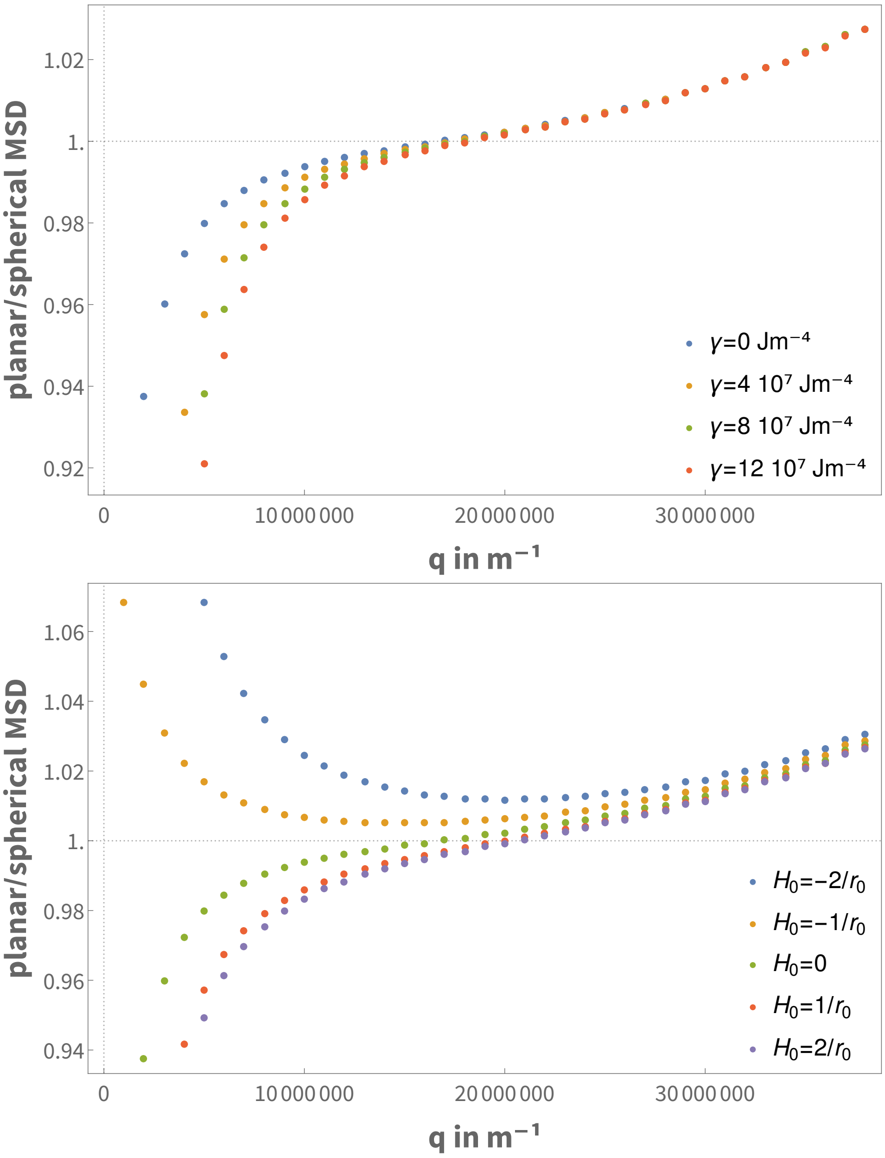

Figure 2.4: Comparison of the mean square displacements (MSD) calculated for a planar and a spherical membrane. In the left graph the confinement is varied while keeping $\mathcal{H}_0 = 0$ and on the right the spontaneous curvature is varied while keeping $\gamma = 0$.

2.2.5 Membrane Dynamics

In order to extract values for the viscosity inside the RBC, it is necessary to look at the dynamics of the RBC membrane and derive an expression for the power spectral density. For this it is essential to incorporate the fluid on either side of the membrane and since inertia is negligible for such small systems (due to having a low Reynolds number), the hydrodynamic flow is described by the Stokes equation [57]

$$-\nabla p(\boldsymbol{r}) + \eta \Delta \boldsymbol{v}(\boldsymbol{r}) = -\boldsymbol{f}(\boldsymbol{r}). \tag{2.39}$$

Here, $p(\boldsymbol{r})$ is the pressure, η is the viscosity, $\boldsymbol{v}(\boldsymbol{r})$ is the fluid velocity and $\boldsymbol{f}(\boldsymbol{r})$ is the force on the fluid. Additionally, the continuity equation, $\nabla \cdot \boldsymbol{v}(\boldsymbol{r}) = 0$, has to hold. A common approach used to solve these types of equations is by using a Green's function. In this approach the point-like force $f(\boldsymbol{r})$ is related to the induced velocity field by a Green's function $\Lambda(\boldsymbol{r})$:

$$v(\boldsymbol{r}) = \int \mathrm{d}^3\boldsymbol{r}' \Lambda(\boldsymbol{r} - \boldsymbol{r}') f(\boldsymbol{r}'). \tag{2.40}$$

In this context, the Green's function is also known as the Oseen tensor. A no-slip condition is required at the membrane, therefore the fluid and membrane velocity are equivalent at the interface. As before, we consider out of plane movement of a flat membrane using Monge parametrisation. For this system, embedded in an infinite homogeneous fluid with viscosity η, the Oseen tensor in real and Fourier space is given by

$$\Lambda(\boldsymbol{r}) = \frac{1}{8\pi\eta|\boldsymbol{r}|} \quad \text{and} \quad \Lambda(\boldsymbol{q}) = \frac{1}{4\eta|\boldsymbol{q}|}, \tag{2.41}$$

respectively. Usually this simple function is sufficient to analyse experimental data, but when looking at time correlation functions the importance on hydrodynamic effects has also been described in several studies [58, 34]. Furthermore, the Green's function has been found for several other more involved cases. Gov *et al.* [59] treated the case of a permeable and impermeable wall next to the membrane. In the case of two different viscosities at either side of the membrane, η is replaced by their average as discussed in Ref. [34]. It is also clear that in general the presence of a wall slows the relaxation of the membrane because of the trapped water. It has been found, that this hydrodynamic damping by another surface is very important for fluctuations in time, but not so much for the spacial analysis [60].

Since we identified the fluid movement at the interface with the membrane movement, we can now write down an overdamped Langevin dynamics equation for the membrane

$$\frac{\partial h(\boldsymbol{r}, t)}{\partial t} = \int \mathrm{d}\boldsymbol{r}' \Lambda(\boldsymbol{r} - \boldsymbol{r}') \left[-\frac{\partial \mathcal{F}}{\partial h(\boldsymbol{r}', t)} + \xi(\boldsymbol{r}', t) \right], \tag{2.42}$$

where $\xi(\boldsymbol{r}', t)$ is a thermal random force. This equation is more easily treated in

Fourier space because the convolution is removed:

$$\frac{\partial h_q(t)}{\partial t} = \left[-\omega_q h_q(t) + \lambda_q \xi_q(t)\right], \tag{2.43}$$

$$\omega_q = \lambda_q(\kappa q^4 + \sigma q^2) = \frac{\kappa q^3 + \sigma q}{4\eta}, \tag{2.44}$$

where the correlations of the thermal noise are given by

$$\langle \xi_q(t) \rangle = 0 \tag{2.45}$$

$$\langle \xi_q(t)\xi_{q'}(t') \rangle = 2k_B T A \Lambda_q^{-1} \delta_{q,-q'} \delta(t-t'). \tag{2.46}$$

We can identify these equations as Ornstein-Uhlenbeck processes and therefore can write down the solution for the time correlations functions:

$$\langle h_q(t) h_{q'}(0) \rangle = \frac{k_b T}{\kappa q^4 + \sigma q^2} e^{-\omega_q t} \delta_{q,-q'}. \tag{2.47}$$

The autocorrelation function is given by the Fourier transform of the time correlation function:

$$\langle |h_q(\omega)|^2 \rangle = \frac{2k_B T \lambda_q}{\omega^2 + \omega_q^2}. \tag{2.48}$$

The power spectral density is now given by the integral over all Fourier modes:

$$\langle |h(\omega)|^2 \rangle = \int \frac{\mathrm{d}\boldsymbol{q}}{(2\pi)^2} \frac{2k_B T \lambda_q}{\omega^2 + \omega_q^2} = \frac{4\eta k_B T}{\pi} \int_{q_{\min}}^{q_{\max}} \frac{\mathrm{d}q}{(4\eta\omega)^2 + (\kappa q^3 + \sigma q)^2}. \tag{2.49}$$

If we assume $q_{\min} = 0$ and $q_{\max} = \infty$, the scaling of the power spectral density with ω can be found for the limit $\omega \to 0$ and $\omega \to \infty$:

$$\lim_{\omega \to 0} \langle |h(\omega)|^2 \rangle = \frac{k_B T}{2\sigma\omega}, \tag{2.50}$$

$$\lim_{\omega \to \infty} \langle |h(\omega)|^2 \rangle = \frac{k_B T}{6\pi (2\eta^2\kappa)^{1/3} \omega^{5/3}}. \tag{2.51}$$

For small frequencies the power spectral density is dominated by tension and does not depend on viscosity directly. Indirectly it still does because for a more viscous fluid the frequency goes down. Betz *et al.* [6] found that by using the planar approach the power spectral density is altered in the low frequency regime, leading to a systematic overestimation of tension. Calculating the power spectral density in the spherical harmonic parametrisation yields

$$\langle |u(\omega)|^2 \rangle = \sum_{l=2}^{l_{\max}} \langle |u_{lm}|^2 \rangle r^2 \frac{\omega_l}{\omega_l^2 + \omega^2} \frac{2l+1}{2\pi}, \tag{2.52}$$

$$\omega_l = \frac{\kappa(l+2)(l-1)l(l+1) + \sigma r(l+2)(l-1)}{\eta r^3 Z(l)}, \tag{2.53}$$

$$Z(l) = \frac{(2l+1)(2l^2+2l-1)}{l(l+1)}. \tag{2.54}$$

2.2.6 Incorporation of Active Elements

All the analysis described so far is based on equilibrium physics. For living cells, however, it is expected that active processes will play a role as well. In the case of RBCs there have been various attempts to identify non-equilibrium processes in the membrane and incorporate these in the theory. Although it is clear that there are active processes taking place, it is still not understood what microscopic processes they originate from and how exactly the RBC fluctuations are influenced. In this section I will give an overview of the ideas that have been implemented and what we can learn from the different approaches. The theories can roughly be divided into two categories; activity induced by active membrane proteins, and activity applied to the membrane by the cytoskeleton.

Evans *et al.* [61] used shallow shell theory to take into account the RBC's discocyte shape when calculating the membrane fluctuations. They were able to show that active processes are not necessary to explain the experimental fluctuation data, but singular curves on the surface and regions with alternating Gaussian curvature lead to an altered fluctuation spectrum. Although this is an aspect that has not been taken into account before, it does not exclude that active processes are relevant. There have been experiments that show changes in membrane behaviour upon switching on activity [62]. In reality both aspects will play a role, but an important question to consider is under specific situations, which one has the bigger effect.

Activity Through Membrane Proteins

The first incorporation of active channels was done by Prost *et al.* [63] by incorporating freely diffusing ion channels into the membrane description. They did this by introducing on/off states whose switching is exponentially correlated and which contribute a force f if they are activated. Therefore, an active noise is added to the Langevin equation:

$$\xi_k^{\text{active}}(t) = f \sum_j S_j(t) e^{i\boldsymbol{q}\cdot\boldsymbol{R}_j(t)}, \tag{2.55}$$

where S_k is either zero or one with the correlation time τ_a and $\boldsymbol{R}_j(t)$ is the location of the ion channel. An estimate for the average channel force was given in Ref. [64]. The authors arrive at a force of 1-10 pN by accounting for a transit time of a single ion of 10^{-7} s.

As we can see in Figure 2.5, the activity due to the ion pumps introduces a shift and alters the scaling properties of the mean squared displacement. Subsequently, this model was extended to take into account coupling between the pump activity and the membrane's curvature, which can lead to instabilities and travelling waves [65, 66].

It was proposed in several studies that the activity can be accounted for by an increased effective temperature [67, 68]. However, the issue is more complicated depending on the source of the activity, and can depend on modes and frequencies [69].

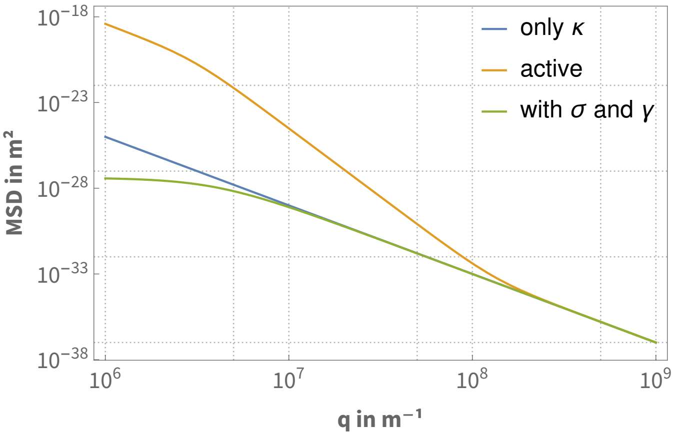

Figure 2.5: Mean squared displacements are plotted for different models as indicated in the legend.

Activity Through Cytoskeletal Effects

Based on the idea that cytoskeleton components can push on the membrane like polymerising actin in cell protrusion, cytoskeleton induced active fluctuations have been investigated. The first such model was developed by Gov *et al.* [67] who considered spectrin actin dissociation events as force kicks on the membrane. The biological foundation for this treatment is the phosphorylation of protein 4.1 through the consumption of ATP, which induced the dissociation of the spectrin end from the actin junction. They managed to reproduce the ATP dependent experimental data with their model and found that these processes can be described by an increased effective temperature. A similar approach was shown to reproduce ATP-dependent experimental data more recently [70].

In a simulation study, Zhang *et al.* [71] treated the bilayer as a continuous sheet that is tethered by entropic springs representing the connections between the cytoskeleton and the bilayer. In their simulations they account for the diffusion of these anchor sites and for dissociation events similar to the approach discussed above. These simulations confirm that experimental data can be reproduced by this approach.

A slightly different approach has been developed by Turlier *et al.* [7]. In their study they show that RBC fluctuations contradict the fluctuation-dissipation theorem and therefore are not of pure thermal origin. The activity enters their theoretical and computational model through a local modulation of the shear modulus.

Overall, it is clear that activity plays an important role in the dynamical behaviour of the RBC membrane. In the following work, we decided to neglect this effect because the focus is on the alterations of the RBC membrane throughout the malaria infection. Since the exact source of the RBC membrane activity is not clear, even less is known about how it would change during a malaria infection. This is a topic that could be treated in the future.

2.3 Experimental Flickering Data for Malaria Infected RBCs

As part of the SFB 1129 Integrative of Pathogen Replication and Spread, a collaboration was established between the groups of Prof. Lanzer, Prof. Tanaka and Prof. Schwarz. The model discussed in the next section was developed to explain the data produced by Benjamin Fröhlich from the group of Prof. Tanaka. In this section, the experimental data is shown and its analysis explained. The aim of the experiments was to measure the mean squared fluctuations and the power spectral density of RBC membranes.

The experiments were conducted with uninfected (HbAA) RBCs as well as ring and throphozoite stage (HbAA) iRBCs in order to see changes during the infection. The analysis was repeated for HBAS and HBAC RBCs, which are known to exhibit differences in their development and the same experiments were also done for knobless parasite mutants.

In the experiments, the Plasmodium falciparum strain FCR3 was used and the RBC cultures were synchronized within a time window of six hours. The cells were kept in an RPMI-1640 medium supplemented with bovine serum albumin at a haematocrit of 0.1% at 37° C. The images of the RBCs were taken with a phase contrast microscope and the cells' rims were detected by a Gaussian fit on the gradient images, so that the Fourier modes of the height spectrum could be extracted. From this the mean squared displacement for the membrane height could be calculated.

As described in the previous section a theoretical model can be fit to the experimental data. Here we choose the formula derived from the Hamiltonian including a confining potential [4]:

$$H = \int \mathrm{dA} \left[\frac{1}{2}\kappa(\nabla^2 h)^2 + \frac{1}{2}\sigma(\nabla h)^2 + \frac{1}{2}\gamma h^2 \right]. \tag{2.56}$$

Previously, I showed how the mean squared fluctuations are derived in Fourier space but that formula was derived for deviations of a two dimensional sheet from the flat reference state. Here, the expression needs to be modified to fit the experimental limitation that only fluctuations in the $y = 0$ plane are measured. A derivation of the following formula is shown in Appendix C.1:

$$\begin{aligned} \langle h(q_x, y=0)^2 \rangle = & \frac{k_B T}{L} \left| \sqrt{\frac{\kappa}{2(\sigma^2 - 4\kappa\gamma)}} \left[\frac{1}{\sqrt{2\kappa q_x^2 + \sigma - \sqrt{\sigma^2 - 4\kappa\gamma}}} \right.\right. \\ & \left.\left. - \frac{1}{\sqrt{2\kappa q_x^2 + \sigma + \sqrt{\sigma^2 - 4\kappa\gamma}}} \right] \right|, \end{aligned} \tag{2.57}$$

where L is the size of the membrane patch. By applying this formula to the data, fits for κ, σ and γ can be extracted and compared for the different infection stages as can be seen in Figure 2.6.

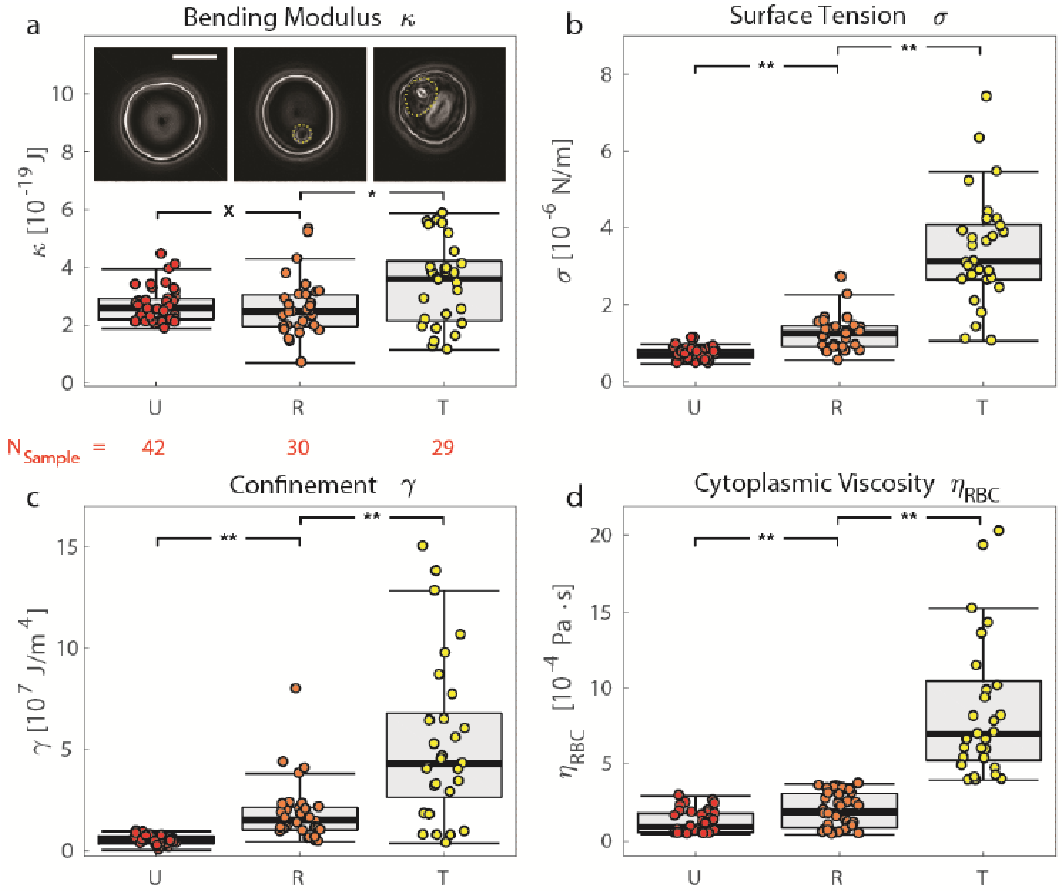

Figure 2.6: a) Bending modulus κ, b) surface tension σ, and c) confinement γ calculated for HbAA cells at uninfected (U), ring (R), and trophozoite stage (T) using (2.57). In a) gradient images are presented of the corresponding infection stages with the parasite marked by the dotted lines. The scale bar indicates 5 µm. d) Corresponding cytoplasmic viscosity η_{RBC} calculated by a fit with Eq. (2.52) (Welch t-test: x no significant difference, $^*p < 0.05$, $^{**}p < 0.001$). This Figure was produced by Benjamin Fröhlich.

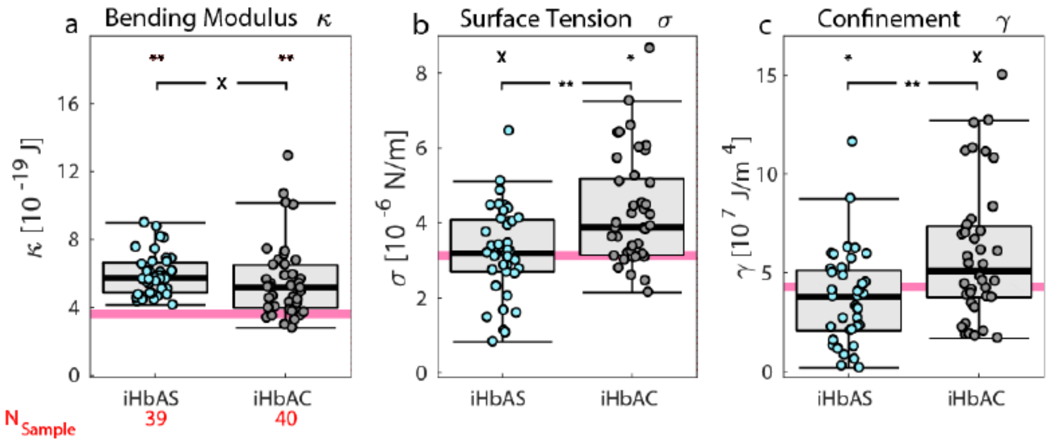

Figure 2.7: a) Bending modulus κ, b) surface tension σ, and c) confinement γ calculated using (2.57) for hemoglobinopathies HbAS and HbAC at the trophozoite stage of infection. Red lines correspond to the median values of HbAA at the identical parasite stage for the respective mechanical parameter. Welch t-test was performed against HbAA (symbols top row) and among the hemoglobinopathies (x no significant difference, $^{*}p < 0.05$, $^{**}p < 0.001$). This Figure was produced by Benjamin Fröhlich.

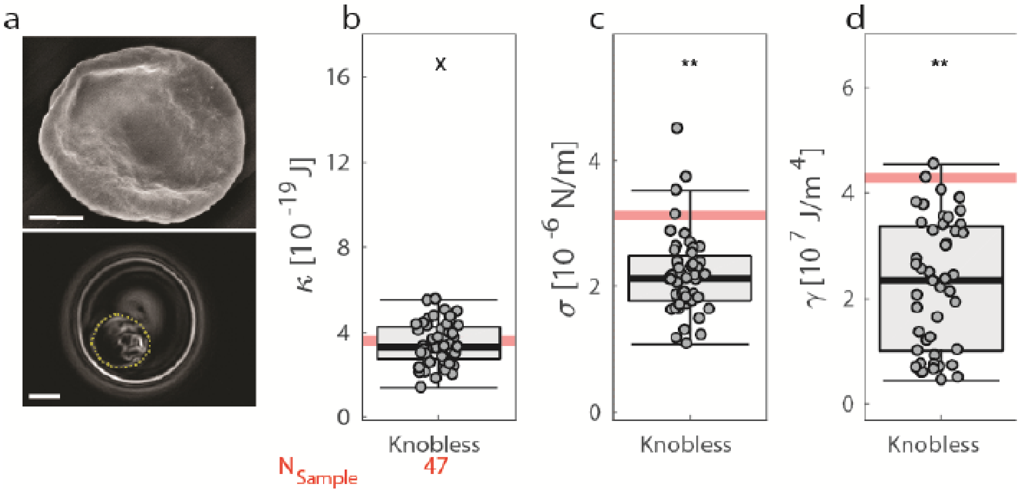

Figure 2.8: a) SEM images of the knobless phenotype (top) and a representative gradient image calculated from phase contrast (bottom). The Scale bar indicates 2 µm. b) Bending modulus κ, c) surface tension σ, and d) confinement γ calculated using (2.57) for the knobless phenotype at trophozoite stage HbAA iRBCs. Red lines correspond to the median values of HbAA for the respective mechanical parameter. (Welch t-test: x no significant difference, $^{*}p < 0.05$, $^{**}p < 0.001$). This Figure was produced by Benjamin Fröhlich.

For the bending modulus, κ, we see an increase from

$$\langle\kappa\rangle_{\mathrm{AA,U}} = (2.7 \pm 0.6) \times 10^{-19}\ \mathrm{J} \quad \text{to} \quad \langle\kappa\rangle_{\mathrm{AA,T}} = (3.4 \pm 1.4) \times 10^{-19}\ \mathrm{J},$$

for the uninfected cells and the trophozoite cells respectively, where the ring stage is not significantly modulated. The surface tension already doubles its value from

$$\langle\sigma\rangle_{\mathrm{AA,U}} = (0.7 \pm 0.2) \times 10^{-6}\ \mathrm{N\,m^{-1}} \quad \text{to} \quad \langle\sigma\rangle_{\mathrm{AA,R}} = (1.3 \pm 0.5) \times 10^{-6}\ \mathrm{N\,m^{-1}},$$

for an uninfected cell and a cell in the ring stage respectively, and reaches five times the uninfected value in the trophozoite stage. Finally, the confinement factor γ changes the most. From the uninfected stage to the ring stage γ increases from

$$\langle\gamma\rangle_{\mathrm{AA,U}} = (0.5 \pm 0.2) \times 10^{6}\ \mathrm{Nm^{-4}} \quad \text{to} \quad \langle\gamma\rangle_{\mathrm{AA,R}} = (1.9 \pm 1.5) \times 10^{6}\ \mathrm{Nm^{-4}}$$

and reaches a ten-fold higher value in the trophozoite stage than in the uninfected stage.

A value for the viscosity could be extracted from a fit to the power spectral density using Formula (2.49) derived from the spherical harmonic treatment of the cell as explained in Chapter 2.2.5. This analysis has been attempted for healthy RBCs before but it is a known issue that this method overestimates the viscosity values. Similar to these studies, a relatively high value of 11.2×10^{-3} Pa s was found for healthy RBCs (the viscosity should be on the order of a few mPa s for the haemoglobin solution inside the RBC [72], compare the viscosity of water at 20°C which is $1 \cdot 10^{-3}$ Pa s). Nevertheless, an increase in viscosity can be measured with parasite development. The viscosity at the ring stage

$$\langle\eta_{\mathrm{RBC}}\rangle_{\mathrm{AA,R}} = (19.1 \pm 10.8) \times 10^{-3}\ \mathrm{Pa\,s}$$

is 1.7 times larger and the viscosity at trophozoite stage is 7.5 times larger than in the uninfected cell.

The mechanical parameters were also measured for HbAS and HbAC RBCs at the different stages. If we focus on the trophozoite stage and compare the values to the HbAA cells (red lines), we can see in Figure 2.7 that the bending modulus κ is slightly higher for both HbAS and HbAC. The surface tension σ only increases for HbAC cells by a factor of 1.27 where there is no change for HbAS cells. In the case of the confinement parameter, the value seems to decrease for HbAS cells and increase by a factor of 1.13 for HbAC cells.

In a final set of experiments, the parameters were also determined for a knobless phenotype which is a result of a chromosomal truncation. For these cells no change in the bending modulus could be detected whereas both σ and γ were found to be smaller than for comparable infected HbAA cells (see Figure 2.8).

2.4 Numerical Treatment of Cytoskeleton

One important difference between the different infection stages in HbAA cells and the hemoglobinopathies is the arrangement of the spectrin network that underlies the RBC membrane. To find out more about the relation between the nature of the network and the flickering parameters, we treat the exact structure of the network in a numerical manner as has been done previously for healthy RBCs [73, 56, 74, 35]. It is important to keep in mind, that the spectrin network is not necessarily the only cause for changes in membrane parameters. Another possible change could be an altered activity of the membrane which we do not consider within the following calculations.

2.4.1 Previous Applications

Frank L. H. Brown developed a framework to simulate fluctuations of membranes that interact with an underlying structure, such as the RBC cytoskeleton, which he termed Fourier Space Brownian Dynamics (FSBD). Using these simulations he treated pinned membranes in variable detail where the effect of different hydrodynamic kernels was also examined [34]. In another application intermembrane junctions were identified as a source for surface tension [5].

For a general anchoring potential, the simulation method just mentioned needs to be applied. However, in the case of a purely harmonic anchoring, a detailed simulation is not necessary but a transformation to normal modes can by applied. Hence, it is possible to calculate the exact time evolution by a matrix inversion (which is done numerically), similar to the transformations that are made in crystals [75] and polyatomic molecules [76]. The normal mode approach yields average membrane shapes, fluctuations about this average and time correlation functions without conducting lengthy simulations. This is the approach that we will use in the following calculations and has also been verified to apply to RBCs by Merath *et al.* [35].

2.4.2 Modelling Approach

We describe the RBC membrane by a Hamiltonian consisting of two distinct contributions; an elastic continuum part and a discrete part modelling the connections between the lipid bilayer and the spectrin network as individual springs. The elastic contribution is given by the Canham-Helfrich Hamiltonian in Monge gauge which takes into account the bending of the bilayer (κ) and a surface tension σ which enters the equation to ensure area conservation:

$$H_{\text{elastic}} = \int_0^{L_x} \mathrm{d}x \int_0^{L_y} \mathrm{d}y \left(\frac{\kappa}{2} [\nabla^2 h(\boldsymbol{r})]^2 + \frac{\sigma}{2} [\nabla h(\boldsymbol{r})]^2 \right), \tag{2.58}$$

where $h(\boldsymbol{r})$ is the normal displacement (in the z-direction) of the membrane from its equilibrium position in the xy-plane. The expression needs to be integrated over the whole membrane patch with dimensions L_x and L_y. The contribution from the springs consists of a sum over the discrete attachment sites ($\alpha = 1, ..., N$):

$$H_{\text{spring}} = \sum_{\alpha=1}^{N} \frac{k_\alpha}{2} h^2(\boldsymbol{r}_\alpha), \tag{2.59}$$

where k_α is the spring constant at position $\boldsymbol{r}_\alpha$. For simplicity the spring constants k_α are assumed to be equal (k) for a given realization. I also define two dimen-

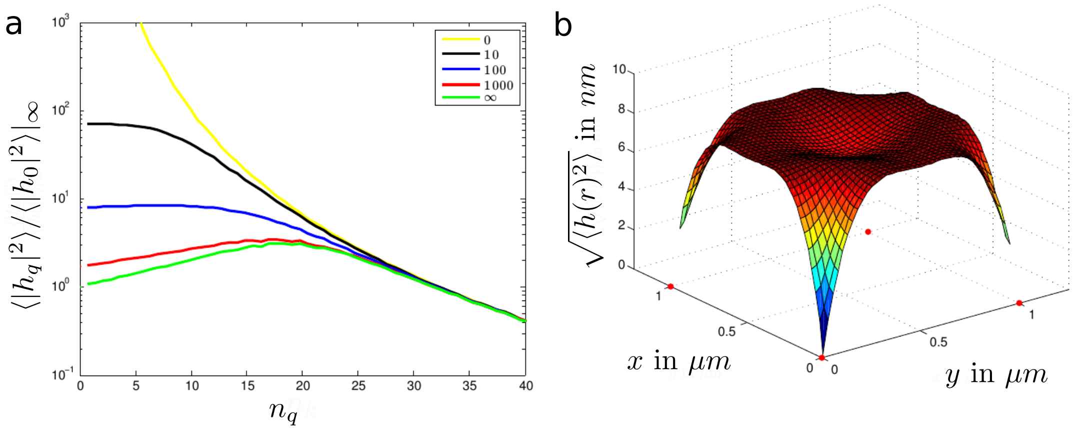

Figure 2.9: a) Normalized mean square fluctuation amplitude as a function of Fourier mode number n_q plotted for different values of the ratio $\frac{q\Delta^2}{\kappa}$ where Δ is the spring lattice constant. b) Average hight of an anchored membrane patch in real space. Anchor points are indicated by the red spheres.

sionless quantities, $\Gamma = \frac{\gamma(L_xL_y)^2}{k_BT}$ and $K = \frac{kL_xL_y}{k_BT}$ which fix the strength of the confinement parameter and the spring constant relative to the size and thermal energy of the system.

After Fourier transforming the above equations, an expression for the mean square amplitudes can be derived using the equipartition theorem. Details about the calculation can be found in Appendix C.2 or in the work by Lin and Brown [34, 5]. An analytic expression can be derived for the purely elastic part since only diagonal elements contribute. However, when considering discrete springs, the problem needs to be treated numerically, since off-diagonal terms are introduced. This numerical treatment limits the size of the membrane patch that can be considered. Here I calculate the fluctuations for square patches of approximately 1×1 µm^2 in size with a resolution of 10 nm. The calculations are done using a self-written *C++* code.

Reproduction of Results of Merath *et al.* [35]

As validation of the code, I started with reproducing the results of Merath *et al.* who focused on a square array of springs with varying spring constant. They find that the flickering spectrum of a discretely tethered membrane can be described by the commonly used continuous harmonic confinement term for weak enough tethers (see yellow, black and blue lines in Figure 2.9a). However, for very strong tethers the system deviates from the continuum approach and would need a negative surface tension to explain the data (red and green lines). Figure 2.9b shows the average fluctuation spectrum of a small patch after converting back to real space. The approach used here only calculates the average fluctuation amplitudes of the membrane; one would have to implement a dynamic simulation to access real instantaneous membrane shapes.

2.4.3 Model for the Malaria Infected RBC Cytoskeleton

We need to look more closely at the RBC cytoskeleton to understand the approach chosen here. The cytoskeleton consists of spectrin filaments that are connected via short actin filaments. In various studies it was found that the network is in a prestressed state. However, the spectrin filaments are also not stretched out fully, such that the network needs to be thought of as a layer of finite thickness. Cryo-electron tomography has shown that the real thickness inside the RBC lies between 54 nm and 110 nm which corresponds to the stretched out and crumpled up states, respectively [77]. Hence, it seems plausible to treat the spectrin network as an elastic shell, and only consider the attachment points between the bilayer and the spectrin nodes.

In Figure 2.10a, a schematic of the membrane is shown, with the spectrin filaments in yellow and the main anchor points at the actin junctions in blue. The large structure on the right corresponds to a knob which is a large structure of KAHRP molecules induced by the malaria parasite. To see how we translate this into our numerical model, a graphic containing the corresponding springs is shown below. As mentioned before, we replace the discrete connections between bilayer and spectrin mesh by springs with a lattice constant a as shown in the Figure. Hence, the attachment is modelled by an array of springs that confines the bilayer at $z = 0$. A natural way to model a knob would be to introduce a cluster of springs as it is also shown in the schematic.

Since we only consider the discrete connection points, we need to know the spring constant at the junction points in the direction perpendicular to the network. A graphic representation of this problem is shown in Figure 2.10b. The junctional complex indicated in orange attaches to a number of spectrin filaments (an average of 4.2 for healthy RBCs [77]) which have a spring constant of k_{sp} along their extension axis. In order to determine the out of plane spring constant several factors need to be accounted for. In general we are most interested in the contribution from the spectrin filaments since these are altered dramatically during the malaria life cycle. Nevertheless, a spring constant will be associated with the junctional complex itself. The actual connection to the bilayer is mediated via a transmembrane protein which can move within the lipid bilayer and hence contributes to the spring stiffness. Additionally, the anchor complex, consisting of several proteins, also behaves spring like and contributes to the overall spring constant.

In Appendix C.3, a formula is derived which shows how the spring constant of the junctional complex depends on the spring constant of the individual spectrin filaments that for simplicity all have the same spring constant. The formula predicts a non-linear dependence on the displacement z in the direction perpendicular to the network:

$$k = n k_{\mathrm{sp}} \frac{z^2}{2a^2}, \tag{2.60}$$

where n is the number of filaments attached to the complex and a the distance to the next anchor point.

In principle, we now know how to calculate the spring constant, so the last piece of information needed is the 2D distribution of the springs. The anchor points in

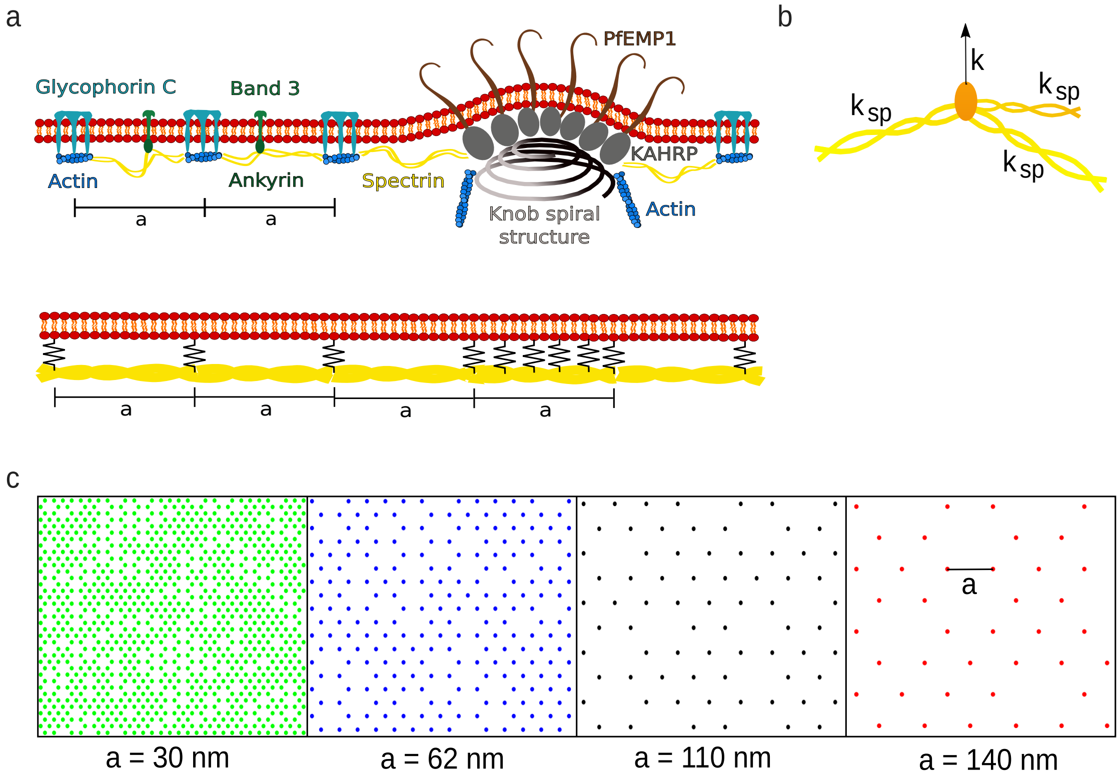

Figure 2.10: a) Molecular components of the RBC membrane are shown with a model schematic introducing springs as anchor points below; the latter have a strength k. The distance between springs is the triangular lattice constant a of the underlying 2D spring distribution. b) The structure of one anchoring point is shown with the connection to the bilayer in orange and the spectrins in yellow. The whole complex can be modelled by a vertical spring with spring constant k. c) The springs' positions are shown for square membrane patches of 1 μm^2. The triangular lattice constants are as indicated and the network is thinned out systematically.

	average spectrin length (in nm)	average mesh size (in μm^2)
uninfected	43	0.0035
ring	48	0.0035
trophozoite	64	0.0067
shizont	75	0.0071

Table 2.1: Data describing the spectrin network architecture for the uninfected RBC and the three infected stages taken from Shi *et al.* [11].

the spectrin network are known to form a triangular (hexagonal) lattice with some naturally occurring defects. Natural parameters are identified to be the lattice constant a, which corresponds to the end-to-end distance of a spectrin tetramer, the number of defects in the lattice and the spring constant for each spring. An example for varying a can be seen in Figure 2.10c.

The motivation for varying mesh size comes from observations of the different stages of the malaria infection. An AFM study of the cytoplasmic side of malaria infected RBCs [11] found that the end-to-end length as well as the mesh size increases over time which can be seen in Figure 2.11. The authors also extracted values from the images, which are summarised in Table 2.1.

One reason for this development might be the mining of actin from the RBC skeleton by the parasite. Cyrklaff *et al.* [23] found that the parasite utilizes the host actin to build long actin fibres that start at the knobs and terminate at the Maurer's clefts. Therefore, there might be less junctional points at later stages of the infection. Another development that takes place, is the formation of knobs, which mediate cytoadhesion via the protein PfEMP1 and have an underlying spiral structure that incorporates the protein KAHRP. These knobs are approximately 100 nm large and act as very strong anchor points between the bilayer and the spectrin network. By modelling the connections between the bilayer and the cytoskeleton explicitly, I will show what effects these observations have on the membrane properties.

Modelling Results

The numerical calculations described above produce two dimensional data sets for the mean square displacements in Fourier modes. An azimuthal average is taken to plot the data as a function of q, because the peaks in the Fourier spectrum clearly show the geometry of very regular lattices and so are different depending on the direction chosen. Therefore, a reasonable approach is to average all values for a given $|\boldsymbol{q}|$, such that the lattice geometry becomes unimportant. An example of data sets can be seen in the points in Figure 2.12 a and b. To compare the data more easily, we fit the three parameters of the continuum description

$$\langle h_q^2 \rangle = \frac{k_B T}{L_x L_y} \frac{1}{\gamma + \sigma q^2 + \kappa q^4}, \tag{2.61}$$

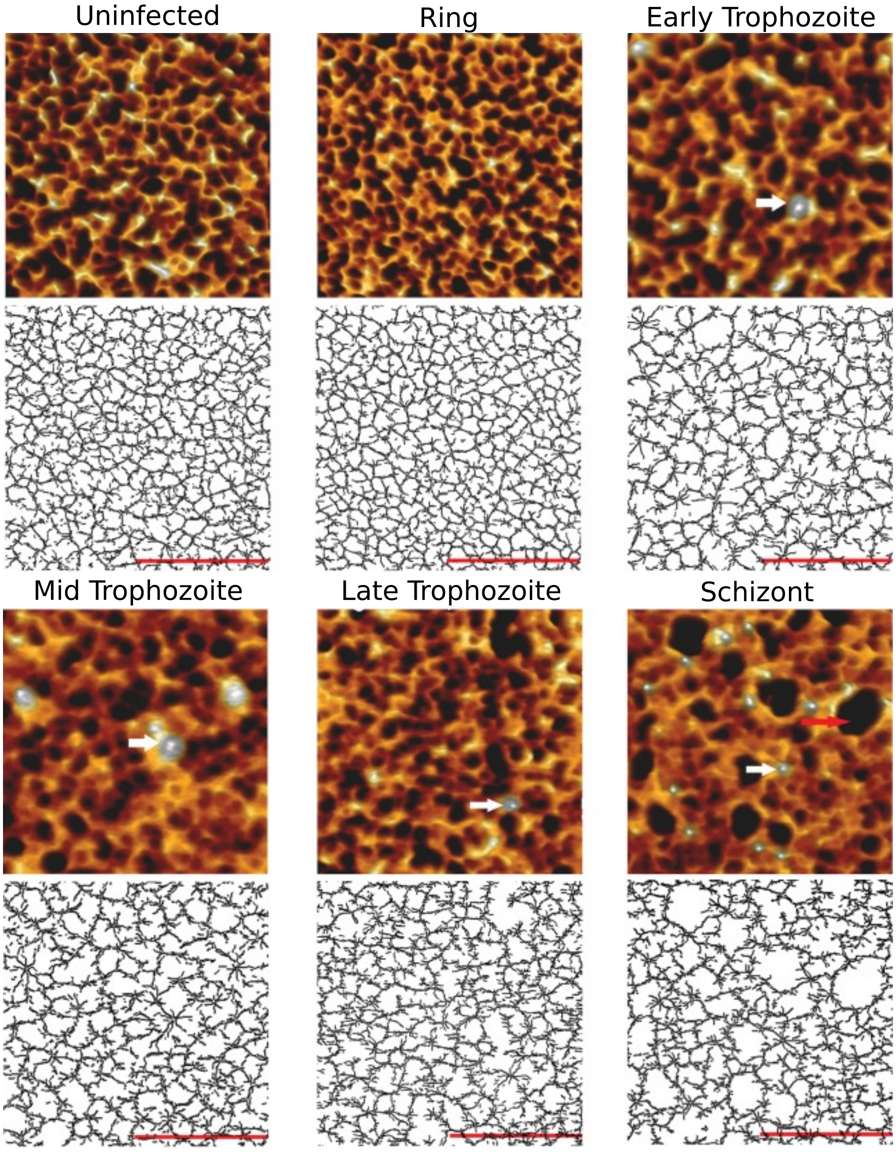

Figure 2.11: AFM images with the corresponding skeletonisation of the RBC's cytoplasmic side. The white arrows point at knobs and the scale bars correspond to 500 nm. The figure is adapted from Ref. [11].

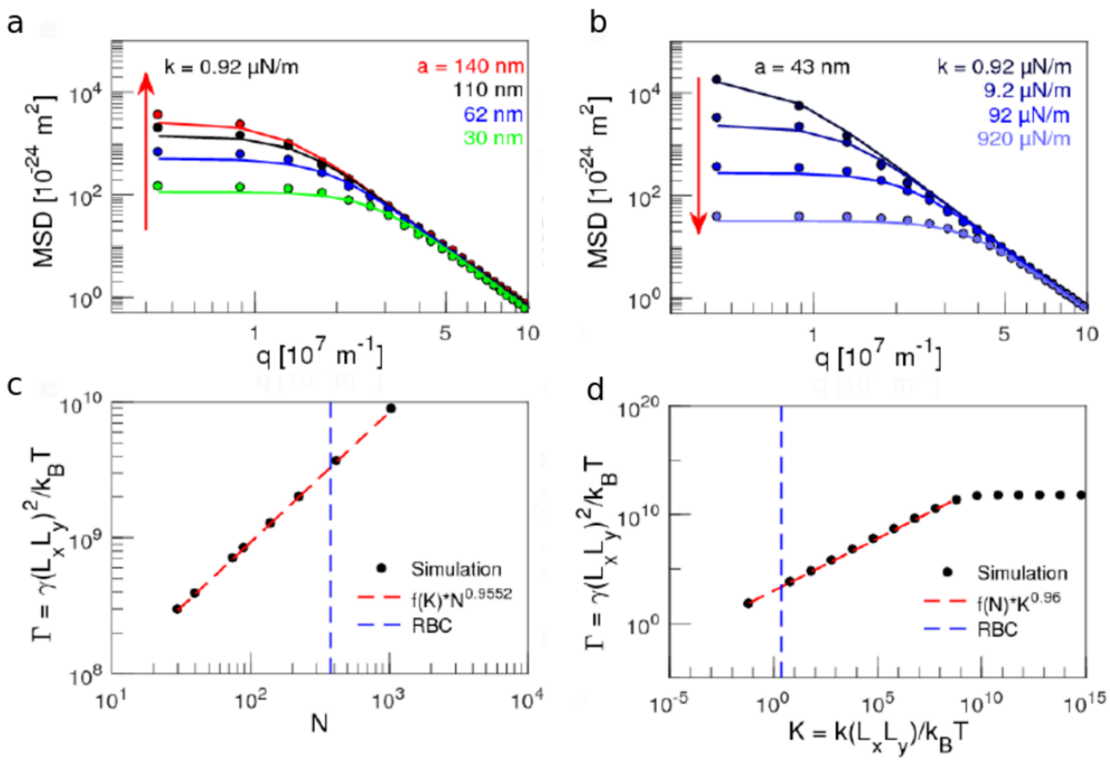

Figure 2.12: a) Simulated mean square displacements as a function of the wave number q for the different lattice constants (see Figure 2.10c) (fixed $k = 9.210^{-5}\ \mathrm{N\,m^{-1}}$) and b) for different spring constants k (fixed $N = 423$). The discrete data points represent the results from the numerical calculations and the continuous lines are a fit of the continuum theory. c) Here the dimensionless confinement parameter Γ is plotted against the number of springs N and d) the dimensionless spring constant K. The red dashed lines indicate the fit for the exponents.

which manages to describe the data well as can be seen in the solid lines in the plots. The formula is fitted to the data by a least square algorithm within MatLab.

In the case of evenly distributed equally strong springs, one expects the following relation between γ, the spring constant K and the number of springs N from dimensional analysis of the Hamiltonian:

$$\gamma \approx \frac{k_B T}{(L_x L_y)^2} N K. \tag{2.62}$$

For our uneven networks, we will use the approach to keep either the number of springs or the spring constants fixed in order to find the dependence on the relevant parameter. Examples are shown in Figure 2.12 c and d. The linear scaling on the log-log plot in the relevant regimes indicates the following relations

$$\Gamma \propto K^{\alpha}$$
$$\Gamma \propto N^{\beta},$$

where the exponents α and β can be extracted from the slopes of the red lines.

To examine the effects of spring density and sprint constant, I varied the lattice spacint, a, from 30 nm to 140 nm while keeping the spring constant fixed, then varied the spring constant, k, from $0.92 \cdot 10^{-6}$ N m^{-1} to $0.92 \cdot 10^{-2}$ N m^{-1} while keeping the lattice spacing fixed (see Figure 2.10). The results of these calculations are shown in Figure 2.12, where the different colours in Figure 2.12a indicate different lattice spacings and in Figure 2.12b they indicate different spring constants. The solid lines show the fits of the analytical formula containing the three parameters κ, σ and γ. In Figure 2.12c and d the dimensionless parameter Γ, which was extracted from the fits, is plotted as a function of spring number and dimensionless spring constant K respectively.

From the slope of the log-log plots in Figure 2.12c and d the scaling of Γ with the two parameters can be extracted. For a very high spring constant in d) a plateau regime can be seen which corresponds to an effectively pinned membrane. Otherwise the scaling behaviour is given by

$$\Gamma \propto N^{0.9552} \tag{2.63}$$

$$\Gamma \propto K^{0.96}. \tag{2.64}$$

The exponents are close to one but they actually depend on the underlying lattice geometry as will be shown later on.

Parameters

To compare the simulated parameter ranges to the values that describe a membrane patch of a healthy RBC, we make the following estimations. First, we neglect the strain hardening property of the spectrin filaments and model it as a simple spring. An individual spectrin filament has a spring constant of approximately $k_{\mathrm{sp}} = 2 \cdot 10^{-6}$ N m^{-1} [78] when extended along its contour length. As explained previously, we can approximate the out of plane spring constant by the formula derived in Appendix C.3, such that

$$k \approx 4k_{\mathrm{sp}} \frac{z^2}{2a^2} \approx 8.8 \cdot 10^{-9} Nm^{-1}, \tag{2.65}$$

where $a = 43$ nm is the rest length of the spectrin filament. We approximate z/a by $2/43 = 0.0465$, since the typical out of plane motion has an order of magnitude of a few nm. This leads to a dimensionless $K_{RBC} = 2.3$ for the simulated membrane patch. Furthermore, we find $N_{RBC} = 378$ for a square membrane patch of $A = 1$ µm^2 , an average mesh size of 3500 µm^2 and a lattice constant of $a = 43$ nm. Figure 2.12c and d show where these values are located within the simulated parameter ranges. It can be seen that the experimentally relevant parameter space is located far below the pinned membrane regime, so that changes in N and K will indeed have an effect on γ.

Now we would like to predict the value of γ from these microscopic quantities and use the previously verified formula. Our analysis suggests the formula

$$\gamma \approx \frac{k_B T}{(L_x L_y)^2} N^{\beta} K^{\alpha} \tag{2.66}$$

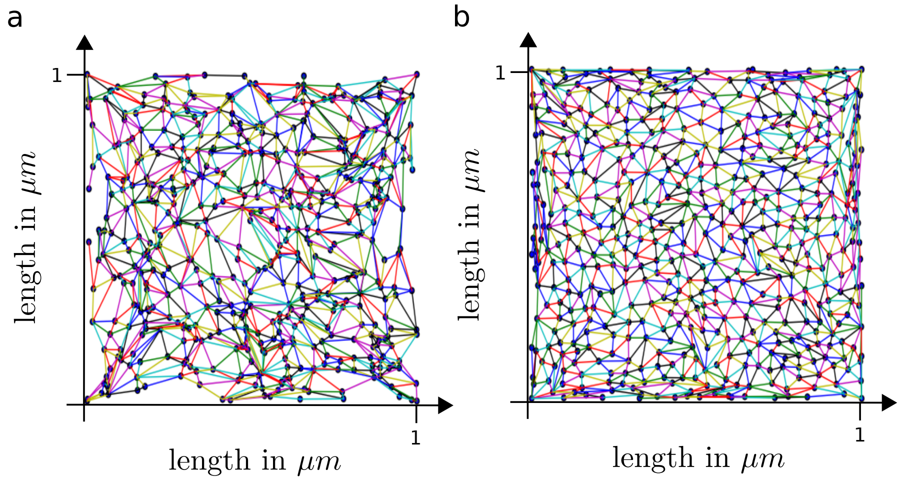

Figure 2.13: a) Examples of a Delauney lattice for $d_{\text{min}} = 1$ nm and b) $d_{\text{min}} = 30$ nm.

will do this. For a RBC area of $A = 2.2 \cdot 10^{-10}$ m^2 , a spring density of $N/A = 408\ \mu\text{m}^{-2}$ and a spectrin spring constant of $k_{\text{sp}} = 2 \cdot 10^{-6}$ N m^{-1} the harmonic confinement parameter is calculated to be $\gamma = 1.7 \cdot 10^6$ Jm^{-4}. The microscopic quantities used for this estimation could only be approximated based on previous knowledge. Nevertheless, the final value for γ is close to the measured value of $\langle\gamma\rangle_{\text{AA,U}} = (0.5 \pm 0.2) \cdot 10^6$ Jm^{-4} for an uninfected cell.

2.4.4 Examining Effects of Network Properties

We numerically analysed several different underlying network structures. Specifically, we looked at the effects of the network geometry, homogeneity, system size and also considered a membrane covering a sphere but this approach is limited to a small radius.

Geometry Effects

Firstly, we wanted to see how the confinement depends on the underlying network structure. The simplest case is a square lattice for the pinning sites. Alternatively, a triangular lattice with defects can be applied to mimic the network structure of the RBC skeleton as described above and can be seen in Figure 2.10c. As a third option a Delauney lattice was used, where the minimum distance between two junctions, d_{min}, determines how regular the lattice is. Two examples of such lattices can be seen in Figure 2.13a and b.

For all of these cases, we extracted the scaling exponents α and β as described above. The results are summarized in Table 2.2. In general, the values are very close to 1 so that the scaling is nearly linear. Nevertheless, the error of the values is very small which shows that the different geometries induce small changes on the scaling exponents. The strongest deviation occurs for the scaling of γ with the spring number N of the square lattice. This is likely due to the averaging over azimuthal angles.

Next, we examined the effects of the homogeneity of the network by gradually

Exponent of spring number N (β)		Exponent of spring constant K (α)	
Square ($k = 9.2 \cdot 10^{-5}$)	0.9292	Square ($N = 400$)	0.9671
Hexagonal ($k = 9.2 \cdot 10^{-5}$)	0.9552	Hexagonal ($N = 423$)	0.9600
Hexagonal ($k = 9.2 \cdot 10^{-8}$)	0.9480	Hexagonal ($N = 379$)	0.9754
Delauney ($k = 9.2 \cdot 10^{-5}$)	1.0173	Delauney ($N = 423$)	0.9447

Table 2.2: Scaling exponents extracted from the fit to the analytical formula for varying N on the left and K on the right. The different lattice geometries are compared and $d_{\text{min}} = 1$ for the Delauney runs.

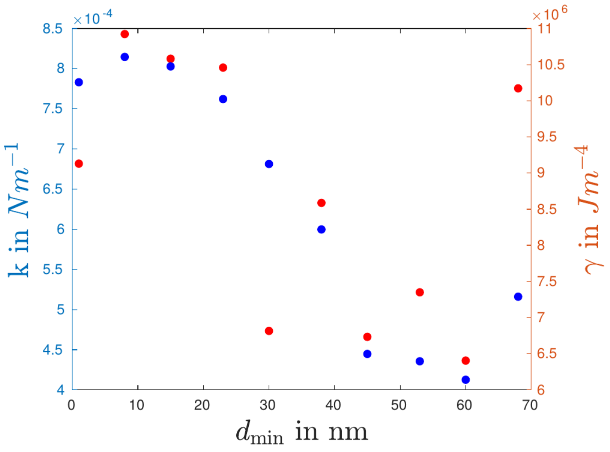

Figure 2.14: The blue data points show the mean spring constant k as a function of d_{min} and the red data points depict the corresponding calculated confinement γ.

changing the value of the parameter d_{min} of the Delauney lattice. In these calculations, the different lengths of the spectrin tetramers are also accounted for. Real spectrin molecules change their stiffness as a function of extension in a complicated manner where different domains can unfold. By approximating the filaments as semi-flexible polymers, a reasonable force extension curve can be found, that predicts the spring constant to be very high for large extensions. Hence, the spring constant for each lattice point is calculated according to the attached filaments and their length. The results are shown in Figure 2.14, where a small d_{min} corresponds to irregular lattices and a large d_{min} produces an evenly spaced out distribution of springs.

Small values of d_{min}, implying an irregular lattice, produce a larger average spring constant k and therefore a larger confinement γ. The data is quite noisy because each Delauney lattice is quite different to another Delauney lattice with the same d_{min}.

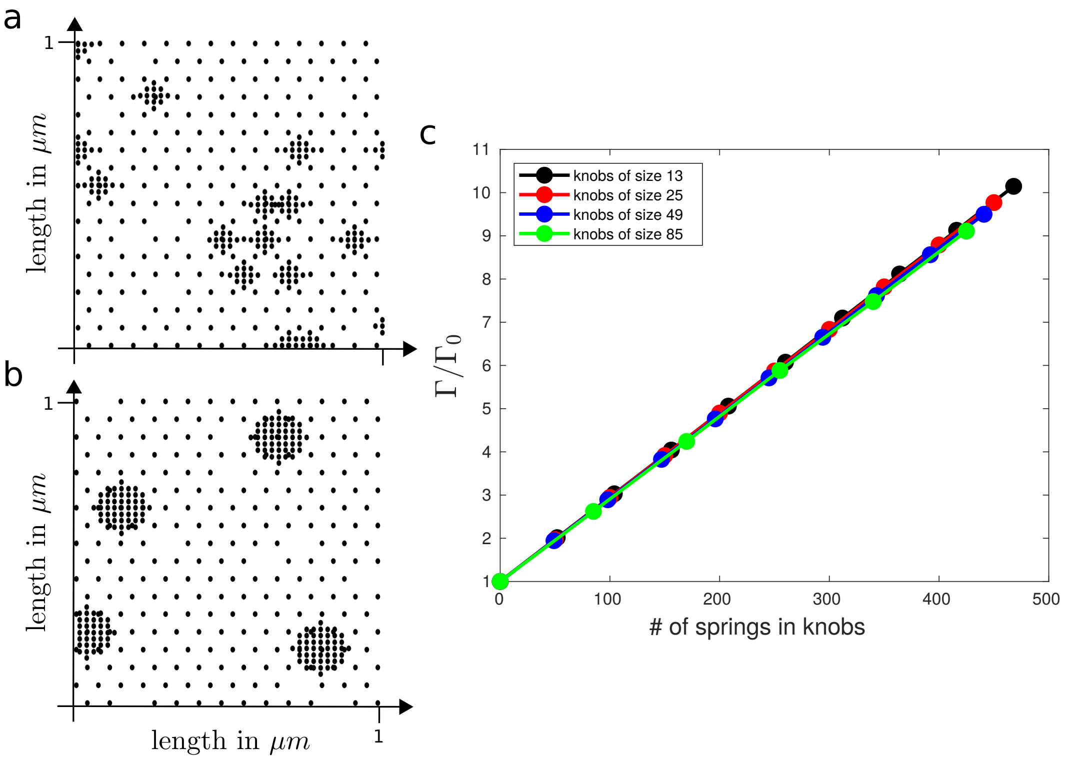

Figure 2.15: a) Example of an array of springs that shows dense regions of springs which resemble the parasite induced knobs. b) The confinement parameter Γ/Γ_0 is plotted as a function of knob density (since two different sizes of knobs exist, it is more convenient to use the number of springs in knobs as parameter). Γ_0 corresponds to the system without knobs and only the springs corresponding to the spectrin network. The hollow points show the data for all springs being equally strong, where the full points correspond to the situation where the springs that lie within knobs are double as strong as the others. Black points correspond to small knobs (25 springs per knob) and red points to large knobs (50 springs per knob).

Effects of Clustering into Knobs

Since the parasite establishes an adhesive system which consists of knob structures that strongly connect the membrane to the spectrin network, we analyse the effects of clusters of springs on the confinement parameter. Since a knob has a diameter of approximately 100 nm, its size is similar to a whole unit of the spectrin network. Hence, it can be modelled by introducing a dense region of springs of the appropriate size as can be seen in Figure 2.15 on the left.

It was found that one of the differences between HbAA and HbAS/HbAC cells is the knob size. Hence, we consider two cases in the calculations, many small knobs (black data) or a smaller number of large knobs (red data), where we keep the total number of springs constant. For example, we would compare 4 small knobs to 2 large knobs with double the number of springs each. For all spring arrays we calculate the corresponding confinement factor as before and plot the result on the right of Figure 2.15. Γ is scaled by Γ_0 of the system without knobs and only with the springs corresponding to the spectrin network.

In all cases we find that the large knobs are less effective in inducing confinement than the small knobs. This makes sense since a completely homogeneous distribution is most effective. As mentioned before, the overall number of springs is kept constant, such that individual springs are only moved around. Therefore, the confinement goes down (hollow points in Figure 2.15), when we start clustering springs into knobs for the same reason why large knobs are less effective than many small knobs.

However, in the real system, the knob areas seem to be strongly connected to the spectrin network by parasite induced proteins like KAHRP. This motivates the choice to make springs belonging to a knob double as strong as the other springs of the background network. The data for these calculations is shown in the full circles in Figure 2.15. Considering the large knobs, the data ranges from a knob density of zero to four knobs per square micrometer, which corresponds to the appropriate range for the iRBCs. For a knob density of 4 $\mu\mathrm{m}^{-2}$ an increase of confinement of 30 % can be reached.

Effects of System Size

To check if the results of our calculations are scalable with system size, we compare a membrane patch of 1 $\mu\mathrm{m}^2$ with one of size 25 $\mu\mathrm{m}^2$. Assuming the exponents α and β to be 1, we would expect that the confinement parameter γ only depends on the spring density and the microscopic spring constant as seen in the relation

$$\begin{aligned}\gamma &\approx \frac{k_B T}{(L_x L_y)^2} N K \qquad (2.67)\\ &= \frac{N}{L_x L_y} k, \qquad (2.68)\end{aligned}$$

where $\frac{N}{L_x L_y}$ is the spring density and K the dimensionless spring constant. As seen in one of the previous sections, α and β can slightly deviate from 1 depending on the underlying network structure but to test the effects of system size, it is sufficient to make this approximation.

To test the prediction, I take the membrane patches of the different sizes and choose the same spring density and constant in both cases. This should lead to the same confinement parameter. The results of the calculations can be seen in Figure 2.16; it should be noted that the mean squared displacement had to be scaled by the system size to compare the data. This scaling introduces a prefactor which shifts the curve as a whole but does not affect the relevant parameters.

The blue and yellow data points show the mean squared displacement for a weak spring constant of $k = 1.3 \cdot 10^{-5}\ \mathrm{N\,m^{-1}}$. The red and green data points are the results for the same spring density but a stronger spring constant of $k = 1.3 \cdot 10^{-5}\ \mathrm{N\,m^{-1}}$. It can be seen that in each case the two system sizes yield similar results. In the weak confinement case the data for the small system in yellow is not sufficient to properly fit a confinement parameter. In the stronger confinement case both curves clearly show the effects of a confinement (plateau for small wavenumbers) and it can be seen that the larger system produces a slightly stronger confinement (compare the green to the red curve). From the fits the values $1.5232 \cdot 10^{11}\ \mathrm{Jm^{-4}}$ and $2.6982 \cdot 10^{11}\ \mathrm{Jm^{-4}}$ are extracted for the small and

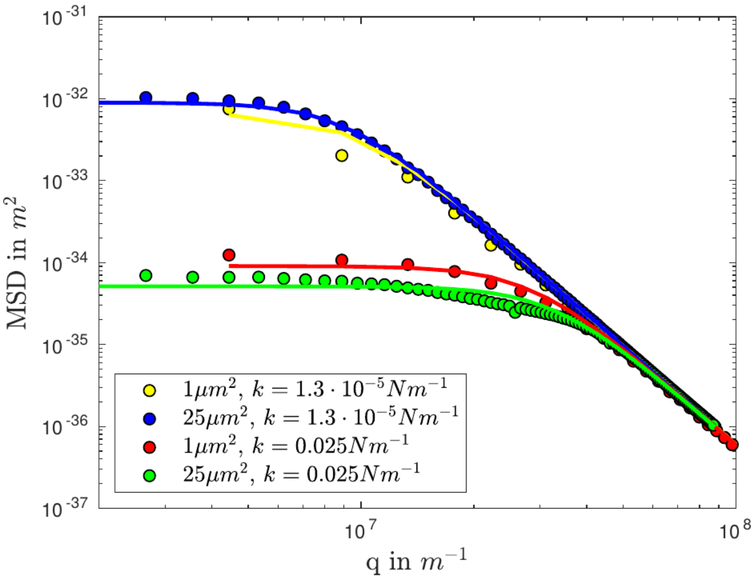

Figure 2.16: MSD normalized by the system size as a function of q plotted for different anchoring strengths and system sizes as indicated in the legend. Solid lines are a fit of the fluctuation formula to the data.

the large system respectively. For large wave numbers all curves are equivalent.

Overall, the system size does not effect the results much. For strong confinements, the larger system produces a slightly larger confinement than the small system.

Spherical Harmonic Approach

All previous calculations were done for a planar patch of membrane. A natural next step would be to look at a membrane of spherical topology and hence using a spherical harmonic decomposition instead of Fourier modes. The limiting factor of this approach is the radius of the treated vesicle since the number of modes, and therefore the size of the matrix that needs to be inverted, becomes very large very quickly when keeping the resolution at an appropriate level.

Here, I show an example of fluctuations on a spherical reference shape. The first step would be to define a triangular lattice on a sphere for the cytoskeleton representation, as can be seen in Figure 2.17a for an even mesh and in Figure 2.17b for a thinned out one. The fluctuations on such a sphere were calculated and converted back to real space. The result is shown in Figure 2.17c plotted on the surface of the sphere.

This approach seems helpful at first sight but it does not lead to further insights into the problem. Additionally, the system size cannot be chosen large enough for comparison to a RBC and there is no direct comparison to experimental data because the resolution of microscopes is usually only sufficiently good in two dimensions.

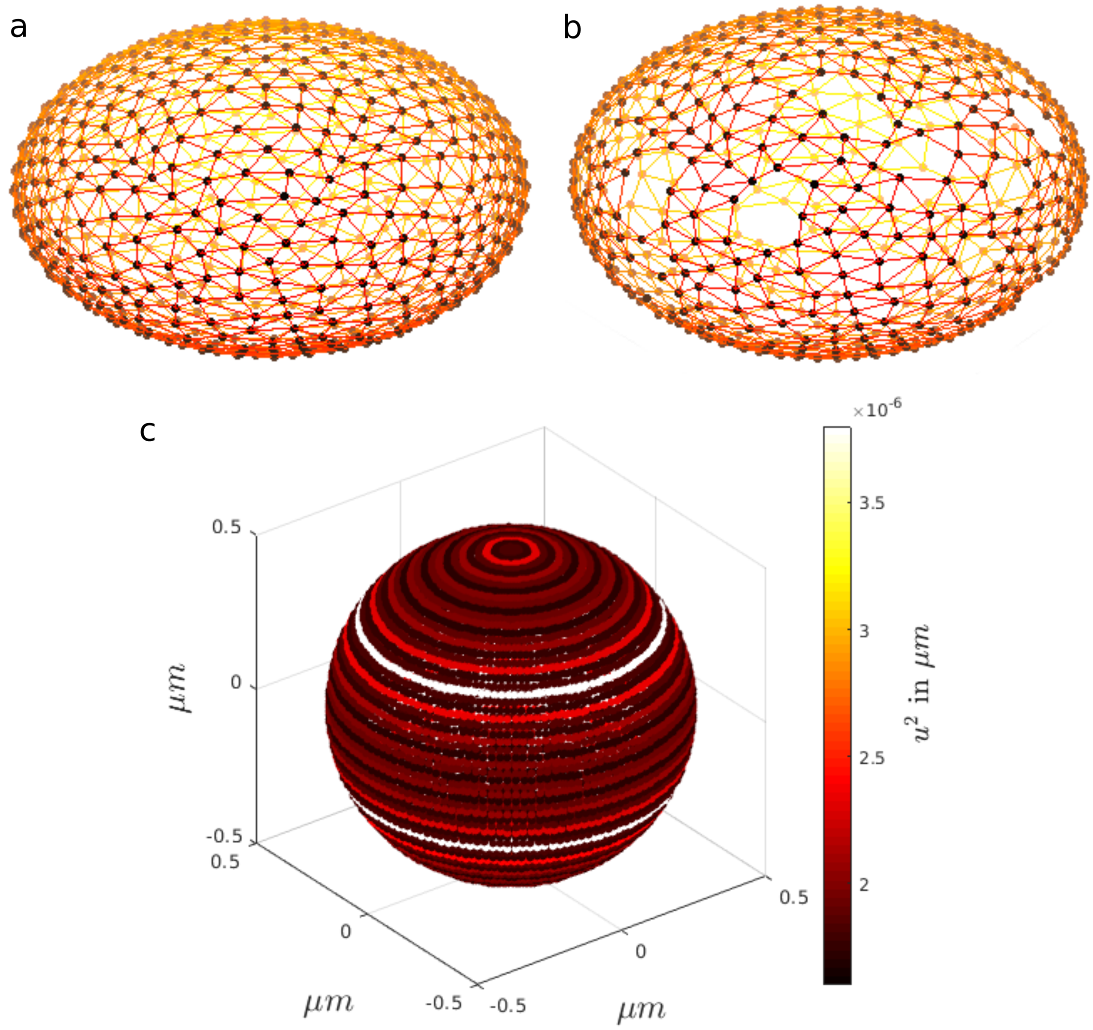

Figure 2.17: a) Triangulation on the surface of a sphere. b) Triangulation with wholes in the network. c) Real space fluctuation modes on the surface of the sphere.

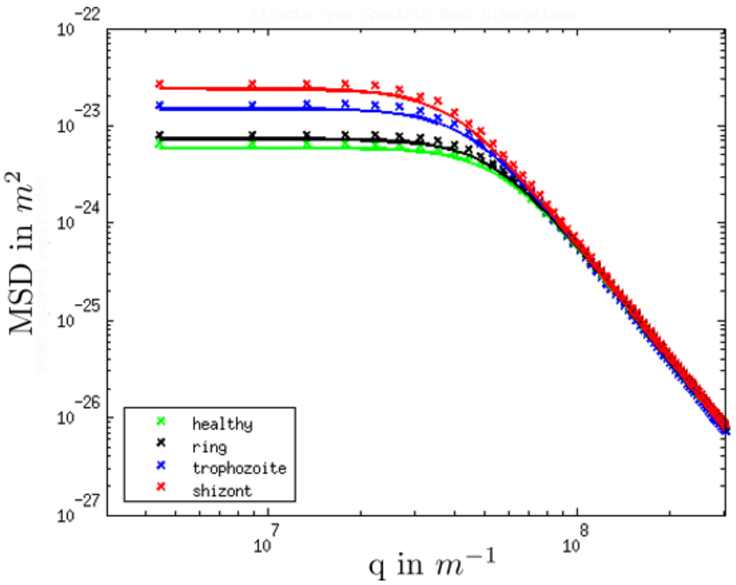

Figure 2.18: Comparison of confinement parameter for underlying network structures that correspond to the data in Table 2.1 but keeping the spring constant equal.

2.5 Implications for Infected RBCs

2.5.1 Network Destruction Decreases Confinement

Now we would like to examine the changes that occur during a malaria infection. In an AFM study of malaria infected RBCs [11] it was found that the spectrin network develops a larger average mesh size and the average spectrin length increases with proceeding infection stage (see Table 2.1). Additionally, they found that the spectrin network condenses around knob areas. It is important to notice that the spectrins exhibit a strain-hardening property [79] so that longer filaments will have a stronger spring constant.

From the data in Table 2.1, the mesh size of the spectrin network seems to increase drastically. To make the effects of the proposed change in network structure clear, we numerically calculated the MSD for the four different cases. We assume, that the reason for the larger mesh size is the destruction of some connections between the bilayer and the spectrin network, so that a system with a large mesh size, has less springs in total.

From our previous analysis we know, that thinning out the network will lead to less confinement and this can also be confirmed in the plot in Figure 2.18. However, experiments show, that the fluctuations decrease with time after infection, such that a thinning out of the network cannot be the only process happening in the iRBC. A hypothesis on what is actually happening is proposed in the next section.

2.5.2 Strong Anchoring Introduces Confinement

In the numerical study we quantified how γ scales with the number of connections between the bilayer and spectrin network and their strength. Hence, there are two ways in which γ can increase. Either the existing connections get stronger or more connections are introduced. An increase in strength of the connections is very plausible since Shi *et al.* [11] found an increase in average spectrin length which results in stronger spring constants due to the strain hardening property of the spectrin filaments. For the number of connections the trend is not completely clear. On the one hand, it is thought that the parasite mines actin from the spectrin network [23] which would result in less connections to the bilayer. On the other hand, the knobs are thought to introduce extra connections so that the overall development could be either way. From the calculations it is clear that more connections will result in a larger γ. However, even if the number of connections reduces, γ can still increase if the spring constants get strong enough.

Based on the results of the calculations, we can now make an estimate of how much the confinement will increase during a malaria infection. Three main effects need to be taken into account:

- I found that γ scales nearly linear with the number of connectors N. Since the parasite mines actin from the cytoskeleton, the spectrin network becomes sparser and the density of connectors decreases. Shi *et al.* [11] found that the mesh size is approximately doubled from the uninfected to the trophozoite stage (compare Table 2.1). Based on the calculations presented in Section 2.5.1, I account for this by a factor of 0.8 for the confinement γ.
- Building on the data by Shi *et al.* [11], the spectrin filaments get elongated during the infection from approximately 43 nm to 64 nm (compare Table 2.1). I explained previously that spectrin gets stiffer when it is stretched out. Applying the formula for the strain hardening behaviour of spectrin yields a factor of approximately 1.5 for the confinement increase due to this effect.
- The assembly of knobs leads to the introduction of strongly anchored regions. Based on the above calculations explained in Section 2.4.4, this can be accounted for by a factor of 4.5 when assuming a knob density of 4 μm^{-2}.

Since these developments all happen simultaneously, overall the calculations predict an increase of the confinement by a factor of 5.4. It has to be taken into account that this is a crude estimate of the order of magnitude because the underlying microscopic changes of the network can only be estimated. Still, it is not so far off the experimentally measured increase by a factor of ten.

2.6 Discussion of Malaria Induced Changes on Flickering

In this chapter, the theory for equilibrium membranes and membrane dynamics was explained and the main advances in this field were summarised. Furthermore, a numerical model was developed in order to explain experimental results for the flickering of malaria infected RBCs.

The numerical model takes into account the microscopic structure of the cytoskeleton and can therefore predict changes that occur during the malaria infection. The main properties that were discussed were the mesh size of the spectrin network, the spring constant of the effective tethering at junctional points and the formation of knobs connecting the bilayer and the cytoskeleton strongly in large areas. Overall, the most dominant factor for an increase in confinement seems to be the formation of knobs. Although it could be shown that a homogeneous tethering is more efficient, a stronger pinning in the relatively large knob areas can make up for this effect.

There are some shortcomings to the model that could not be prevented. As seen in the theoretical section, a spherical approach or even better a parametrisation of the discocyte would be more fitting to describe the fluctuation data of a RBC. However, we also saw that an approach with altered geometry gets complicated very quickly. For the numerical model anything but a plane is not feasible for a thorough analysis, since the matrices involved in the calculations get too large for an efficient inversion. Furthermore, active contributions to the membrane movement were not treated here. The reason for this is the microscopic origin of the RBC activity is still not completely clear and the focus of this work was on the cytoskeletal modifications by the malaria parasite.

Overall, we have learned, that the parasite stiffens the membrane by stretching out the individual spectrin filaments and by assembling knobs in the membrane. It is not entirely clear if the stiffening is a necessary effect or if it is a side effect of the knob assembly, which is necessary for the RBCs can to gain adhesive properties.

Chapter 3

Molecular Red Blood Cell Cytoskeleton Model

3.1 Motivation for a Molecular Model

This chapter aims at improving the understanding of the molecular details of the RBC cytoskeleton in its native state and after the infection with malaria. During the malaria disease the RBC cytoskeleton is remodelled drastically. By studying the malaria induced alterations we can also learn something about how the healthy RBC cytoskeleton keeps its structure in its equilibrium state. There has been various evidence that the RBC spectrin-actin network is more dynamic than previously thought, specifically, the actin junctions have been found to disassemble and assemble constantly (see Section 3.2.4). All previous models of the RBC cytoskeleton assume actin junctions of a constant length or model the junction as one particle. Some models allow for a dynamically changing network topology through breaking of bonds but filament growth was not incorporated in such models. However, actin filament dynamics in other contexts has been modelled frequently, e.g. actin treadmilling and lamellipodium generation.

The aim of our model is to establish a RBC cytoskeleton model that takes into account actin dynamics and reproduces the well-known RBC membrane properties. From there, we can test our hypotheses, how the malaria parasite attacks the network in order to build its own filaments and stiffens the RBC membrane. The model that is developed here, is a coarse-grained model, hence does not incorporate all molecular details of the system but enough to capture the structural details that are needed. As a basis the reaction diffusion software ReaDDy is used which has been developed in the group of Frank Noé and evolves particles according to the Brownian dynamics equations, with external potentials and also incorporated reactions at the same time.

First, the components of the RBC cytoskeleton are discussed in Section 3.2 and details about the relevant malaria exported proteins are given in Section 3.3. Then experimental data from our collaboration partners in Prof. Lanzer's group is discussed in Section 3.4. After that, the reaction-diffusion model for the RBC cytoskeleton is introduced and possible alterations by the malaria parasite are shown in Section 3.5. The placement of PfEMP1 molecules is analysed in Section 3.6, before the conclusions of this chapter are drawn.

3.2 Components of the RBC Cytoskeleton

3.2.1 Cytoskeleton Structure

RBCs have a unique cytoskeletal structure which enables the cells to squeeze through narrow capillaries in the microvasculature having a third the diameter of a RBC and still recover their shape throughout their lifetime [80]. The cytoskeleton mainly consists of spectrin, actin and associated proteins which regulate the structural organization. Due to various studies the overall structure and the components of the RBC cytoskeleton are well known. A comprehensive review of the current knowledge is given by Lux *et al.* [81]. However, the exact nature of some of the interactions is still unclear, e.g. the binding between spectrin and actin. The network's elasticity mainly comes from the flexibility of the spectrin filaments. They are mainly thought to be in the form of tetramers which consist of two dimers and have a stretched-out contour length of approximately 180 nm. Each dimer consists of an α- and a β-spectrin molecule which are wound around each other in a helical fashion (see Figure 3.1). Actin is found in short approx. 35 nm long filaments which form junctional complexes and hence the network's connection points. The binding of spectrin is stabilized by protein 4.1R and would be a lot weaker otherwise. It was found that on average six spectrins and six proteins 4.1R attach to one junctional complex.

The network is anchored to the bilayer through transmembrane proteins (such as Band 3) associated to ankyrin and the actin junctional complexes (compare top graphic in Figure 3.1). Ankyrin binds to the 13th to the 15th repeats within β-spectrin [82] which is close to the midpoint of the tetramer. The ankyrin complex is thought to contain one akyrin, one Band 3 tetramer, two glycophorin A/B (hetero-)dimers, two protein 4.2 molecules and one Rh complex. The binding of an akyrin also promotes tetramer formation and Band 3 strengthens the spectrin self-association [81]. The other complex is centered around a short actin protofilament of approximately 35 nm length. Several spectrin N-termini can attach to this filament mediated by a protein 4.1R each. The attachment to the membrane is mediated via p55, glycophorin C/D and Band 3. It still remains unclear, how many Band 3 molecules are present in one complex [81].

3.2.2 Spectrin

The structure of spectrin in the native RBC membrane has been debated frequently because different microscopy techniques seem to lead to different results. Especially the contour length has been reported to have very different values. Part of this problem comes from the preparation techniques, the thus induced stretching and possible rearrangements of the network.

From the amounts of spectrin tetramers ($\approx$ 105000 per cell [83]) and actin protofilaments ($\approx$ 35000 per cell [81]) in a RBC, the distance between actin protofilaments can be calculated to be on average 67 nm and the length of spectrin tetramers to be on average 65 nm [83], based on a hexagonal network and a surface area of 135 μm^2. In the table in Figure 3.1, we see that similar values are obtained from computing the average distance between junctions bases on various RBC proteins such as ankyrin, adducin and others. All these values for the distance between junctions are approximately a third of the actual spectrin contour length of 200 nm [82].

Negative stain electron microscopy yields a stretched out network with straight spectrin filaments which have a length close to their contour length of 200 nm. Actin filaments and ankyrin sites can be seen clearly and 5-6 spectrins are attached to each actin junction [84, 85, 77]. It has been realized that this highly extended state is far from the structure present in native RBCs. From the amount of cytoskeletal components discussed above it is clear, that the network must be a lot denser and thicker as well. In order to get a better view on the native structure quick-freeze, deep-etch rotary replication (QFDERR) [85, 86] and AFM on unexpanded skeletons [87] have been applied. In contrast to the negatively stained samples, the spectrin contour length was found to be $29 - 50$ nm and between 3 and 4 spectrins were attached to one junction. Electron microscopy

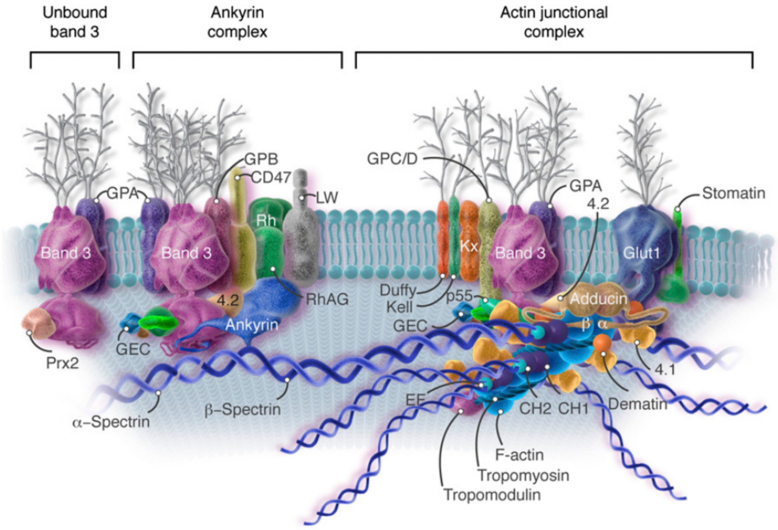

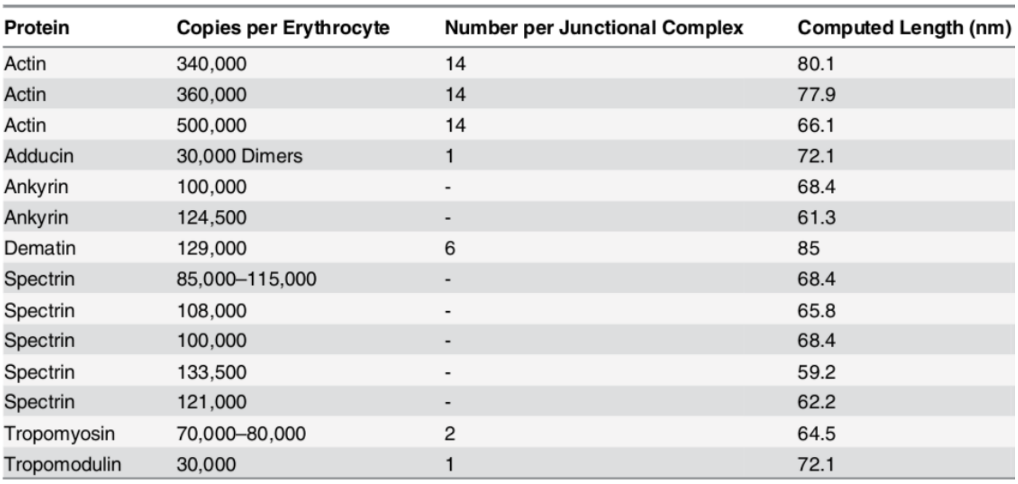

Protein	Copies per Erythrocyte	Number per Junctional Complex	Computed Length (nm)
Actin	340,000	14	80.1
Actin	360,000	14	77.9
Actin	500,000	14	66.1
Adducin	30,000 Dimers	1	72.1
Ankyrin	100,000	-	68.4
Ankyrin	124,500	-	61.3
Dematin	129,000	6	85
Spectrin	85,000–115,000	-	68.4
Spectrin	108,000	-	65.8
Spectrin	100,000	-	68.4
Spectrin	133,500	-	59.2
Spectrin	121,000	-	62.2
Tropomyosin	70,000–80,000	2	64.5
Tropomodulin	30,000	1	72.1

Figure 3.1: Top) Schematic of the membrane anchored complexes taken from [81]. On the left an ankyrin complex and its associated proteins can be seen and on the right the larger actin junctional complex is shown. Bottom) Table taken from Ref. [83] summarizing the experimentally measured values for the number of proteins in a RBC and the calculated length of the spectrin filaments assuming a hexagonal structure in the last column.

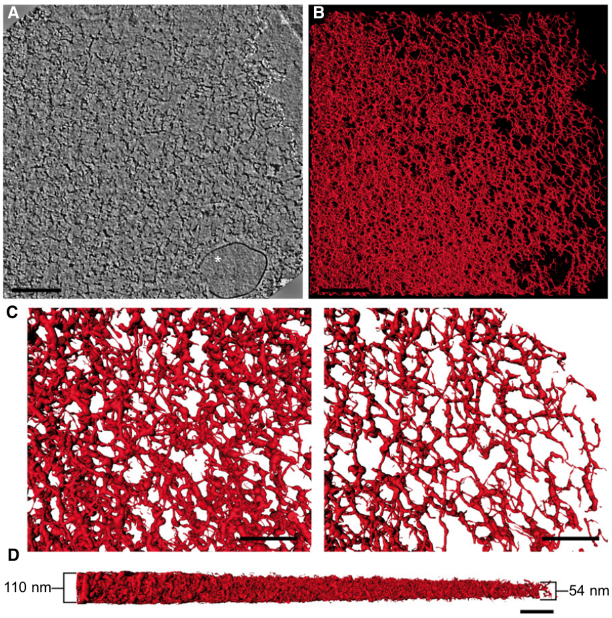

Figure 3.2: a and b) Nans *et al.* [77] prepared healthy erythrocyte skeletons and reconstructed the tomograms to arrive at the networks shown in red. c and d) Parts of the network taken from the middle and the edge are enlared, respectively.

of quickly-frozen and deeply-etched skeletons also found contour lengths between 30.6 and 82.6 nm [88]. When resolving the three dimensional structure of the RBC cytoskeleton, Nans *et al.* found an average contour length of 46 nm, a network thickness between 47 and 90 nm and on average 4.2 spectrins per junction. The tomograms used for their study can be seen in Figure 3.2.

It has been debated over many years, how these two pictures fit together. In principle a very flexible polymer like spectrin would be shortened dramatically due to entropic reasons. Assuming a contour length of 200 nm and a persistence length of $0.1 - 10$ nm, the theory for worm-like chains gives a value of $17.8 - 61.6$ nm for the end-to-end distance of the polymer. Theories based on this principle have been applied [91, 92, 93, 94] but the highly crumpled state of the filaments seems to contradict experimental observations. Therefore, people proposed, that spectrins could associate laterally [86], that the observed filaments could be spectrin dimers instead of tetramers and that spetrin could be in higher oligomeric states [77].

A different approach considers the sub-structure of spectrin and proposes structural rearrangements that lead to considerable shortening of the tetramer. As already discussed, a tetramer consists of an α and a β strand that wind around each other in a helical fashion. Based on this structure a possible mechanism for changing the contour length of the filament lies in adjusting the helical pitch and diameter. Images of negatively stained filaments seem to support this mechanism [90] (see Figure 3.3c). It was also found that bending in the linker region between spectrin repeats can lead to a shortening of 30 % while keeping the filament straight [89] (see Figure 3.3b). Brown *et al.* [83] developed a model exploiting the above mechanisms which they term the Chinese finger-trap model which is shown in Figure 3.3a. By varying the pitch, the contour length changes from

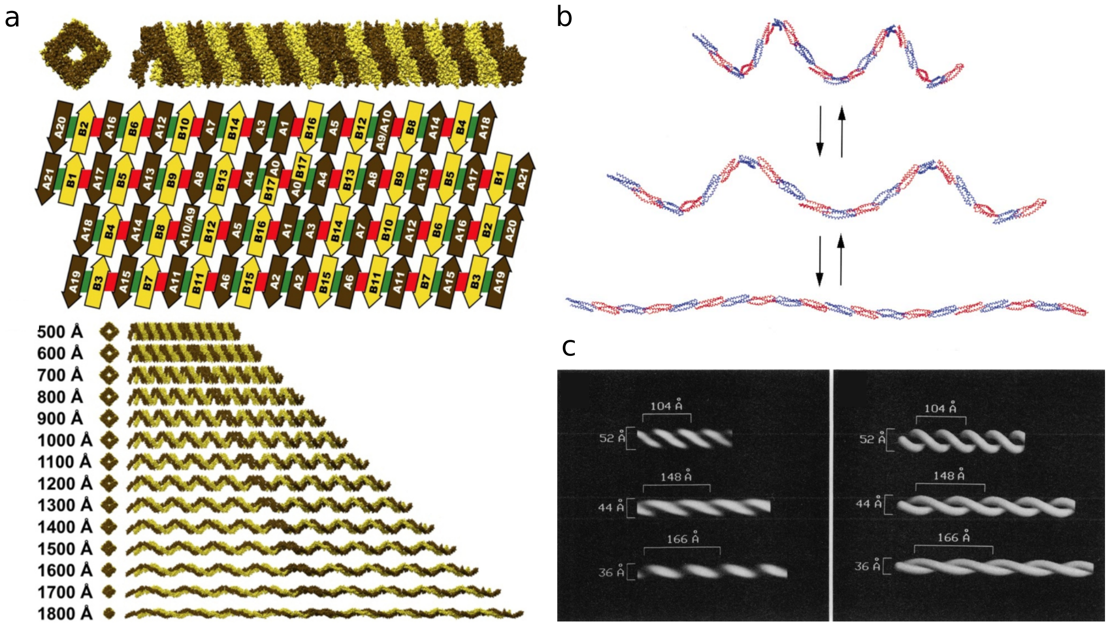

Figure 3.3: a) Schematic of the Finger Trap model discussed by Brown *et al.* [83]. The top row shows the front and side view of the compacted spectrin whereas the graphic in the middle gives a possible molecular organization of this structure. At the bottom the different configurations for various contour lengths are shown. b) Spectrin model from Ref. [89] and c) filtered microscopy images from Ref. [90] showing a possible relation between spectrin pitch and diameter.

180 nm to 50 nm. At the same time the filament diameter changes and the short filaments are hollow in the middle which they also seem to observe experimentally. This model would explain, why microscopy images mainly show straight filaments. However, it does not explain why the spectrin network was observed to have a thickness of up to 90 nm [94] (a 40 nm soft and a 50 nm stiffer regime beneath) with tangentially oriented actin filaments [93] as the base.

When pulling on single spectrin filaments, more information can be found about its behaviour under large strains. The filament can actually be stretched out further than it's contour length of 200 nm because the single repeat structures can unfold. This has been shown in an AFM study by Rief *et al.* [95]. Although this unfolding is important for large forces in situations where the RBC is stretched a lot, it does not play a role in the discussion about the equilibrium structure of the RBC cytoskeleton.

Overall, the entropic picture of a flexible polymer that shortens due to entropy and forms a thick layer seems most plausible. Especially since the theory of such a polymer gel yields the right macroscopic quantities like the shear modulus which is discussed in the next section. Additionally, in recent years this picture has been accepted by most researchers in the field.

3.2.3 Shear Modulus: Experimental and Theoretical Results

Until now, the microscopic structure of the RBC cytoskeleton was discussed. However, in most cases the mechanics of RBCs are probed on more macroscopic scales. To access the stiffness of the membrane and the cell as a hole, one important quantity is the shear modulus. In a shear experiment either a force (stress τ) or a deformation (strain γ) is applied. These two quantities are related by the shear modulus μ:

$$\tau_{\mathrm{xy}} = \mu \ \gamma_{\mathrm{xy}} . \tag{3.1}$$

Note that this description assumes an isotropic response of the material. Although the cytoskeleton will not be isotropic on the microscopic scale, it can be treated as an isotropic continuum on the scale of a shear experiment.

Such an experiment is useful, since it indirectly gains information about the small scale by probing the membrane on the whole cell level. The RBC shear modulus has been measured to be $2.4-2.75\ \mu\mathrm{N\,m}^{-1}$ and a review of the outcome of different measurment techniques can be found in [96]. Possible techniques to probe the shear modulus are micropipette aspiration, optical tweezers or flow chamber experiments.

Another way to probe the shear modulus is observing fluctuations of the network. This can be done by attaching nano-particles to the actin nodes [97] and observing the fluctuations for different locations. This way Lee *et al.* found that fluctuations are increased along the strain axis if a large strain is applied. A possible explanation are dissociation events or unfolding. In a similar approach, the shear modulus can be probed by analysing the fluctuations of the membrane by a method called flickering analysis. How this works in detail is treated in Chapter 2.

A study on RBCs has shown that the network gets softer with increasing temperature [98]. This result contradicts the picture of an entropic cytoskeleton elasticity. However, the RBC is complex enough that there could be also other reasons that explain this observation.

3.2.4 Dynamic Actin Junction

It is still generally excepted, that the actin junctional points consist of static filaments of equal lengths which are kept at this length by additional proteins. However, there has been evidence that this is not true in general. Motivated by the malaria community, people have started looking into the possibility of dynamic actin junctions that are partly stabilized by capping proteins. An interesting question is, how the malaria parasite uses this dynamic equilibrium to take actin out of this system in order to build its own trafficking system.

When labelling junctional complex components, it became clear that even the healthy cytoskeleton seems to have 200 nm large voids [99]. Hence, the network seems to be more disordered than previously thought. In malaria infected RBCs it has been shown, that the parasite uses host derived actin monomers to build filaments that connect to the membrane [23, 100]. The reduction of actin junctional complex number also fits the observation that infected RBCs develop large voids in the network.

In 2015 the first RBC study showed evidence for actin exchange in healthy RBCs. By labelling the G-actin monomers it was shown that one third of actin filaments dynamically exchange actin monomers at a given time [101, 102]. This observation is in agreement with the observation that the actin capping proteins are localized to a subset of junctional complexes [99].

Actin Filaments

The actin filament itself has a persistence length around 0.1 µm and is polarized such that it has one fast growing end (”barbed” or plus) and one slow growing end (”pointed” or minus). The magnitude of rate constants at the barbed end is significantly larger than at the pointed end. However, the situation is further complicated by ATP hydrolysis within the actin monomer and different rate constants associated to the different states. Although ATP hydrolysis occurs very slowly for free actin subunits, it is faster (rate of 0.3 s^{-1} in the presence of Mg, assuming random hydrolysis uninfluenced by neighbouring monomers [103]) once the subunit is bound in a filament and hence, the hydrolysis plays a role for actin filament assembly. Shortly after the hydrolysis occurred, the phosphate is released from the filament at a rate of $0.002 - 0.006$ s^{-1} [104], leaving ADP-actin behind. This leads to 3 different states, ATP-actin, ADP/P-actin and ADP-actin which detach at different rates. There has been some debate whether the hydrolysis happens randomly or vectorially, which would mean that hydrolysis occurs next to already hydrolysed monomers. Although not completely clear, many studies suggest the random hypothesis [105, 106].

Because of the accumulation of hydrolysed subunits at the pointed end the filaments can be in a state termed ”treadmilling”, where the depolymerization rate at the pointed end is equal to the polymerization rate at the barbed end, so that the filament stays at constant length but the subunits are constantly renewed. For this to occur the free monomer concentration must be between the critical concentrations of the pointed and barbed end. These concentrations can only be different because one end is hydrolysed and the other one is not.

Actin filaments have many different functions in cells depending on their length and organization. Where the short actin filaments hold the RBC cytoskeleton together, the dynamic actin polymerization is the foundation for cell motility. The filaments are built from 43 kD globular G-actin (see Figure 3.4a) and form a two-stranded right-handed helix with a diameter of 8 nm (see Figure 3.4b). To fulfil all different functions, the filament length and dynamics can be controlled by adjusting the actin monomer concentration or by addition of actin binding proteins, such as capping proteins which will be described in more detail hereafter. In most non-muscle vertebrate cells, only half of the actin is bound to filaments. This leads to a monomer concentration of $50 - 200$ µM which is a lot higher than the critical concentration.

Rate Constants

On the experimental side there have been various studies to measure how actin growth depends on monomer concentration and to observe the phenomenon of treadmilling [107, 108]. Early studies measured the rates by electron microscopy

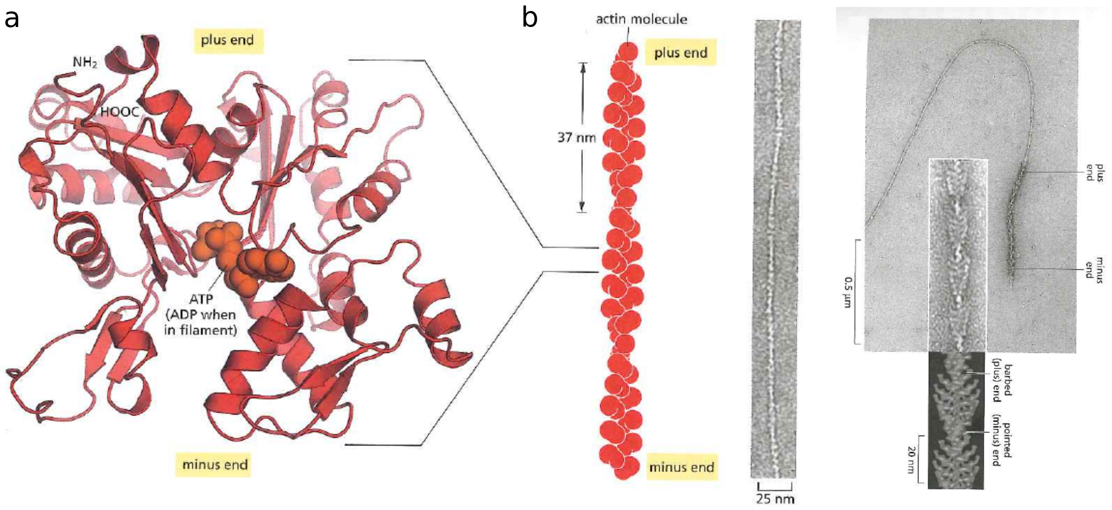

Figure 3.4: Structure of actin monomers in a) and filaments in b) taken from Alberts *et al.* [3]. The right image clearly shows that an actin filament has two distinct sides.

which requires fixation (values in Table D.1). Other approaches used fluorescence microscopy but a major problem in real-time measurements is the background fluorescence of the labelled monomers. To circumvent this problem Kuhn *et al.* [108] used total internal reflection fluorescence microscopy to follow the filament growth. In order to distinguish between the pointed and barbed end, the filaments were attached via N-ethylmaleimide inactivated myosins or different fractions of labelled actin were used to establish a clear border which can be tracked. In this study treadmilling was observed and the different association and dissociation constants for ATP-actin and ADP-actin were found as shown in Table D.1. The ADP dissociation rates were measured after the filaments were aged in treadmilling conditions so that most actin was converted to ADP-actin. Additionally, vitamin D binding protein was added to sequester the dissociated monomers during the dissociation process.

The rates are extracted from a plot of the time derivative of the filament length $\frac{\mathrm{dl}}{\mathrm{dt}}$ against free actin monomer concentration C since the slope corresponds to the association constant k_+ and the y-axis interception to the dissociation constant k_-:

$$\frac{\mathrm{dl}}{\mathrm{dt}} = k_+ \, C - k_- . \tag{3.2}$$

The association of monomers is concentration dependent, since more monomers have the chance to associate to the filament if the monomer concentration is high. For a dissociation however, it does not matter, how many monomers are available.

When considering binding interactions, an important quantity is the dissociation constant $\mathrm{K_D}$. It given by

$$\mathrm{K_D} = \frac{k_-}{k_+} \tag{3.3}$$

and hence, a smaller $\mathrm{K_D}$ implies more likely binding. The dissociation constant has a unit of concentration.

Modelling Actin Dynamics

There have also been various approaches to model actin filament growth. Analytical studies taking into account ATP hydrolysis based on probability distributions [109] and a master equation approach [110] reproduce the actin filament dynamics as well as predict an ADP-P and ATP cap and maximal length fluctuations just above the critical concentration, although not as large as experimentally observed.

The stochastic nature of the process is well captured in particle-based models like a Brownian Dynamics approach. In a series of papers Guo *et al.* [111, 112, 113] established such a BD scheme which models an actin monomer by three connected BD particles and speeds up the reactions by rescaling the reaction rates. This model also incorporated ATP-hydrolisis. The basic equation of the BD scheme is

$$\boldsymbol{r}_i(t+\Delta t) = \boldsymbol{r}_i(t) + \frac{\Delta t}{k_{\mathrm{B}}T}\sum_j D_{ij}\cdot \boldsymbol{F}_{ij} + \boldsymbol{R}_i(\Delta t), \tag{3.4}$$

where $\boldsymbol{r}_i$ is the position of the particle, Δt the time step, $k_{\mathrm{B}}T$ the Boltzmann constant multiplied by the temperature and $\boldsymbol{F}_{ij}$ the force tensor due to interparticle potentials. The diffusion tensor D_{ij} reduces to

$$D_{ij} = \frac{k_{\mathrm{B}}T}{6\pi\eta r_{\mathrm{particle}}}\delta_{ij} \tag{3.5}$$

without hydrodynamic interactions. The random displacement $\boldsymbol{R}_i(\Delta t)$ has mean $\langle \boldsymbol{R}_i(\Delta t)\rangle = 0$ and $\langle \boldsymbol{R}_i(\Delta t)\cdot \boldsymbol{R}_j(\Delta t)\rangle = 6D_{ij}\Delta t$. A soft-core potential is used between free monomers. Reactions take place when monomers enter a capture zone at the end of the tetramer which is a conical cut from a sphere with internal angle 60°. Reaction rates can then be tuned by varying the size of this capture zone. Additionally, all particles get a flag for their type (T,D,P), corresponding to ATP-actin, ADP-actin and ADP-actin plus bound phosphate. The simulation reproduces most features of the experimental data but length fluctuations near the critical concentration are not as large as in experiments.

Capping Proteins

The RBC uses the the capping proteins tropomodulin and adducin as well as the actin binding protein tropomyosin in order to control filament length. These proteins associate to the actin filaments and prevent further polymerization. The highly conserved length of 35 nm is thought to be dictated through tropomyosin. Tropomyosin is a rod like protein that binds 6-7 actin monomers. With its length of 34 nm it is thought to act as a molecular ruler in the actin junctions, with one tropomyosin binding to each actin strand.

Polymerizaiton stops at the length of tropomyosin because tropomodulin associates to the pointed end of actin filaments better in presence of tropomyosin ($\mathrm{K_D} < 1$ nM) [114]. In absence of tropomyosin the affinity is much smaller ($\mathrm{K_D} \approx 0.3$ µM) [115]. Adducin ($\mathrm{K_D} \approx 100$ nM) caps the barbed end of actin filaments and recruits additional spectrin filaments to the junctional complex [116], such that more spectrins are recruited to the fast growing side of the filament [117]. When comparing these dissociation constants, we observe that adducin has a much larger dissociation constant than tropomodulin (with tropomyosin present). This means that adducin is less strongly bound.

3.3 Details on Malaria Induced Changes

The malaria parasite uses the RBC to hide inside the body and to replicate. In order to do so, it consumes haemoglobin and alters the properties of the membrane by exporting proteins [24]. The consumption of haemoglobin generates toxic reactive oxygen species and free heme which is known to destabilize the membrane (compareable to the situation in sickle cells) by interacting with the cytoskeleton. The parasite needs to prevent premature rupture but also uses host actin to transport proteins to the membrane such that adhesion complexes can be formed. In HbAS and HbAC cells the remodelling process seems to be less efficient such that these cells are less adhesive and lead to less severe symptoms. One reason might be the increased level of hemichromes [118] which alter the cytoskeletal interactions. However, it is unclear, which parts of the parasite's remodelling process are most affected by the haemoglobin variants. A detailed review about the malaria induced changes inside the RBC can be found in Ref. [17].

3.3.1 Knob Associated Histidine Rich Protein

An important parasite exported protein is the knob associated histidine rich protein (KAHRP) (80-108 kDa [119]) which is essential to form knobs on the RBC surface [120]. The N-terminal half of the protein is called K1 and is the the histidine-rich part. Then there is a lysine rich region termed K2 and the C-terminal repeat region is called K3 [121]. Overall, KAHRP is a highly disordered protein, such that it can bind to many different sites of the RBC cytoskeleton.

The parasite starts synthesizing KAHRP in the mid ring stage and then exports it into the RBC cytosol. Hence, the protein reaches the membrane through diffusion and then binds to various locations within the spectrin-actin network, as I will exlain in the following paragraphs. This attachment of KAHRP to the cytoskeleton leads to a drastic stiffening of the membrane [24]. Since the RBC gains its flexibility through the spectrin network this means that KAHRP somehow interacts with the spectrin filaments. However, its main purpose seems to be the formation of protrusions, termed knobs, on the RBC surface. It was shown that after the disruption of the KAHRP gene, knobs do not form properly and the cytoadhesion of the infected cells is reduced dramatically under flow conditions [122]. With immunoelectron microscopy it was found, that KAHRP can cluster at actin junctions and also attach along the cytoskeleton [123]. It is also believed that KAHRP forms the electron dense layer just below the bilayer in knob areas but the exact structure of the knobs and where exactly KAHRP binds to form knobs is still unclear. People have tried to solve this question by determining dissociation constants of the binding processes between different protein fragments which are summarized hereafter.

First of all, it has been observed that KAHRP self-associates into clusters similar to the size of knobs (≈ 100 nm diameter). These clusters have also been shown to bind to the spectrin-actin-protein 4.1 junction [124, 123]. Therefore, it might be possible, that KAHRP forms larger aggregates in the cytosol and then attaches to the membrane. The alternative would be, that KAHRP first attaches to the cytoskeleton and then assembles to larger structures.

The interaction between KAHRP and spectrin has been narrowed down to two distinct interaction pairs. Pei *et al.* [125] found that a 72-amino-acid stretch of KAHRP associates with repeat 4 of α spectrin and the 5-repeat region of KAHRP binds β spectrin repeats 10-14. The second of these lies directly next to the spectrin-ankyrin interaction site [120, 126, 127] and is strengthened through complementary electric charges. Cutts *et al.* [127] measured dissociation constants and conducted molecular dynamics simulations to confirm the β spectrin binding site with a dissociation constant of $k_D = 50 \pm 15$ µM. However, for the α spectrin binding site they obtained contradicting results. They pinpointed the bining site to repeats 12-16 instead of repeat 4 and found this binding to be three times weaker with a dissociation constant of $k_D = 160 \pm 60$ µM.

Additionally, a binding site for ankyrin was found and could be narrowed down to a 79-residue segment on KAHRP [126]. The site on ankyrin that it binds to was identified as the band 3 binding domain. Magowan *et al.* [119] found dissociation constants for the 89 kDA membrane-binding domain (MBD) and the 43 kDa subdomain with full length KAHRP to be $k_D = 1.8$ and $k_D = 1.3$ µM, respectively. Weng *et al.* [126] only considered the K1 domain of KAHRP but the same ankyrin domains. Here they found dissociation constants of $k_D = 0.046$ and $k_D = 0.038$ µM, respectively. It makes sense that the binding is stronger (smaller k_D) for the smaller KAHRP domain, since there are no entropic repulsion effects.

3.3.2 Plasmodium Falciparum Erythrocyte Membrane Protein 1

Another very important parasite exported protein is called plasmodium falciparum erythrocyte membrane protein 1 (PfEMP1) which interacts with various ligands on epithelial cells [137] and hence mediates cytoadhesion. This 200-350 kDa transmembrane protein clusters on knobs such that it interacts more easily with endothelial receptors to induce adherence. This clustering only happens in the presense of KAHRP and otherwise cytoadhesion is reduced [122]. PfEMP1 is transported to the membrane in vesicles with the cytoplasmic domain pointing outwards. This cytoplasmic domain which is the acidic terminal sequence (ATS) of PfEMP1 is called VARC and is highly disordered (similar to KAHRP) [138]. The export is a very slow process and goes through the parasite induced Maurer's clefts. Transcription peaks at 12 h past invasion but the protein only reaches the membrane 16 hours past invasion [139].

First, the binding interactions of the extracellular part of PfEMP1 to endothelial receptors are discussed. These turn out to be slightly different for different PfEMP1 variants, whereas the cytoplasmic region is highly conserved. Most PfEMP1 variants have a binding site for CD36 which lies in the cysteine-rich interdomain region [140]. Binding sites to chondroitin sulphate A (CSA) are only

Protein 1	**Protein 2**	K_D **in** μM	**References**
Spectrin	F-actin	200	Ohanian *et al.* 1984 [128]
Spectrin	protein4.1	0.1	Tyler *et al.* 1980 [129]
		0.1	Podgorski *et al.* 1985 [130]
		2.0	Eder *et al.* 1986 [131]
		0.2	Li *et al.* 2014 [132]
	(phosphorylated)	9.6	Eder *et al.* 1986 [131]
Spectrin	Ankyrin	0.1	Tyler *et al.* 1980 [129]
		0.05	Bennet *et al.* 1980 [133]
Ankyrin	Band3	0.01	Bennett *et al.* 1980 [133]
		0.01	Thevenin *et al.* 1990 [134]
Spectrin	Spectrin	2	Liu *et al.* 1981
Tropomyosin	F-actin	0.4	Fowler *et al.* 1984 [135]
KAHRP	Ankyrin (MBD)	1.8	Magowan *et al.* 2000 [119]
KAHRP	Ankyrin (D3)	1.3	Magowan *et al.* 2000 [119]
KAHRP K1D	Ankyrin (MBD)	0.038	Weng *et al.* 2014 [126]
KAHRP K1D	Ankyrin (D3)	0.046	Weng *et al.* 2014 [126]
VAR_{CD}	F-actin	0.04	Oh *et al.* 2000 [123]
VAR_{CD}	KAHRP	0.01	Oh *et al.* 2000 [123]
VARC	KAHRP (K1A)	0.1	Waller *et al.* 1999 [136]
VARC	KAHRP (K2A)	3.3	Waller *et al.* 1999 [136]
VARC	KAHRP (K2A1)	32.06	Ganguly *et al.* 2015 [121]
VARC	KAHRP (K3)	13.0	Waller *et al.* 1999 [136]

Table 3.1: Dissociation constants are listed, that have been found by various groups for different protein(fragment) pairs. The three parts of the table show interactions of host cytoskeletal proteins, interactions with KAHRP and interactions with the cytoplasmic domain of PfEMP1 from top to bottom.

present in some isolates [141] and other receptors that can potentially be bound are the intercellular adhesioin molecule 1 (ICAM-1) and thrombospondin [136].

On the cytoplasmic side PfEMP1 needs to be anchored by the VARC domain to the RBC cytoskeleton to transmit the forces due to adhesion. Oh *et al.* found very low dissociation constants in the order of magnitude of 10 nM for the binding of VARC to F-actin and KAHRP such that a direct anchorage to the host cytoskeleton and the knob was proposed. Subsequently, a more detailed picture of the PfEMP1 binding sites was developed.

One parasite induced binding partner is KAHRP which is thought to make up the base of the knobs and hence can anchor PfEMP1 to knob regions. The VARC domain can bind to KAHRP via long range electrostatic interactions [119]. Actually, there are 3 distinct KAHRP fragments (the N-terminal region of K1 and K2 termed K1A and K2A and K3) that PfEMP1 can bind to. Out of these three, K1A and K2A have strong binding affinities, namely $\mathrm{K_D} = 0.1$ µM and K2A $\mathrm{K_D} = 3.3$ µM, whereas K3 only binds weakly with $\mathrm{K_D} = 13.0$ µM [136]. The binding to K2A is mediated via the first 291 residues of VARC [121]. Overall, the binding of PfEMP1 to KAHRP is enhanced through the phosphorylation of the VARC domain by the RBC casein kinase II [142].

It has further been found that VARC can bind spectrin close to the spectrin actin junction [119, 123]. Although the core of the VARC domain interacts broadly with spectrin, the strongest interaction could be specified to the 17th repeat of the spectrin α-chain [127] and the C-terminus of VARC. Mayer *et al.* [138] found a dissociation constant of $K_d = 59 \pm 6$ µM.

Since PfEMP1 arrives in vesicles at the membrane, it is most likely that it enters knob areas by 2d diffusion in the membrane. As we will see in Section 3.6, there is only a small number of PfEMP1 molecules present in each knob and they have been found to cluster towards the middle.

3.3.3 Actin Mining

When examining the internal structures of RBCs with different haemoglobin variants, Cyrklaff *et al.* observed long actin filaments inside the RBC cytosol [23]. The aim of the study was to show, why some haemoglobin variants protect the host from severe malaria pathology and they answered this question by reconstructing cryo-electron tomogram images of rapidly frozen RBC samples. An example can be seen in Figure 3.5 where we see an uninfected RBC on the left, an infected HbAA RBC in the middle and an HBCC RBC on the right. The most important features that can be seen are the yellow filaments that form for the infected RBCs. From additional experiments it is clear, that this is host derived actin which grows in direction of the Maurer's clefts (cyan membrane structures).

The existance of these filaments is thought to aid transport of proteins from the parasite to the membrane. In the figure we see how vesicles are possibly transported along the filaments. The source of the motion could either be actin polymerization close to the Maurer's clefts or a molecular motor could be used. Rug *et al.* found that interfering with PfEMP1 trafficking prevents proper assembly of the Maurer's clefts [143].

In Figure 3.5c we see a HbCC RBC and observe that actin filaments are a

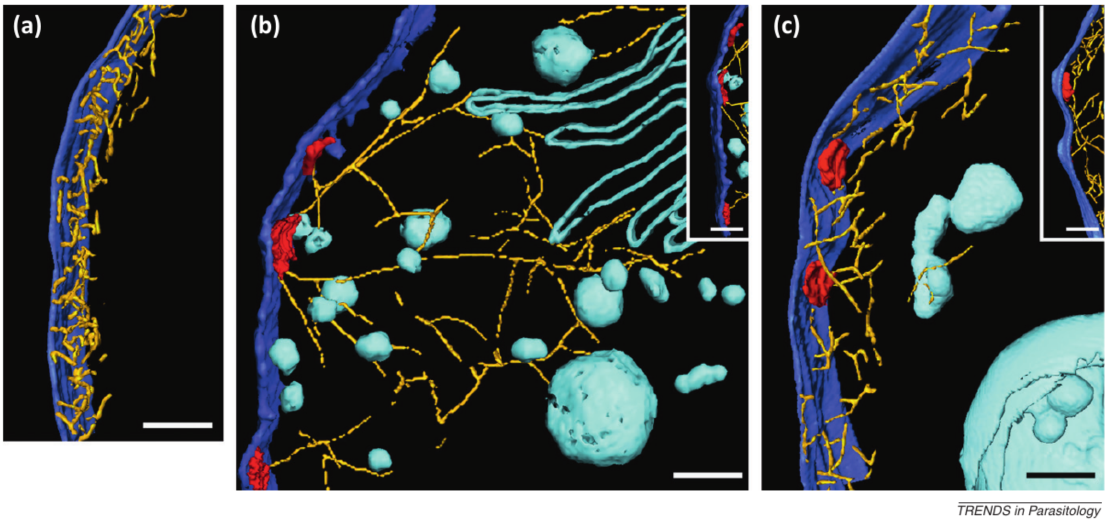

Figure 3.5: Reconstructed tomograms of an uninfected HbAA erythrocyte in a), a trophozoite-infected HbAA erythrocyte in b) and a trophozoite-infected HbCC erythrocyte in c), taken from [100]. The scale bar is 100 nm and the colours highlight the following compartments: blue, plasma membrane; yellow, actin filaments; red, knobs and cyan, vesicles and Maurer's clefts.

lot shorter. An explanation might be that haemoglobin oxidation products which are present in HBCC and HBSS erythrocytes interfere with the actin polymerisation [23].

3.3.4 Phosphorylation

Phosphorylation of proteins (the attachment of a phosphoryl group) can alter their binding affinities dramatically. For example, phosphorylation of protein 4.1 amplifies its dissociation constant with spectrin by a factor of five (compare Table 3.1). In the healthy RBC phosphorylation is regulated by human kinases, such as cAMP-dependent kinase or protein kinase C [17].

Where most proteins are dephosphorylated in the early parasite life-cycle [144], phosphorylation is increased at the end of the ring stage by parasite exported kinases. The parasite seems to export at least 20 different kinases [145]. Hence, it is very likely that binding affinities change during the parasite life-cycle.

An increased level of phosphorylation has been measures for protein 4.1 and band 3 in malaria infected RBCs [146, 147]. This phosphorylation is assumed to destabilize the membrane skeleton. The phosphorylation of KAHRP has not been studied very well, but it could potentially change its binding properties during the infection. For further information see the analysis of the KAHRP cluster formation in Section 3.5.4.

3.3.5 Oxidative Stress

In order to carry oxygen through the body, the Fe(II) haemoglobin in RBCs can bind oxygen reversibly. At the same time 3 % of haemoglobin is oxidized in 24 hours, producing superoxide [148] and further oxidation products. It has been found that haemoglobin oxidation products have different effects on the membrane skeleton stability. Some stabilize the skeletons via promotion of spectrin self-association to tetramers and others decrease the spectrin-protein 4.1-actin binding.

Whereas the oxidation products are held at a low level in healthy red blood cells, in sickle cell disease the hemin level is increased three to five-fold. This is due to the redox imbalance that is associated with sickle cell anemia. Furthermore, it has been found that there is 50% less spectrin-ankyrin binding in sickle cells. The situation is even worse in malaria infected red blood cells. The parasite consumes haemoglobin and thus, generates toxic reactive oxygen species and free heme. To prevent complete destruction of the red blood cell, some of this is converted to inert hemozoin by the parasite [149].

3.4 Experimental Data

In order to determine where exactly knobs form in the RBC cytoskeleton experiments were set up in which two proteins are labelled by distinct colours. The experimental work was done by Cecilia Sanchez from Prof. Michael Lanzer's group at the University Clinics Heidelberg and the data analysis was done by Pintu Patra from Prof. Ulrich Schwarz's group.

The experiments were conducted on uninfected, ring stage infected and trophozoite infected RBCs in order to see temporal changes. In each RBC two proteins were labelled by anti-bodies such that their relative position could be determined. The RBCs were opened up, such that the cytoplasmic side could be examined with super-resolution microscopy. Three examples of the obtained data can be seen in Figure 3.6, where Figure 3.6a shows labelled ankyrin and protein 4.1 in an uninfected cell, Figure 3.6b shows ankyrin and KAHRP in a ring stage infected RBC and in Figure 3.6c ankyrin and KAHRP are labelled in a trophozoite iRBC.

These images were then analysed by Pintu Patra's python scripts, which determine the pair cross-correlation of the two distinctly labelled proteins. The pair cross-correlation for localization points is calculated by

$$C(r, r+\Delta r) = \frac{\sum_{\rho=r}^{\rho=r+\Delta r} \sum_{i=1}^{n_R} \sum_{j=1}^{n_G} \delta(|\boldsymbol{r}_i - \boldsymbol{r}_j| - \rho)}{\pi \Delta r (2r + \Delta r)\eta}, \quad \eta = \frac{n_R \times n_G}{A_{\text{image}}}, \tag{3.6}$$

where r is the distance between point pairs, Δr the bin width of the radial bins, $\boldsymbol{r}_i$ is the position vector of a point and η gives the density of pair-wise distances ($\eta_{R/G}$ is the number of total red/green points). A cross-correlation of 1 indicates a random distribution, such that for long distances all cross-correlations decay to 1. A value above 1 shows that a lot of protein pairs have the specified distance to each other, whereas a value below 1 means that there are less proteins of the given distance than for a random distribution.

In Figure 3.7 selected cross-correlation curves are shown for healthy RBCs in Figure 3.7a, ring stage iRBCs in Figure 3.7b and trophozoite iRBCs in Figure 3.7c. For the healthy RBC positive correlations can be seen for protein 4.1 with actin and tropomodulin but not for ankyrin. This validates that the method works correctly, since protein 4.1, actin and tropomodulin are part of the actin junctional complex but ankyrin is not.

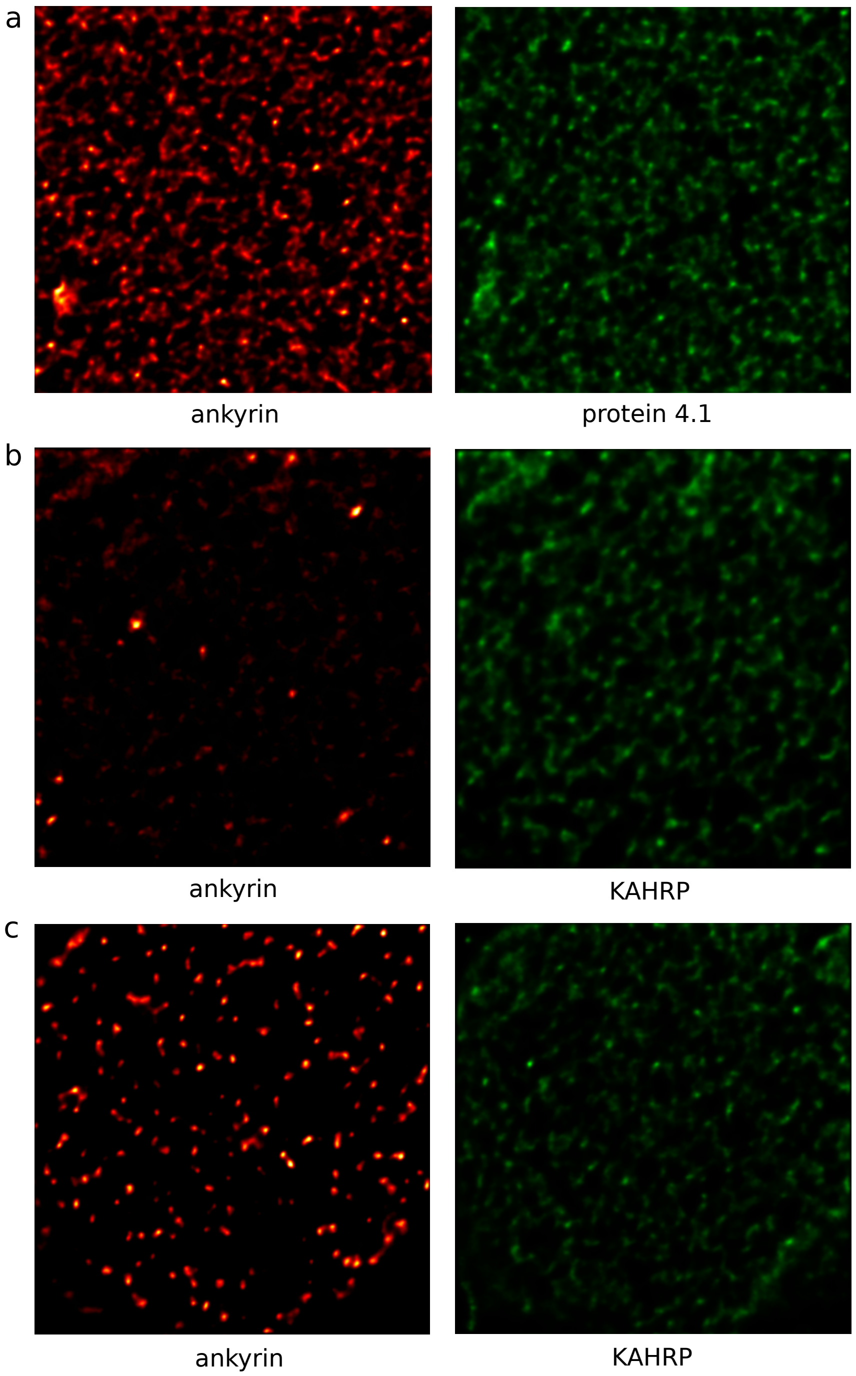

Figure 3.6: Experimental data from the cross-correlation study done in Prof. Lanzer's Lab is shown. Two colour channels, red and green, were observed as shown in each row. a) Antibodies associated to ankyrin and protein 4.1 are labelled in an uninfected RBC. b) Ankyrin and KAHRP are labelled in a ring iRBC. c) Ankyrin and KAHRP are labelled in a trophozoite iRBC.

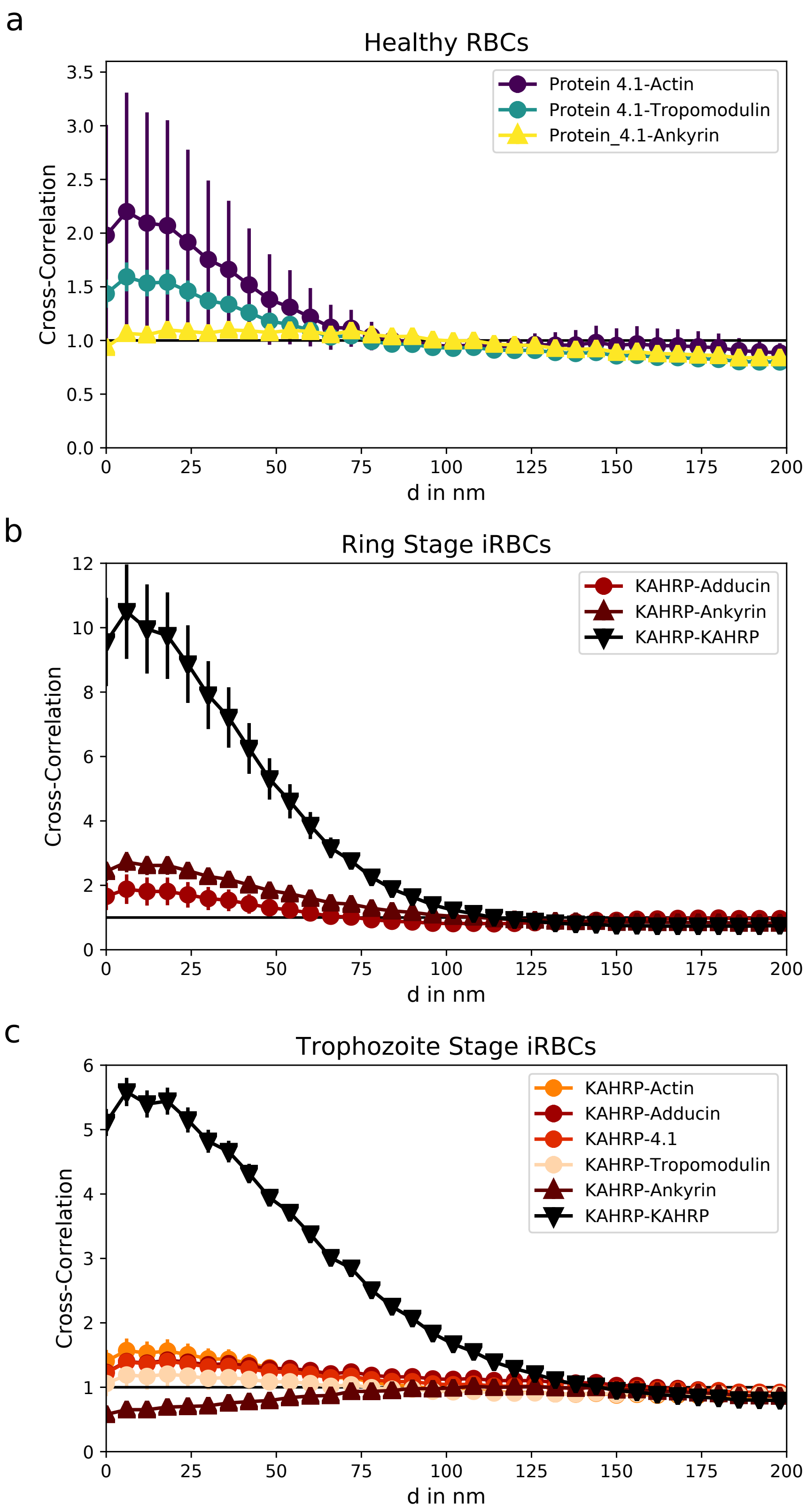

Figure 3.7: The analyis of the experimental data from the cross-correlation study done in Prof. Lanzer's Lab is shown. The data analysis was done by Pintu Patra. The calculated cross-correlations are shown for a) the uninfected RBC, b) the ring iRBC and c) the trophozoite RBC. Each curve is the average of approximately 30 images.

For the iRBCs, two different tags for KAHRP were used and tested by correlating one of these with the other. As expected a very high correlation is found for small distances. In ring stage positive correlations were also found for KAHRP with adducin, which is one of the actin capping proteins, and ankyrin. Hence, we conclude that KAHRP attaches all along the cytoskeleton during ring stage.

In trophozoite stage adducin and other actin junctional proteins also show a positive correlation with KAHRP at small distances, but ankyrin starts with a value below 1 which indicates that KAHRP is not near the ankyrin sites during this infection stage.

Overall, this study seems to suggest, that KAHRP first binds to all its possible binding sites during ring stage but later moves away from the ankyrin sites. The binding interactions of KAHRP with the cytoskeleton were explained in the last section and were shown to exist both close to the actin junction and the ankyrin site. It remains unclear which mechanism is responsible for this configuration change. I try to find an explanation by applying a reaction-diffusion model to the RBC cytoskeleton in the next section.

3.5 Reaction-Diffusion Model for Healthy and Infected RBCs

3.5.1 Modelling Technique and Software

Reactive Brownian Dynamics

A convenient way to model the RBC cytoskeleton seems to be a reactive Brownian dynamics approach where particles are represented as solid spheres. In this type of model, the particles diffuse through the reaction volume using a Brownian dynamics scheme and can additionally react with each other once they are close enough and specific conditions are fulfilled. On top of this, inter-particle potentials can be introduced, such that particles can repel each other form a chain of a given persistence length. Two reviews on such algorithms can be found in [150] and [151].

When reactions take place in solution, the molecules have to find each other through diffusive motion before the reaction can take place. Hence, several rates are important, the rate for forming the reactive complex within a solvent cage, k_1, the rate for disassembly of this complex, k_{-1} and the rate of reaction, k_2. The reactive complex has a typical lifetime of 100 ps [152].

Because of these two different processes, two limits can be considered; the diffusion-controlled limit and the reaction controlled limit. In the diffusion controlled limit ($k_2 \gg k_{\pm 1}$) the reaction is determined by the formation of the reactive complex with reaction rate k_1. In the reaction-controlled limit an equilibrium between reactive complexes and single molecules builds up $\frac{C_{\{AB\}}}{C_A C_B} = K = \frac{k_1}{k_{-1}}$, so that the overall reaction rate is given by $k_2 K$ (C denotes concentrations of the different species A, B or AB).

ReaDDy

The simulation software that we will use is called ReaDDy and was developed by the group of Prof. Frank Noé. ReaDDy models the movement of particles with generalized Langevin dynamics in the overdamped limit, where interaction potentials are incorporated naturally. Before particles can react, an encounter complex has to be formed and then the reaction happens with a specified activation rate.

The rate at which an encounter complex is formed is given by the Smoluchowski equation:

$$k_{\mathrm{enc}} = 4\pi(D_1 + D_2)(r_{i,1} + r_{i,2}), \tag{3.7}$$

where D_i the diffusion constant of particle i and r_i is the reaction radius of the particle. This radius can be different from the collision radius r_c of each particle, which determines the particles spacial extend via a repulsion potential. The macroscopic and microscopic on-rates (k^+ and k^+_{micro}) are related by the following equation:

$$k^+ = 4\pi(D_1 + D_2)\left[R_{12} - \sqrt{\frac{D_1 + D_2}{k^+_{\mathrm{micro}}}}\tanh\left(R_{12}\sqrt{\frac{k^+_{\mathrm{micro}}}{D_1 + D_2}}\right)\right]. \tag{3.8}$$

All reactions are set up in a way that ensures detailed balance which is important to reproduce the right equilibrium properties. Since 2018 it is also possible to model membranes in ReaDDy which might be beneficial to us in the future. For initial steps it is sufficient to constrain the cytoskeleton to a 2D plane.

Previous RBC Modelling Approaches

The RBC membrane has been modelled on several scales by various methods. When doing so, a compromise has to be found between including molecular detail and reaching a reasonable system size for the relevant problem. Therefore, models either consider a small membrane patch with a few junctional complexes or the RBC as a whole, where molecular detail is lost. These large scale models are usually more easily comparable to experimental data.

On the small scale there is two main modelling approaches. In the so called coarse grained molecular dynamics (CGMD) model, all agents are modelled as spherical particles that interact via potentials. Typically, the membrane consists of a one agent thick layer with specific potentials that insure the correct membrane mechanics. Spectrin filaments are then modelled as chains of particles that are connected with unbreakable springs and connect at actin junctions which consist of one slightly larger particle [18]. The actin junctions are constrained to stay within the bilayer but can freely diffuse. This kind of model has been altered to incorporate effects like dissociation between actin and spectrin [153] and strengthening of the network by the formation of spectrin octamers instead of tetramers [154].

On an even smaller scale the dynamics of a fixed length actin filament has been considered by modelling it as a cylindrical rod. After calculating forces and torques on it, an average angular orientation could be determined and the question of how the spectrin filaments are attached could be discussed [155]. This model is limited to a very small number of junctional complexes.

For whole RBC simulations, the membrane is usually depicted as a triangular surface, each representing a rather large patch of membrane. The hydrodynamics of the surrounding liquids is then simulated by dissipative particle dynamics (DPD) [156] or mulit-particle collision dynamics (MPCD) [157]. In a different approach it is also possible to consider the spectrin filaments as a triangular network and extract elastic constants via an effective medium theory [79]. Although these models can capture the RBC properties very well, they do not tell much about the molecular details that lead to the behaviour.

3.5.2 Model Details

The key to modelling the right cytoskeletal behaviour is choosing all rates and parameters in an appropriate way. Here, we try to extract as many parameters as possible from previous experiments and choose the rest according to successful previous modelling approaches. For the simulations of the malaria infected cells, very little is known about the exact interactions, thus a wide range of parameters is probed in that case.

Model Elements

In the presented RBC model, the following constituents are incorporated:

- G-actin monomers:
  The monomers diffuse in the cytosol and can react with actin filament ends.

- actin filaments:
  Actin filaments are implemented with two distinct ends (corresponding to barbed and pointed) and can react with G-actin according to the rates explained hereafter.

- actin capping proteins:
  Two types of capping proteins are introduced corresponding to adducin and tropomodulin. These can bind to one actin filament end each and block polymerization.

- spectrin filaments:
  These consist of 39 beads and can bind to actin filaments with their end beads such that a cytoskeletal network can be formed.

- KAHRP monomers:
  The KAHRP monomers diffuse in the cytosol and can bind to spectrin and actin filaments as described in the next section.

The two filament types are implemented in ReaDDy as so-called topologies. These behave as one entity with specific potentials between its constituents (see Inter-Particle Potentials). In the case of actin the polymerization is included as topology reaction.

Rates

First, reaction rates need to be set correctly to model actin dynamics. The rates that are accessible in experiments are called macroscopic and can be extracted from the elongation rate ω of a filament under constant G-actin concentration C:

$$\omega = k^+ C - k^-, \tag{3.9}$$

where k^+ and k^- are the association and dissociation rates, respectively. The addition of monomers depends on the concentration whereas the dissociation is independent. Therefore, we introduce a microscopic rate k^+_{micro} which decouples the reaction from the diffusion such that the microscopic and macroscopic association rates are related as follows:

$$k^+ = 4\pi(D_1 + D_2)\left[R_{12} - \sqrt{\frac{D_1 + D_2}{k^+_{\text{micro}}}}\tanh\left(R_{12}\sqrt{\frac{k^+_{\text{micro}}}{D_1 + D_2}}\right)\right], \tag{3.10}$$

where D_i are the diffusion constants of the two interacting particles and R_{12} is the sum of the two reaction radii. Hence, the microscopic rate which needs to be known as simulation input can be determined from the macroscopic rate using this equation.

Fujiwara *et al.* [158] used fluorescence microscopy to determine the macroscopic rates of actin assembly with a special focus on the presence of phosphate, which we neglect here. Their rates are commonly used as reference when considering actin polymerization:

$$\begin{aligned}
k_b^+ &= 11.6\ \mu\text{M}^{-1}\text{s}^{-1}\\
k_p^+ &= 1.3\ \mu\text{M}^{-1}\text{s}^{-1}\\
k_b^- &= 1.4\ \text{s}^{-1} = 1.4\cdot 10^{-9}\ \text{ns}^{-1}\\
k_p^- &= 0.8\ \text{s}^{-1} = 8\cdot 10^{-10}\ \text{ns}^{-1}.
\end{aligned}$$

The subscripts indicate the barbed or pointed end and we see that both association and dissociation rates are larger at the barbed end.

By comparing diffusion and reaction time scales it can be seen that there is a mismatch in time scales. The time scale set by actin rates is given by:

$$t_{\text{diss}} = \frac{1}{k_b^-} = 0.7\ \text{s}. \tag{3.11}$$

For the diffusion timescale t_{diff}, we consider the time a G-actin particle needs to diffuse its own size $r_0 = 3$ nm. The simulation time step Δt needs to be chosen as a fraction of this time, we choose $\Delta t = 10^{-3}\ t_{\text{diff}}$. Hence, we find

$$D_{\text{Gactin}} = 71.5\ \mu\text{m}^2\,\text{s}^{-1} \quad\rightarrow\quad t_{\text{diff}} = \frac{r_0^2}{D_{\text{Gactin}}} = 350\ \text{ns}, \tag{3.12}$$

$$\Delta t = 10^{-3} t_{\text{diff}} = 0.35 \text{ ns} \tag{3.13}$$

and see that only approximately every 10^9 time steps a dissociation event would occur which is not practical in a simulation.

Hence, we introduce a factor b that speeds up the elongation rate, as introduced in [111] and indicate the scaled rates by a hat symbol:

$$\hat{\omega} = b\omega = b(k^+ C + k^-) = \hat{k^-}\hat{C} + \hat{k^-}. \tag{3.14}$$

Therefore, we find

$$\hat{k^+} = k^+ b_k, \ \hat{C} = \frac{b}{b_k} C \text{ and } \hat{k^-} = b k^- \tag{3.15}$$

and choose $b = 1000$ and $b_k = 25$ according to [111]. This leads to the following macroscopic and microscopic rates ($\hat{C} = 40C$):

$$\begin{aligned}
\hat{k}_b^+ &= 289.5 \ \mu\text{M}^{-1}\text{s}^{-1} = 0.4825 \ \mu\text{m}^3 \ \text{s}^{-1} & \hat{k}_{b,micro}^+ &= 563521 \ \text{s}^{-1} \\
\hat{k}_p^+ &= 32.55 \ \mu\text{M}^{-1}\text{s}^{-1} = 0.05425 \ \mu\text{m}^3 \ \text{s}^{-1} & \hat{k}_{p,micro}^+ &= 60323 \ \text{s}^{-1} \\
\hat{k}_b^- &= 1400 \ \text{s}^{-1} = 1.4 \cdot 10^{-6} \ \text{ns}^{-1} & \hat{k}_{b,micro}^- &= 1400 \ \text{s}^{-1} \\
\hat{k}_p^- &= 800 \ \text{s}^{-1} = 8 \cdot 10^{-7} \ \text{ns}^{-1} & \hat{k}_{p,micro}^- &= 800 \ \text{s}^{-1}.
\end{aligned}$$

The deterministic equation for actin filament growth is given by

$$\frac{\mathrm{d}L}{\mathrm{d}t} = (\hat{k}_b^+ + \hat{k}_p^+)\hat{C} - (\hat{k}_b^- + \hat{k}_p^-), \tag{3.16}$$

where L is the filament length. By setting the elongation rate to zero, we can calculate the critical concentration for treadmilling:

$$\hat{C}_D = \frac{\hat{k}_b^- + \hat{k}_p^-}{\hat{k}_b^+ + \hat{k}_p^+}. \tag{3.17}$$

Substituting in the scaled actin rates, we find

$$\begin{aligned}
\hat{C}_D &= \frac{1400 + 800}{0.05425 + 0.4825} \ \mu\text{m}^{-3} \\
&= 4098 \ \mu\text{m}^{-3} = 4.098 \cdot 10^{-6} \ \text{nm}^{-3}.
\end{aligned}$$

Keeping the Particle Concentration Fixed

When studying polymer growth or processes in cell-like environments, it is useful to be able to keep the concentration of the diffusing monomers A at a constant level. However, the simulation software does not allow to manually adjust the number of monomers A after every reaction event, such that a different approach needs to be chosen. I do this here by introducing another species of particles N that do not interact with the system except of producing and absorbing monomers of the relevant particle species:

$$N \rightleftharpoons N + A, \tag{3.18}$$

where the rate for creating an A particle is k_c and the rate of absorbing an A particle is k_a. By tuning the rates correctly, the average value of the concentration can be set under some conditions. A relation between the rates and the concentration can be found by applying the law of mass action:

$$K = \frac{[N]_{\text{eq}}[A]_{\text{eq}}}{[A]_{\text{eq}}} = [A]_{\text{eq}} = \frac{k_c}{k_a}. \tag{3.19}$$

Sine the absorption depends on the diffusive formation of an encounter complex, the rates k_c and k_a are related to the microscopic rates f_c and f_a as follows:

$$\begin{aligned} k_c &= f_c \\ k_a &= 4\pi DR \left(1 - \sqrt{\frac{D}{f_a}} \frac{\tanh(R\sqrt{\frac{f_a}{D}})}{R}\right). \end{aligned}$$

When putting these formulas together, we find the following relation, that enables us to calculate f_c from the concentration and the previously chosen microscopic absorption rate f_a:

$$f_c = [A]_{\text{eq}} 4\pi DR \left(1 - \sqrt{\frac{D}{f_a}} \frac{\tanh(R\sqrt{\frac{f_a}{D}})}{R}\right). \tag{3.20}$$

Note that this result is only valid in the $\sqrt{\frac{f_a}{D}}R \ll 1$ regime.

As the next step we want to keep the concentration stable while an actin filament growth in the box. In that case, we additionally need to take into account the attachment and detachment from the actin filament ends:

$$\begin{aligned} N &\rightleftharpoons N + A \quad (3.21) \\ F^b &\rightleftharpoons F^b + A \quad (3.22) \\ F^p &\rightleftharpoons F^p + A, \quad (3.23) \end{aligned}$$

where F is the assembling filament with a barbed and a pointed end. These reactions lead to the following continuum differential equation:

$$\frac{\mathrm{d}[A]}{\mathrm{d}t} = [N]k_c - [N][A]k_a - [F][A](k_b^- + k_p^-) + [F](k_b^+ + k_p^+). \tag{3.24}$$

Setting this to zero and hence obtaining the equilibrium condition for A, we find an expression for f_c:

$$f_c = [A]_{\text{eq}} k_a + \frac{[F][A]_{\text{eq}}}{[N]}(k_p^- + k_b^-) - \frac{[F]}{[N]}(k_b^+ + k_p^+). \tag{3.25}$$

Note that the k^+ rates are macroscopic and need to be specified further by introducing the microscopic rates.

Particle Size and Diffusion

In ReaDDy each particle is defined by a reaction radius r_i and a collision radius r_c. The first one defines the sphere around the particle, in which it can react with other particles. The collision radius represents the extend of the particle itself so that it enters the formula for the particle-particle potentials.

The diffusion constants for each particle type also need to be known. In the framework of ReaDDy the diffusion is assumed to be isotropic. In general proteins will have directionally dependent diffusion properties but this is not important for the problem considered here and is hence neglected. If a value for the diffusion constant has been measured experimentally, this value is used. Otherwise, it can be approximated by the following formula for the diffusion of a spherical particle:

$$D = \frac{k_\mathrm{B} T}{6\pi\eta r}, \tag{3.26}$$

where k_B is the Boltzmann constant, T the temperature, *eta* the fluid viscosity (assumed to be the viscosity of water here) and r is the particle radius. The values, that are used in the simulations, are shown in Table 3.2.

Anchoring to the Bilayer

The lipid bilayer is neglected in this study because we would like to focus on the properties of the cytoskeleton. However, the confinement to the membrane plane is still important. In the RBC, the cytoskeleton is attached to the bilayer via transmembrane proteins, with band-3 being the most abundant. The parts of the cytoskeleton, that are anchored to the bilayer are the actin junctional complexes and the ankyrin binding sites (roughly in the middle of the spectrin filaments). It has further been found, that actin filament are oriented nearly parallelly to the bilayer. Therefore, all beads that are part of actin filament and the ankyrin binding sites within spectrin are confined to a 4 nm thick layer centred 10 nm above the wall of the simulation box which indicates the position of the bilayer.

Additional to the spacial confinement the anchoring reduces the diffusion of the attached proteins. Since band-3 is the most common anchor, its diffusion constant is used for the anchored beads such that the structures diffuse more slowly in the membrane plane than in free 3D space.

The diffusion constant of band-3 within the membrane has been measured to be $D = 0.53\ \mathrm{\mu m^2\,s^{-1}}$ [159] on the small scale. When looking at larger displacements, the cytoskeleton hinders the free diffusion of band-3. Therefore, the diffusion constant of the anchored particles is set to $D = 0.53\ \mathrm{\mu m^2\,s^{-1}}$.

Inter-Particle Potentials

Furthermore, the inter-particle potentials need to be tuned. We distinguish between free particles and particles topologies. In Ref. [153] Li *et al.* introduce a computational model for spectrin filaments which we implement similarly in our simulations. Specifically, in our simulations spectrin binds to actin via a Lennard-Johns potential

$$V(r) = -\frac{\epsilon}{\left(\frac{\sigma}{r_{\min}}\right)^{12} - \left(\frac{\sigma}{r_{\min}}\right)^{6}} \left[\left(\frac{\sigma}{r}\right)^{12} - \left(\frac{\sigma}{r}\right)^{6}\right], \tag{3.27}$$

which is shifted to $-\epsilon$ at the bottom of the well (at position $r_{\min}$). As in Ref. [153], we choose $\epsilon = 58.576\ \mathrm{kJ\,mol^{-1}}$ and $\sigma = 7.36$ nm. For the association of spectrin with actin in the presence of protein 4.1 association energies up to 70 $\mathrm{kJ\,mol^{-1}}$ have been calculated [128]. Further, excluded volume effects are included by a repulsion potential

$$V(r) = \frac{k_{\text{repulsion}}}{2}(r - r_0)^2, \tag{3.28}$$

with

$$k_{\text{repulsion}} = 36 \cdot 2^{2/3} \epsilon \sigma^{-2}. \tag{3.29}$$

When considering the two filament types that are present, actin and spectrin, angle and bond potentials are used to tune the filament properties. The angle potential

$$V(\theta) = k_{\text{angle}}(\theta - \pi)^2 \tag{3.30}$$

is proportional to k_{angle} which is determined by the filament persistence length l_{p}:

$$k_{\text{angle}} = \frac{l_{\text{p}} k_{\text{B}} T}{a}, \tag{3.31}$$

where a is the monomer size which roughly corresponds to the particle diameter. The bond potential is given by

$$V(d) = k_{\text{bond}}(d - d_0)^2 \tag{3.32}$$

and the bond force is chosen to have the same curvature at the bottom of the well as the spectrin-spectrin repulsion curve:

$$k_{\text{bond}} = 36 \cdot 2^{2/3} \epsilon \sigma^{-2}. \tag{3.33}$$

A summary of the values can be seen in Table 3.3 and Table 3.4 and the potentials as a function of separation can be seen in Figure 3.8.

Incorporation of KAHRP

In order to simulate effects of the malaria infection, particles are introduced that have the properties of the malaria exported protein KAHRP. Their size and diffusion constant is given by $r_c = r_i = 2.8$ nm and $D = 76.6\ \mathrm{\mu m\,s^{-1}}$, respectively, as indicated in Table 3.2. In Section 3.3 we saw, that KAHRP can self-associate, can bind spectrin at different locations and also bind to the actin junction. These binding interactions are modelled by Lennard-Johns potentials, as described in the subsection about inter-particle potentials.

Here, we implement the binding sites described in Ref. [125], which are the 4th repeat of the α-spectrin chain and the 10th to the 13th repeats of the β-

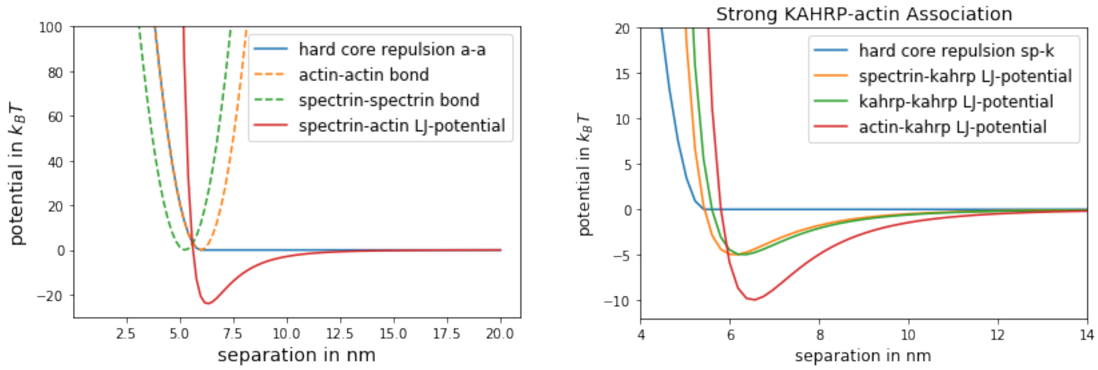

Figure 3.8: Inter-particle potentials are shown which are used in the simulation. In the left graph the interactions of cytoskeletal proteins are plotted where the right graph concernes the interactions with the KAHRP particles.

particle type	r_c in nm	r_i in nm	D in $\frac{\mu m^2}{s}$
G-actin	3	3	71.5^a
adducin	4.2^b	4.2	51.07
tropomodulin	7.25	7.25	29.59
spectrin monomer	5.26	5.26	41.1
KAHRP	2.8	2.8	76.6

Table 3.2: Values used for collision radius, the reaction radius and the diffusion constant in my simulations. a is taken from [160] and b is taken from [161].

	k_{angle} in $\frac{\text{kJ}}{\text{mol}}$	k_{bond} in $\frac{\text{kJ}}{\text{mol nm}^2}$	persistence length in nm
actin	4280	10	10000
spectrin	4.28	38.11	10 taken from [79]

Table 3.3: Parameters for the bond and angle potentials of actin and spectrin filaments.

$k_{\text{repulsion}}$ in $\frac{\text{kJ}}{\text{mol nm}^2}$	actin	spectrin	adducin	tropomodulin
actin	10	38.11	10	10
spectrin		38.11	38.11	38.11
adducin			10	10
tropomodulin				10

Table 3.4: Parameters for repulsive potentials between actin, spectrin, adducin and tropomodulin.

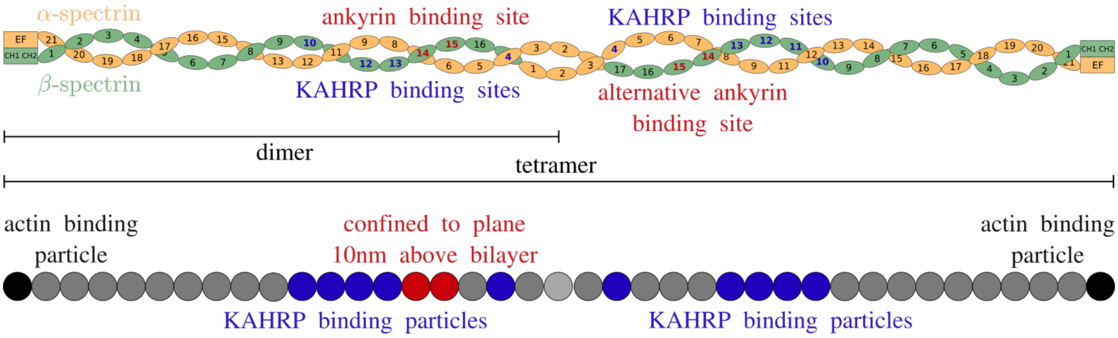

Figure 3.9: To set up the spectrin filament in the simulations, the molecular details and known binding sites are considered (top). In analogy to the number of spectrin repeats, a chain of 39 beads is set up in the simulations (bottom). Red particles indicate the ankyrin binding site and are therefore confined to the membrane plane. Their position is randomly chosen left or right of the midpoint. Blue beads model the KAHRP binding sites building on interactions that have been proven experimentally.

spectrin chain. These sites are labelled blue in the spectrin schematic at the top in Figure 3.9. Here it can also be seen, that these sites lie very close to the ankyrin binding sites labelled in red. As described above, the spectrin tetramer is modelled as a chain of 39 beads (compare bottom in Figure 3.9). Complementary to the schematic of the spectrin tetramer, 10 beads of the spectrin chain are chosen to interact with KAHRP (beads 10 to 13, bead 17, bead 21 and beads 25 to 28 as shown in Figure 3.9). The two beads coloured in red (ankyrin binding sites) are confined to the membrane plane. The two end beads of the spectrin chain (coloured black) can bind to the actin junction as explained previously.

To implement the binding to actin, KAHRP can interact with any actin bead in an actin filament and all KAHRP particles can interact with each other to self-associate.

3.5.3 Model Results

Achieving a Constant Concentration in ReaDDy

To test the method that was explained in the last section, we set up a periodic box of size $30 \times 30 \times 400$ nm^3. We further introduce G-actin particles which have a diffusion constant of $D_{\mathrm{Gactin}} = 10\ \mu\mathrm{m}^2\,\mathrm{s}^{-1}$ and a proposed concentration of $177777\ \mu\mathrm{m}^{-3}$ which corresponds to 64 particles in the box. As described above, N-particles (with $D_{\mathrm{N}} = D_{\mathrm{Gactin}}$) are introduced which can produce and absorb G-actin. As can be seen in Figure 3.10a, this reaction manages to keep the concentration relatively stable close to the desired concentration of 64 particles per box for $f_- < 0.0005\ \mathrm{ns}^{-1}$. See two examples for the time evolution of the particle numbers in Figure 3.10b and c.

These simulations show which value should be chosen for f_a. On the one hand the value should be as large as possible such that the concentration equilibrates more quickly (see Figure 3.10c compared to Figure 3.10b), but on the other hand the theoretical description breaks down for f_a too large (see Figure 3.10a). Hence,

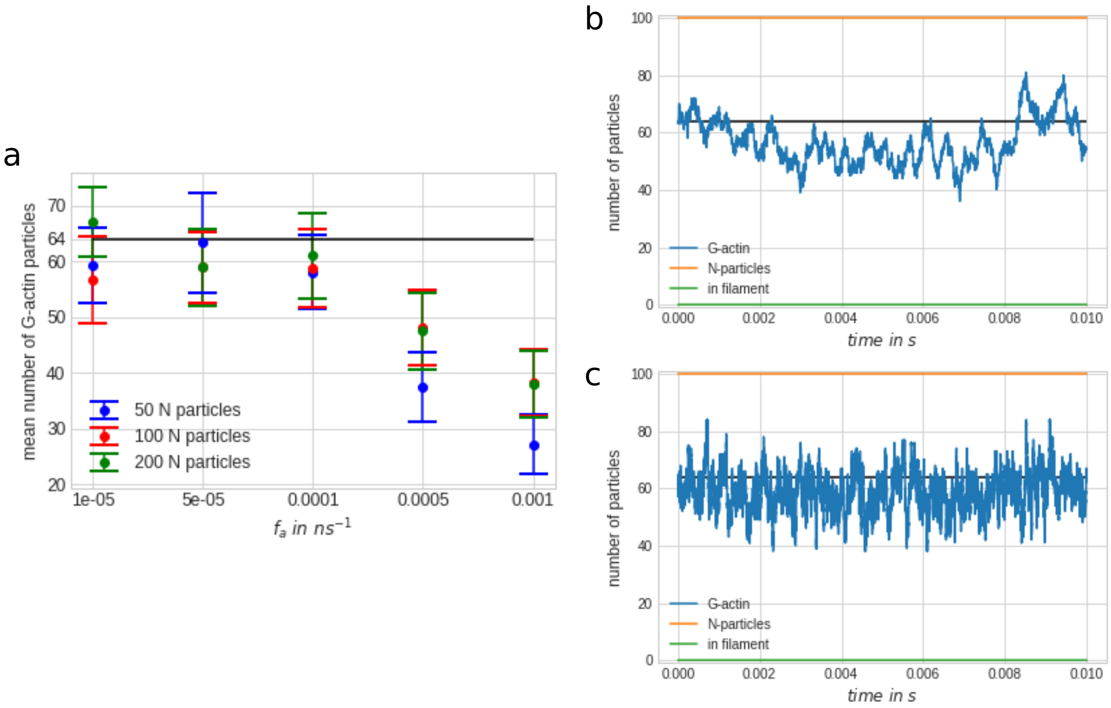

Figure 3.10: a) The mean G-actin number is plotted for different f_a rates and N-particle numbers as indicated in the legend. Each point corresponds to one simulation. The black line shows the calculated concentration of 64 particles per box (corresponding to a concentration of 177777 µm^{-3}). b and c) The amount of each particle species is shown as the time course of one simulation. b) shows a simulation with 100 N-particles and an absorption rate of $f_a = 0.00001$ ns^{-1}. c) The absorption rate f_a is ten times larger and the rate f_c is changed according to equation (3.20).

we see that the optimal value lies around $f_a = 0.0001\ \text{ns}^{-1}$. We further find that the number of N-particles is not so important in the suitable range for f_a. To see effects of the particle number it would have to be decreased even more.

Now, we add reactions that simulate growth of F-actin ($\lambda_b^+ = 5.64 \cdot 10^{-4}\ \text{ns}^{-1}$, $\lambda_p^+ = 6.03 \cdot 10^{-5}\ \text{ns}^{-1}$, $\lambda_b^- = 1.4 \cdot 10^{-6}\ \text{ns}^{-1}$ and $\lambda_p^- = 8 \cdot 10^{-7}\ \text{ns}^{-1}$) to the previously described system. This enables us to look at growth of F-actin under a constant G-actin concentration. As the F-actin filament growth, the N-particles need to produce enough G-actin to keep the concentration at a constant level.

We now vary the number of N-particles (from 50 to 200) and the absorption rate f_a (from $10^{-5}\ \text{ns}^{-1}$ to $10^{-3}\ \text{ns}^{-1}$) to see the effects on the G-actin concentration. The results can be seen in Figure 3.11. As observed previously, the desired concentration is kept for $f_a < 0.0005$ (Figure 3.11a). In Figure 3.11b and c the constant elongation rate of the actin filament can be seen, as predicted under constant concentration.

For $f_a = 0.00001$, 50 N-particles do not seem to be enough but this effect disappears for larger rates. We find an optimal value around $f_a = 0.0001\ \text{ns}^{-1}$. Note that the concentration adapts very quickly to the actin filament growth which takes away monomers.

The growth rate in the simulations is $0.2879 \pm 0.0099\ \text{mm}\,\text{s}^{-1}$ (determined from 15 runs). This is a factor of 2 smaller than the analytically calculated value of

$$\begin{aligned}\frac{\mathrm{d}L}{\mathrm{d}t} &= \left[\left(0.4825\ \frac{\mu\text{m}^3}{\text{s}} + 0.05425\ \frac{\mu\text{m}^3}{\text{s}}\right) \times 177777\ \frac{1}{\mu\text{m}^3} - 1400\ \frac{1}{\text{s}} - 800\ \frac{1}{\text{s}}\right] \times 6\ \text{nm} \\ &= 0.559\ \frac{\text{mm}}{\text{s}}.\end{aligned}$$

One reason why the growth rate could be reduced is the reduced diffusion of the assembled filament which is not accounted for in the calculation of the macroscopic rates or the N-particle reactions.

Controlling Filament Length

In the RBC cytoskeleton the actin filaments are held at a relatively constant length of 35 nm. In this section the different mechanisms for length control are examined. Actin is found to fulfil may different functions inside cells depending on its environment, it can form branched networks or enable the cell to move by polymerization.

First, we would like to see how well we can control single filament length by fixing the overall G-actin concentration. In principle there is a specific concentration for which the filament elongation is zero, hence the addition of monomers at the barbed end is balanced by the release of particles at the plus end. This treadmilling concentration is calculated to be $C_{\text{tread}} = 4098\ \mu\text{m}^{-3}$. To examine the filament behaviour, simulations were set up at seven different concentrations. As explained above, the reactions with the additional particle species N control the G-actin concentration. From the reaction rates used in the simulation, the analytical concentration C_{analytic} can be calculated. However, the measured concentration value fluctuates around a mean value of $C_{\text{simulation}}$ as shown in Table 3.5.

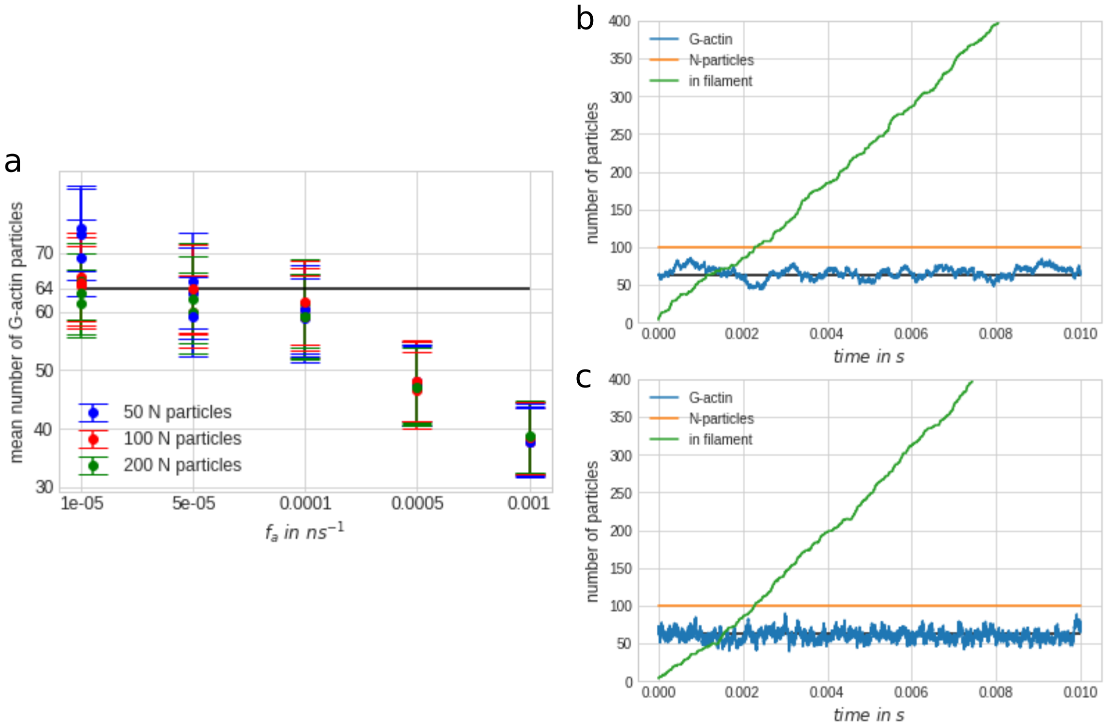

Figure 3.11: a) The mean G-actin number is plotted for different f_a rates and N-particle numbers as indicated in the legend. Each point corresponds to one simulation. The black line shows the calculated concentration of 64 particles per box (corresponding to a concentration of 177777 µm^{-3}). b and c) The amount of each particles species is shown as the time course of one simulation. b) shows a simulation with 100 N-particles, an absorption rate of $f_a = 0.00001$ ns^{-1} and the actin on and off rates as described in Section 3.5.2. c) The absorption rate f_a is ten times larger and the rate f_c is changed according to equation (3.20).

C_{analytic} in µm^{-3}	$C_{\text{simulation}}$ in µm^{-3}
2778	2253 ± 0.24
3427	3128 ± 0.29
4167	3813 ± 0.27
4861	4618 ± 0.33
5556	5162 ± 0.34
6250	5923 ± 0.36
6944	6598 ± 0.37

Table 3.5: The analytically calculated concentrations are compared to the ones extracted from the simulations.

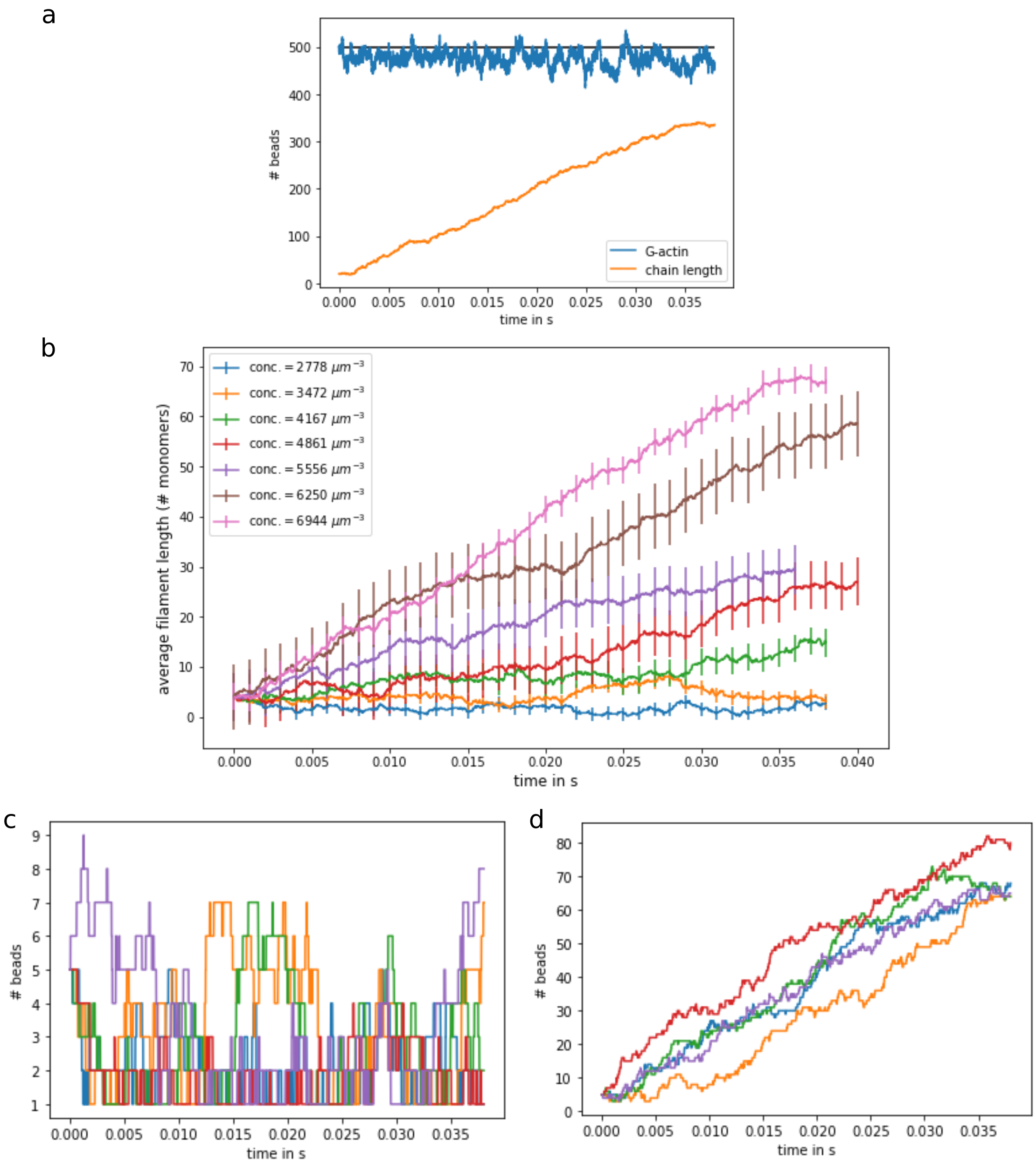

Figure 3.12: a) Five filaments are set up to grow in a simulation box while keeping the concentration of G-actin at a fixed calculated value of $C = 6944\ \mu\text{m}^{-3}$. The graph shows the number of G-actin monomers in blue and the overall number of monomers in filaments in orange. The predicted number of G-actin is indicated by the black line. b) The average filament length is plotted for each simulated concentration with the error bars showing the standard error of the mean. The concentration in the legend is the theoretically predicted concentration. c and d) Trajectories of individual filaments over the whole simulation time period. The concentration was fixed at $2778\ \mu\text{m}^{-3}$ in c) and at $6944\ \mu\text{m}^{-3}$ in d).

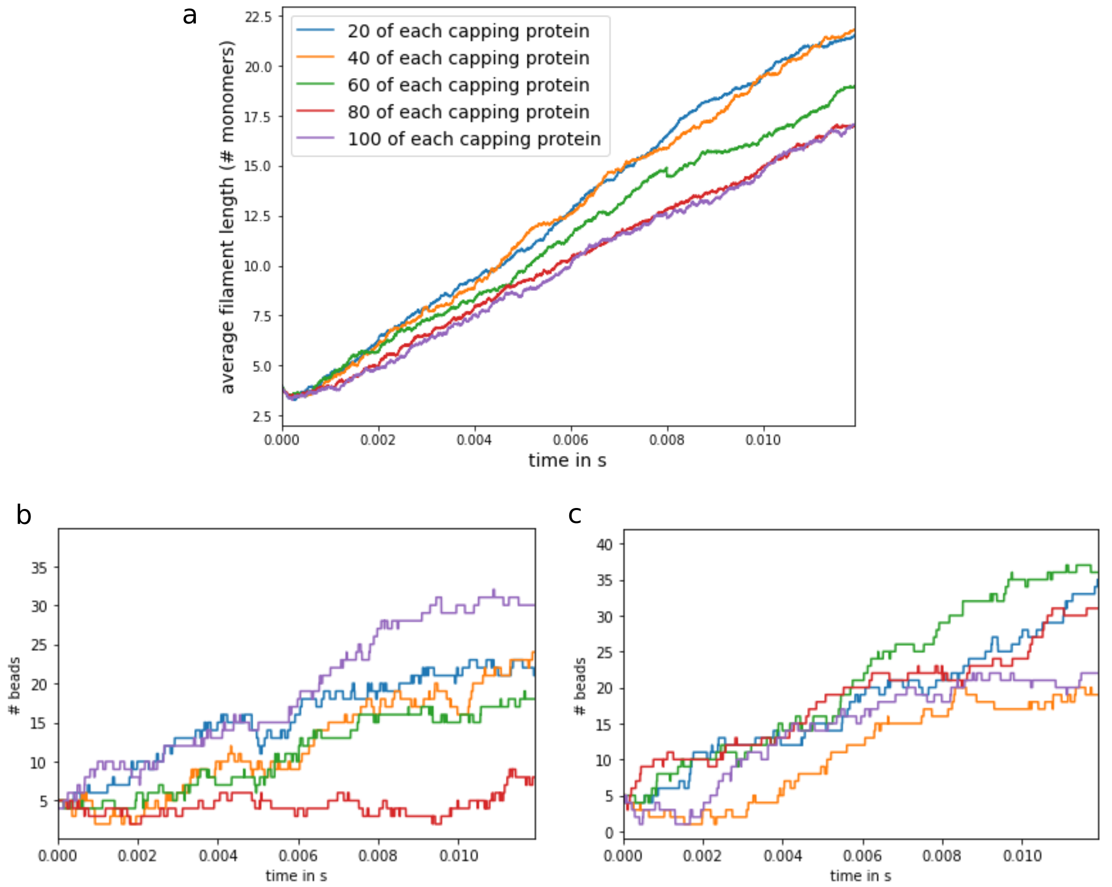

Figure 3.13: a) Average filament length is plotted for different numbers of capping proteins present. The G-actin concentration is kept constant at $C = 6944\mu m^{-3}$ and the error bars show the standard error of the mean. b) and c) The lengths of the five individual filaments are plotted against time for 100 capping proteins in b) and 20 capping proteins in c).

An example for the G-actin number over the whole simulation period is shown in Figure 3.12a by the blue data points. The orange line shows the overall number of actin bound to filaments. In Figure 3.12b the average filament length is compared for all seven concentrations. Where the overall filament length grows in most simulations, it stays approximately constant for the two smallest concentrations. Hence, the treadmilling concentration is predicted to be close to $\approx 3000\ \mu\text{m}^{-3}$ which is a factor of 1.37 smaller than the calculated value. This plot also shows that the average filament length has quite a large error which comes from the deviation of single filaments within one run. To explain this further, individual filament trajectories were plotted in Figure 3.12c for $C_{\text{analytic}} = 2778\ \mu\text{m}^{-3}$ in the top graph and $C_{\text{analytic}} = 6944\ \mu\text{m}^{-3}$ in the bottom graph. Here it becomes clear that single filaments can have quite a different length, whereas the overall number of bound G-actin is more stable.

In the RBC actin dynamics is mainly controlled through the capping proteins tropomodulin and adducin as explained in Section 3.2. Tropomodulin binds better if tropomyosin is also attached to the actin filament and in this case the dissociation constant has been measured to be smaller than 1 nM. Adducin, which binds the

	$\frac{K_D}{40}$ in nM	K_D in nM	D in µm^2 s^{-1}	k_- in s^{-1}	$k_+^{\text{mac.}}$ in µm^3 s^{-1}	$k_+^{\text{mic.}}$ in s^{-1}
adducin	100.7	4026	51.07	8000	3.3	$7.0 \cdot 10^7$
tropomodulin	1	40	29.59	53	2.2	$1.0 \cdot 10^9$

Table 3.6: Rates used in the capping protein simulations.

barbed end, has a much larger dissociation constant, which has been measured to be 100 nM.

We choose the capping protein rates as given in Table 3.6. If a capping protein is attached in the simulation, the dynamics at this end is completely blocked until the protein dissociates again. Hence, the addition of more capping proteins will slow down the polymerisation as compared to the case discussed above. The largest concentration $C = 6944$ µm^{-3} from the simulations without capping proteins was taken and a varying number of capping proteins was inserted into the simulation box (20, 40, 60, 80 and 100). The results of these runs are summarized in Figure 3.13a where the average filament length is shown as a function of time. Without capping proteins, the average filament length grew up to 26 in 0.02 s, whereas the capped filaments reach a length between 17 and 22, where more capping proteins lead to a slower growth. The individual trajectories are shown in Figure 3.13b and c where one can also see plateaus in for limited temporal periods which is an effect of the capping proteins.

Although we saw that the average filament length can be controlled reasonably well, the individual filament lengths fluctuate quite dramatically. This was also tested at the treadmilling concentration and while the average filament length is fixed, the individual filaments fluctuate in length dramatically (results shown in Appendix D.3). This is due to the effect that has been described by Mohapatra *et al.* [162]. They found that many filament growing at the same time cannot be controlled by concentration because one filament might take up the monomers of the other without changing the concentration of free monomers. Previously it had been claimed, that organelle size can be controlled by the so-called limiting pool mechanism [163]. However, this only applies to the case of one filament. In the RBC other proteins, like tropomyosin, are used to stabilize the size.

Network Structure and Properties

As the next step, simulations of a small patch of RBC cytoskeleton were set up incorporating the following elements: randomly oriented short actin filaments (yellow beads in Figure 3.14) that are free to grow/shrink and diffuse in the membrane plane, capping proteins that inhibit this dynamics (purple and green), freely diffusing G-actin monomers (light grey) and spectrin filaments (cyan and blue beads) that bind actin with their end beads (white). The actin filaments and the ankyrin binding sites (red beads) of spectrin are confined to a 4 nm thick plane 10 nm above the bottom of the simulation box. In the real RBC this distance comes from the spacial extend of the anchoring proteins. We set up a perfect hexagonal array (as in Figure 3.14a) with spacial extension 140 × 242.48 nm^2 and run the

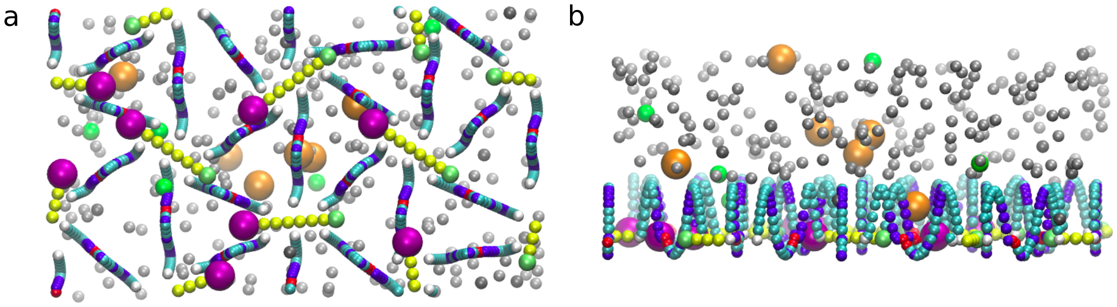

Figure 3.14: Snapshots from a simulation modelling KAHRP cluster formation in the cytosol and the RBC cytoskeleton. Grey beads represent KAHRP particles, spectrin filaments contain cyan, blue and red beads, actin filament units are shown in yellow and the other colours represent actin capping proteins. The images show the starting configuration looking from a) below and b) the side.

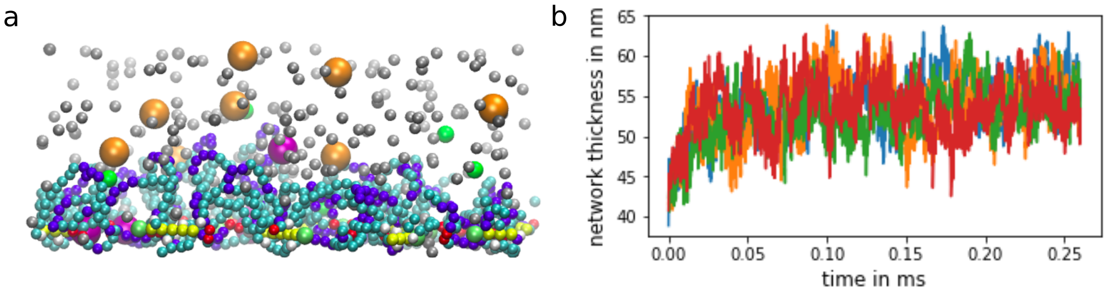

Figure 3.15: a) A snapshot (in side view) from a simulation of the cytoskeletal network. The thickness of the cytoskeletal network is defined as the maximal extend out of the membrane plane (y-direction). Grey beads represent KAHRP particles, spectrin filaments contain cyan, blue and red beads, actin filament units are shown in yellow and the other colours represent actin capping proteins. b) The membrane thickness is plotted for four independent simulations over the whole simulation period each.

	ϵ_{k-k}	ϵ_{k-sp}	ϵ_{k-a}
all equal	ϵ	ϵ	ϵ
weak self-associtiion	ϵ	2.0 ϵ	2.0 ϵ
strong self-association	ϵ	0.5 ϵ	0.5 ϵ
strong actin-association	ϵ	ϵ	2.0 ϵ

Table 3.7: The interaction energies of the four different simulation types are given in terms of the overall energy scale ϵ.

simulation for 0.26 ms using a timestep of Δt = 0.01 ns. The timestep cannot be chosen any larger because of the strong potentials that keep the spherical beads in place.

First, the height of the network can be determined by finding the maximal thickness at each timestep. The network thickness is plotted for 4 independent runs in Figure 3.15. We see that the system needs some time to equilibrate, such that the thickness grows for 0.06 ms and then fluctuates about a mean of 54.21nm with a standard error of the mean given by 0.03 nm as calculated from 4 independent runs.

Effects of KAHRP on Cytoskeletal Network

To examine the effects of a malaria infection on the RBC cytoskeleton a new particle was incorporated that mimics the binding interactions of the malaria parasite exported protein KAHRP. This protein is known to bind to many cytoskeletal components and itself as discussed in Section 3.3. The aim of these simulations is the examination of KAHRP cluster formation as this protein is known to self-assemble in solution and attach to the RBC cytoskeleton. To do so, the interaction strength between KAHRP and KAHRP/spectrin/actin is varied and the effect on the cluster size and position is studied. It is of special interest to know where these clusters form since they develop into adhesion mediating knobs in the iRBC.

As basis a hexagonal array of spectrin and actin filaments is set up as discussed before. The actin dynamics do not play such an important role at the timescale of KAHRP assembly discussed here. However, for the time scale set by the parasite life time the actin dynamics will play a role and should be examined in a further study. Since KAHRP reaches the membrane via diffusion through the cytosol in the iRBC, the simulations start with 200 KAHRP particles uniformly distributed in the free space starting 30 nm above the membrane plane as can be seen in Figure 3.14b. The binding interactions of KAHRP particles are modelled by a Lennard-Johns potential with potential depth ϵ as discussed in Section 3.5.2. Hence, there are 3 parameters that are varied: the interaction energy of KAHRP with KAHRP ϵ_{k-k}, the interaction energy of KAHRP with the binding sites on the spectrin filaments ϵ_{k-sp} and the interaction energy of KAHRP with the actin particles ϵ_{k-a}. The value of ϵ is varied from 0.1 k_BT to 20 k_BT and four cases are examined as shown in Table 3.7; the case of all interactions equal, a weak self-association, a strong self-association and a strong actin-association.

The simulation data (two independent runs) was used to determine the clustering properties depending on the four different cases. A particle belongs to a cluster if it is closer than 1.5 nm to a particle of that cluster. First, the average size of clusters is calculated distinguishing between free clusters which are not attached to the RBC cytoskeleton and clusters that are attached to the cytoskeleton.

In Figure 3.16 the average cluster size is shown for all KAHRP interaction energies equal. In Figure 3.16a we see, that the free clusters are in general larger than the attached clusters and cluster formation starts from $\epsilon = 1.5\ \mathrm{k_B T}$. Additionally, the clusters also grow in time (see darker colours of red and green). In Figure 3.16b and c the same data is plotted as a heat map with more time points along the x-axis and ϵ along the y-axis. The colour indicates the size of the free clusters in Figure 3.16b and the size of the attached clusters in Figure 3.16c. These two graphs show that the attached clusters grow more slowly, whereas the free clusters grow until 70 µs are over and then fluctuate around a similar value. We can also note that there are two distinct regimes in ϵ. Up to $1.0\ \mathrm{k_B T}$ the clusters are very small and above that value the behaviour is very similar for all ϵ. In Figure 3.16d and e the temporal evolution for two specific ϵ are shown with the standard error of the mean indicated by the error bars. Note that the standard error of the free clusters is larger than the attached clusters.

In Figure 3.17 the same graphs are shown for strong self-association of KAHRP because these simulations show a slightly different behaviour. When focusing on the green data points in panel a, we see a peak in attached cluster size at $\epsilon = 3\ \mathrm{k_B T}$. This phenomenon can also be appreciated in Figure 3.17c, where yellow squares appear for late times around $\epsilon = 3\ \mathrm{k_B T}$. The data for the free sizes is a lot noisier in the sense that several size peaks appear for different ϵ (compare Figure 3.17a and b) also for large ϵ. This large noise in the data can also be seen in the standard error in Figure 3.17e for free clusters.

As the next step of the analysis the positioning of the clusters was considered. Here, three cases were distinguished: free clusters, clusters in the cytoskeleton mesh (attached to spectrin binding sites) and clusters around the actin junctions (a distance of at most 1.5 nm to the next actin junction). This concept is depicted in Figure 3.18. The top four images show simulations for equal KAHRP interaction energies and increasing ϵ towards the right. The black circles indicate KAHRP clusters that have formed within the cytoskeleton mesh pulling the spectrin filaments together. The bottom row of images shows simulations with strong KAHRP-actin association. Here we see clusters at the actin junctions (red circle) for $\epsilon = 2\ \mathrm{k_B T}$.

To quantify this cluster positioning, it was decided for each cluster, if it is free, associated to an actin filament or otherwise attached in the mesh of the cytoskeleton. Hence, the fraction of clusters in these three categories was calculated for all time points and ϵ. A graphical representation of this data is shown in Figure 3.19, with red data points indicating the fraction of free clusters, green data points showing the fraction of spectrin attached clusters and blue data points indicating the fraction of actin-attached clusters. How the fractions develop for specific ϵ in time, can be seen in Appendix D in Figure D.2.

First, we would like to see how the positioning changes with the parameter ϵ by considering the same four interaction cases as before. We find, that for small epsilon ($\epsilon < 1\ \mathrm{k_B T}$) most clusters are free whereas for high epsilon, the clusters are preferentially attached in the mesh of the cytoskeleton with very little attachment

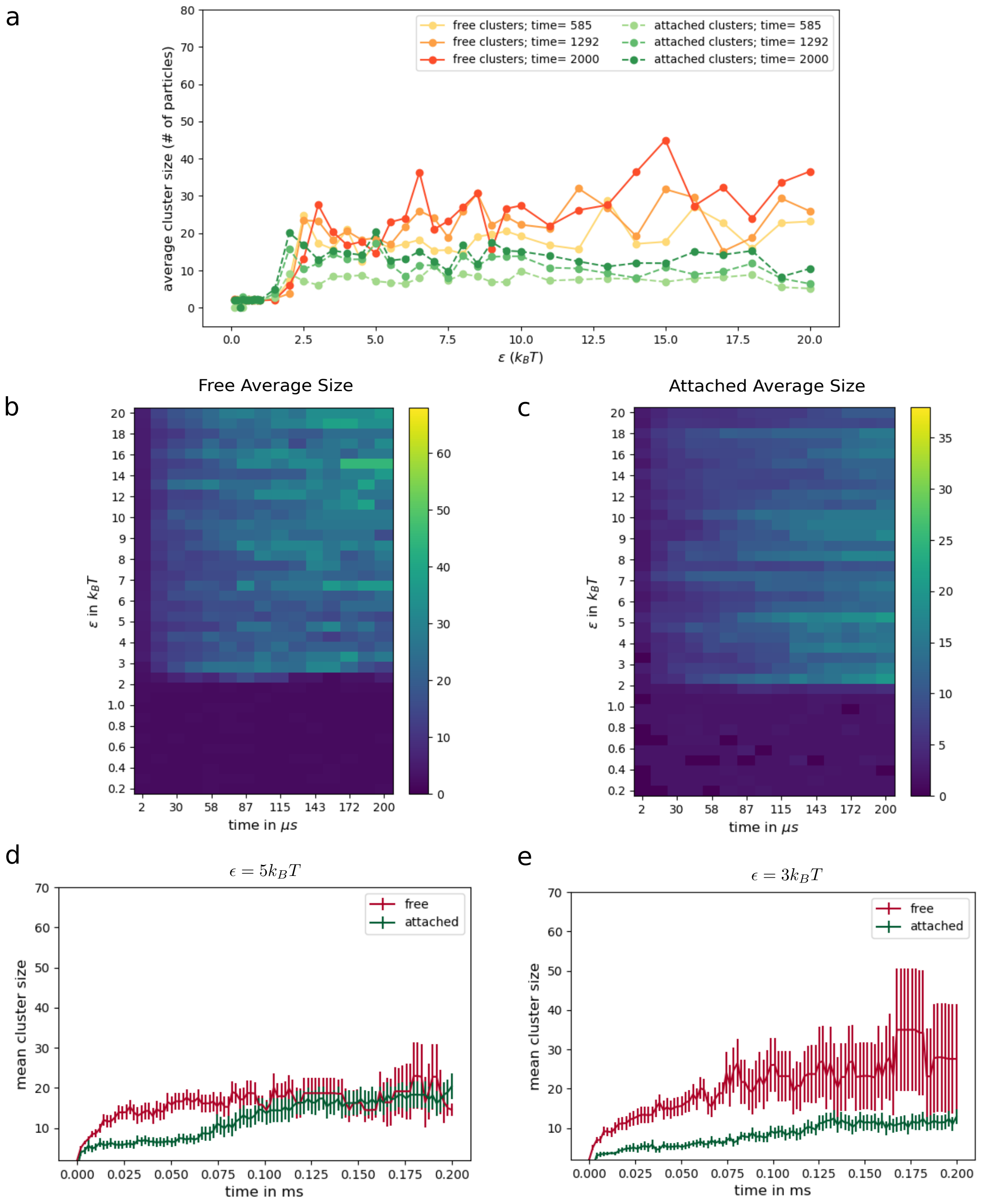

Figure 3.16: The average KAHRP cluster size is depicted in various ways for all interaction energies equal taking into account two independent runs. a) displays the average cluster size at four timepoints as a function of the potential depth ϵ. Free and attached clusters are considered separately as indicated in the legend. b and c) are two dimensional colour plots of the free and attached average sizes depending on time and the potential depth ϵ. The colour bar indicates the size in number of KAHRP particles. d and e) show the temporal evolution of the average sizes for interaction energies $\epsilon = 5$ $\mathrm{k_B T}$ and $\epsilon = 3$ $\mathrm{k_B T}$, respectively. The error bars indicate the standard error of the mean.

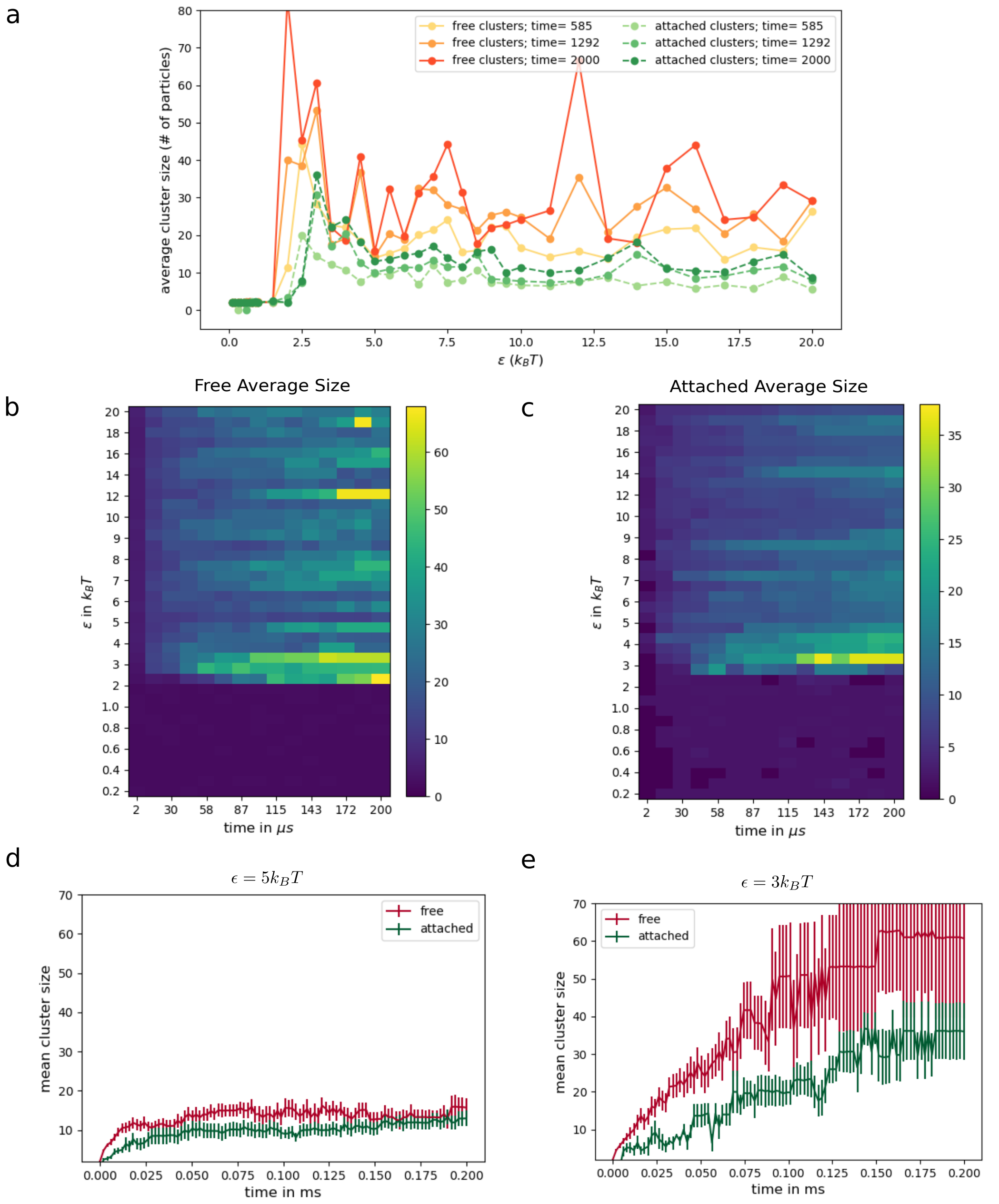

Figure 3.17: Same as in Figure 3.16 but for a strong self-association energy of KAHRP as defined in Table 3.7.

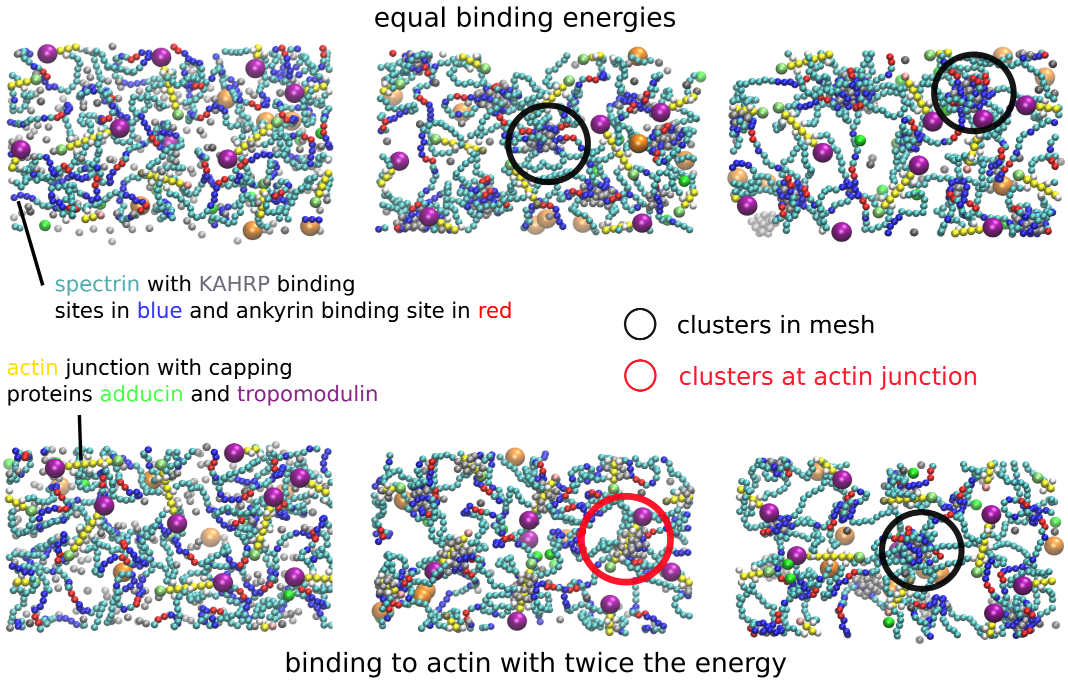

Figure 3.18: Snapshots from six simulations illustrating the positioning of KAHRP clusters for all equal binding energies at the top and strong actin association at the bottom. From left to right the interaction energy used in the simulations is 0.5, 2, 5 and 20 $\mathrm{k_B T}$, respectively. Clusters in the cytoskeleton mesh are highlighted by black circles and clusters at actin junctions by red circles.

to actin filaments. Note that, if the KAHRP-KAHRP association is stronger than the association to the cytoskeleton, the free clusters are even dominant up to $\epsilon = 2.5\ \mathrm{k_B T}$ (Figure 3.19c). When looking at the fraction of actin associated clusters (in blue in Figure 3.19) more closely, we see that it behaves differently for the four interaction cases but in general, there is hardly any actin associated clusters for $\epsilon < 1\ \mathrm{k_B T}$. Another common feature is that the percentage of clusters at the actin junction increases with time for all simulations which means that it takes time to form actin associated clusters (compare Figure D.2 in Appendix D).

A very interesting feature can be observed for the strong actin-association simulations (Figure 3.19d). In the range from $\epsilon = 1\ \mathrm{k_B T}$ to $\epsilon = 2.5\ \mathrm{k_B T}$ the fraction of actin-attached clusters is above 0.4 and hence, most clusters are located near actin junctions. This behaviour will be analysed more closely in the following paragraphs.

Furthermore, it can be seen from the graphs in Figure 3.19 that a strong self-association (panel c) decreases the actin-association of the clusters (blue data points). For a weak self-association (panel b) the fraction of actin-associated clusters outruns the free clusters within the simulated time interval (see $\epsilon = 20\ \mathrm{k_B T}$).

The temporal evolution for specific ϵ (Figure D.2 in Appendix D) shows that for small ϵ the trajectories fluctuate strongly in time, whereas the curves for higher ϵ are very smooth. For the weak self-association, the fluctuations are already reduced for $\epsilon = 1.5\ \mathrm{k_B T}$ because the cytoskeleton association energy is doubled in that case and hence it would be comparable to $\epsilon = 3\ \mathrm{k_B T}$ for the other cases.

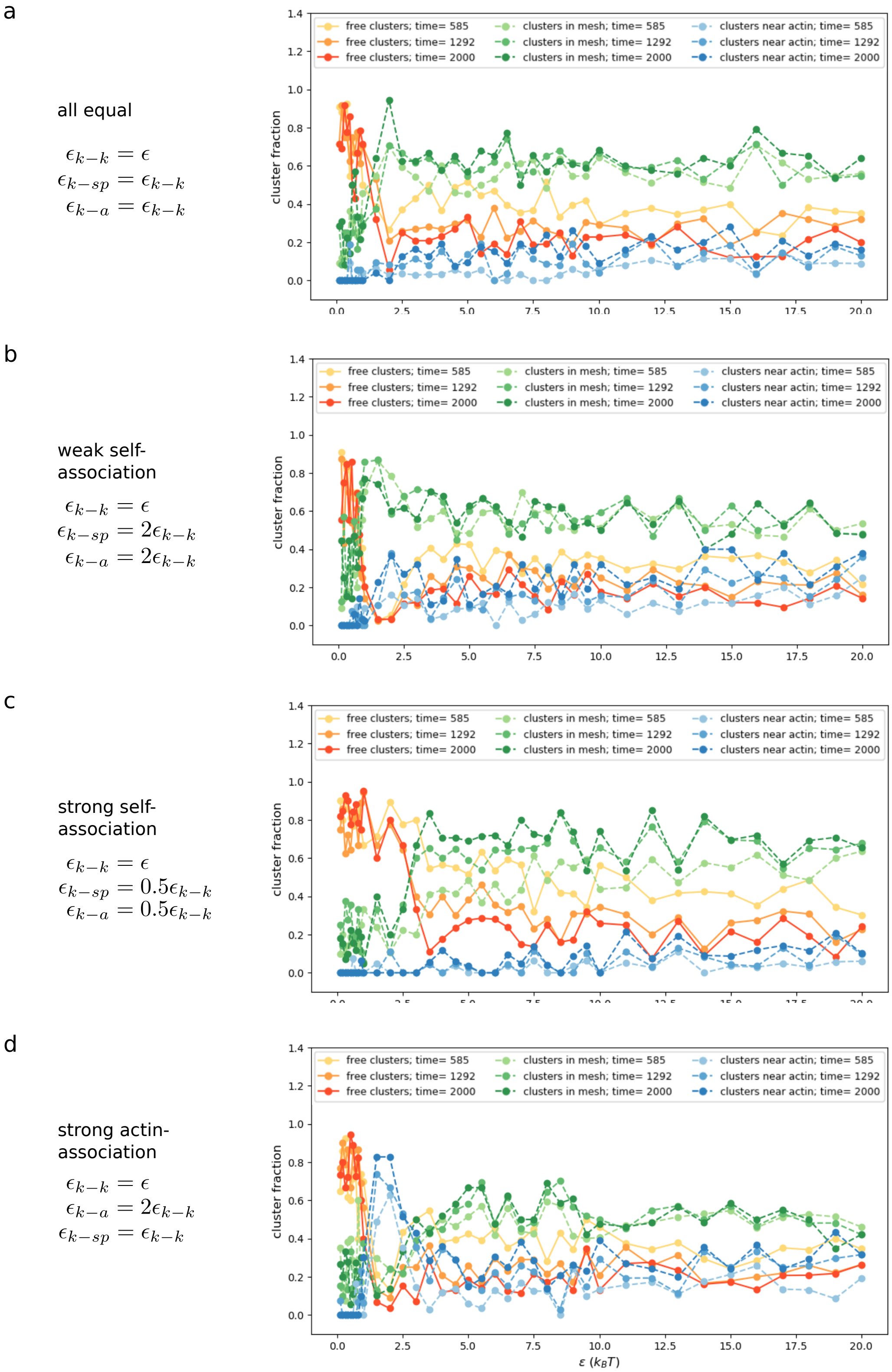

Figure 3.19: The positioning of KAHRP clusters is compared for the four interaction cases; a) all equal, b) weak self-association, c) strong self-association and d) strong actin association. The graphs shows the fraction of free clusters in red, the fraction of clusters in the mesh in green and the clusters around actin junctions in blue for three different timepoints each as indicted in the legend.

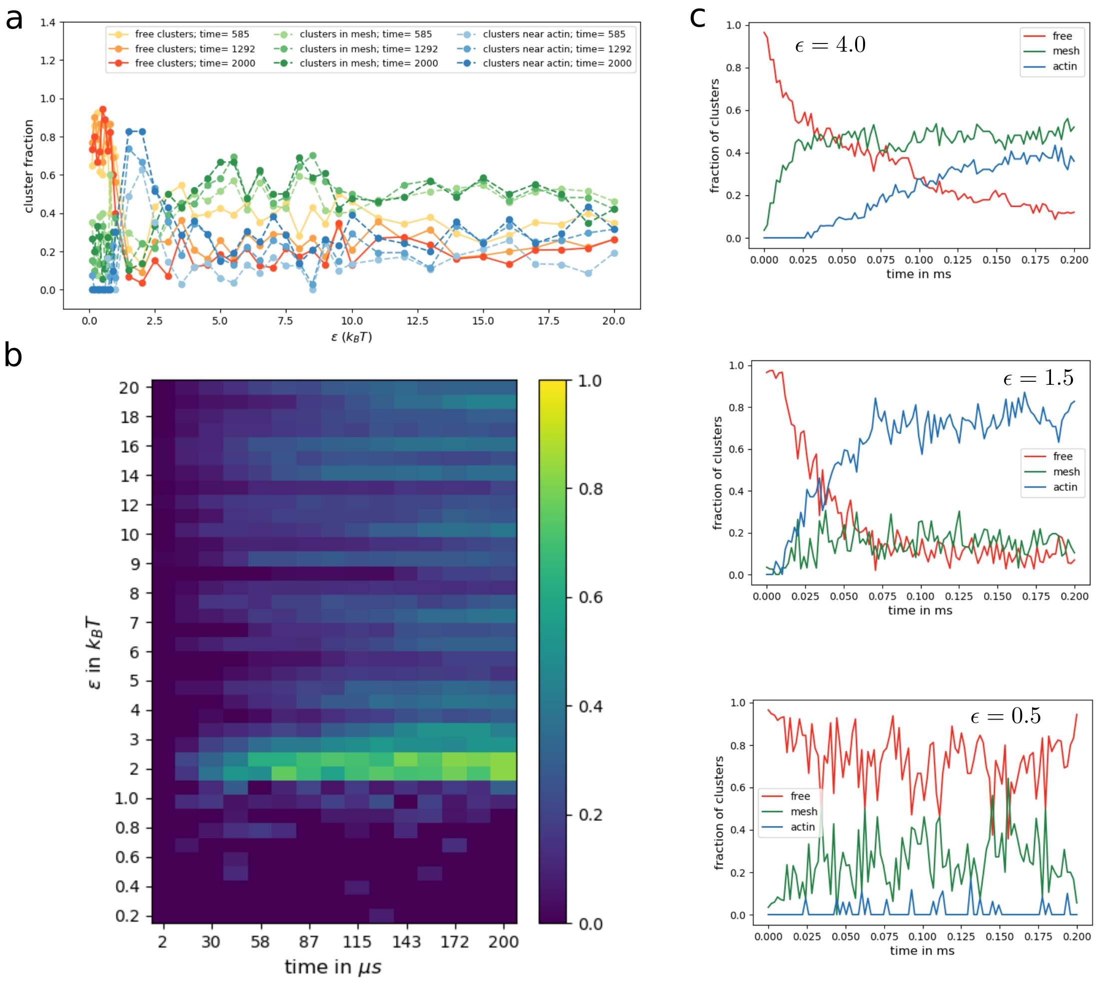

Figure 3.20: This data comes from simulations with strong KAHRP-actin association as defined in the text. a) This graph shows the fraction of free clusters in red, the fraction of clusters in the mesh in green and the clusters around actin junctions in blue for three different timepoints each as indicted in the legend. b) The colour in this heat map indicates the fractional occurrence of actin-associated clusters. A bright colour indicates a large percentage of the clusters attached to actin filaments. c) The three plots show the temporal evolution of the fractions for $\epsilon = 0.5$ k_BT, $\epsilon = 1.5$ k_BT and $\epsilon = 4$ k_BT.

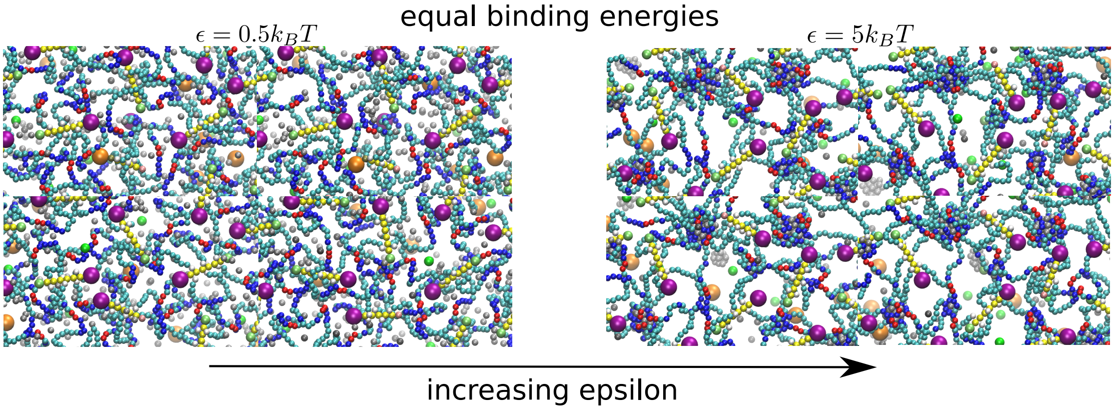

Figure 3.21: Each image is built up out of four snapshots from the same simulation at different timepoints. The left images were taken from an equal binding energy run at $\epsilon = 0.5$ k_BT, whereas for the ones on the right the binding energy was set to $\epsilon = 5$ k_BT. It can be seen, that the holes in the network get larger with increasing ϵ. Grey beads represent KAHRP particles, spectrin filaments contail cyan, blue and red beads, actin filament units are shown in yellow and the other colours represent actin capping proteins.

We saw, that actin associated clusters are very prominent in a specific parameter regime. This behaviour is shown in more detail in Figure 3.20. As mentioned before, the high affinity for actin-associated clusters is found for 1 k_BT $\leq \epsilon \leq$ 2.5 k_BT. The blue data shown in Figure 3.20a is plotted again in panel b as a heat map showing the dependence on ϵ along the y-axis and on time along the x-axis. The green-yellow regime indicates the dominance of actin-associated clusters. Here it can be seen, that this phenomenon starts between 28 and 56 µs and the behaviour does not change much with time from then onwards. The temporal behaviour is also shown in Figure 3.20c where the behaviour is exemplified for $\epsilon = 0.5$ k_BT, $\epsilon = 1.5$ k_BT and $\epsilon = 4$ k_BT. In the middle plot it can be clearly seen, that the fraction of free clusters drops dramatically early on with the appearance of actin-associated clusters. The fraction of clusters in the mesh stays in the range of 0.1. For higher ϵ the fraction in the mesh wins with time as seen in the other simulations as well and for smaller ϵ the free clusters are dominant.

Finally, it can be asked how the KAHRP clusters change the appearance of the simulated network. Figure 3.21 shows examples for simulations with all binding energies equal for $\epsilon = 0.5$ k_BT and $\epsilon = 5$ k_BT. At $\epsilon = 0.5$ k_BT nearly no KAHRP is attached to the network. Hence, the left image represents the apprerance of a healthy RBC cytoskeleton which is relatively dense and evenly distributed. For increased epsilon (right image) KAHRP clusters have formed in the mesh and lead to an irregularly distributed network with the appearance of larger voids, where one would be able to see the underlying bilayer.

3.5.4 Analysis of KAHRP Cluster Formation

The results showing the network thickness imply that this modelling approach captures the main structural features of the RBC cytoskeleton. In the past there have been various debates about the native structure of the spectrin filaments in the RBC cytoskeleton but modelling it as a flexible polymer seems to fit most observations. Additionally, this model is the first to incorporate the actin junction dynamics on a network scale. The actin dynamics was tested in simulations without additional cytoskeletal structures and yields the predicted behaviour.

The malaria protein KAHRP was successfully incorporated into the simulations and was seen to form clusters in solution and clusters in the cytoskeleton as expected. It makes sense that clusters only start forming for a interaction depth larger than k_BT but it is somehow surprising that the clustering behaviour does not change much for higher ϵ except for some specific cases. This means that already a relatively weak binding interaction is sufficient to change the clustering behaviour.

Free clusters are in general larger for the discussed cases. The reason is, that the cytoskeleton is confined to a plane with a smaller diffusion constant of the anchored elements and it is basically close to a wall such that new KAHRP particles can only arrive from one side. Hence, the particles are more quickly accumulated into free clusters and the assembly of a cytoskeleton associated cluster takes more time. Evidently, the cluster size is not tuned by ϵ. However, it was found that the KAHRP concentration has a large impact on cluster sizes but not the other qualitative behaviour (see Figure D.3 in Appendix D).

When considering the strong KAHRP self-association runs, very large cluster sizes were observed for specific parameters. Especially, for $\epsilon = 3\ k_BT$ both the free and attached clusters were a lot larger for late times than for other parameters. This regime of large cytoskeleton attached clusters lies just above the boundary for cluster formation. Hence, ϵ is strong enough to keep KAHRP particles together but still small enough to have dissociation events in small clusters that help build larger ones. Note, that there have been only 2 independent runs for each parameter set because such molecular simulations are time consuming. Therefore, it is possible that more runs would lead to larger cluster sizes for all $\epsilon > 2\ k_BT$. It was also observed that for small ϵ the cluster sizes deviate more from the mean. A possible reason for this is the larger particle turnover in free clusters. There will be more dissociation events and hence the clusters change their size quicker.

Examining the cluster positioning yielded some very interesting results, namely, for strong KAHRP-actin association there is a small range in ϵ where most clusters associate to actin filaments. This is the case for $1\ k_BT \leq \epsilon \leq 2.5\ k_BT$ and the association with actin even grows with time. Finding actin associated clusters is very promising with respect to experimental data from the Lanzer group. They saw, that depending on the parasite development, first KAHRP attaches at most cytoskeletal components and after some time, KAHRP is mostly found around actin junctions. Here we see, that depending on the interaction parameters such a behaviour is possible. This means that binding affinities would have to change in the iRBC to observe a displacement of clusters towards the actin junctions. A possible mechanism for this could come from the phosphorylation of KAHRP during the malaria life cycle. As explained in Section 3.3, phosphorylation is known to effect binding affinities.

Finally, the appearance of the cytoskeletal network was seen to change with the accumulation of KAHRP clusters. Because the spectrin filaments are very flexible, clusters form in the mesh of the cytoskeleton and pull large portions of the spectrin

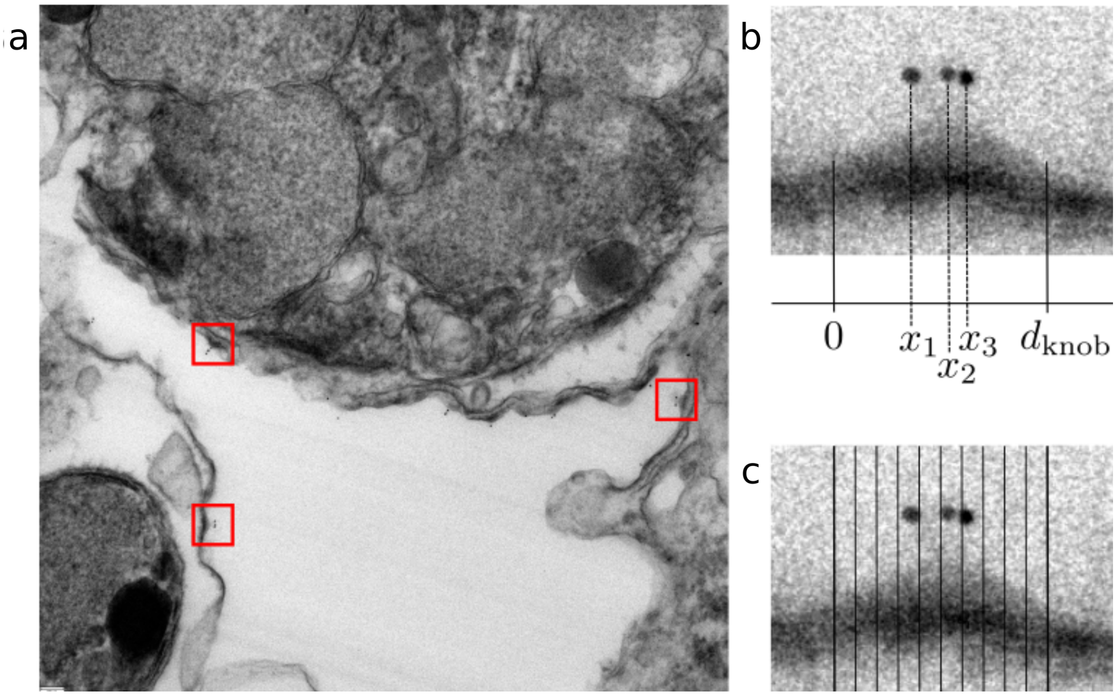

Figure 3.22: a) The microscopy image shows malaria infected RBC with immuno-labelled PfEMP1 molecules which are associated to knobs in the red boxes. b) The position of the gold particles is determined with respect to the projected 1D diameter of the knob. c) The knob is divided into ten segments which need correction terms due to the surface area that lies within each segment.

filaments towards the cluster leaving the rest of the spectrin relatively straight and stretched out. Hence, the network appears more sparse in some regions and denser in others. This has previously been seen in experimental images of malaria infected cytoskeletons. These show a similar behaviour but an even stronger effect. Previously it has been explained by actin mining by the parasite, which takes away some junctions and hence makes the network more heterogeneous. Here, we found another reason for the altered appearance of the network. It is a combination of the two effects which leads to the strongly altered appearance of iRBC cytoskeletons.

3.6 Examining the PfEMP1 Distribution

Now we turn to a different protein which is important for the malaria knob formation, namely PfEMP1. We also move away from the molecular model of the last section and show how geometrical considerations can help to understand experimental data on protein positioning. The experimental data obtained by Marek Cyrklaff from Prof. Lanzer's group was used to determine the exact positioning of PFEMP1 molecules on the knob. The here discussed analysis method was applied in the paper "Single-molecule imaging and quantification of the immune-variant adhesin VAR2CSA on knobs of Plasmodium falciparum-infected erythrocytes" [164].

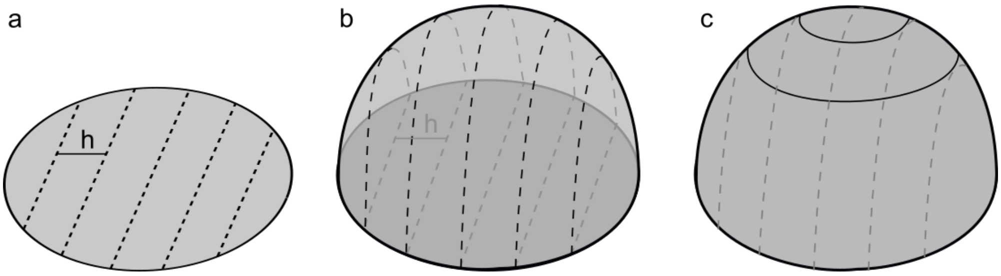

Figure 3.23: a) Graphical illustration of parallel cuts of thickness h through a 2D circle and b) a 3D half sphere. We are interested in the area of the surface that lies within each section. c) The circular divisions corresponding to the parallel cuts are shown.

3.6.1 Analysis of Experimental Data

To access the localization of PfEMP1 molecules these were labelled by immunogold particles (see Figure 3.22). The images show a clear localization to the parasite induced knobs. The efficiency of labeling is 10 % and the uncertainty of the gold label position is 25 nm where the gold particle has a diameter of 10 nm and the linker to the membrane has a length of $10 - 15$ nm.

We assume that the whole knob lies within the imaging plane so that markers at the back and front of the knob would be equally shown at the same position along the horizontal axis of the knob. Figure 3.22a shows a few examples of labelled molecules, where approximately one to three molecules are labelled per knob. Using an image analysis software the position of the gold particles can be determined with respect to the horizontal axis of the knob as can be seen in Figure 3.22b. Hence, we know, which of the ten equally thick sectors (see Figure 3.22c) the label belongs to.

When constructing the distribution of PfEMP1 molecules, an assumption has to be made for the shape of the knob since the shape determines the surface area in the different segments of the image. In general, correction factors need to be introduced for the ten segments introduced in Figure 3.22. Figure 3.23 shows the division of the circle and a half-sphere into four segments.

On the one hand it is clear for a circle, that a segment in the middle of the circle has a larger surface area than a segment at the side. Hence, there is more opportunity to observe a PfEMP1 molecule. The final distribution needs to be corrected for this. Numerical values for a circle of radius $5d$ and segments of thickness $1d$ are shown in Table 3.8, where d is a unit length. On the other hand, the curved surface area of a segment of a sphere only depends on the thickness h of the segment and not the location along the x-axis. Therefore, all segments of the half-sphere have the same area ($A = \pi Rh$) and the weighting factors are all one as it is indicated in Table 3.8.

From the recorded data we now want to know, how the molecules are distributed along the arclength on the surface which is discretized according to the slices of the sphere (see Figure 3.23c). To calculate the density of molecules in each circular segment, the surface areas A_i as shown in Figure 3.24 need to be calculated. These are created by vertical and horizontal cuts through the half sphere.

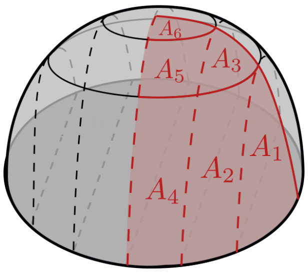

Figure 3.24: Areas that are created by the vertical and horizontal cuts.

segment		1	2	3	4	5	6	7	8	9	10
circle	area	4.1	7.1	8.6	9.5	9.9	9.9	9.5	8.6	7.1	4.1
	factor	1.0	0.58	0.47	0.43	0.41	0.41	0.43	0.47	0.58	1.0
half-sphere	area	15.7	15.7	15.7	15.7	15.7	15.7	15.7	15.7	15.7	15.7
	factor	1.0	1.0	1.0	1.0	1.0	1.0	1.0	1.0	1.0	1.0

Table 3.8: Numerical values for the area (unit of d^2) and associated correction factor for segments of a circle and sphere of radius 5d.

To do this, the surface element on the sphere can be numerically calculated by applying the following formula:

$$A = \int\int \mathrm{d}x\mathrm{d}z \; |\boldsymbol{R}_x \times \boldsymbol{R}_z| \quad \text{with} \;\; \boldsymbol{R} = \begin{pmatrix} x \\ \sqrt{R^2 - x^2 - z^2} \\ z \end{pmatrix}, \tag{3.34}$$

where $\boldsymbol{R}_i$ is the derivative with respect to i of the position vector $\boldsymbol{R}$. Plugging $\boldsymbol{R}$ in leads to

$$A = \int\int \mathrm{d}x\mathrm{d}z \sqrt{\left|\frac{x}{\sqrt{1-x^2-z^2}}\right|^2 + \left|\frac{z}{\sqrt{1-x^2-z^2}}\right|^2 + 1} \tag{3.35}$$

and this formula can be numerically integrated between the corresponding x and z-boundaries.

The densities in the circular segments are calculated in an iterative manner starting from the element with area A_1 (see Figure 3.24) since its density corresponds to the density in the outer x segment. For example, the density in the second ring from the bottom (ϕ_4), can be calculated with the following formula, taking into account the areas as indicated in Figure 3.24:

$$\rho(\phi_4) = \frac{A_{\mathrm{sec}}\rho(x_4) - \rho(\phi_5)A_2}{A_3}, \tag{3.36}$$

where A_{sec} is the area in each slice of thickness h, x_m indicates the slice m and ϕ_{N} stands for the ring n. Note that we start counting from the centre of the sphere. The results are shown in Figure 3.25 for HbAA and HbAS malaria iRBCs.

We find that the PfEMP1 molecules are clustered towards the middle of the knob. This also explains, why the knob radius determined from the fluorescence

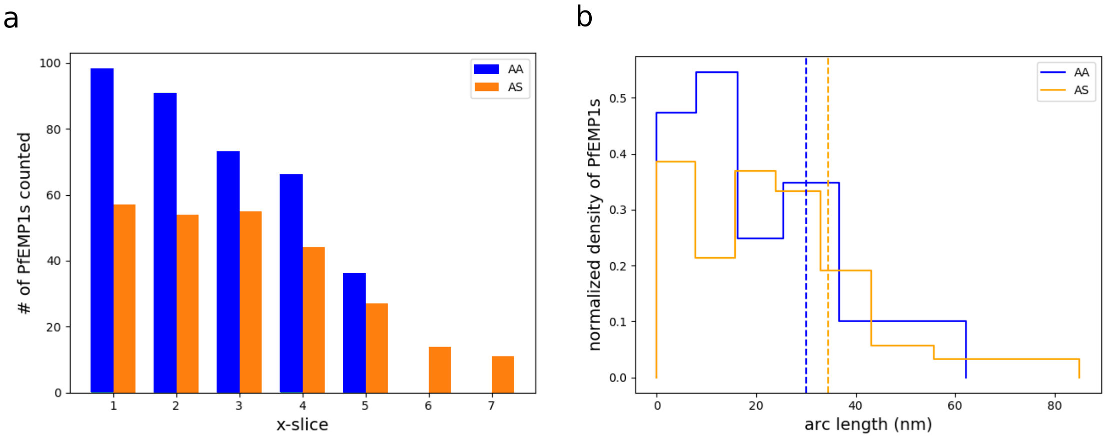

Figure 3.25: a) Experimental data of the PfEMP1 number in the x-slices. b) The distribution along the arc-length on the sphere. The vertical lines show the arclength corresponding to the radius of the PALM flourescence signal.

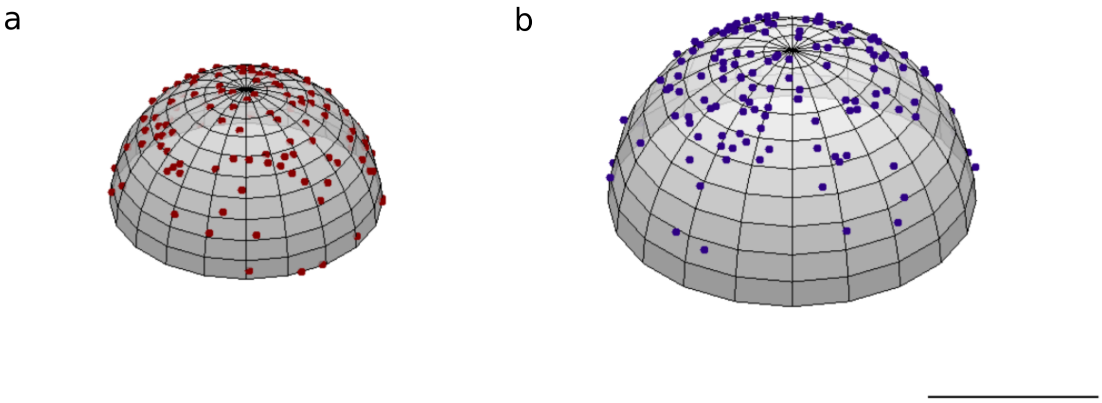

Figure 3.26: a) The calculated distribution is examplified for an HbAA and b) an HbAS knob. The scale bar has the size of 50 nm.

PALM signal ($r_{\mathrm{PALM/AA}} = 27.2$ nm, $r_{\mathrm{PALM/AS}} = 32.2$ nm) is smaller than the SEM radius ($R_{\mathrm{SEM/AA}} = 40$ nm, $R_{\mathrm{SEM/AS}} = 54.5$ nm) which measures the hight profile of the knob. In Figure 3.25b the PALM radius is indicated by vertical dashed lines and we find, that it corresponds well with the high probability area of finding a PfEMP1 molecule.

Finally, we visualize the reconstructed 3D distribution of PfEMP1 molecules by distributing 25 markers according to the calculated discrete distribution in arclength (see Figure 3.26). The clustering towards the top of the knob becomes apparent in the graphic.

3.6.2 Geometrical Aspects

We consider a half sphere and assume a given distribution $g(\phi) = g(s/R)$ along the arclength on the surface of the sphere. The arc-length s and the angular coordinate ϕ can be treated equivalently, since they are related by a linear transformation $s = R\phi$, where the radius of the sphere R is a constant.

	$g(\theta,\phi)$	$f(r)$	$\rho(x)\ \ (R=1)$
uniform in arclength	$\frac{1}{\pi^2}$	$\frac{1}{\pi^2\sqrt{1-(r/R)^2}R}$	$\frac{2\ \text{EllipticK}(1-1/x^2))}{\pi^2 x}$
Gaussian in arclength	$0.254402\ e^{-2\phi^2}$	$\frac{0.254402\ e^{-2\arcsin^2(r/R)}}{\sqrt{1-(r/R)^2}R}$	*numerical*
uniform on sphere	$\frac{\sin\phi}{2\pi}$	$\frac{0.159155r}{\sqrt{1-(r/R)^2}R^2}$	$\frac{0.5}{R}$

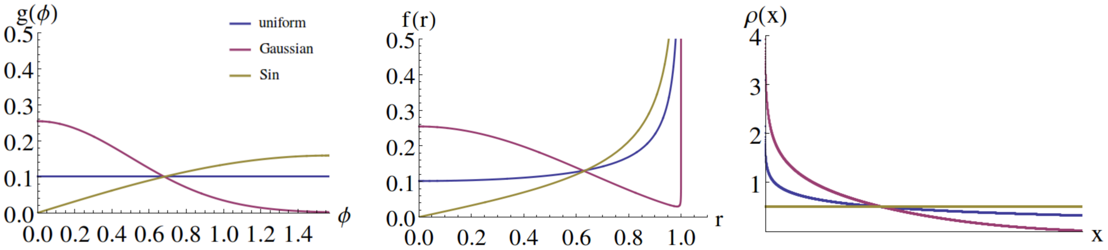

Figure 3.27: Starting from a distribution along the arc-length of the sphere, the distributions along the polar coordinate r and the projected distribution along the x-direction are shown.

When looking at the dome shape from the top, the distribution appears two dimensional and is characterized by the radial coordinate r (in the x-y-plane). The distribution $f(r)$ can be calculated by a coordinate transformation:

$$g(\phi)d\phi = f(r)dr \qquad f(r) = g(\phi(r))\left|\frac{\partial\phi}{\partial r}\right| \qquad \phi = \arcsin\left(\frac{r}{R}\right) \tag{3.37}$$

$$f(r) = g(\phi(r))\frac{1}{R\sqrt{1-(r/R)^2}}. \tag{3.38}$$

Experimentally, the view from the side is more important which means, that the distribution along the x-axis is important where the y-direction is integrated out. Again, we start with a distribution along the coordinate on the surface ϕ which could in general also depend on the azimuthal coordinate θ, $g(\theta,\phi)$. Then we convert to Cartesian coordinates in x and y:

$$\rho(x,y) = g(\theta,\phi)\left|\frac{\partial(\theta,\phi)}{\partial(x,y)}\right|, \tag{3.39}$$

$$\theta = \arctan\left(\frac{y}{x}\right) \qquad \phi = \arccos\left(\frac{\sqrt{R^2-x^2-y^2}}{R}\right), \tag{3.40}$$

$$\rho(x,y) = g(\theta,\phi)\frac{1}{R\sqrt{(R^2-x^2-y^2)\frac{x^2+y^2}{R}}}, \tag{3.41}$$

$$\rho(x) = 2\int_0^{\sqrt{R^2-x^2}} \rho(x,y)\mathrm{d}y. \tag{3.42}$$

Depending on the input function, this integration needs to be done numerically. Three examples are calculated and plotted in Figure 3.27, a normalized constant distribution in ϕ, a normalized Gaussian distribution and a distribution proportional to ϕ which corresponds to a uniform 2D distribution on the sphere (to see this consider the surface element in spherical polar coordinates which is given by $\mathrm{d}A = \sin\phi \mathrm{d}\theta \mathrm{d}\phi$). We see, that the distribution in the polar coordinate r is enhanced towards the edge of the sphere since the curvature is highest there when seen from the top. The distribution along the x-axis compensates for this by averaging over the y-direction. As expected, the distribution that is uniform on the sphere (called "Sin" in the plot) is also uniform in x. This is due to the previously mentioned property that each equally thick segment (cut by 2 parallel planes) of the sphere has the same surface area.

3.7 Discussion of Molecular Structure Formation

By employing a reaction-diffusion model, it was possible to understand the molecular structure of the RBC cytoskeleton better. The simulations show clearly, how the flexibility of spectrin leads to a thick dense network that is elastic enough to extend under stress. We also found that the actin filament length cannot be controlled by simple measures (concentration, capping) for all filaments simultaneously. An additional mechanism such as using tropomyosin as a ruler is needed which favours capping at specific lengths.

Regarding the formation of KAHRP clusters a large parameter space was examined and only for one specific set-up with a specific interaction strength KAHRP clusters at the actin junctions could be found. However, this is a remarkable result since there is evidence that knobs are associated with the actin junction for late times of the infection. The parasite might change the binding affinity of KAHRP through phosphorylation in order to assemble knobs near the actin junctions.

Furthermore, the modelled cytoskeleton was found to reproduce the appearance of malaria infected cytoskeletons, when it contained KAHRP clusters. The clusters condense the network in some places and make it more sparse in other regions, such that the plain bilayer would be exposed in some places. This effect would be enlarged if actin disassembly would be considered. However, simulations with actin dynamics take a long time to run and have not been considered for this work.

In the last chapter a slightly different aspect of the cytoskeletal modifications was examined. It was found that the adhesion protein PfEMP1 clusters preferentially towards the middle of the knob. This is a good strategy for the parasite because it becomes easier to reach receptors on other cells.

It remains an open question, how the PfEMP1 and KAHRP interact to form stable knobs of known morphology. Additionally, there are also other proteins that are essential for the knob formation. For example a spiral like structure is frequently observed below knobs but it is not clear, what exactly makes up this spiral.

Chapter 4

Finite Element Model for Red Blood Cells in Flow

4.1 RBCs in Capillaries and Microfluidic Devices

The ability of RBCs to squeeze through narrow capillaries in our body is remarkable. In larger vessels blood can be treated as a continuum fluid but in capillaries of approcimately the size of the RBS the dynamics of single RBCs becomes important. In this case, the shape of individual cells is influenced by the flow rate and vessle diametre [165, 166, 167]. In larger capillaries the cells assume a slipper-like shape, whereas they adopt a parachute-like shape in smaller capillaries. Pries *et al.* [168, 169] examined the behaviour of RBCs at microvascular bifurcations and developed a model for large microcirculatory networks.

To mimic the environment in the microvasculature in a controlled manner, microfluidic devices have been used to study the behaviour of RBCs. Two possilbe experimental realisations are shown in Figure 4.1. In Prof. Guck's group Otto *et al.* [170] developed a high throughput device which detects the deformation of cells in a narrow tube of 20 µm. Because the set-up can process many cells in a short time period, they are able to produce deformation graphs as shown on the right in Figure 4.1a. A theoretical model is applied to study the cell deformations and extract parameters [171]. With this device it is possible to distinguish cells within a population such as malaria iRBCs mixed with healthy RBCs [172]. Figure 4.1b shows the device developed by Ito *et al.* [173]. The distinguishing feature of this device is a high precision robotic pump which enables the users to hold the cell in the narrow constriction for different periods of time and study its subsequent relaxation.

Great effort has been made to model the RBC's behaviour in flow, whereby the difficulties lies in coupling the RBC mechanics to the surrounding liquid. The striking advantage of theoretical modelling is that RBC parameters can be accessed and tested to determine their implications. Since the whole-cell properties of the RBC play an important role, these models differ from the ones discussed in the last chapter. In the following, the cell is modelled on a much coarser scale.

Besides the properties of a RBC, the modelling approach has to account for the surrounding fluid as well. Two very common techniques to model three dimensional flow behaviour are dissipative particle dynamics (DPD) and multiparticle collision dynamics (MPCD) which have been applied to the RBC by Fedosov [156, 174] and Gompper [175] respectively. Other techniques based on the Finite Element Method have also been developed and will be discussed in Section 4.2.2. The model applied in this chapter is a two-dimensional model because the reduction of dimension reduces the computational complexity dramatically. It has been shown by Seifert [176] in a numerical manner, that two-dimensional models can capture the shape and adhesion properties of RBCs sufficiently good. Subsequently, Secomb *et al.* [177] showed that a two-dimensional model can also reproduce the tank-treading frequency of RBCs, while keeping the computation time for a typical simulation at the order of minutes due to the reduced dimensionality.

The outline of this chapter is as follows. First, an overview of the relevant hydrodynamic theory and modelling approaches for RBCs in flow are given in Section 4.2. Then the experimental approach used by Maya Harms in the group of Prof. Tanaka is explained in Section 4.3, which is aimed to be simulated by the model developed here. In Section 4.4 the two-dimensional finite element model

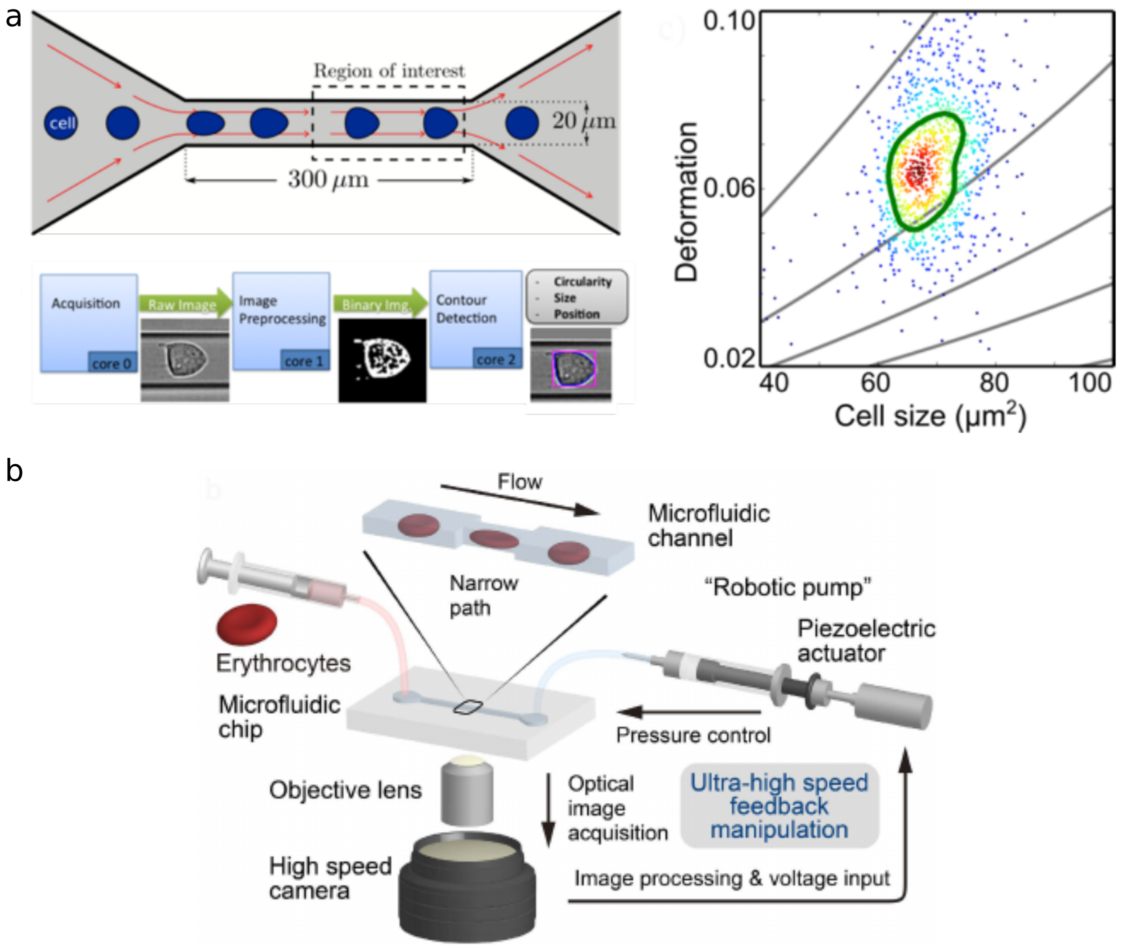

Figure 4.1: a) Microfluidic device developed by Otto *et al.* [170]. Cells flow through a narrow constriction and their deformability is analysed. b) Ito *et al.* [173] fabricated a microfluidic channel with a robotic pump which enables them to hold the cells inside the narrow constriction. Images taken from the respective papers.

is explained and the results of the simulation are analysed. A discussion of this chapter's material is given in Section 4.5.

The work discussed in this chapter has been initiated during the Bachelor Thesis of Hanno Iwasaki Hennighausen who I supervised. The title of his thesis was *A Two-Dimensional Finite Element Implementation of a Red Blood Cell in a Microfluidic Channel.*

4.2 Models for RBCs in Flow

4.2.1 Hydrodynamic Theory

The equations describing hydrodynamic flow in general are the Navier-Stokes equations, here given for an incompressible fluid [57]:

$$\frac{\partial \boldsymbol{u}}{\partial t} + (\boldsymbol{u} \cdot \nabla)\boldsymbol{u} = \frac{\mu}{\rho}\nabla^2 \boldsymbol{u} - \frac{1}{\rho}\nabla p \tag{4.1}$$

$$\nabla \cdot \boldsymbol{u} = 0, \tag{4.2}$$

where μ is the dynamic viscosity, ρ the fluid density, $\boldsymbol{u}$ the flow field and p the pressure field. The qualitative behaviour of this equation is determined by the dimensionless Reynolds number Re. When Re $\ll 1$, the non-linear inertial force (second term in Equation 4.1) can be ignored. For the relevant parameter range of a RBC in a microfluidic system, we find:

$$\mathrm{Re} = \frac{\rho u d}{\mu} \approx \frac{997 \cdot 0.1 \cdot 10\ 10^{-6}}{8.9\ 10^{-4}} = 0.011 \ll 1, \tag{4.3}$$

where d is the channel diameter and u the magnitude of the fluid velocity. Hence, the simpler equations of the Stokes flow apply [178]. Then the steady flow profile ($\frac{\partial \boldsymbol{u}}{\partial t} = 0$) is given by:

$$\mu \nabla^2 \boldsymbol{u} - \nabla p = 0 \tag{4.4}$$

$$\nabla \cdot \boldsymbol{u} = 0. \tag{4.5}$$

Treating this description explicitly, the velocity of particle i at position $\boldsymbol{r}$ surrounded by a fluid is given by

$$\boldsymbol{v}_i(\boldsymbol{r}) = \frac{1}{k_\mathrm{B}T}\sum_j H_{ij}(\boldsymbol{r})F_j, \tag{4.6}$$

with $k_\mathrm{B}T$ the Boltzmann constant times the temperature T, F_j the external force due to particle j and H_{ij} the Onseen tensor [179] capturing the hydrodynamic interactions of different particles in the fluid, given by:

$$H_{\alpha\beta}(\boldsymbol{r}) = \frac{1}{8\pi\mu r}\left[\delta_{\alpha\beta} + \frac{r_\alpha r_\beta}{r^2}\right]. \tag{4.7}$$

The hydrodynamic interactions are long-range forces that decay as r^{-1}. It is obvious that in a many-particle system these interaction terms become very complex. Hence an analytical calculation of the velocity is not advisably.

Whenever hydrodynamic interactions are important for a system, the Stokes equation is commonly solved by one of the simulation methods discussed in Section 4.2.2. They either resolve the fluid by so-called solvent particles or solve the above equations numerically. In either case, the exact modelling of the fluid behaviour is quite computationally expensive such that it should be avoided whenever possible. In such a case, only the resistance, induced by the viscosity of the solvent, is important and particles move according to their diffusive properties. Solvent particles are not modelled in this case. The method used in these kinds of systems is called Brownian Dynamics and is explained and employed in Chapter 3.

However, in the case of RBCs in capillaries the hydrodynamic effects are essential. An important effect that originates from hydrodynamic interactions is the Fåhræus-Lindqvist effect. It describes how the apparent viscosity of blood changes with vessel diameter. Specifically, the viscosity decreases with decreasing diameter and reaches a minimum at 7 µm because a cell free layer develops at the wall of the vessel and hence the RBCs can flow more easily. This effect was first described in Ref. [180] and has been confirmed both experimentally and by simulations. The cross-stream migration of RBCs necessary for the development of the cell-free layer is caused by hydrodynamic cell-wall interactions and hydrodynamic cell-cell interactions as described in Ref. [181].

4.2.2 Fluid-Structure Interactions

When a structure deforms in flow, the body and the fluid necessarily need to interact. In general this is a two-way coupled system because the evolving flow deforms the surface of the structure such that the flow domain is changed itself. In special cases, the situation can be simplified, if one of the couplings is much weaker than the other, such as a fixed rigid object in flow. However, the RBC definitely belongs to the two-way coupled systems.

In order to bridge the scale between the solvent constituents and the objects surrounded by these, a mesoscopic approach is necessary to reach the relevant time scales. This is done by numerically treating the fluid. The concepts of the different model approaches described here apply in two and three dimensions. Necessarily, it will always be a lot more computationally expensive to model a three-dimensional system. Although qualitative behaviours can also be captured in the reduced dimension, a full three-dimensional computation is necessary to obtain quantitative results. I now briefly explain the most common modelling approaches focusing on the simulation strategy for the fluid.

Finite Element Method

The Finite Element Method makes it possible to solve the Stokes equations with a continuum approach. For this purpose, a finite element lattice is introduced on which the equations are solved numerically. In fact, not the exact equation is solved but what is called the weak form. To obtain the weak form, the equation is multiplied by a test function v and then integrated over the whole domain.

Hence, the solution of the Finite Element Method fulfils the original equation in an average sense [182].

If this procedure is applied to the Stokes equation (4.5), the following weak form is obtained after using integration by parts to get rid of higher order derivatives:

$$\int_\Omega (\nabla u \cdot \nabla v + \nabla \cdot v\ p + \nabla \cdot u\ q)\,\mathrm{dx} = \int_\Omega f \cdot v\ \mathrm{dx}, \tag{4.8}$$

with f an externally applied force. Special care has to be taken with the boundary conditions, because they enter the integral expression through the integration by parts. For simplicity, they are neglected in this section.

In the next step the involved functions are expressed as sums of basis shape functions $\phi_i(x, y)$, which are defined on the finite elements, i.e. a subsection of the underlying mesh. The basis functions are typically chosen to be piecewise linear or quadratic. Hence, the approximations of u and v read:

$$\boldsymbol{u}_h(x, y) = \sum_i^N \boldsymbol{\alpha}_i\ \phi_i(x, y) \quad \text{and} \quad \boldsymbol{v}_h(x, y) = \sum_i^N \boldsymbol{\beta}_i\ \phi_i(x, y), \tag{4.9}$$

where $\boldsymbol{\alpha}_i$ and $\boldsymbol{\beta}_i$ contain the coefficients for the x and y components. The shape functions are chosen such that $\boldsymbol{\alpha}_i$ and $\boldsymbol{\beta}_i$ correspond to the values of the function at the nodal points, i.e each shape function is equal to 1 at exactly one nodal point and 0 at the others.

By plugging these expressions into the weak form, the equation can be written as a matrix equation. The term, which is independent of the external force f, is called the stiffness matrix K_{ij} and the part depending on f is called the load vector F_i. Consequently, the problem is reduced to the following matrix equation:

$$K_{ij}\ \gamma_j = F_i, \tag{4.10}$$

where γ_j contains the coefficients $\boldsymbol{\alpha}_i$ and $\boldsymbol{\beta}_i$. Since many of the entries of K will be zero it is a sparce matrix which can be solved by common approaches.

In case of the Stokes equation, two function spaces need to be defined; a vector function space for u and a scalar function space for p. To ensure stability of the solution the common choice is a continuous piecewise quadratic space for u and a continuous piecewise linear space for p. This mixed finite element space is called the Taylor-Hood elements [183].

Other Methods

The boundary integral method has emerged as an alternative to the Finite Element Method for problems that require a better accuracy or have infinite domains. Since the problem is formulated as a boundary integral equation, only the surface needs to be discretised [184]. After the solution on the boundary is found, it can be extrapolated throughout the whole domain. However, when applied to hydrodynamic flows, the boundary-integral method is limited to viscous flows and cannot include inertial effects [10].

The immersed boundary method was developed by Charles Peskin in 1972 [185, 186]. The basis of the method are two separate grids, Eulerian coordinates for the fluid and Lagrangian coordinates for the immersed structure. The latter one is described as a collection of one-dimensional fibres and their resulting force on the fluid is incorporated in the momentum equation. In principle, any existing fluid solver can be coupled to the equations for the fibres. Besides treating the fluid as a continuum, it can also be modelled by introducing solvent particles. The following methods can be used:

The Lattice Boltzmann method was first developed in 1988 [187] based on the previously employed lattice gas automata. A review of this method can be found in Ref. [188]. The idea of the method relies on the statistics of the Boltzmann equation as derived in Ref. [189]. In the simulation, the fluid is depicted by solvent particles moving on a regular lattice. The simulation alternates between streaming and collision events. The streaming involves a propagation between the nodes according to a discrete velocity and the collision events are based on interactions of the particle densities according to the Boltzmann transport equation. During the collisions mass and momentum are interchanged. In this method special care has to be taken to conserve the stress tensor and the incorporation of fluctuations is not straight forward [190].

Dissipative Particle Dynamics was introduced in 1992 [191] as an attempt to free the previous modelling approaches from the lattice. Hence, the solvent is represented by particles that are free to move and interact via dissipative, stochastic and conservative interactions. The dissipative and stochastic nature comes from the idea that each solvent particle represents a thermodynamic subsystem with many microscopic constituents. During the simulation the solvent particles are evolved in time according to Newton's equations. The dissipative force acts as a friction and hence cools the system, whereas the stochastic force heats the system up. By imposing specific criteria on the forces, it is possible to conserve the overall momentum and hence reproduce hydrodynamic behaviour [190]. Several extensions of the model have been developed which are adjusted to specific situations. Solid objects are represented as particles that are frozen in location with respect to each other.

The latest of these approaches is called Multiparticle Collision Dynamics and was developed in 1999 [192, 193]. In this method the fluid is also modelled by solvent particles which are in principle free to move. The algorithm can be divided in two steps, the streaming and the collision steps. During streaming the particles do not interact and move ballistically according to their individual velocities. For the collision time step, the simulation box is divided into small collision boxes with a few solvent particles in each of them. In each box the center of mass velocity is calculated and the particle velocities relative to this center of mass velocity are rotated by a random rotation matrix. This procedure assures that all particles change their speed and direction while conserving the momentum and kinetic energy within the box. Furthermore, the collision grid is moved before the next time step. If objects are incorporated into the solvent, they are usually propagated with conventional molecular dynamics and they exchange momentum with the solvent particles during the streaming and/or the collision steps.

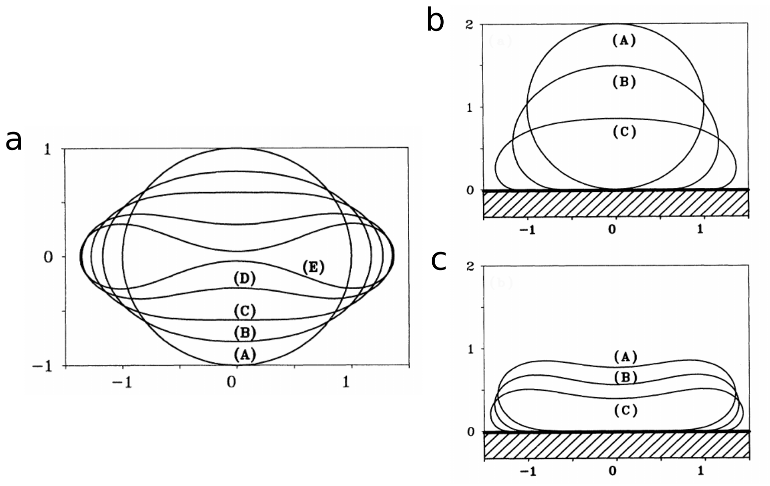

Figure 4.2: a) Numerically calculated shapes of two dimensional free vesicles. The different shapes correspond to different pressure differences. b and c) Various shapes of adhering vesicles are shown. Images taken from Ref. [176].

4.2.3 Existing Three-Dimensional RBC Models

Full three-dimensional simulations of RBCs in flow are computationally expensive and need to be run on large computation clusters. Nevertheless, various models have been developed by different groups, of which some will be discussed hereafter.

One of the first models was developed by Gompper and Noguchi [175, 194, 195]. They used Mulitparticle Collision Dynamics to describe the fluid and a dynamically triangulated surface model for the RBC membrane, which includes shear and bending elasticity. This model was used to simulate flow through narrow capillaries.

During his PhD work Dr. Fedosov developed a RBC model using the Dissipative Particle Dynamics approach. The RBC is depicted as a triangulated surface and exhibits the necessary mechanical properties. In their papers Fedosov *et al.* [156, 174] and Pivkin *et al.* [196] showed that this model can be successfully be applied to experimental set-ups such as laser traps and capillary flow. The modelled RBC also exhibit the experimentally known properties in shear flow.

Dr. Dasanna from the group of Prof. Schwarz also established a model for RBCs in flow which is based on the triangulated surface model developed by Dr. Fedosov and uses Multiparticle Collision Dynamics to model the fluid. He used his model to simulate the effects of the malaria parasite on RBCs' flow and adhesion behaviour [157, 8].

4.2.4 Two-Dimensional Approaches

There have been various approaches considering two-dimensional vesicles, meaning a one-dimensional loop in a plane as depicted in Figure 4.2. The advantage of this two-dimensional approach is that the high complexity of a three-dimensional shape does not apply here but still many properties are carried over from the three-dimensional case.

Without hydrodynamic interactions, this problem can be treated numerically

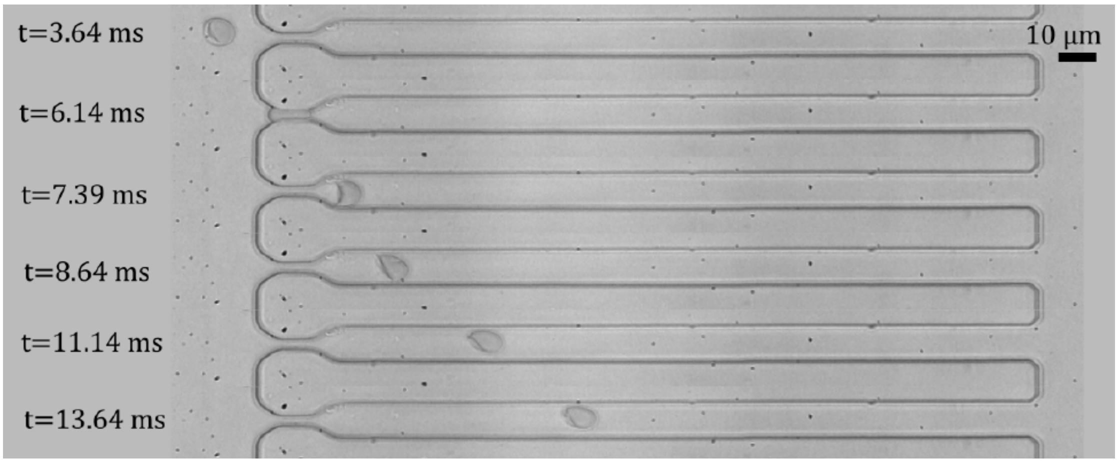

Figure 4.3: A RBC is passing through a microfluidic device produced in Prof. Tanaka's laboratory. Image is adapted from Maya Harms' Master Thesis.

to solve for equilibrium shapes of the vesicles. This was done by Seifert [176], who calculated the shapes of free and adhering vesicles for different pressure differences and adhering forces (see Figure 4.2).

Based on this success to study vesicle behaviour in two dimensions, Bagchi [197] developed a two-dimensional model including hydrodynamic interactions by using the immersed boundary method. The strength of his model is the ability to model large cell populations of up to 2500 cells. Hence, the behaviour in large blood vessels can be studied. He could reproduce the Fåhræus-Lindqvist effect explained above.

On a similar basis Lattice-Boltzmann simulations of two-dimensional vesicles were developed [198, 199]. With this approach the flow resistance at various haematocrits and vessel diameters was estimated and white blood cells were also included in the simulations to determine their effects on the resistance to flow. An example of a boundary-integral calculation of two-dimensional vesicles is given in Ref. [200].

Overall, the two-dimensional approach is very promising in predicting the behaviour of blood flow. The gain in computational simplicity enables one to reach much large system sizes and length scales. However, one cannot be sure that there are no artefacts from the dimensional reduction such that a proper three-dimensional simulation cannot be avoided eventually to confirm the properties found in two dimensions.

4.3 Experimental Microfluidic System

The motivation for this project were microfluidic experiments using soft lithography done in the group of Prof. Tanaka. The model described in the next section tries to simulate the experimental set-up. The shortcomings of the model with respect to the experiment will be discussed in Section 4.5.

The experiments done by Maya Harms aim to determine the relaxation behaviour of RBC after passing through a narrow constriction. Healthy RBCs as well as malaria iRBCs were examined and different relaxation timescales were found.

The microchannels shown in Figure 4.3 consist of a polydimethylsiloxane (PDMS) stamp and a glass slide beneath forming the microfluidic channels. The height of these channels with rectangular cross sections is 4.5 µm and the constriction at the entrance of the channels has a length of 10 µm and a width of 3 µm. A flexible tube connects the inlet and outlet of the channels and the blood suspension is added by a syringe. Using an inverted microscope with an ultra fast camera, the whole channel of $243.81 \times 20.32\ \mu\text{m}^2$ was recorded every 0.027 ms. The flow speed is $1.7\ \text{mm}\,\text{s}^{-1}$ before the constriction and $3.4\ \text{mm}\,\text{s}^{-1}$ afterwards.

The results of Maya Harm's analysis of the obtained images yield the residence time t_res and relaxation time τ_rel of each RBC. The residence time describes the time the cell spends in the constriction and the relaxation describes the recovery of the initial shape after leaving the constriction. She found the following values for uninfected RBCs and iRBCs respectively:

$$t_\text{res,uRBC} = 0.11 \pm 0.06\ \text{ms} \quad \text{and} \quad \tau_\text{rel,uRBC} = 0.255 \pm 0.086\ \text{ms}, \tag{4.11}$$

$$t_\text{res,iRBC} = 0.42 \pm 0.28\ \text{ms} \quad \text{and} \quad \tau_\text{rel,iRBC} = 0.603 \pm 0.737\ \text{ms}. \tag{4.12}$$

A clear increase of the mean value can be seen in both times which can be explained by the increased stiffness of the RBC membrane discussed in the previous chapters.

4.4 A Two-Dimensional Finite Element Model

In this work a two-dimensional RBC model developed by Secomb *et al.* [177] is employed. The model consists of interconnected viscoelastic elements describing the RBC membrane which is coupled to a surrounding medium fulfilling the Stokes equation. The mechanical equations and the Stokes flow are solved simultaneously by a finite element software. Here, a similar approach is used, in which the relevant equations are implemented in the finite element software FEniCS [201].

This specific modelling approach was chosen because of the following reasons. First of all, a two dimensional approach makes it possible to examine larger systems with less computational resources. A proper three-dimensional model takes long to develop and test out different simulation set-ups. With a model that produces simulation results within minutes instead of days, the interaction with experimental groups becomes easier since predictions can be made and adapted more frequently. Further, the model by Secomb treats the RBC membrane as interconnected viscoelastic elements which is directly comparable to one-dimensional models for the relaxation of RBC height, but with the extra complexity of a two-dimensional shape.

The fluid structure interaction in this model is implemented in an uncommon way. By inserting the equations into the finite element software, the mechanical equations are solved simultaneously to the Stokes flow on the finite element mesh. Therefore, the mechanical equations are fulfilled exactly. How this is implemented in this thesis is explained in Section 4.4.4.

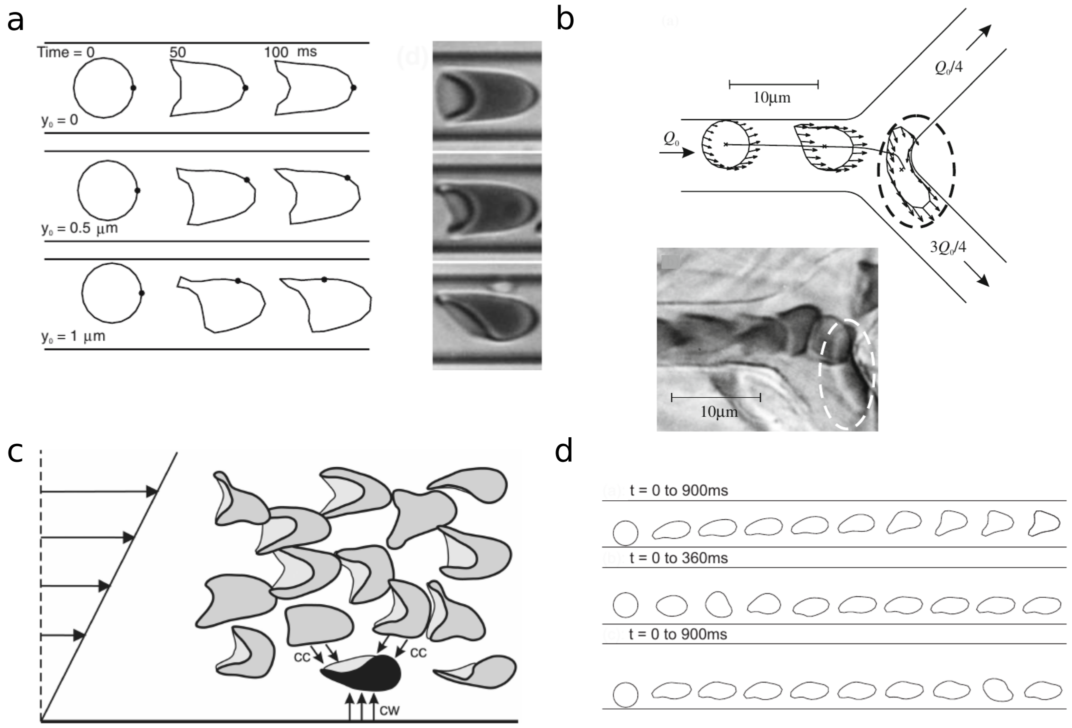

Figure 4.4: Simulation results from the two-dimensional model developed by Prof. Secomb are shown. a) The simulated tank-treading frequency matches the experimentally obtained values. Graphic is taken from Ref. [177]. b) RBC behaviour at bifurcations is studied. This comparison between the model at the top and a microscopy image at the bottom is taken from Ref. [202]. c) The hydrodynamic interactions with the other cells result in an outwards pointing force on the cell. Image is taken from Ref. [203]. d) Simulation results showing the off-centreline positioning of cells in a 12 µm channel. Graphic is taken from Ref. [204].

4.4.1 Previous Applications

The model by Secomb *et al.* has been used to simulate different aspects of the flow in narrow tubes. In the original paper, they validate their model by examining the tank treading frequency (see Figure 4.4a). In previous two-dimensional models the frequency was overestimated compared to the three-dimensional case [177]. The reason why their model describes this behaviour better are viscous elements that connect all membrane nodes to one RBC midpoint. In a second paper, the RBCs' behaviour at bifurcation points in the microvasculature was examined (see Figure 4.4b). It could be reproduced that more RBCs migrate into the branch with the higher flow rate [202].

Some years later the group of Prof. Secomb took up this modelling approach again in order to look more closely at the cell positioning with respect to the wall. First, they found that a strong force pushing the cell towards the wall (compare Figure 4.4c) induces a tank treading motion and smaller force induces tumbling of the cell [203]. The origin of this force in real blood flow would be the cell-cell interactions which push the cell outwards. Following up on this study, they found that RBCs can be positioned off-centreline for some initial conditions in a 12 µm channel [204] (see Figure 4.4d).

4.4.2 Equations for the RBC

The RBC is depicted as a discrete envelope with n external nodes as shown in Figure 4.5a. To capture the visco-elastic behaviour of the membrane, the external elements are modelled as Kelvin-Voigt elements, which consist of an elastic and a viscous element in parallel. Additionally, each is connected to one midpoint by a viscous element which models both the viscosity of the cytosol and the viscosity within the membrane.

Contributions from the RBC mechanics as well as the surrounding fluid have to be accounted for when determining equations for the nodes of the system (see Figure 4.5b). Let us focus on segment i and parametrize all forces by s, varying between 0 and the segment length l_i. The relevant forces acting on the segment are a tension force $t_i(s)$, a shear force $q_i(s)$ and a bending force $m_i(s)$, all given as forces per unit length. The force acting through the internal element is called T_i. For the force balance equations, the values at the nodes are relevant. In contrast to this, the mechanical properties of the membrane and the fluid loads are defined along the segments. Therefore, averages of the relevant forces are evaluated. Specifically, mean tension and shear are defined as:

$$\bar{t_i} = \frac{1}{l_i} \int_0^{l_i} t_i(s)\ \mathrm{d}s \quad \text{and} \quad \bar{q_i} = \frac{1}{l_i} \int_0^{l_i} q_i(s)\ \mathrm{d}s. \tag{4.13}$$

Using the node, angle and segment numbering as introduced in Figure 4.5c and d, the equilibrium conditions, which are split up in x and y components, for node i

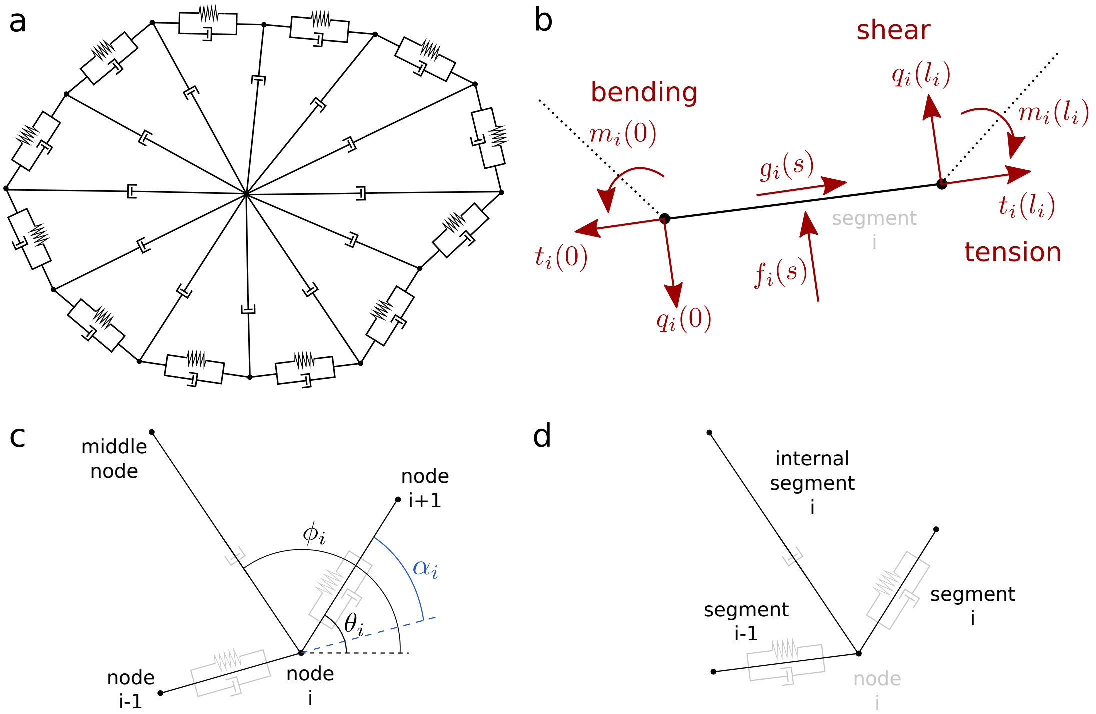

Figure 4.5: a) Mechanical model for the RBC consisting of Kelvin-Voigt elements on the RBC envelope and purely viscous dashpots inside the RBC. b) Forces that act on an external element. The tension force t acts parallel to the envelope, the shear force q acts perpendicular to it, the bending force m acts between this and the neighbouring segment and the normal and tangential fluid loadings f and g act all along the segment. c) Definitnion of node and angel numbering is shown. The angles θ and ϕ are measured with respect to the horizontal dashed line. d) Segment numbering is done anti-clockwise with the ith segment extending from the ith node in the anti-clockwise direction.

are:

$$\begin{aligned} t_i(0)\cos\theta_i - t_{i-1}(l_{i-1})\cos\theta_{i-1} - q_i(0)\sin\theta_i + q_{i-1}(l_{i-1})\sin\theta_{i-1} & \\ +T_i\cos\phi_i = 0, & \qquad (4.14) \\ t_i(0)\sin\theta_i - t_{i-1}(l_{i-1})\sin\theta_{i-1} + q_i(0)\cos\theta_i - q_{i-1}(l_{i-1})\cos\theta_{i-i} & \\ +T_i\sin\phi_i = 0. & \qquad (4.15) \end{aligned}$$

Additionally, the equilibrium equation for the middle node reads:

$$\sum_{i=1}^{n} T_i\cos\phi_i = \sum_{i=1}^{n} T_i\sin\phi_i = 0. \qquad (4.16)$$

Now the tension and shear forces used in these equations need to be expressed in terms of RBC and fluid properties. Let us first consider the Kelvin-Voigt elements in the RBC envelope. These produce a tangential force within the segment and hence enter the equation for the average tension:

$$\bar{t_i} = k_t\left(\frac{l_i}{l_0} - 1\right) + \mu_m\frac{1}{l_i}\frac{\mathrm{d}l_i}{\mathrm{d}t}, \qquad (4.17)$$

with k_t is the elastic modulus, l_0 the average length of the segment and μ_m the viscosity coefficient of the external segment. Bending forces between neighbouring elements introduce a shear force at each segment end and hence an average of

$$\bar{q_i} = \frac{k_b(\alpha_i - \alpha_{i+1})}{l_0 l_i}, \qquad (4.18)$$

with k_b the bending modulus and $\alpha_i = \theta_i - \theta_{i-1}$ (see Figure 4.5c). The viscous internal elements produce a force of:

$$T_i = \mu'_m\frac{1}{L_i}\frac{\mathrm{d}L_i}{\mathrm{d}t}, \qquad (4.19)$$

with μ'_m the internal viscosity coefficient and L_i the length of the internal segment. All together these are $2n+2$ equations that determine the system's behaviour. Depending on the present node positioning, the velocity of the $n+1$ nodes can be calculated.

Note that the segment forces are related by the following mechanical equilibrium equations

$$\begin{aligned} \frac{\mathrm{d}t_i}{\mathrm{d}s} &= -g_i(s), & (4.20) \\ \frac{\mathrm{d}q_i}{\mathrm{d}s} &= -f_i(s), & (4.21) \\ \frac{\mathrm{d}m_i}{\mathrm{d}s} &= q_i(s), & (4.22) \end{aligned}$$

such that the forces at the nodal points can be determined in terms of the fluid loadings and the mean tension and shear:

$$t_i(0) = \bar{t}_i + \frac{1}{l_i}\int_0^{l_i} g_i(s)(l_i - s)\ \mathrm{d}s, \tag{4.23}$$

$$t_i(l_i) = \bar{t}_i - \frac{1}{l_i}\int_0^{l_i} g_i(s)s\ \mathrm{d}s, \tag{4.24}$$

$$q_i(0) = \bar{q}_i + \frac{1}{l_i}\int_0^{l_i} f_i(s)(l_i - s)\ \mathrm{d}s, \tag{4.25}$$

$$q_i(l_i) = \bar{q}_i - \frac{1}{l_i}\int_0^{l_i} f_i(s)s\ \mathrm{d}s. \tag{4.26}$$

Whereas in three dimensions RBCs keep a constant volume, this conservation cannot directly be applied to the two-dimensional area. Since the area can be imagined as a cross-section of a three dimensional RBC, it should still be restricted to values close to a reference area A_{ref}. This is done by introducing an internal pressure:

$$p_{\text{int}} = k_p\left(1 - \frac{A}{A_{\text{ref}}}\right), \tag{4.27}$$

with k_p the area modulus.

4.4.3 Hydrodynamic Equations

The blood plasma surrounding RBCs in our body mostly consists of water. Therefore, it is modelled as a viscous incompressible fluid at low Reynolds number. The governing equations are the ones of the Stokes flow which is formulated in terms of a pressure and a velocity field,

$$p(x,y) \quad \text{and} \quad \boldsymbol{u}(x,y) = \begin{pmatrix} u(x,y) \\ v(x,y) \end{pmatrix}. \tag{4.28}$$

Depending on these quantities, the components of the stress tensor are:

$$\sigma_{xx} = 2\mu\frac{\partial u(x,y)}{\partial x} - p(x,y), \tag{4.29}$$

$$\sigma_{xy} = \mu\left(\frac{\partial v(x,y)}{\partial x} + \frac{\partial u(x,y)}{\partial y}\right), \tag{4.30}$$

$$\sigma_{yy} = 2\mu\frac{\partial v(x,y)}{\partial y} - p(x,y), \tag{4.31}$$

where μ is the viscosity. For an incompressible flow the divergence of the velocity field is zero:

$$\frac{\partial u(x,y)}{\partial x} + \frac{\partial v(x,y)}{\partial y} = 0. \tag{4.32}$$

Now a no-slip condition is applied at the fluid-RBC interface and therefore, the fluid loadings are given by:

$$f_i = -p_{\text{int}} - \sigma_{xx} \sin^2 \theta_i + 2\sigma_{xy} \sin \theta_i \cos \theta_i - \sigma_{yy} \cos^2 \theta_i, \tag{4.33}$$

$$g_i = (\sigma_{xx} - \sigma_{yy}) \sin \theta_i \cos \theta_i - \sigma_{xy}(\cos^2 \theta_i - \sin^2 \theta_i). \tag{4.34}$$

Note that the internal pressure, introduced in Equation (4.27), enters the normal fluid loading. Further, the values along the segment are calculated by a linear interpolation between the values at the nodes.

The surrounding flow is modelled as a Stokes flow on the finite element grid as explained in Section 4.2.2. Boundary conditions for the flow have to be chosen at the vessel walls and the inflow and outflow boundaries. On the walls, no-slip Dirichlet boundary conditions are chosen. In order to minimise boundary effects, the inflow and outflow are set to the values given for a Poiseuille flow in a two-dimensional channel. Specifically, the equation for laminar flow in a channel of 12 µm height with pressure gradient and viscosity set to 1 reads:

$$u_x(y) = 1 - (y - 6\ \mu\text{m}) \frac{12\ \mu\text{m} - (y - 6\ \mu\text{m})}{36\ \mu\text{m}^2}. \tag{4.35}$$

4.4.4 Implementation in the Finite Element Software

To couple the RBC mechanics with the hydrodynamic flow, the mechanical equations are implemented as conditions on the finite element nodes that represent the RBC envelop (see blue points in Figure 4.6). Since the finite element software will eventually solve for the velocities at all nodes, these represent the variables of the system. All mechanical equations explained above, need to be written in terms of these velocities. Afterwards they can be implemented in the finite element matrix similar to boundary conditions. As seen in the last section, the fluid loadings (4.33) and (4.34) actually depend on the derivatives of $\boldsymbol{u}(x, y)$. How the derivatives can be expressed in terms of the nodal velocities is explained hereafter. In this work, I choose to implement the RBC equations as a constraint on the flow using the penalty method explained later in this section. Likewise, a Lagrange multiplier method could be used but its implementation in FEniCS was not as straight forward as expected.

Regarding the initial implementation of the RBC on the finite element mesh, several modifications have to be made by hand. The initial RBC envelope is implemented as a polygon in the mesh and the interior of the cell is excluded from the mesh as can be seen in Figure 4.6a. However, this raises a problem because the elements on the RBC envelope are not equally long and consequently, the elasticity of the elements would lead to large initial forces. Therefore, the nodes are moved to equal distances by hand, such that the distortion of the surrounding mesh is minimized. An example is shown in Figure 4.6b. For the coupling to the central node, another modification needs to be applied. The central node and the corresponding triangular elements are added manually as seen in Figure 4.6c.

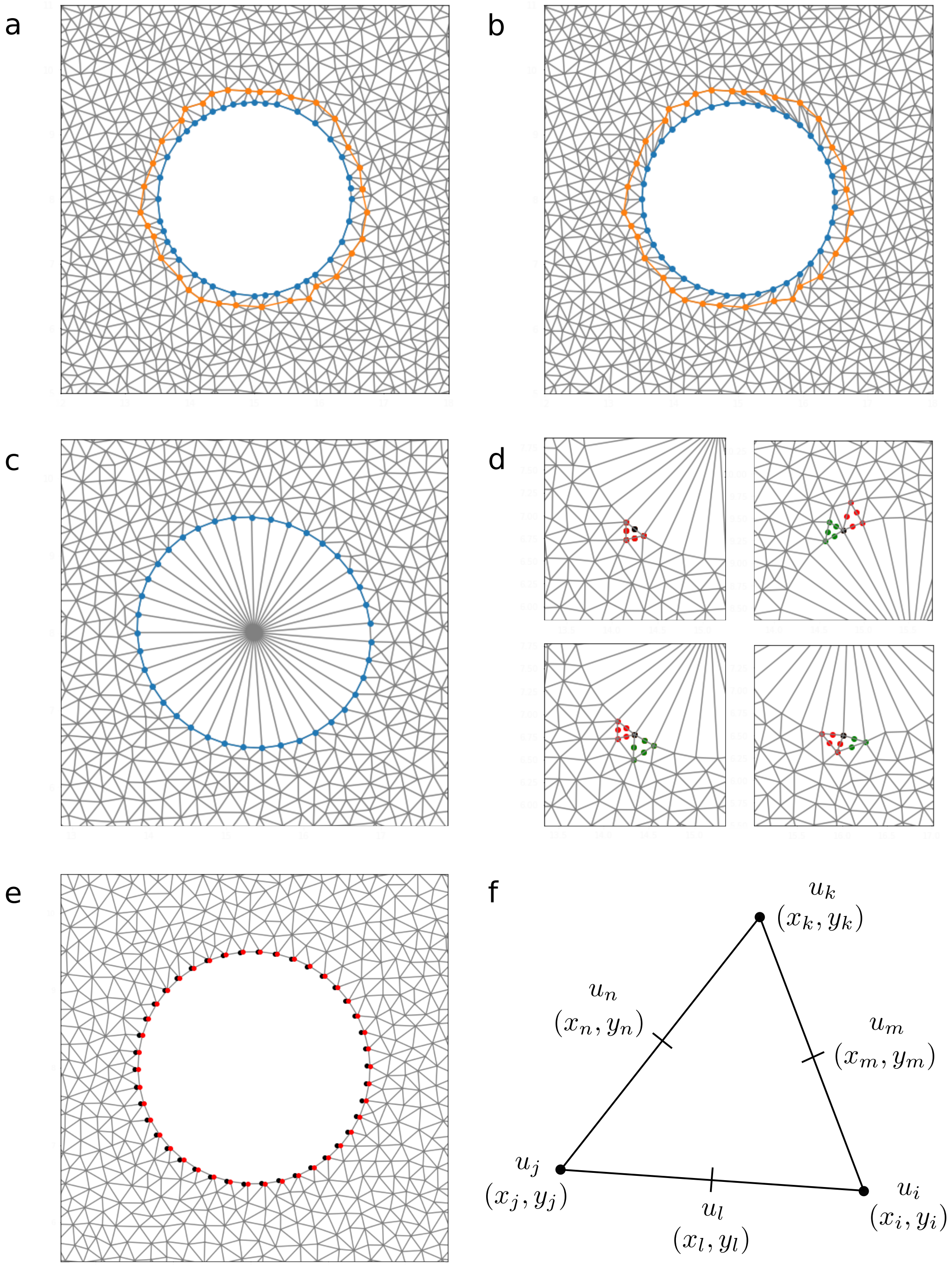

Figure 4.6: a) Boundary points and neighbours are marked on the lattice as created by FEniCS. b) Boundary points were moved manually, such that all elements connectin neighbouring points have an equal length. c) New mesh after manually adding the midpoint of the RBC. d) Points used to calculate the derivatives at a specific point (black) are shown. e) The red points show the new nodal points on the new mesh after moving the RBC vertices according to the dynamical equation. The black points show a configuration from the previous time step. f) Definition of nodes on one quadratic finite element triangle.

Treatment of Derivatives

In order to implement the mechanical equations (4.14) and (4.15) based on the fluid loadings (4.33) and (4.34), the derivatives of the velocity at a point (x_i, y_i) need to be rewritten in terms of the nodal velocities (u_i, v_i). Note that u indicates the x-component and v the y-component of the velocity.

For the finite element calculation quadratic elements were used for the velocities. This means that on a triangular element, there are six nodes as shown in Figure 4.6f and the speed is determined by a quadratic equation. Hence, the x-component of the velocity on this particular element is described by the function:

$$u(x, y) = a_0 + a_1\ x + a_2\ y + a_3\ x^2 + a_4\ xy + a_5\ y^2, \tag{4.36}$$

with six parameters a_i. These can be determined by the six constraints at the nodal points. These conditions are given by $u_i = u(x_i, y_i)$. Writing this as a matrix equation yields

$$\begin{pmatrix} u_i \\ u_j \\ u_k \\ u_l \\ u_m \\ u_n \end{pmatrix} = \underbrace{\begin{pmatrix} 1 & x_i & y_i & x_i^2 & x_iy_i & y_i^2 \\ 1 & x_j & y_j & x_j^2 & x_jy_j & y_j^2 \\ 1 & x_k & y_k & x_k^2 & x_ky_k & y_k^2 \\ 1 & x_l & y_l & x_l^2 & x_ly_l & y_l^2 \\ 1 & x_m & y_m & x_m^2 & x_my_m & y_m^2 \\ 1 & x_n & y_n & x_n^2 & x_ny_n & y_n^2 \end{pmatrix}}_{M} \begin{pmatrix} a_0 \\ a_1 \\ a_2 \\ a_3 \\ a_4 \\ a_5 \end{pmatrix} \tag{4.37}$$

and the coefficients are given by $\boldsymbol{a} = M^{-1}\boldsymbol{u}$. On this basis $u(x, y)$ is determined by the positions and speeds at the triangle nodes, such that derivatives can also be found as follows:

$$\frac{\partial u(x, y)}{\partial x} = a_1 + 2a_3\ x + a_4\ y, \tag{4.38}$$

$$\frac{\partial u(x, y)}{\partial y} = a_2 + 2a_5\ y + a_4\ x. \tag{4.39}$$

Equivalently, the derivatives of the y-component v can be found by introducing six new coefficients b_i. Each coefficient a_i/b_i depends on all six nodal values u_i, u_j, u_k, u_l, u_m and u_n, such that the final expressions for the mechanical equations are rather long. However, these can now be written in terms of the nodal speeds and pressures (u, v, p) and implemented in the finite element matrix.

Figure 4.6d shows examples of the nodes that contribute to the mechanical equations at a node i (highlighted in black). Since derivatives at the previous and following nodes contribute, their triangular points are highlighted in green and red, respectively. If the relevant node i lies on a triangle edge, the two triangles are the same one, because only nodes of the same triangle can be coupled to node i. This is necessary in order to keep the sparsity pattern of the overall matrix which is important for the solution process.

Penalty Method

In order to explain the used method, we need to revisit the formulation of the finite element problem again. As described previously, the finite element software solves the matrix problem:

$$K_{ij}\ \gamma_j = F_i. \tag{4.40}$$

In the penalty method a second matrix P_{ij} and a corresponding load vector Q_i are introduced, which contain the constraints on the RBC boundary [205, 206, 207]. Note, that only entries corresponding to the nodes on the RBC boundary are populated in P_{ij}:

$$(K_{ij} + P_{ij})\ \gamma_j = F_i + Q_i, \tag{4.41}$$

where the entries of P_{ij} and Q_i are both multiplied by a penalty parameter. To assemble these structures, the equations for the RBC need to be formulated in terms of the nodal values u_i and p_i.

Regarding the penalty parameter, its value is not predefined and depends on the system that is modelled. If it is chosen too small, the constraint is not enforced properly. In contrast, a large parameter increases the condition number of the system, which might lead to a poor convergence of the solver.

4.4.5 Dynamics

The Finite Element Method described above yields the instantaneous velocities $\boldsymbol{u}_i^n$ at time step n for a given positioning of the nodes $\boldsymbol{x}_i^n$. Using these velocities for the $n+1$ nodes, the RBC can be evolved in time whereby the time step dt has to be chosen sufficiently small to avoid numerical instabilities.

In this work, an order-two scheme is applied according to Ref. [202], where the next positions $\boldsymbol{x}_i^{n+1}$ are given by

$$\boldsymbol{x}_i^{n+1} = \boldsymbol{x}_i^n + \frac{\mathrm{dt}}{2}(\boldsymbol{u}_i^n + \tilde{\boldsymbol{u}}_i^{n+1}), \tag{4.42}$$

where $\tilde{\boldsymbol{u}}_i^{n+1}$ is calculated using the predicted nodal positions

$$\tilde{\boldsymbol{x}}_i^{n+1} = \boldsymbol{x}_i^n + \mathrm{dt}\ \boldsymbol{u_i^n}. \tag{4.43}$$

In contrast to a forward Euler scheme, this approach reduces the required time step from 1 ms to 0.2 ms [202].

Once the new positions are found, the finite element mesh needs to be updated. Firstly, the new nodal points are set as nodes of the new finite element mesh. Secondly, the FEniCS software creates a triangular finite element mesh around the RBC and thirdly, the midpoint of the new RBC is added manually. To illustrate this process the moving of the nodes is depicted in Figure 4.6e with the new mesh already plotted in the background.

4.4.6 Model Results

During the implementation of the method described in the previous section, several difficulties occurred. Regarding the implementation in FEniCS, it turned out

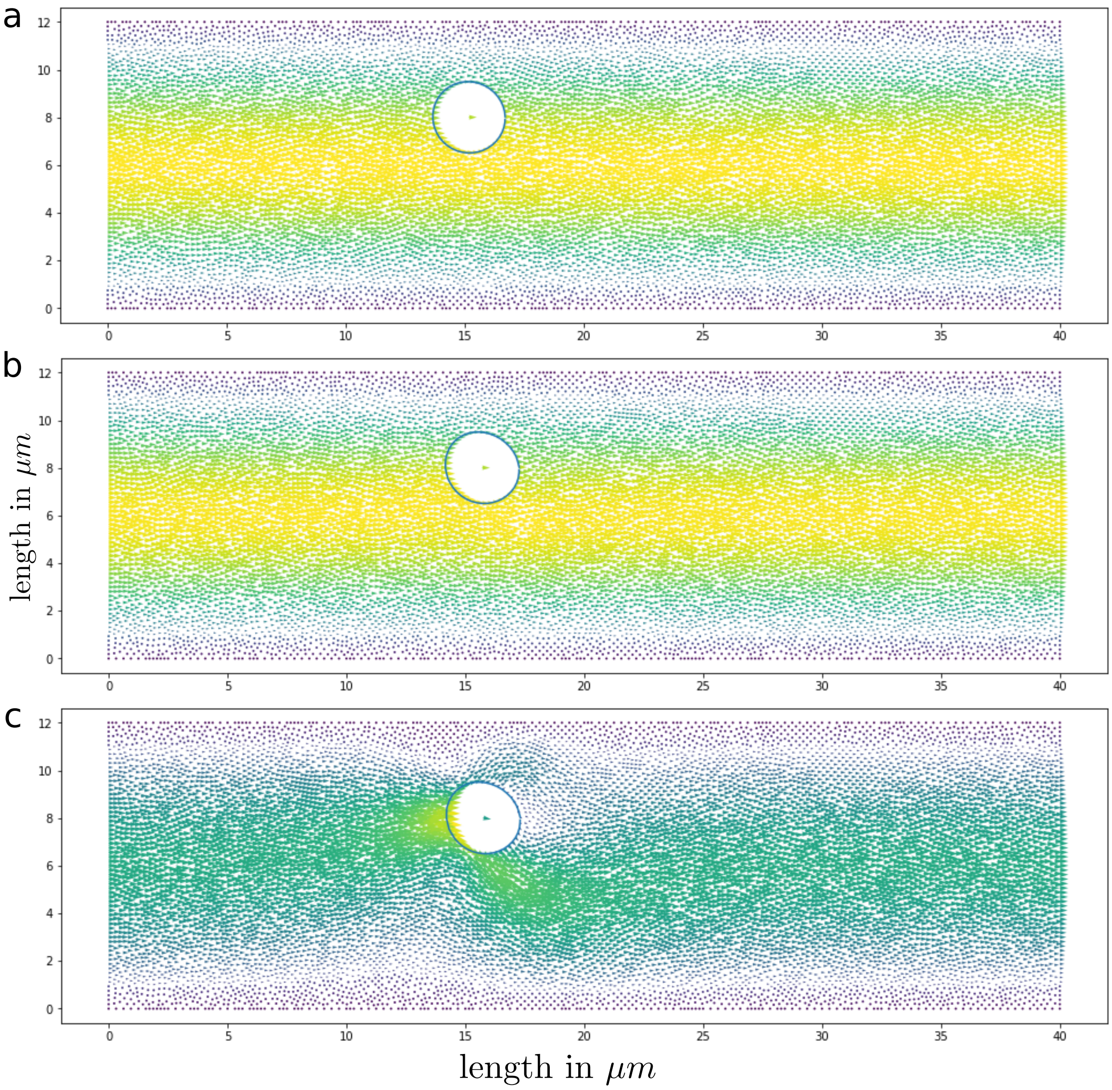

Figure 4.7: a) Flow field calculated from the round initial shape. The blue line indicates the position of the RBC envelope. Yellow arrows indicated velocities with large magnitudes and blue ones with small magnitudes. b) Same as in a) but at a later time. The deviation from the spherical shape can be seen clearly. c) The flow field at another time point gets distorted because of numerical instabilities.

parameter		value
bending modulus	k_b	$9 \cdot 10^{-7}$ µN µm
rest length	l_0	0.12 µm
initial RBC radius	r_{RBC}	1.5 µm
reference area	A_{ref}	7.07 μm^2
area modulus	k_p	$5 \cdot 10^{-6}$ µN μm^{-2}
fluid viscosity	μ	1 µN ms μm^{-1}
elastic modulus	k_t	$1.2 \cdot 10^{-5}$ µN μm^{-1}
time step	dt	0.05 ms
penalty parameter	P	10^5

Table 4.1: Overview of the parameters used in the simulations.

that accessing the internally numbered nodes is not straight forward and requires converting back and forth between differently numbered degrees of freedom. It was possible to find the indices of the relevant nodes by defining restrictions on specific areas of the mesh. To achieve this, the python library multiphenics was used which was developed at SISSA mathLab by Dr. Ballarin, under the supervision of Prof. Rozza.

Despite all challenges, the deformation of a RBC envelope in flow was simulated and the results are shown in Figure 4.7. When the flow fields and RBC shape in Figure 4.7a and b are compared, it can be seen that the RBC becomes thinner in direction of the flow. This is in line with expectations, because the flow field pushes against the membrane in the direction of the flow. The simulation validates that the more central side of the RBC envelope is moved forward more quickly because of the parabolic flow field in the channel.

However, there is still a problem with the code, such that long evolutions of the RBC shape cannot be achieved. This problem is allocated to numerical instabilities of the used penalty scheme. Potential problems with the penalty method have been reported and discussed in Ref. [207]. An example of such an instability is shown in Figure 4.7c, where the flow field is clearly distorted in an unphysical way.

The detailed implementation of the derivatives explained above, already improves the numerical convergence. During Hanno Henninghaus' thesis we tried to implement the equations with a simpler two point difference scheme, but this implementations was even more unstable. In summary, the model implementation was improved during this thesis but some numerical issues are still persistent.

4.5 Discussion of Flow Behaviour

In this chapter the properties of a RBC in hydrodynamic flow were examined in more detail. A two-dimensional method was chosen because the implementation seemed suitable for our purposes at the start. The advantage of the proposed model is the treatment of the membrane mechanics in an exact manner; meaning that the nodes of the membrane are coupled explicitly, in contrast to a continuum manner as done in other models.

The implementation of a new method to include forces, relying on derivatives of fluid velocity, improved the convergence of the numerical results for the flow profiles. This enables me to model the initial deformation of the two-dimensional RBC envelope and the expected behaviour was produced. However, the solution still seems to be unstable in some cases, such that the RBC evolution in time could only be achieved for few time steps before numerical instabilities occurred. The reason for these lie in the way the mechanical constraints are implemented on the finite element mesh.

To resolve these problem its origin would have to be found by a detailed mathematical analysis of the problem. Other ways of implementing the constraints could also be tested to achieve better results. A Lagrange multiplier approach seems most promising.

Besides the problems with the implementation of this model, the two-dimensional approach has shortcomings with respect to modelling the experiments. In experimentally obtained videos it can be seen, that RBCs seem to fold when flowing through the narrow constriction. Such a phenomenon would not occur in a two-dimensional simulation. However, for the experimentally studied shape relaxation, a two-dimensional approach would be sufficient because for the height recovery process the exact shape is not the most relevant aspect. The process is rather determined by the membrane properties.

Chapter 5

Cellular Potts Model for Cells on Micropatterns

5.1 Modelling Cellular Spreading and Migration

In order to simulate cell shape and dynamics there have been two major modelling approaches which are applied at the single cell level as well as the tissue scale. These two approaches are the Cellular Potts Model (CPM) and the Phase-Field Model. Whereas in CPMs a cell is described as a collection of spins on a lattice, in Phase-Field Models it is depicted by a scalar field which has a sharp but smoothly decaying interface at the cell boundary.

Here, the focus lies on a CPM which has been developed by Philipp Albert in the group of Prof. Ulrich Schwarz [14]. In general CPMs differ in the terms that are included in the Hamiltonian describing the system. The first CPM was introduced by Graner and Glazier [208] and modifies the well known idea of modelling phase transitions with an Ising-type model. The key feature to model cells with this type of model is to include an area constraint for each cell and in the case of Graner and Glazier also a cell type specific cell-cell interaction. Their model enabled them to show that cells with different interaction energies sort into islands of same cells and phase separate for long time scales.

Following this idea of modelling cell migration there have been various attempts to improve on this simple model and incorporate different aspects of cell dynamics. Particularly the group of Prof. Roeland Merks has developed several models including different features of real cells; they were able to describe tumor growth [209], include mechanisms for cell polarity, couple the CPM to a finite element method for the substrate [210] and include internal structures such as focal adhesions [211].

There have been different approaches to model cell polarity. Biologically it has its origin in cytoskeletal rearrangements which can lead to cell contraction at the cell rear, pushing at the cell front and hence lead to movement. Since cells control this process by means of internal signaling, the most accurate way is to set up a reaction-diffusion system inside the cell. This was done by the group of Prof. Edelstein-Keshet who included Cdc42, Rac and Rho dynamics inside a CPM [212, 211]. Even a simple reaction-diffusion system with one slow and one fast diffusion constituent can lead to a polarization front which has been described as wave-pinning [213]. However, including a whole reaction-diffusion system is computationally expensive. Therefore, other appoaches have been found which produce the same behaviour using minimal computational effort. The model by Albert and Schwarz [14] couples cell migration to a polarization vector which is specific to each cell. Another way is to utilize a scalar field which captures cytoskeletal modifications through local feedback [214, 215].

In order to understand internal cell structures better it is beneficial to examine cells in confined areas. To achieve this, cells have been placed on micropatterns which act as adhesive islands. To model this experimental set-up, the model of Albert and Schwarz is suited well [14]. It has been shown that cells develop invaginated arcs when they span non-adhesive areas. These arcs are formed by strong peripheral bundles and have an elastic component additional to the normal line tension. Albert et al. incorporate this feature by employing the tension elasticity model [216].

In this thesis it is shown how internal stress fibres can be added to the CPM by Albert and Schwarz. In collaboration with the group of Prof. Sanjay Kumar from the University of California Berkeley the model was used to describe a simple mechanism of stress fibre evolution in spreading cells.

This chapter starts with discussing important biological aspects of cell spreading in Section 5.2. Then the details of the here employed CPM are given in Section 5.3, where I also explain and discuss a different implementation of the tension elasticity model. In Section 5.5 the model is applied to understand the stress fibre evolution during spreading and finally the employed CPM is discussed in Section 5.6.

5.2 Biological Background

5.2.1 Cell Cytoskeleton and Migration

Cell migration is a complex process involving various biochemical and mechanical processes. It is made possible by the polymerization of actin, which forms bundled filaments as well as branched networks within the cell. These structures will be explained in this section and are shown in the cartoon in Figure 5.1. Forces can only lead to a forward movement if the cell can pull/push on the substrate. This is accomplished through so-called focal adhesions that also act as mechanosensors, such that cells react differently in soft and stiff extracellular matrices.

The general mechanism behind migration on a flat substrate is the polymerisation of actin at the front of the cell in a region called lamellipodium and depolymerisation and contraction at the rear of the cell. Additionally, focal adhesions are formed within the lamellipodium where the cell can exert forces. Aspects of the cell membrane mechanics also play a role, since it is easier to push the membrane forward if it is less tense [218, 219].

As mentioned above, actin forms structures with different mechanical properties and functions. There are dense networks like the cell cortex and the lamellipodium and contractile as well as non-contractile fibres. Actin monomers assemble into polar double stranded filaments which are the building blocks of most structures. The higher level structure is determined by the associated proteins; i.e. the protein Arp2/3 can induce branching points. Contractility relies on non-muscle myosin II forming mini-filaments which can pull in both directions and walk towards the barbed ends of actin filaments. A comprehensive review can be found in Ref. [217].

The lamellipodium spans across the whole front of the cell and consists of entangled branched actin networks. The main polymerisation factor for the assembly is the Arp2/3 complex which is activated via the WAVE complex [220, 221]. At the rear of the lamellipodium, myosin motors are present and help disassembling the network [222, 223]. Over all a retrograde flow develops [224] where actin polymerises at the front of the cell and flows towards the rear over time. This actin turnover makes the lamellipodium viscous on longer time scales.

Without anchoring to the substrate, the cell would not be able to move. The connection to the extra-cellular matrix is accomplished through focal adhesions which are also mechanosensitve structures [225, 226]. A schematic of their structure and stained microscopy images can be seen in Figure 5.2. Integrins (red in

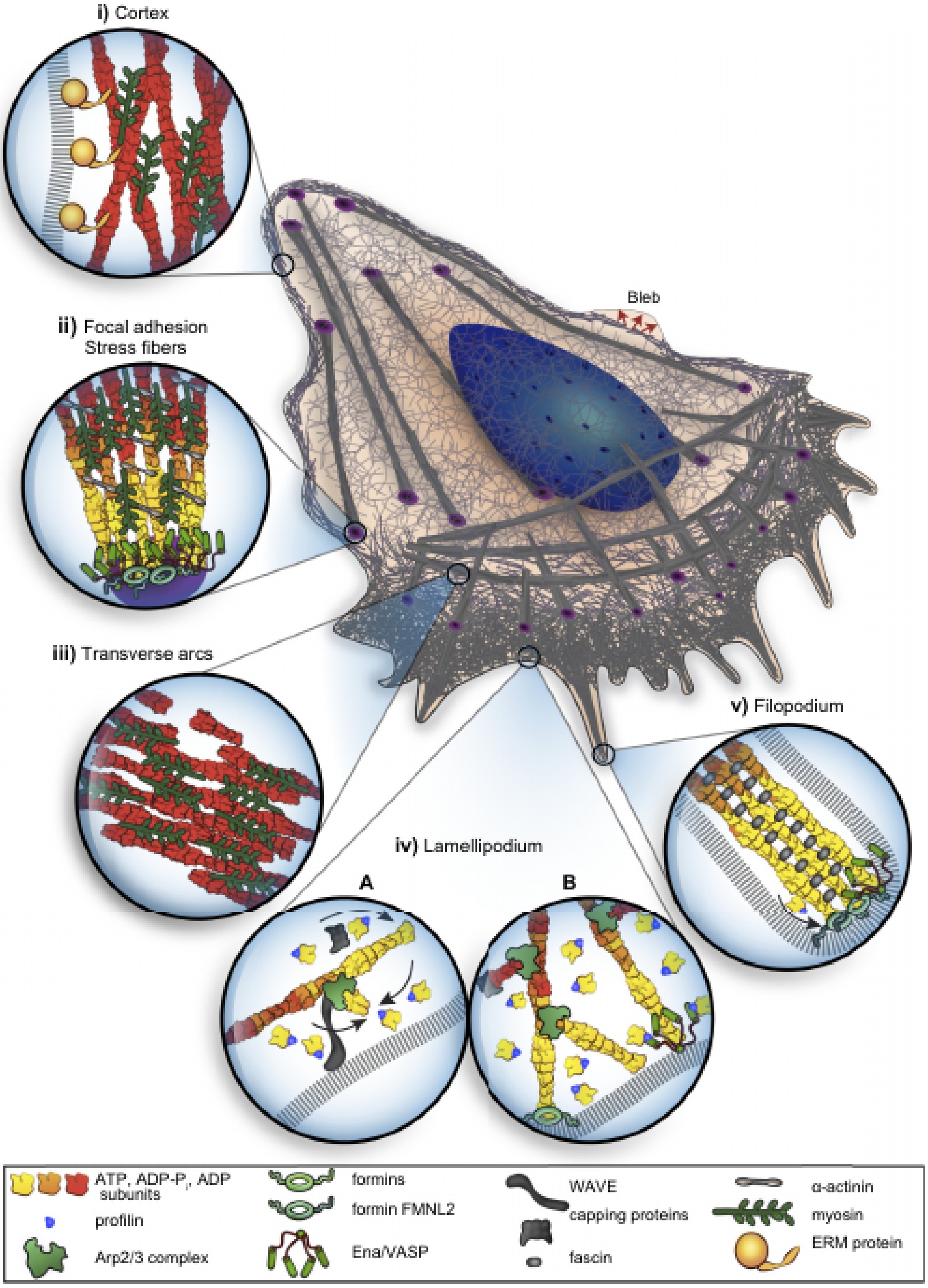

Figure 5.1: The graphic is adapted from Ref. [217]. A cartoon of a migrating cell (migration towards bottom-right) is shown, highlighting the different types of actin organisations inside the cell as indicated in the magnifications. For illustration purposes the upper part of the cell is not shown, such that the internal structure is visible. The blue oval in the middle is the cell nucleus.

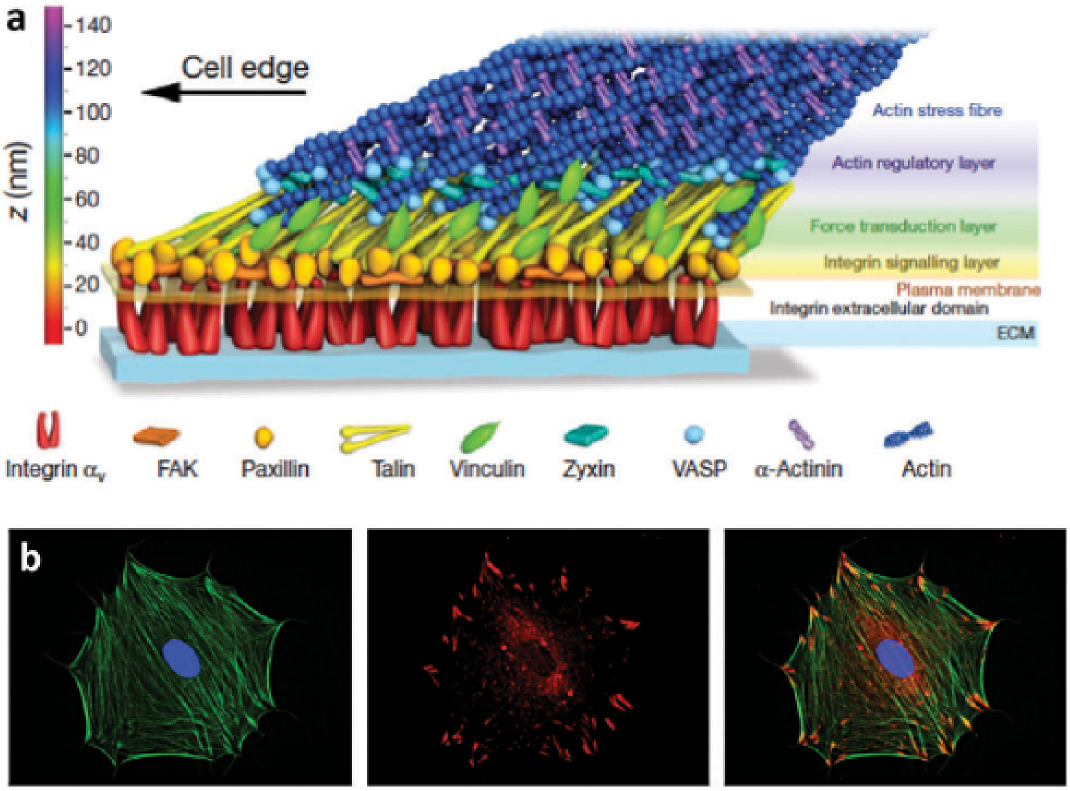

Figure 5.2: Graphic of integrins and focal adhesions form Ref. [230]. a) Cartoon of the structure of a focal adhesion. It is shown how integrins incorporated in the plasma membrane are connected to the actin stress fibre by proteins. b) The left image shows the stained actin cytoskeleton, in the middle image vinculin is stained and the right image is a superposition of the two.

Figure 5.2a) connect the structure through the plasma membrane to the extracellular matrix and several different proteins mediate the connection to stress fibres. For example, talin binds to the cytoplasmic domain of the β integrin subunit and unfolds upon the application of force such that binding affinities are changed. This conformational change also enables vinculin to bind to talin [227, 228]. In this way the cell reacts to mechanical signals since vinculin enhances the clustering of integrins. The assembly of focal adhesions is also force dependent. So-called nascent adhesions of approximately 100 nm diameter form first. Then forces produced from the retrograde flow are necessary for these to grow further and finally myosin IIA is needed for the transition to mature focal adhesions [229].

Another type of actin organisation within cells is the formation of bundles. Extending from the lamellipodium towards the front there are filopodia which are cross-linked equally oriented actin filaments. The cross-linking proteins are α-actinin, fimbrin, and fascin. As can be seen in Figure 5.1, the filopodia extend towards the front and enable the cell to sense its environment. By adding myosin to actin bundles composed of differently oriented filaments they become contractile, the so-called stress fibres [231]. In cells there are two main types, ventral stress fibres and transverse arcs. The ventral stress fibres are approximately aligned with the direction of motion and end at focal adhesions. These consist of equally

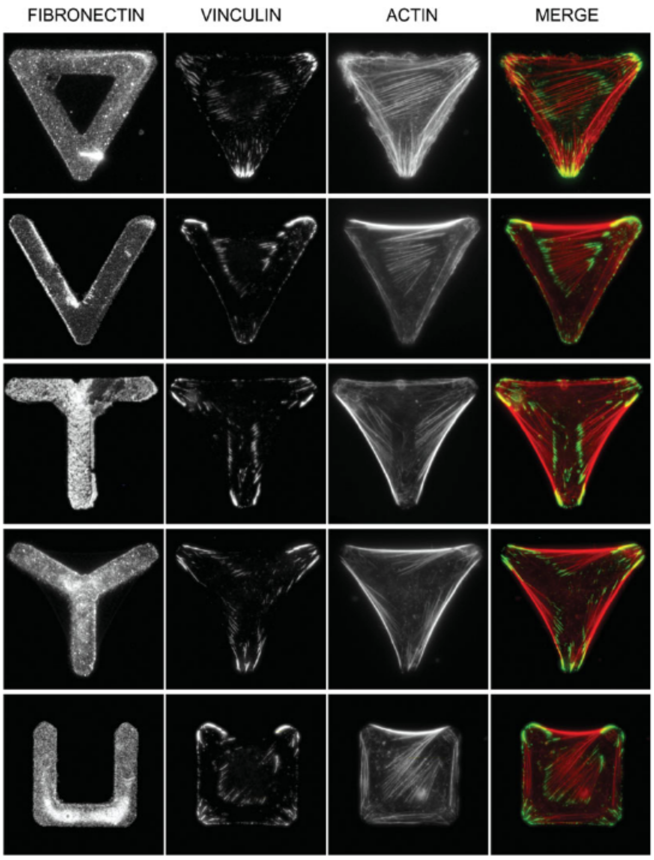

Figure 5.3: Each row shows a different fibronectin pattern and the triangle edge length is 46 µm. The second column shows the location of the focal adhesions through the labeling of vinculin, in the third row actin marks the location of stress fibres and in the fourth row a superposition of both can be seen. Images are taken from Thery et al. [13].

oriented actin filaments which are cross-linked by myosin II motors. Transverse arcs lie perpendicular to the direction of movement and are not attached to focal adhesions. They are assembled from the destructed actin network behind the lamellipodium [232]. Similar to the ventral stress fibres there are dorsal stress fibres which extend between the transverse arcs and the focal adhesions in the lamellipodium, but these do not contain myosin.

5.2.2 Micropatterns in Cell Experiments

Randomly moving cells are out-of-equilibrium systems and adopt very heterogeneous structures such that a detailed examination of internal architecture is difficult. In order to circumvent this problem the use of micropatterns was established. These are (in most cases) two dimensional prints of fibronectin, a material that cells can adhere to. Since the background is chosen such that cells cannot adhere, they spread in a predictable manner until the pattern is covered. Compare the images of Thery et al. [13] in Figure 5.3. In this very influential study Thery et al. described how non-adhesive areas can be covered by spanning thick actin cables across the region. They also observed a reproducible network of internal stress

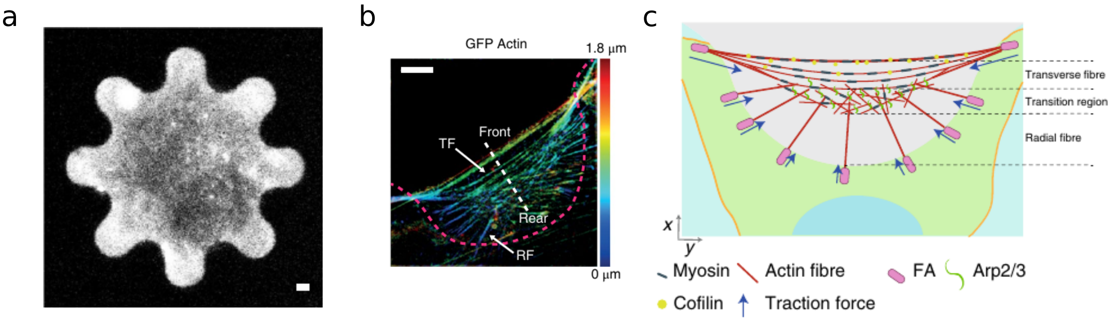

Figure 5.4: Chen et al. examined the internal structure of cells on micropatterns of alternating concave and convex regions. a) Examined fibronectin pattern. b) 3D live SIM image of a concave region. Radial fibres (RF) and transverse fibres (TF) are indicated. The colour code shows the height within the cell and the scale bar corresponds to 5 µm and the magenta line shows the edge of the pattern. c) Illustration of the underlying structure. The figure is adapted from Chen et al. [233].

fibres spanned between adhesive sites.

By employing micropatterns of alternating curvature along the edge, as can be seen in Figure 5.4a, Chen et al. examined the exact structure of the actin network above non-adhesive regions. Where the cells form protrusions at positive curvatures, the cell extends further outwards in negative curvature regions such that it spans the non-adhesive area with an actin edge-bundle. By this mechanism the curvature in the cell circumference is reduced. Surprisingly, they found an actin flow, which is directed towards the edge-bundle, opposite to the commonly known retrograde flow. The architecture in this region can be seen in Figure 5.4b and c, where the edge-bundle is located at the top.

The mechanical properties of stress fibres in these edge-bundles have also been investigated in much detail. After finding that stress fibres behave like viscoelastic cables tensed through actomyosin motors in cells adhered to a homogeneous substrate [234], Kassianidou et al. [235] also examined the mechanics of stress fibres in cells adhered to micropatterns. They were able to show, that the overall stress fibre network structure plays a very important role in the retraction dynamics. Hence, the connections to other fibres was found to dominate the viscous response during the retraction after laser ablation. Furthermore, it was confirmed that longer stress fibres dissipate more energy and are stiffer and more contractile.

When comparing these cells on micropatterns, one might notice that the invaginated arcs spanning non-adhesive areas always appear to be circular arcs with varying arc radii. Bischofs et al. [216] explained this by introducing the tension elasticity model. By incorporating surface tension, a line tension in the circumference and an elastic contribution from the edge-bundles, the model predicts circular arcs whose arc radius depends on the spanning distance. The relation was successfully shown to hold for many experimental data sets and is also employed in this thesis.

5.3 The Cellular Potts Model

A CPM is based on the Monte Carlo Method [236] and uses the Metropolis algorithm to sample the cell's phase space efficiently. The idea is that states are chosen with a weight according to the Boltzmann distribution, hence incorporating stochastic effects during time evolution. On average, the system will move towards the lowest energy state although it may get stuck in local minima.

Our CPM is implemented on a two-dimensional square lattice so that each lattice site can either belong to the cell or the surroundings. Additionally, lattice sites can be defined as adhesive, which makes it possible to implement underlying patterns. The Metropolis algorithm is used to simulate cell spreading by randomly trying to flip a lattice site at the cell periphery. If the flip reduces the value of the energy functional, it is accepted, otherwise the flip is accepted according to the Boltzmann factor $e^{-\Delta E/(k_B T)}$. The energy change is calculated from the system's Hamiltonian which is shown hereafter. Instead of counting single spin flips as time units, the concept of a Monte Carlo Sweep (MCSweep) is used. For this, the number of possible inversion sites N at the cell periphery is counted. One MCSweep then picks N sites along the cell periphery at random.

In principle the interactions between several cells on one common lattice can be treated but additional rules need to be implemented. Here, we only model one cell at a time and are not interested in cell-cell interactions.

5.3.1 Energy Functional

All aspects that are thought to be important for cell spreading on patterns need to be incorporated in the Hamiltonian. The real cell lives in a 3D environment, which is encountered for by imagining the 3rd dimension as an area reservoir so that a cell can spread out as long as it has not reached its maximal size. The Hamiltonian as introduced by Albert and Schwarz [14] consists of four terms corresponding to the main mechanisms regulating the spreading process:

$$H = \sigma A + \lambda_{\text{simple}} l + \sum_{arc\ i} \frac{EA}{2L_{0,i}} \left(L_i - L_{0,i}\right)^2 - \frac{W A_{\text{ref}}}{A_{\text{ref}} + A_{\text{ad}}} A_{\text{ad}}, \tag{5.1}$$

where the first term accounts for surface tension σ and hence scales linearly with the cell area A. The second term is the contribution due to simple line tension λ_{simple} which is proportional to the cell perimeter l. In addition to this simple line tension, we account for an extra elastic line tension present in free arcs, seen in the third term, and EA is the associated elastic modulus. L_i is the length of the invaginated contour and $L_{0,i}$ its resting length which we assume to be the spanning distance. The last term considers the adhesion energy due to the adhesive pattern, where A_{ad} is the adhered area. A_{ref} is the cell's reference area and W the adhesive energy density which reflects the number of available adhesion receptors.

5.3.2 Parameter Estimation

Depending on the cell type, the parameters have to be chosen slightly differently to reproduce the right cell behaviour. In Section 5.5 the case of U2OS cells spreading

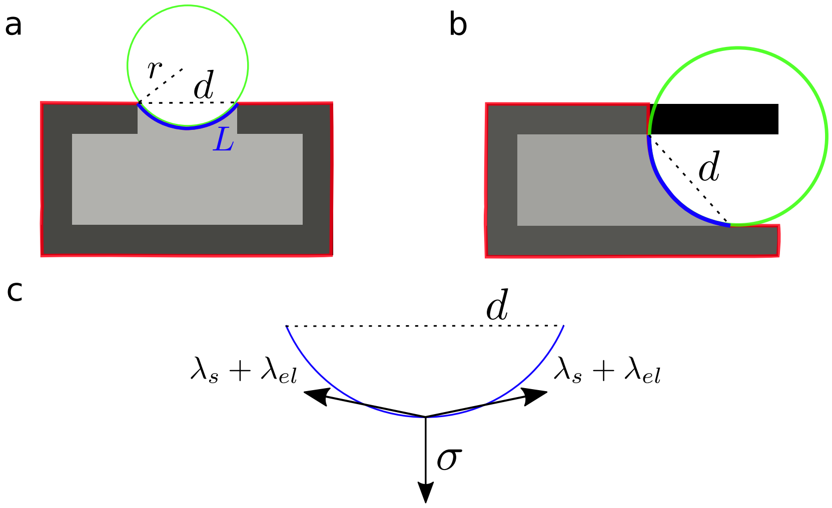

Figure 5.5: a and b) show schematics of micropatterns in black with a simulated cell (grey) spreading on them. The green circle indicates a fit to the free arc (blue) of the spreading cell. The spanning distance d is also indicated. c) The forces acting in a free arc are exemplified. The surface tension pulls the contour inward and the simple and elastic line tension pull it outwards.

on micropatterns will be discussed. The relevant parameters for these cells are already adopted here. In the experiments as well as the simulations two kind of patterns were used, the Top Pattern and the Side Pattern as shown in Figure 5.5a and b.

The surface tension should be of the order of 1 $\mathrm{nN\,\mu m^{-1}}$ and can vary between different cell types. Previous studies suggest $\sigma \approx 2\ \mathrm{nN\,\mu m^{-1}}$ for endothelial cells [237] and $\sigma \approx 0.7\ \mathrm{nN\,\mu m^{-1}}$ for epithelial cell sheets [238]. The simple line tension arises due to the actin cytoskeleton and hence should be $\lambda_{\text{simple}} \approx 10$ nN [225]. The value of the elastic modulus EA can be calculated assuming the tension elasticity model and measuring the radii of the cells' invaginated arcs. Finally, the adhesion strength depends on the number of adhesion receptors available to the cell. Previous estimates yield a value of $W = 20$ nN µm [239]. For our parameter set a value of $W = 10$ nN µm is sufficient for spreading.

5.3.3 Tension Elasticity

Additional to the simple line tension λ_{simple} that acts along the contour of the cell, we employ an elastic line tension, $\lambda_{\text{elastic}} = EA(L - L_0)/L_0$, acting in arcs which span non-adhesive areas (see blue arcs in Figure 5.5). This idea has been formulated within the tension-elasticity model (TEM) by Bischofs et al.[216] and the main difference to a simple tension model is that the arc radius now increases with spanning distance. The TEM leads to the following self-consistent equation for the arc radius R:

$$R = \frac{EA}{\sigma}\left(\frac{2R}{L_0}\arcsin\left(\frac{d}{2R}\right) - 1\right) + \frac{\lambda_{\text{simple}}}{\sigma}, \tag{5.2}$$

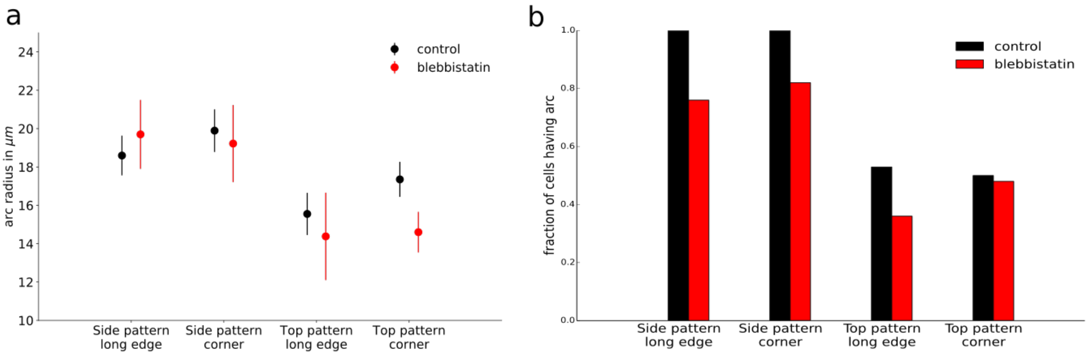

Figure 5.6: a) Measured arc radii for the two different patterns, sorted according to binding position. Black data shows the data for untreated cells and red data corresponds to blebbistatin treated cells. b) Fraction of cells for which an arc radius could be measured. The rest of the cells has a straight edge bundle which prevents invagination.

where EA is the one-dimensional elastic modulus of the edge bundle which has a contour length L and its rest contour length L_0 is assumed to be equal to the spanning distance d. Surface tension is denoted by σ.

Since this relation uniquely determines the arc radius through the three tension parameters EA, λ_{simple} and σ, we can calculate one of them when knowing the others. Since we only use one cell type here, we assume the surface and simple line tension to be equivalent in all cells ($\sigma = 0.7$ mN m^{-1} and $\lambda_{\text{simple}} = 7$ nN, unless otherwise stated) and determine the elastic modulus depending in the final arc radius of the cells on a given pattern.

We extracted the cells' final arc radii from the experimental spreading data and found these to be different for the Side and Top Patterns (see Figure 5.6a) with little difference between the binding positions. On average, the Side Pattern seems to result in a larger arc radius even after blebbistatin treatment (see red data points). However, we could only fit radii to about half of the cells on the Top Pattern because the other cells ended up with a strong edge bundle across the gap which was approximately straight. In Figure 5.6b the fraction of cells having a measurable invaginated arc is plotted and a clear reduction can be seen for the cells on the Top Pattern compared to the Side Pattern.

We propose that this difference originates within the geometry of the top-spacing pattern and the cells can be sorted into two types. The first type bridges the gap with a mostly straight fibre because the cell has to bridge a much larger gap which requires a stronger edge bundle. However, if this edge bundle breaks down before the end of the spreading process by forming very strong diagonal stress fibres, the final edge bundle will be weaker and result in stronger invaginated arcs. For the following calculations we only deal with type two which has a measurable arc radius.

Using formula (5.2) and the measured arc radii of 19.25 ± 0.76 μm and 16.45 ± 0.75 μm (Side and Top Pattern respectively) we calculate the elastic moduli to be $EA = 238 \pm 40$ nN and $EA = 118 \pm 26$ nN, respectively. Here we see that the cells on the Side Pattern have a considerably larger elastic modulus than the cells that have an invaginated arc on the Top Pattern. A similar trend can be confirmed for

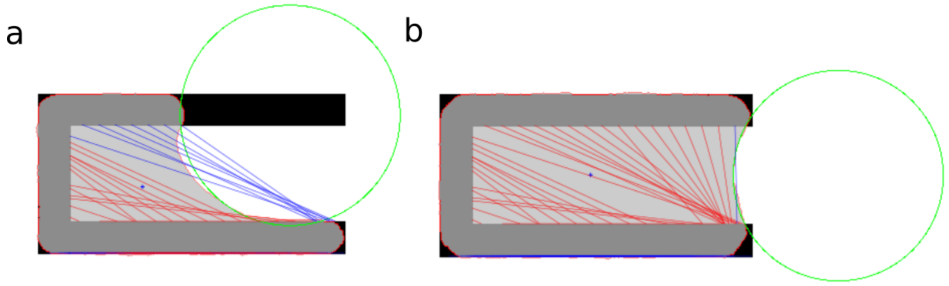

Figure 5.7: Example of the stress fibre deposition procedure. a) The cell is in the spreading process and does not cover the whole pattern yet. The red stress fibres lie within the cell and are thus recorded as proper stress fibres. The blue lines depict potential stress fibres which are not covered by the cell area yet. b) Once the cell has spread further, the previously blue lines, are now recorded as stress fibres.

blebbistatin treated cells.

To simulate cell spreading on the Side Pattern the choice of $EA = 238$ nN is the most plausible. For the Top Pattern the choice is not so clear because of the division in two different kinds of spreading events, the ones where the final edge bundle has a lower elastic modulus and the ones where a much larger modulus prevents a visible invagination of the bundle. Therefore, we choose the same modulus for cells on the Top Pattern as on the Side Pattern to be able to compare them more easily and avoid the unambiguity in spreading events on the Top Pattern.

5.3.4 Circumference and Arc Detection

To calculate the energy of a given configuration the cell perimeter needs to be known. To extract this quantity from the sites on the square lattice the marching square algorithm is used. This algorithm uses the local neighbourhood of each spin in order to define a smooth outline of the cell. The cell area is simply calculated from the number of occupied spins.

As part of the simulation, free arcs are treated in a special way and hence need to be detected during the simulation, this procedure works as follows: An algorithm walks along the contour of the cell until a potential arc starting position is found which is defined as a transition between an adhesive and non-adhesive site. From here the algorithm walks along the contour which lies above the non-adhesive area until another adhesive site is reached which then marks the end of the arc. In a final step, a circle is fitted to the defined arc so that the arc radius can be determined.

5.3.5 Stress Fibre Definition

The implementation of stress fibres originates in the idea that stress fibres are formed parallel to the lamellipodium in a periodic process. Hence, we integrate a rule that stress fibres are formed between two points that previously supported an arc spanning a non-adhesive area. However, a minimum distance is introduced that corresponds to the experimentally observed mean distance between two adjacent stress fibres. Before defining a specific stress fibre, the distance to the previously introduced stress fibre is checked and the stress fibre is only accepted if at least this minimum distance is fulfilled at the faster spreading side (see left and top leg in Figure 5.7). Furthermore, stress fibres are always introduced as straight lines but are only shown if completely covered by the cell body (red fibres in Figure 5.7, blue fibres are not covered by the cell yet in Figure 5.7a). Although stress fibres might be remodelled in the living cell, the model does not allow for changes after the fibres have been put down. The non-uniform distribution results from the stochastic nature of the CPM dynamics.

5.3.6 Fitting Parameters to Experimental Data

We use a minimization procedure based on the Nelder-Mead algorithm [240] (as implemented in SciPy) to fit the simulation parameters to the experimentally obtained data. As a quantitative comparison, we use the time evolution of the central point on the invaginated arc. Therefore, a distance measure can be calculated by evaluating the mean squared deviation between the two corresponding trajectories. The parameter fit is accomplished through the following steps: First, a suitable set of initial parameters is found by a coarse scan of the relevant parameter ranges. Then, the optimization procedure is started, which runs the CPM with the given initial parameters and uses the Nelder-Mead simplex algorithm to determine the next set of parameters according to the minimization of the distance measure. Finally, once the algorithm converges to the optimal parameter set, it stops. In principle, an additional parameter also scales the time of the simulation. However, this value must be fixed across all simulations to allow meaningful comparison of the extracted parameter values.

5.4 Treatment of Invaginated Arcs in the Model

5.4.1 Previously Implemented Method

The procedure described here was used in the model published by Albert et al. [14]. For the Monte Carlo procedure it is necessary to calculate the energy change upon inversion of an element. We already know that the energy functional depends on the cell area and circumference, such that the change in these quantities needs to be calculated. Since the area is calculated from the number of pixels, the change will be ±1. For the change in circumference all neighbouring sites need to be taken into account as well, which leads to a slightly more complicated procedure using the Marching Square algorithm.

Whenever the chosen border element lies on one of the declared elastic arcs, the change due to the TEM contribution also needs to be calculated. The arc energy depends on the difference between the arc length of the concave circular border and the spanning distance between the two anchor points. These quantities are calculated when the circle fitting algorithm is applied to the cell. Because of computational reasons, this is only done after every MCSweep.

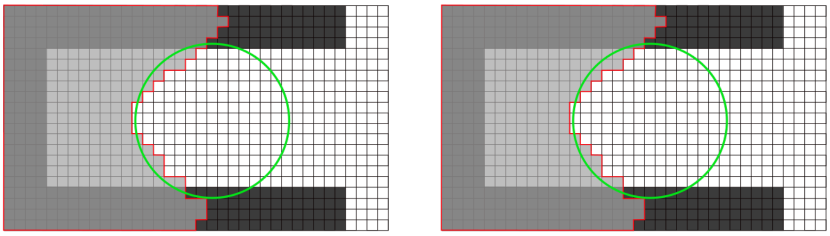

new circle should be fitted after site was inverted

reference circle is wrong because arc is not updated

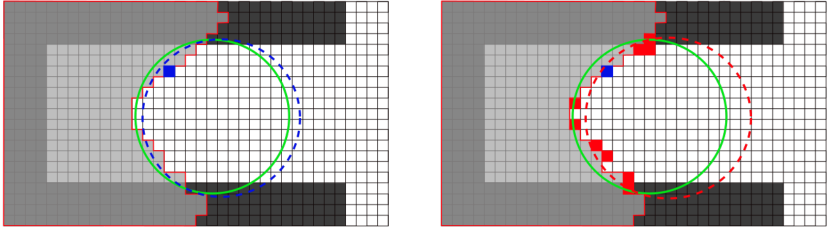

Figure 5.8: Cartoon showning the problems with the arc fitting procedure applied by Albert et al. [14]. The blue square in the bottom graphs is the one that is chosen to be inverted. The left column examplifies that it would be better if a new arc is fitted to the non-adhesive region. The right column shows the errors that occur by only fitting arcs every MCSweep.

When trying to invert an arc site, the already calculated change in circumference can only be caused by a change in the arc length of the specified arc. This means that we assume that the new arc length $L_{new} = L + \delta C$ and hence the change in elastic energy is calculated from δC.

Although this procedure, which will be called Circle Fitting Method (CFM) from here onwards, is computationally very efficient, there are a few drawbacks:

- During the spreading process the arc sometimes deviates from the circular form. Strictly speaking only the final configuration on the pattern is an equilibrium configuration and will produce a nearly perfect circular arc. Cell spreading is an active process which is driven through the strong adhesion to the micropattern. Therefore, the cell contour will deviate slightly from this configuration. The use of the CPM for this process can be justified because spreading of a biological cell is sufficiently slow.

- When a circle along the arc is inverted, the above procedure determines the new arc length from the previously fitted arc plus the change in circumference δC. However, this new length does not have a physical meaning. Rather, a new circle would have to be fitted to the updated region indicated by the blue circle in the left column in Figure 5.8.

- The problem from the last point is amplified because arcs are only fitted every MCSweep. Hence, the reference arc shape does not correspond to the present cell configuration, as can be seen in the right column in Figure 5.8.

A possible solution to this problem would be fitting a new circle every time the algorithm attempts inverting a site along an arc. However, this means that for an unsuccessful inversion, the site needs to be inverted again and the old arc data needs to be restored. I implemented a version of this suggested procedure but this attempt ran into a lot of problems, i.e. arcs always split into two if there is the chance because two short arcs are energetically preferable to one long arc. Therefore, I decided to implement another method, which is explained in the following section.

5.4.2 Newly Implemented Method

Instead of fitting a circular arc to invaginated regions, I test a method here which determines the actual contour length of the arc and uses this to calculate the TEM contribution to the energy change. This new method will be called Marching square Arc length Method (MSAM) from now on. The method is advantageous because it circumvents the above mentioned problems. Since now the arc length l_{arc} is the arc part of the actual circumference of the cell, it makes a lot of sense to use δC to calculate ΔE_{TEM}. The problem of only fitting arcs every MCSweep does not apply any more, since the actual arc length can be simply adjusted after a possible inversion.

To determine the arc length, a rectangular box is set around the arc (determined by the maximum and minimum position of the arc data in x and y-direction) and the contribution from all of these sites to the arc length is added up. Sites on the adhesive pattern and sites, that do not lie on the contour or a neighbouring position, have a zero contribution. Note, that for the circumference of the cell the whole lattice is scanned.

In most cases this method leads to larger arc length than the fitted circle contour because the cell edge lags behind the ideal circle and is more uneven than the analytically calculated equilibrium shape. The difference between the two arc length during spreading on the Side Pattern (all three initial binding positions) lies around 0.32 µm with a typical length of 16 µm. This is not a very large difference but Figure 5.9 shows that it has an impact on the spreading process. In the figure we see the area of the cell plotted as a function of MCSweeps for the three initial binding positions in the different plots. In each plot, the area increase is compared for the CFM (red), the MSAM (yellow) and simulations with just the simple line tension (green). Initially, spreading occurs faster with the elastic line tension. For the cells that have to turn around corners because they start on the long edge of the Side Pattern (middle and bottom plot), initial spreading is faster with the MSAM. The data was averaged over ten simulations.

The difference between the simple tension model and the TEM can be explained from the following observations. The TEM prefers less invaginated arcs because the energy depends on the difference between the arc length and the spanning distance, which is smaller for less concave arcs (see Figure 5.10). By increasing the spanning distance in Figure 5.10b the contribution from the TEM is made smaller but for this pattern geometry, a larger spanning distance also means a larger cell area (compare the difference between Figure 5.10a and b). Therefore, the TEM reaches larger areas earlier during the spreading. The TEM curve also fits better to experimental observations, as will be discussed in Section 5.5.2.

In Figure 5.10b another reason can be seen why the MSAM is more accurate. The green circle, which is fitted between the two anchoring points, touches the

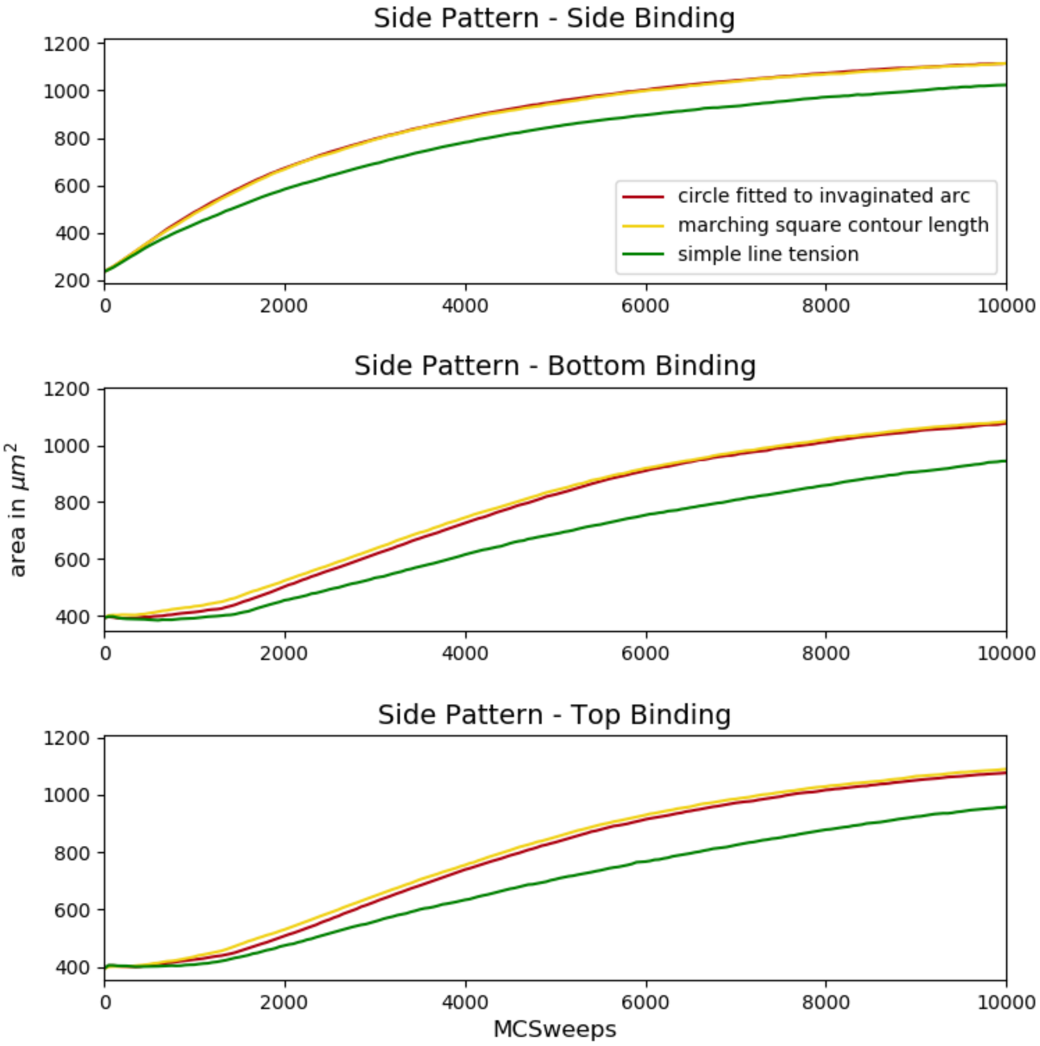

Figure 5.9: Cell area simulated with different energy functionals is shown. The top, middle and bottom correspond to different starting configurations, where the cell starts as an ellipse on the left, bottom and top edge of the Side Pattern (see Figure 5.5b), respectively. The red lines correspond to the previously introduced method where a circle is fitted to each arc and the yellow lines correspond to the newly implemented method which calculates the actual arc length. All data points are averaged over 10 equivalent simulations.

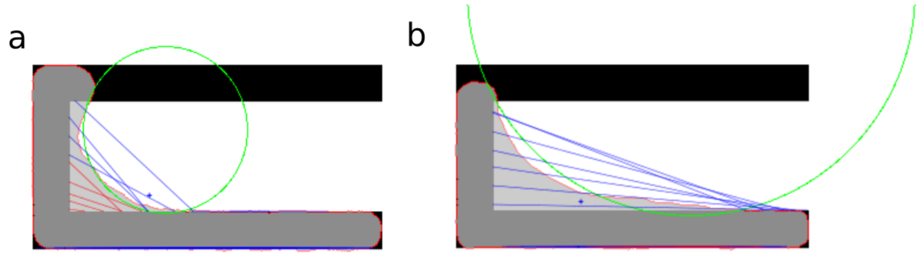

Figure 5.10: a) A cell spreading on the Side Pattern just employing simple line tension without any elastic contributions. b) Here, an elastic contribution is added for each invaginated arc, where the arc length is calculated by fitted circular arc to the invaginated cell contour.

adhesive pattern region. In this specific geometry a circular arc is not possible and using the actual arc contour length is a much better choice. From the data in Figure 5.9 we saw that using the marching square contour length speeds up the area increase even more than using a circle fitted to the invaginated arc.

5.4.3 Energy Contributions During Spreading

To examine the differences between the two TEM methods more closely, I extracted the contributions to the accepted energy changes during the Monte Carlo simulation (a site inversion is always accepted if the energy change is negative and with probability $e^{-\Delta E/(k_B T)}$ if the energy change is positive). For this, the energy changes over 50 MCSweeps were added up and extracted from the simulation. This enables us to see, which part of the Hamiltonian drives the spreading process most in each time interval during the spreading process.

In Figure 5.11 the energy changes during simulations using the arc-fitting-method are shown, were the data points are averaged over 10 independent simulations. The three plots show the three possible initial binding positions on the Side Pattern; note that the bottom and top binding are equivalent by symmetry.

Let us first discuss the side binding plot which describes the case of a cell that does not have to turn corners, but spreads evenly from the left to the right. Here we see that the total energy (black points) starts off in the negative regime and asymptotically approaches an averaged energy change of zero. This means that the cell initially spreads very quickly in a directed manner and then slowly approaches its final shape. The cell only reaches its final configuration at the vertical dashed line. As the cell approaches this point, the gain of negative energy changes becomes less strong in magnitude and more positive energy changes are accepted such that on average the energy change is zero. The reason for this is, that the cell approaches its equilibrium configuration and a single site inversion does not contribute as much energy any more. In the plot we can also see the different energy contributions. The changes due to simple line and surface tension are mostly positive or close to zero, whereas adhesion and elastic line tension are mostly negative which shows that these two drive the spreading. The elastic line tension (red), which is calculated with the circle fitting procedure, first increases in magnitude and then approaches zero again. During the initial period the arc

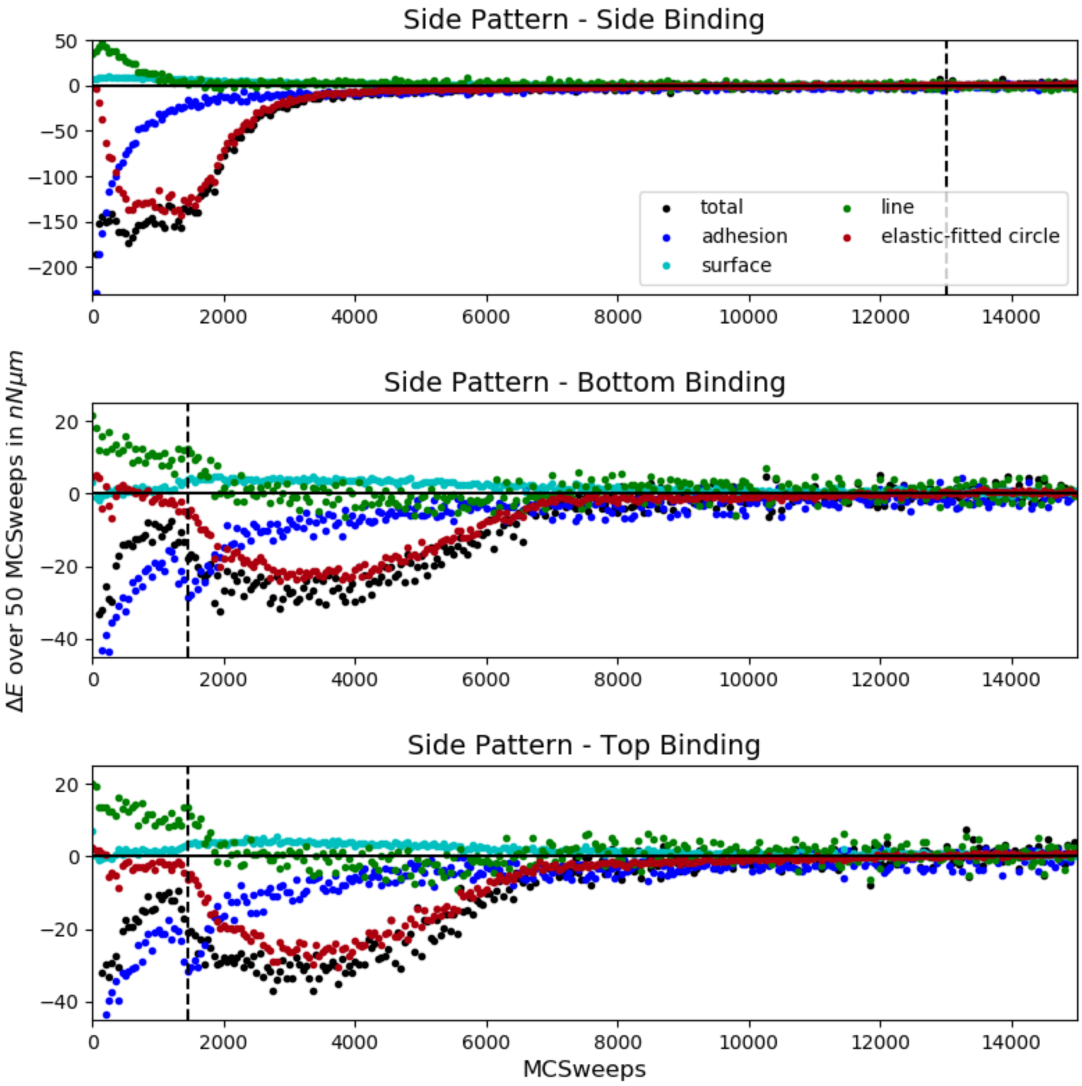

Figure 5.11: Accepted energy changes during the previously developed CPM simulation of a cell on the Side Pattern (see Figure 5.5b) are shown. Each point in the plot corresponds to the sum over 50 accepted MCSweeps. The top, middle and bottom correspond to different starting configurations, where the cell starts as an ellipse on the left, bottom and top edge of the Side Pattern, respectively. The total energy is shown in black, whereas the other colors depict the different energy contributions as indicated in the legend. All data points are averaged over ten equivalent simulations. The vertical lines depict specific configurations during the spreading process; in the top plot, the line indicates that the cell has reached its final configuration that covers the whole pattern. In the other two plots, the lines show, when the cell has reached the opposite (second) corner of the pattern.

first has to form properly, then the elastic energy change is largest, as the contour approaches the optimal arc shape. Once this configuration is reached, the contour moves forwards as a whole entity and hence its energy contribution does not change much any more.

Now we consider the initial bottom and top binding. Here the vertical dashed line indicates when the cell has reached the opposite corner from its starting position; i.e. when the cell starting at the bottom has reached the top left corner of the pattern. In contrast to the total energy of the previously discussed side binding cell, these total energies have a peak just before reaching the corner, but overall also approach zero. The reason for this peak can be identified as the contribution from the adhesion energy, as that energy jumps down at the corner. The reason for that is of geometric nature, because the outer part of the corner offers some additional adhesive area to cover. When considering the elastic contribution, we see that it only starts to matter much after turning the corner. From there onwards the curve shape is similar to the one of the initially side binding cell, but more spread out and weaker in magnitude.

If we now jump to Figure 5.12, a similar plot can be seen which is based on simulations using the newly implemented method of finding the actual arc length with the Marching Square algorithm. The new elastic contribution is shown in yellow and the red empty circles show the previously calculated energy change from the CFM as comparison. Overall, the energy change contributions behave very similar to the ones discussed for Figure 5.11 but the magnitude of the elastic contribution is now larger for the main spreading phase in all three cases. This agrees with the observation in Figure 5.9 that the area increases quicker when the new MSAM is used.

Overall it can be said that the two implementations of the TEM produce qualitatively similar results but the spreading rate is affected slightly. When comparing to experimental results, both methods would be suited well since the difference is a lot smaller than the variations in experimental data. However, the MSAM is physically more accurate. Nevertheless, the old circle-fitting method is used in the remainder of this chapter, since this model has been previously published and approved.

5.5 Results on Stress Fibre Organisation

The CPM described in the previous section is applied to U2OS (Human Bone Osteosarcoma Epithelial Cells) red fluorescent protein (RFP)-LifeAct cells spreading on fibronectin micropatterns, in order to understand the mechanical properties underlying the spreading process better. All experiments done for this work were conducted by Elena Kassianidou in the Kumar Laboratory in the Department of Bioengineering at the University of California. The image analysis on the experimental data was done by Dimitri Probst from the Theoretical Biophysics group of Prof. Ulrich Schwarz and the simulations and their analysis was done by myself. The findings of this collaboration were published in Cell Reports; "Extracellular Matrix Geometry and Initial Adhesive Position Determine Stress Fiber Network Organization during Cell Spreading" [29].

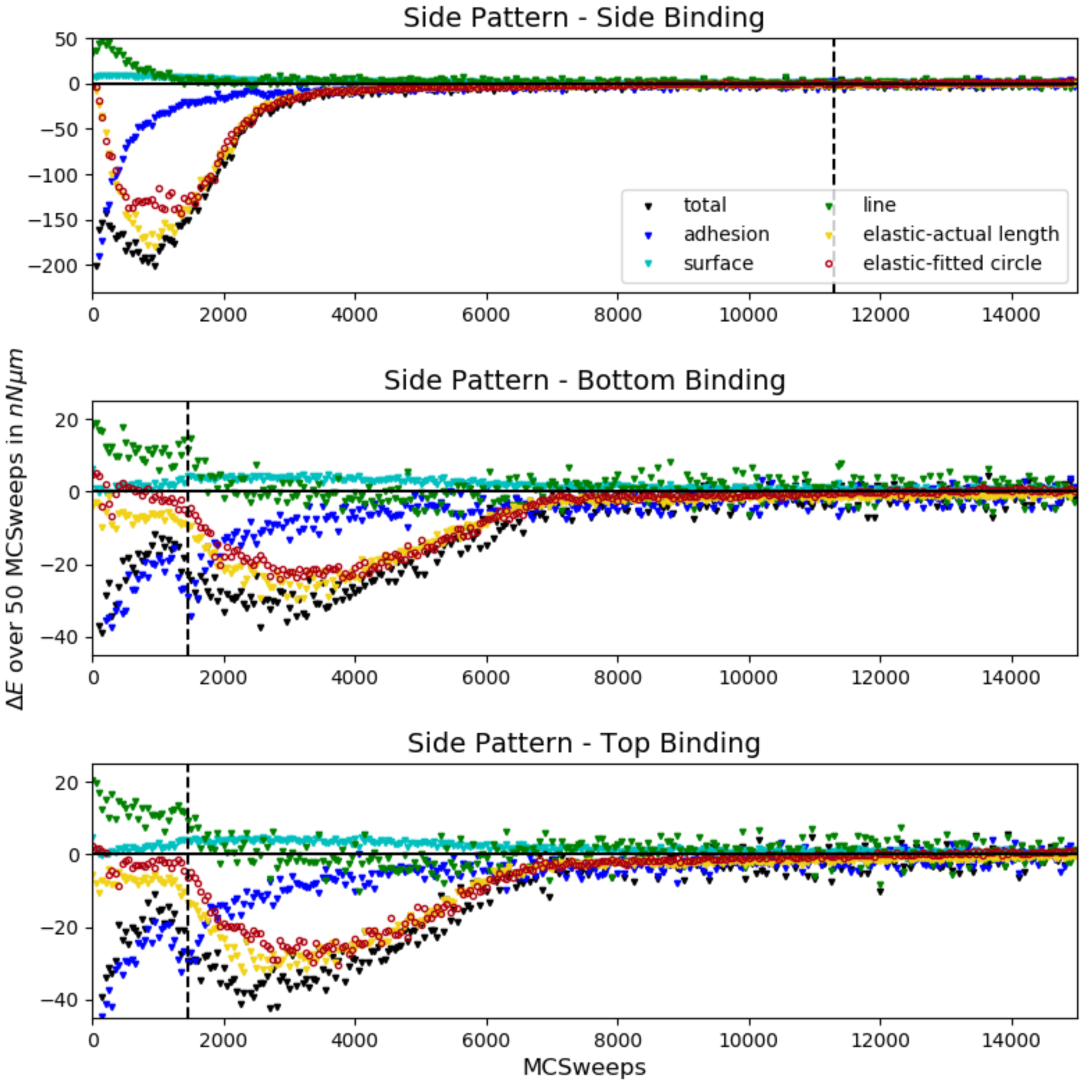

Figure 5.12: Accepted energy changes during a CPM simulation with the newly implemented arc detection are plotted for the Side Pattern. A detailed description of the plot is given in the caption of Figure 5.11. The yellow data points show the contribution from the new method, whereas the empty red circles show the previous method.

The main focus of this section lies on the stress fibre architecture inside the cells and how it depends on the pattern geometry and spreading process. The CPM with internal stress fibres is applied and their spatio-temporal architecture compared to the experimental results. I also show that by fitting simulation parameters to the experimental data, alterations in mechanical parameters of the cell can be predicted.

5.5.1 Details on Experimental Data

For the experiments two rectangular patterns of size 48×25 µm were designed. A 15 µm gap was left either at the top or at the side of the pattern as can be seen in Figure 5.13. These are called the Top Pattern and Side Pattern henceforth. The pattern area was coated with fibronectin which the cells can adhere to and will spread on after seeding. U2OS cells were used in this study because they are known to adhere well, spread fast and show clear stress fibres. After the cells sedimented from solution, the spreading process was captured by time-lapse epifluorescence imaging to visualize the actin dynamics and hence the stress fibres (see Figure 5.13a and b). We distinguished between initial binding to the short edge or the long edge.

There are two types of motion during the spreading process; the cells spread along the fibronectin line or they turn around corners which requires spanning across the non-adhesive area in the middle of the pattern. When spanning the non-adhesive area, stress fibres are put down and build up a network throughout the cell. At the advancing front the cell spans a peripheral stress fibre across the non-adhesive gap. It has one lamellipodium at each end which lies on a pattern leg. The presence of the lamellipodium was confirmed by differential interference contrast and epifluorescence microscopy.

5.5.2 Comparing Area Increase

In the CPM simulations the initial shape of the cells is chosen as ellipses covering one side of the pattern to mimic the experiments. The parameters of the CPM have to be adapted to the cell type under consideration as described earlier [241]. One important parameter is the adhesion strength, which determines the speed and ability of cells to spread on the micropatterns. Here, we choose the adhesive energy to be just strong enough to allow spreading ($W = 10$ nN µm and $A_0 = 1200$ µm^2). The cell shape during spreading is determined by a balance between this adhesive energy and tension terms, in particular the surface tension, the simple line tension and the elastic line tension. Some time points from the simulations can be seen in Figure 5.13d and e.

The surface tension represents cortical contractility over the whole surface and was previously estimated to be approximately $\sigma = 0.7$ mN m^{-1} for keratinocytes [238]. The simple line tension represents the tension along the cell periphery and, similar to the surface tension, is expected to be generated primarily by non-muscle myosin II motors. The simple line tension is also the main determinant of traction force at focal adhesions pinning the contour of strongly adhesive cells between inward curved peripheral stress fibres, which typically is of the

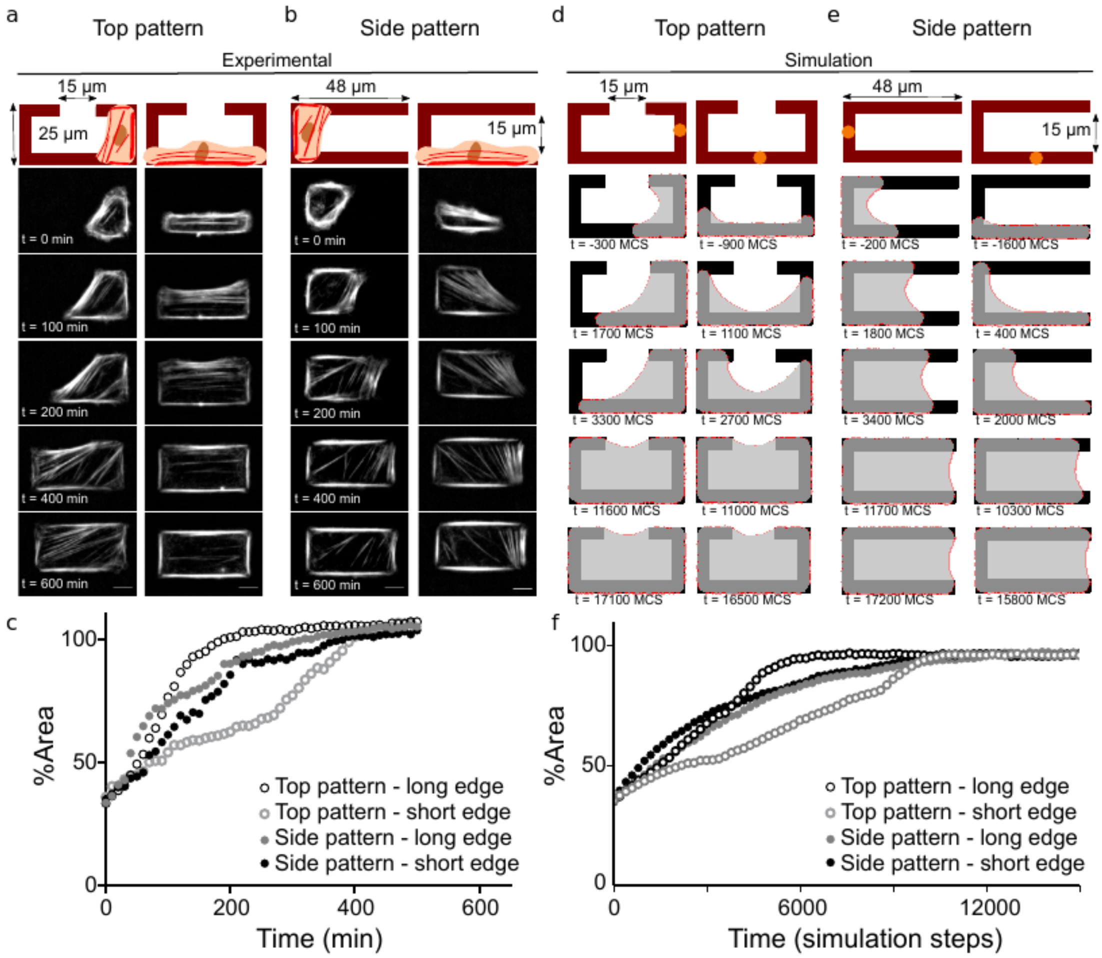

Figure 5.13: a and b) Schematic of Top Pattern and Side Pattern respectively. Dark red represents the region with fibronectin. Representative images of U2OS RFP-LifeAct cells spreading on each pattern initially adhering to either the short edge (left) or long edge (right) of each pattern at different time points are shown below. Scale bars correspond to 10 mm. c) Spreading kinetics for cells shown in a and b, expressed as the percentage of the final area at each time point. d and e) CPM simulation of a cell adhered to and spread on Top Pattern or Side Pattern respectively. f) Simulations of cell area over time as cells adhere to and spread on each pattern.

order of a few nanonewtons [237]. For these simulations, we chose the simple line tension as $\lambda_s = 7$ nN. The elastic line tension represents additional forces in the cell periphery generated by actin cross-linkers such as α-actinin that are stretched in peripheral stress fibres. The corresponding elastic modulus ($EA = 238$ nN) is estimated by applying the tension-elasticity model described in Section 5.3.3 and by fitting circles to the experimental cell images.

In order to validate the CPM we compared the trajectories of area increase from the experiments and the simulations and plotted these in Figure 5.13c and f. All simulations were averaged over 100 spreading events for each binding position on each pattern. For the Top Pattern, we observed qualitatively similar trends between the CPM and the experimentally obtained data (open circles); in particular, the spreading of cells that initially adhered to the long edge was much faster than for cells that initially adhered to the short edge. For the Side Patterns, the differences between the spreading kinetics of cells adhered to either the short or long edge were small, both experimentally and computationally (filled circles). The simulation captures a delay in spreading at the first corner, but not a slowdown at the second corner. Overall, the good agreement between experiments and model suggests that the interplay between the gain in cellular adhesion energy and tension is sufficient to explain the global dynamics of cell spreading onto these patterns. In our experimental system cells always exhibited round arcs during spreading, suggesting that cell shape is determined mainly by the mechanical equilibrium between cortical and peripheral tensions at each time point. Further, this implies that contractility is the main determinant of spreading kinetics for cells with concave shapes bridging adhesive gaps, as assumed in the CPM. This is in contrast to cells spreading on uniformly coated ECM substrates, where actin polymerisation and formation of many adhesions over a broad front lead to convex shapes [232, 242].

5.5.3 Comparing Stress Fibre Orientation

For the next step we wanted to examine the stress fibre architecture inside the spreading cells. The experimental data is shown in Figure 5.14 where the orientations were determined using the OrientationJ Distribution plug-in in ImageJ. To better align the experimental data of cells that spread on different timescales, we introduced three time points for each pattern depending on its geometry, as can be seen on the left in Figure 5.14. The experimental data shows a clear change in orientations in the cells that have to turn corners and a stable distribution in the other cases.

In order to understand the stress fibre formation process better, we generated similar data with the CPM. Internal stress fibres were introduced into the CPM as straight lines between two focal adhesions that anchor an arc above the non-adhesive areas. They were defined to appear as soon as they laid completely within the cell body. This encapsulates the idea that internal stress fibres are formed as transverse arcs behind the advancing front and later straighten due to non-muscle myosin II contractility and surface anchorage. We incorporated a minimum distance between stress fibres at the faster-spreading side of the cell, as suggested by our quantitative image analysis (see Figure 5.15). Note that according to these sim-

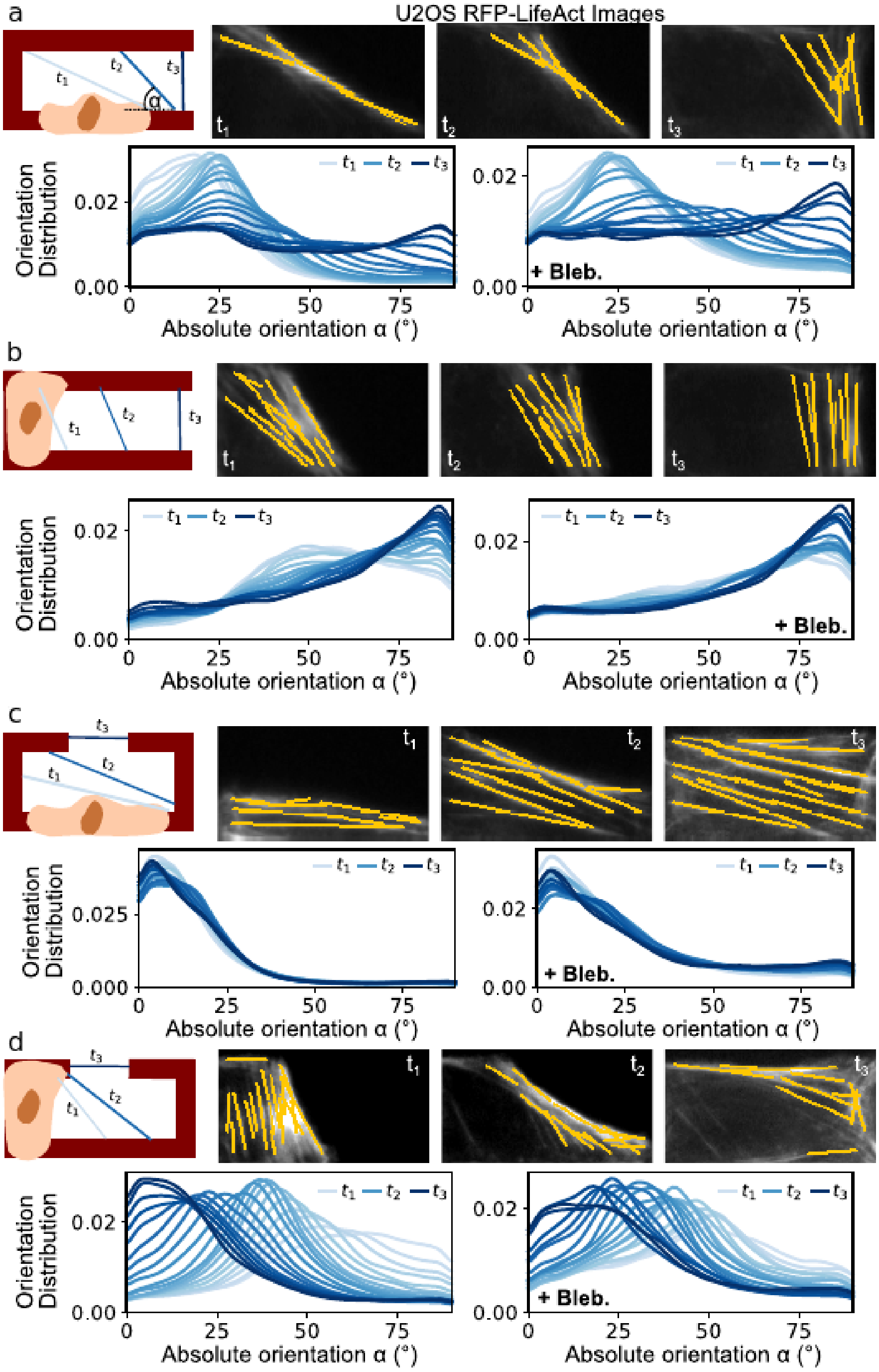

Figure 5.14: Top row of each panel: schematic showing the time points used to normalize individual cells. a and b) illustrate adhesion onto a Side Pattern at the long edge and short edge, respectively. c and d) illustrate adhesion onto a Top Pattern at the long edge and short edge, respectively. Snapshots show the typical stress fibre architecture, with highlighted stress fibres at the given time points as given by FilamentSensor. Bottom row of each panel: mean distribution of stress fibre orientations for naive U2OS RFP-LifeAct and blebbistatin-treated U2OS RFP-LifeAct (+ Bleb.) (n = 33, 32, 17 and 56 cells; n = 17, 14, 11 and 23 +Bleb cells). This Figure was produced by all authors for Ref. [29].

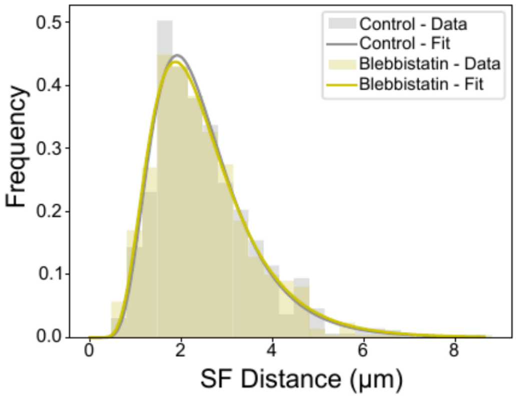

Figure 5.15: The spatial distances between stress fibres follow a log-normal distribution with mean 2.5 ± 1.0 mm for naive U2OS cells and 2.5 ± 1.1 mm for blebbistatin-treated cells. This Figure was produced for Ref. [29].

ple rules, internal stress fibres have no influence on the spreading process, although the underlying feedback processes are contained in the experimental observation of a typical distance between subsequent stress fibres. With this simple ansatz, we are able to predict the experimentally observed distributions (Figure 5.14). The distributions from the simulations were constructed taking CPM data from different regions of the pattern according to the benchmark times shown in the left column in Figure 5.16. Early stress fibres formed during the initial spreading phase (t_1) are highlighted in light blue and later stress fibres formed during t_2 and t_3 are highlighted in darker shades of blue.

We found that cells initially adhering to the long edges of the Side Pattern had an initial stress fibre configuration that peaked at 20° (light blue stress fibres), and as the spreading continued, the stress fibre configuration (darker shades of blue) switched to 90°, which is vertical to the long edge (Figure 5.16a). However, cells adhering to the short edge of the Side Pattern exhibited vertical stress fibre configurations throughout the spreading process (Figure 5.16b). For the Top Pattern, cells adhering to the long edge exhibited an initial stress fibre configuration peaking at 15° (light blue), and as the spreading process continued, the configuration of most stress fibres converged to 0°, which is horizontal to the long edge (Figure 5.16c, darker shades of blue). It should be noted that in the simulation, a second peak appears at 30°, which is not observed experimentally. We hypothesize that this is because most simulated cells undergo a symmetry break during spreading and reach one free corner of the pattern before the other. Intermediate stress fibres with a diagonal orientation are therefore incorporated between the newly occupied corner and a point along the long edge. Finally, cells initially adhered to the short edge of the Top Pattern showed a vertical initial stress fibre configuration, and with increasing time, the stress fibre configuration first approached a diagonal and then a horizontal configuration (Figure 5.16d). The superposition of stress fibre distributions onto our earlier CPM simulations of spreading cells illustrates that stress fibres track the advancing front and store a memory of the turning process affected by the combination of pattern geometry and initial position. Overall, we conclude that a simple CPM for cell shape dynamics augmented

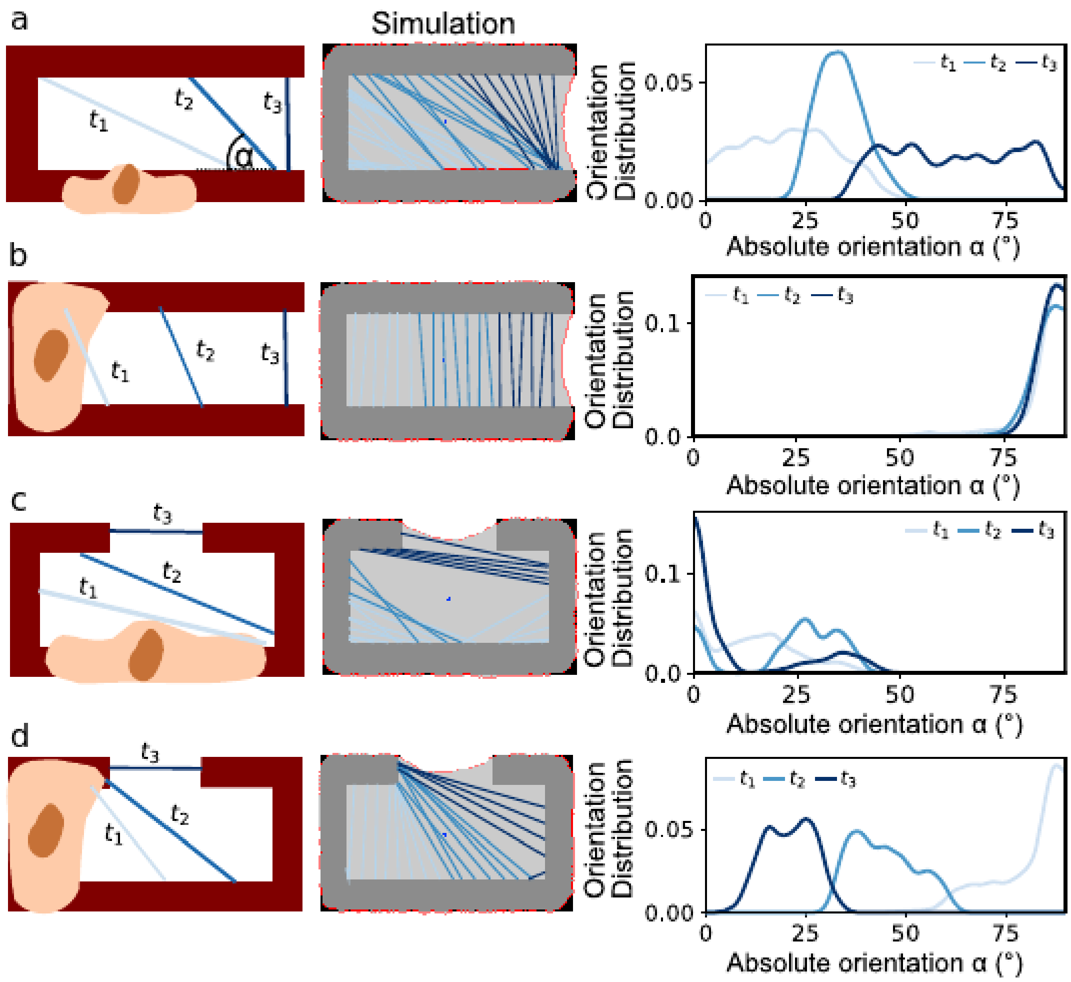

Figure 5.16: The first and second rows illustrate adhesion onto a Side Pattern at a) the long edge and b) the short edge. The third and fourth rows illustrate adhesion onto a Top Pattern for c) initial binding at the long edge and d) the short edge. Left column: schematic showing the time points used to normalize individual cells adhered to the short or long edge of each pattern to allow for comparisons to be made. t_1 (light blue) represents the initial time point, t_2 (blue) is an intermediate time point, and t_3 (dark blue) is the final time point at which the cell has spread fully on the pattern. Center column: simulated stress fibre architecture using a modified CPM with color-coded stress fibres, using light blue for time point t_1 and dark blue for time point t_3. Right column: simulated mean distribution of stress fibre orientations.

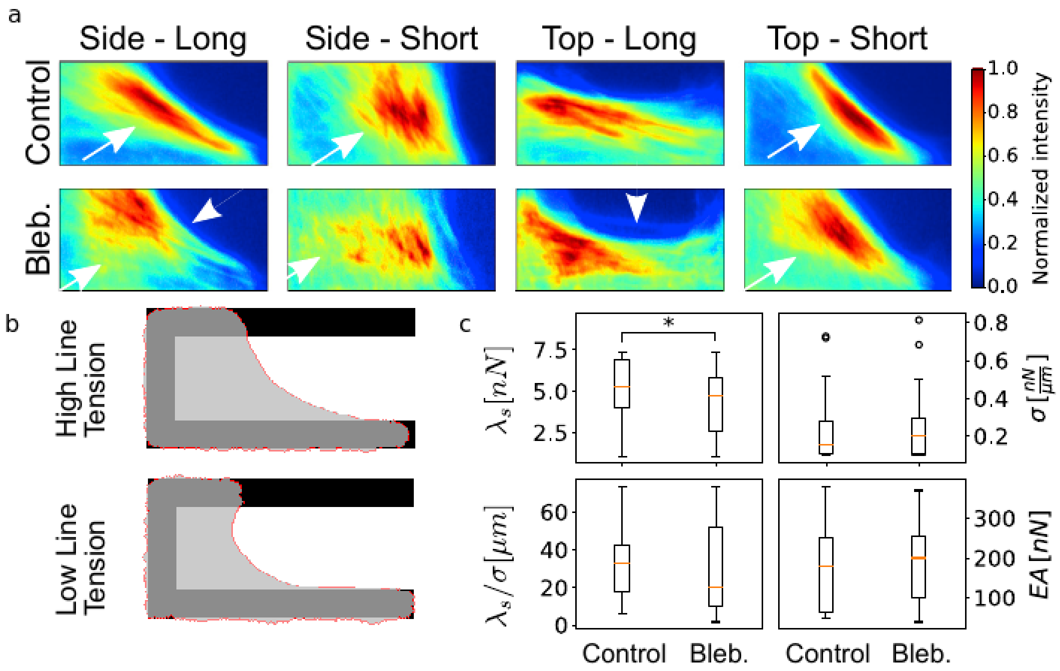

Figure 5.17: a) Average intensities of naive or blebbistatin-treated U2OS cells spreading on each pattern with different initial adhesive positions (intensities of $n = 33, 32, 17$, and 56 naive cells and $n = 17, 14, 11$, and 23 blebbistatin-treated cells). White arrowheads point to the arc of the peripheral stress fibre, whereas white arrows point to the confinement of the stress fibre network relative to the peripheral stress fibre. b) Snapshots from CPM simulations of one cell with higher line tension ($\lambda = 6$ nN, $\sigma = 0.2$ nN mm^{-1}, and $EA = 300$ nN) at the top and lower line tension ($\lambda = 3$ nN, $\sigma = 0.2$ nN mm^{-1}, and $EA = 100$ nN) at the bottom. c) Comparison of the line tension λ, surface tension σ, and elastic rigidity EA of control and blebbistatin-treated cells. The box represents the 25th and 75th percentiles; whiskers extend from the first datum $> Q1-1.5IQR$ to the last datum $< Q3+1.5IQR$, with $Q1$ and $Q3$ being the first and third quartiles and IQR being the interquartile range.

with a simple rule for geometrically defined formation of stress fibres, based on experimental observations, can robustly predict stress fibre orientations observed during cell spreading.

5.5.4 Blebbistatin Effects

To qualitatively visualize the average effect of blebbistatin compared to control cells, we overlaid the stress fibre network architecture of all of the analysed cells at time point t_2. The average stress fibre intensity of blebbistatin-treated cells spreading on the Side Pattern (Figure 5.17a) exhibited a more invaginated arc than control cells (Figure 5.17a, white arrowhead), which is in agreement with earlier results [216]. Moreover, the stress fibre network was not confined to the spreading edge as tightly as in control cells (white arrows). Similarly, the average stress fibre intensity of blebbistatin-treated cells spreading on the Top Pattern also exhibited increased curvature (white arrows in Figure 5.17a). Specifically, we observed a rearrangement of stress fibres to favour shorter stress fibres for cells bound on the long edge of the Top Pattern.

We next used the CPM to arrive at a quantitative characterization of the effects of blebbistatin treatment. To this end, we used a minimization procedure to determine a set of parameter values for each experimentally obtained trajectory. By calculating the deviation between the spatio-temporal evolution of the cellular envelope of experimentally recorded cells and a series of simulated cells, we were able to determine stresses and elastic moduli for each cell and compare control versus blebbistatin-treated cells. Overall, we found that our mild blebbistatin treatment resulted in a significantly lower line tension, but it did not influence the surface tension or the rigidity of the free arcs (Figure 5.17b and c). To visualize the effects of lower line tension, we ran simulations with varying line tension parameters (Figure 5.17b). By shifting to low values, we observed that the simulated free arc showed more pronounced curvature, which was also observed in individual blebbistatin-treated U2OS cells during spreading. Furthermore, the contour appeared more uneven, which is due to stochastic effects in the model. Overall, our analysis confirms that the low dose of blebbistatin used in these experiments leads to cells that exhibit a lower line tension (NMMII contractility in peripheral stress fibres), with little to no significant effects on the surface tension (NMMII contractility in the cortex).

5.6 Disscussion of Modelling Cell Spreading

I started by discussing the biological background of cell spreading and continued by describing how this process can be modelled on a coarse grained scale in a CPM. The microscopic components of the cell only appear in the various tension and adhesion parameters. Nevertheless, it could be shown that such a model captures the experimental behaviour of a cell on micropatterns well which means that the most relevant physical principles are captured within the model.

We further saw that the TEM is necessary to describe cells with strong peripheral stress fibres as cells on micropatterns. The elastic contribution was shown to be necessary for the cell to quickly cover a large area. I compared to methods for implementing the TEM, where the method implemented by Albert et al. [14] computes the arc contour length by fitting a circle to the invaginated arc and my method calculates the actual length of the contour between the two attachment points. Both methods were shown to produce similar results, whereas the MSAM produces longer arc contours and hence energy changes of a slightly higher magnitude. This leads to a small advantage in area increase when the cell has to turn around corners. Although the MSAM seem physically more plausible, the difference between the two methods is too small to decide, which one is more suitable to describe experimental cell spreading data.

Finally, the stress fibre architecture was examined in the last section. I was able to show, that the configuration could be explained by a simple model which introduces stress fibres parallel to the advancing cell front. An average spacing between stress fibres of 2.5 µm was found experimentally and the spreading history was shown to determine the stress fibre architecture at least for some time, since stress fibres were shown to have a half life of 50 minutes on average by our experimental collaborators.

By fitting the CPM to the experimental data, I also showed that blebbistatin treatment results in a reduction in line tension while leaving the other parameters mostly unaffected. Therefore, blebbistatin is found to reduce the NMMII contractility in peripheral arcs most. This is in agreement with earlier results that showed that peripheral stress fibres are more susceptible to blebbistatin treatment than the cell cortex [216].

Overall one can say that the CPM has been shown to describe the cell shape as well as the stress fibre architecture of cells on micropatterns well. Besides reproducing the experimental data, the CPM was able to explain the changes induced by a mild blebbistatin treatment.

Chapter 6

Conclusion and Outlook

For this thesis, I applied biophysical models in order to understand the malaria-induced modifications of the RBC better. As these models span several scales, the whole-cell properties can be related to changes on the molecular level. A deeper understanding of the processes used by the parasite to modify the RBC might eventually lead to a treatment for this devastating disease.

The modelling approaches used in this thesis were chosen to cover the main physical aspects of cell properties. Firstly, the fluctuations of the RBC membrane were examined by treating the Helfrich Hamiltonian numerically. Secondly, the interactions between parasite and host proteins were considered in a reaction-diffusion model and the distribution of PfEMP1 molecules on knobs was calculated. Thirdly, I aimed at employing a model for the RBC in blood flow and finally, the cytoskeletal structures in human bone osteosarcoma epithelial cells were modelled using a Cellular Potts Model. The first two models treat parts of the RBC membrane in much detail, whereas the latter two models treat whole cells on a continuous level. Both approaches are important and complement each other. The molecular foundation of cell parameters is determined in microscopic models, whereas the whole cell models find the influence of these parameters on the cell behaviour.

In Chapter 2, the theoretical background of treating RBC membranes was explained in detail. The application of flickering analysis to malaria-infected RBCs had not been done before, such that our collaborators provided us with unique data on the RBC remodelling process. In order to understand the flickering spectra on the basis of alterations in the cytoskeletal network, I implemented the anchor points of the spectrin network as discrete summations into the Hamiltonian for the membrane. Using this method made it was possible to make a connection between the confinement factor, commonly used to interpret experimental flickering data, and the parasite's cytoskeletal modifications. Specifically, the experimentally found increase in confinement could be explained by the addition of connections between the RBC bilayer and the underlying cytoskeleton. The parasite does so, by assembling knobs of 100 nm diameter, which are strongly anchored to the cytoskeleton. This is necessary because these knobs act as a platform for the adhesion molecules PfEMP1, which transmit large forces during the adhesion process. Another effect that increases the membrane confinement was found to be the stretching of spectrin filaments. During the infection, the parasite disassembles actin junctions in order to build its own filament network. Therefore, the remaining network is stretched out which leads to an increased stiffness of the individual filaments. The model also predicts an increased confinement for such a case. Although the model helped to find the microscopic origin of the increased confinement, there are some shortcomings that could potentially be improved in the future. The main discrepancy between the equilibrium model and the living RBC is the missing incorporation of active elements, which have been found to make a significant contribution. In order to do so, dynamical simulations need to be run incorporating the suitable active elements. However, it is not entirely clear which membrane components cause the activity, so this issue will require a thorough treatment in the future. For the purpose of this work, I focused on influences of the cytoskeleton, which were shown to contribute to the flickering spectrum in the described way.

Based on these finding, the nature of the molecular changes inside the RBC is treated in Chapter 3 by employing a reaction-diffusion model to the molecular constituents of the system. The RBC cytoskeleton is a delicate system which relies on short actin filaments as junctional points. Therefore, actin dynamics was treated within this modelling approach and deduced that specific length dependent factors are necessary to control the lengths of a filament population. A major protein forming the parasite induced knobs is KAHRP which has a large number of binding partners within the cytoskeleton because it is highly disordered. Based on information in the literature on protein-protein interaction parameters, I modelled the assembly of KAHRP clusters within the cytoskeletal network. The most striking result is a very narrow parameter range that shows an association of the assembled KAHRP clusters to the actin filaments. This result delivers a potential mechanism by which the parasite could move the initially spectrin associated KAHRP towards the actin junction. This behaviour was found by our collaborators in malaria infected RBCs through experimentally obtained colocalization data. Consequently, this shows that the parasite changes binding affinities during its maturation within the RBC. A potential way to do this is phosphorylation of the relevant proteins. The appearance of the cytoskeleton was also shown to change as KAHRP clusters form, hence the network condenses around the clusters and gets stretched out in the remaining regions. This directly relates to the results from Chapter 2, which determined the stretching of the spectrin filaments to be one of the causes of increased confinement. Finally, the role of the adhesion molecule PfEMP1 in the knob structure was examined. Through mathematical analysis of microscopy images containing immunolabelled PfEMP1 molecules, it was possible to show a clustering of these molecules at the top of the knob. Based on the analysed aspects, there are obvious additions to the model that should be considered in the future. Most importantly, the actin dynamics should be combined with the assembly process to determine the mechanism by which the parasite builds long host derived actin filaments inside the RBC. Further, the incorporation of PfEMP1 molecules could be modelled by making these diffuse laterally within the bilayer plane. Overall, first conclusions could be drawn from the modelling approach on the very complex mechanisms behind the knob formation.

The idea of the project discussed in Chapter 4 was modelling the shape change of RBCs in hydrodynamic flow, which treats the cell on a much larger scale. As a matter of fact, the malaria infection is known to change hydrodynamic properties of RBCs. Besides becoming adherent, experimental results show that iRBCs need longer to recover their shape. A suitable approach seems to be simplifying the problem to two dimensions and thus treating the RBC as a closed loop in the two-dimensional plane. In this model, the nodes on the RBC membrane are coupled through viscoelastic elements and their mechanics are directly coupled to the finite element solver for the Stokes flow describing the surrounding fluid. During the implementation of this method unforeseen difficulties occurred. For that reason, a stable solution is still missing. I was only able to simulate very few time steps before a numerical inconsistency destroyed the flow profile. In the future, a different way of implementing the mechanical equations should be tested to prevent these problems. In my opinion a Lagrange multiplier approach seems most promising.

Finally, I examined a different kind of actin organisation in Chapter 5, namely actin stress fibres forming in cells on micropatterns. The model that I employed here models the cell on a very coarse scale and thus reduces the spreading kinetic to the contour of the cell. This is also a two-dimensional model similar to the previous finite element model. In this project, the tight collaboration between experiments and the theoretical modelling were of great importance. As a result, the model could be validated to describe the cell spreading very accurately and also predict cell parameters from the spreading dynamics. In particular, the modelling of the stress fibre architecture led us to the conclusion that stress fibres are formed by a simple rule: the fibres form parallel to the advancing front and become straight fibres as soon as the cell has spread far enough. This leads to a memory of the cell spreading process in the stress fibre architecture. Experimentally, the half life of this memory was determined to be 50 minutes. Although this model describes the experimental data sufficiently well, an improvement could be made by including a feedback between the stress fibres and the spreading. Since the biological foundation for such a feedback is not entirely clear, this extension of the model would require a large effort and was not within the scope of this thesis. Nevertheless, the success of the current model implies that such a feedback mechanism would not qualitatively change the outcome.

Overall, several models on different length scales were implemented successfully. The main conclusion, which is strongly supported by several of these models, is that the stiffening of the RBC membrane on a macroscopic level is caused by specific parasite proteins that interact with the RBC cytoskeleton. The additional anchoring points between the bilayer and the cytoskelton, and the stretching of the spectrin filaments are most important in causing this effect. Additionally, the parasite needs to finely tune the interactions between the different proteins to achieve a knob assembly at the right moment during the infection. It is likely that phosphorylation causes this change in binding affinities which would also explain why the different haemoglobin variants, which show altered phosphorylation, are partly protected from severe malaria.

In conclusion, we see that the parasite has adapted to the RBC environment in a remarkable manner, by not only using its own but also the host cell's proteins to achieve its goal of staying within the human body and replicating. My findings help to understand the molecular details of the underlying processes of the RBC remodelling to allow for potential future interventions in the spreading of malaria.

Appendices

Appendix A

Abbreviations

RBC	red blood cell
iRBC	malaria infected red blood cell
HbA	heterotetramer consisting of two α- and two β-globin chains
HbS	variant of the beta-globin gene called sickle haemoglobin
HbC	another variant of the beta-globin gene
HbAS	heterozygous carrier of HbA and HbS
HbAC	heterozygous carrier of HbA and HbC
Pf	Plasmodium falciparum
KAHRP	knob-associated histidine-rich protein
PfEMP1	Plasmodium falciparum erythrocyte membrane protein 1
PTEX	Plasmodium Translocon of Exported proteins
CPM	Cellular Potts Model
FSBD	Fourier Space Brownian Dynamics
AFM	atomic force microscopy
QFDERR	quick-freeze, deep-etch rotary replication
ATP	adenosine triphosphate
ADP	adenosine diphosphate
G-actin	globular actin
ATS	acidic terminal sequence
ICAM-1	intercellular adhesioin molecule 1
CGMD	coarse grained molecular dynamics
MPCD	mulit-particle collision dynamics
DPD	dissipative particle dynamics
RE	Reynolds number
FEM	finite element method
TEM	tension elasticity model
MCSweep	Monte Carlo Sweep
CFM	circle fitting method

MSAM	marching square arc length method
RFP	red fluorescent protein
ECM	extra cellular matrix
NMMII	non-muscle myosin II

Appendix B

Theory of Membranes

B.1 Spherical Geometry

A point on the surface of the vesicle is given by $\mathbf{r} = r_0(1+u)\hat{\mathbf{r}}$ and hence the reference configuration is a sphere with radius r_0. The sphere is parametrized in terms of the polar angle θ and the azimuthal angle ϕ, such that $\hat{\mathbf{r}}$ reads:

$$\hat{\mathbf{r}} = \begin{pmatrix} \sin(\theta)\cos(\phi) \\ \sin(\theta)\sin(\phi) \\ \cos(\theta) \end{pmatrix}. \tag{B.1}$$

In this geometry the mean curvature is $\mathcal{H} = -\frac{2}{r_0}$ and the Gaussian curvature is $\mathcal{K} = \frac{1}{r_0^2}$. Further, the first and second fundamental forms are given by:

$$g = r_0^2 \begin{pmatrix} 1 & 0 \\ 0 & \sin^2\theta \end{pmatrix} \qquad h = -r_0 \begin{pmatrix} 1 & 0 \\ 0 & \sin^2\theta \end{pmatrix}. \tag{B.2}$$

Having specified this geometry, the variations are given by:

$$\delta^1(dS) = 2udS \tag{B.3}$$

$$\delta^2(dS) = (2u^2 - u\Delta u)dS \tag{B.4}$$

$$\delta^1 H = \frac{2u}{r_0} + \frac{\Delta u}{r_0} \tag{B.5}$$

$$\delta^2 H = -\frac{4u^2}{r_0} - \frac{4u\Delta u}{r_0} \tag{B.6}$$

$$\delta^1 V = ur_0 dS \tag{B.7}$$

$$\delta^2 V = 2u^2 r_0 dS. \tag{B.8}$$

These can be easily deduced from the general formulas in covariant notation given in Ref. [44].

B.2 Monge Parametrization

In Monge parametrization the surface is described by the height $h(x, y)$ from a planar reference configuration. Here, the mean curvature and Gaussion curvatures are $\mathcal{H} = \mathcal{K} = 0$ in the reference configuration. In this case the first fundamental form is the identity matrix and the second fundamental form is zero. For the first deviation of these we find:

$$\delta g = \begin{pmatrix} (\partial_x h)^2 & \partial_x h \cdot \partial_y h \\ \partial_x h \cdot \partial_y h & (\partial_y h)^2 \end{pmatrix} \qquad \delta h = \frac{1}{\sqrt{\det(g)}} \begin{pmatrix} \partial_{xx} h & \partial_{xy} h \\ \partial_{xy} h & \partial_{yy} h \end{pmatrix}. \tag{B.9}$$

For the variations we find:

$$\delta^1(dS) = 0 \qquad \delta^2(dS) = \frac{1}{2}(\nabla h)^2 dS \tag{B.10}$$

$$\delta^1 H = \frac{1}{2}\nabla^2 h \qquad \delta^2 H = 0. \tag{B.11}$$

B.3 Conversion Between Fourier Modes and Spherical Harmonics

This result in spherical harmonics can be converted to a function of the Fourier mode q which is a common representation of experimental data (e.g. paper [243] or [244]). Experimentally, only the fluctuations in the equatorial plane are measured $\langle |v_q(t)|^2 \rangle$, hence $\theta = \pi/2$ and $\mathbf{r}$ is only a function of ϕ and t. $v_q(t)$ and u_{lm} are related as follows:

$$\mathbf{r}(\phi, t) = r_0 + \sum_{q=0}^{q_{max}} v_q(t) e^{-iq\phi} = r_0 + r_0 \sum_{l,m} u_{l,m} Y_{l,m}(\pi/2, \phi). \tag{B.12}$$

Now both sides are multiplied by $e^{iq'\phi}$ and ϕ is integrated form 0 to 2π.

$$2\pi v_{q'}(t) = r_0 \int_0^{2\pi} d\phi \sum_{l,m} u_{l,m} Y_{l,m}(\pi/2, \phi) e^{iq'\phi}. \tag{B.13}$$

This can be further simplified by noting that $Y_{l,m}(\pi/2, \phi) = N_{l,m} e^{im\phi} P_l^m(\cos(\theta))$, where $N_{l,m} = (-1)^m \sqrt{\frac{2l+1}{2} \frac{(l-m)!}{(l+m)!}}$ is the normalization factor and depends on how the exact definition of the spherical harmonics. Hence,

$$\int d\phi N e^{i(m+q')\phi} P_l^m(0) = \delta(m+q') N 2\pi P_l^m(0) \tag{B.14}$$

and for the dimensionless $\langle |v_q(t)|^2 \rangle$ we find

$$\langle |v_q(t)|^2 \rangle = r_0^2 \sum_{l=q}^{l_{max}} N_{l,-q}^2 \langle |u_{l,-q}|^2 \rangle P_l^{-q}(0)^2, \tag{B.15}$$

$$N_{l,-q}^2 = \frac{2l+1}{2} \frac{(l+q)!}{(l-q)!}. \tag{B.16}$$

To understand the boundaries of the sum appearing in the expression, one needs to notice that $\delta(m+q)$ requires that $m = -q$ which influences the sum over l and m. Usually, for a given l the sum for m runs from $-l$ to l but now $m = -q$ and hence only terms with $l \geq q$ contribute. This is why the sum starts at $l = q$ and there is no sum over m any more. The sum is cut off at 120 which is large enough to ensure convergence. It is necessary that $l_{max} > q$.

In MatLab the spherical harmonics are defined slightly differently and the polynomials for $-q$ need to be expressed in terms of the positive ones. This leads to the final expression:

$$\langle |v_q(t)|^2 \rangle = r_0^2 \sum_{l=q}^{l_{max}} \langle |u_{l,-q}|^2 \rangle (l + \frac{1}{2}) \frac{(l-q)!}{(l+q)!} P_l^q(0)^2, \tag{B.17}$$

(multiply by r_0^2 to reintroduce dimensions).

Appendix C

Membrane Confinement from Microscopic Properties

C.1 Equatorial Projection of Fourier Modes

When using the formula derived for a planar geometry, and comparing it to experimental data, the modes in y-direction need to be projected onto $y = 0$. To find $\langle h(q_x, y = 0)^2\rangle$ from $\langle h_q^2\rangle$, one has to do an inverse Fourier transform in q_y and evaluate the resulting expression at $y = 0$:

$$\langle h(q_x, y = 0)^2\rangle = \frac{1}{2\pi}\int_{-\infty}^{\infty}\langle h^2_{q_x,q_y}\rangle e^{iq_y y}dq_y\bigg|_{y=0}, \tag{C.1}$$

with

$$\langle h^2_{q_x,q_y}\rangle = \frac{k_BT}{L^2}\frac{1}{\gamma+\sigma(q_x^2+q_y^2)+\kappa(q_x^2+q_y^2)^2}. \tag{C.2}$$

The integral can be done using the Residue Theorem and was first calculated by Yoon et al.[245]. Depending on the values of κ, σ and γ, the poles of (C.2) change sign on the imaginary axis. The proper sign is obtained by taking the absolute value of the final expression. This is possible, because either the poles lie in the positive imaginary plane and the contour is positively oriented giving a positive result; or the poles lie in the negative imaginary plane which gives a negative result, but the contour is negatively oriented so that another minus sign needs to be introduced giving a positive final result:

$$\begin{aligned}\langle h(q_x, y = 0)^2\rangle =& \frac{k_BT}{L}\left|\sqrt{\frac{\kappa}{2(\sigma^2-4\kappa\gamma)}}\left[\frac{1}{\sqrt{2\kappa q_x^2+\sigma-\sqrt{\sigma^2-4\kappa\gamma}}}\right.\right.\\ &\left.\left.-\frac{1}{\sqrt{2\kappa q_x^2+\sigma+\sqrt{\sigma^2-4\kappa\gamma}}}\right]\right|,\end{aligned} \tag{C.3}$$

note that h has units of m^2, $q_x = n/r_0$ and $L = 2\pi r_0$.

C.2 Numerical Calculation of Fluctuation Amplitudes

Equations (2.58) and (2.59) are more easily treated in Fourier space by assuming periodic boundary conditions, where $h(\boldsymbol{r})$ and $h_{\boldsymbol{k}}$ are related by

$$h(\boldsymbol{r}) = \sum_{\boldsymbol{k}}^{\boldsymbol{k}_{max}} h_{\boldsymbol{k}}e^{i\boldsymbol{k}\cdot\boldsymbol{r}} = real \qquad \text{(hence, } h^*_{\boldsymbol{k}} = h_{-\boldsymbol{k}}\text{)},$$

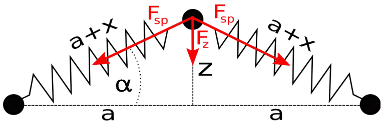

Figure C.1: Sketch of horizontally attched springs that are deflected in z-direction.

with $k_{x,y} = (0, \pm 1, ...)2\pi/L_{x,y}$. Using these, the Fourier Transform of the sum of (2.58) and (2.59) can be written as

$$\begin{aligned} H &= \frac{1}{2L_x^2 L_y^2} \sum_{k,k'} \left[\left(\kappa k^4 + \sigma k^2\right) |h_k|^2 \delta_{k,k'} + \sum_{\alpha=1}^{N} k_\alpha h_k h_{k'} e^{-i(\boldsymbol{k}-\boldsymbol{k'})\cdot \boldsymbol{r}_\alpha} \right] \\ &= \frac{1}{2} \sum_{k,k'} h_k^* D_{kk'}, h_{k'}, \end{aligned}$$

where the contributions from the springs introduce non-diagonal elements to the matrix $D_{kk'}$. Now it is convenient to change to a set of independent coordinates c, which treat real and complex components of the independent h_q-modes separately ($h_{q_c} = a_{q_c} + i\ b_{q_c}$). The Hamiltonian becomes

$$H = \sum_{r,r'} c_r M_{rr'} c_{r'}, \quad c = \begin{pmatrix} \frac{1}{\sqrt{2}} h_{q_{real}} \\ a_{q_c} \\ b_{q_c} \end{pmatrix},$$

such that, by use of the equipartition theorem, the mean squared fluctuations take the easy form

$$\langle c_r c_{r'} \rangle = \frac{k_B T}{2} M^{-1}_{rr'}.$$

In a final step we convert back to h_k:

$$\langle |h_k|^2 \rangle = \begin{cases} 2k_B T\ M^{-1}_{k,k} & k = \textit{real mode} \\ \frac{k_B T}{2}(M^{-1}_{Re\ k,k} + M^{-1}_{Im\ k,k}) & k = \textit{complex mode}, \end{cases}$$

where explicitly real and complex modes have to be treated differently.

C.3 Derivation of Vertical Spring Constant

For the fluctuation analysis we are interested in the membrane's motion orthogonal to its plane. Therefore, we consider the simplified case of two attached springs that lie on the horizontal axis and the connection point is now moved in the z-direction as depicted in Figure C.1. For simplicity we assume both springs to be equal in strength and length.

By Hooke's Law the force along the extension direction of the spring is given by $F_{sp} = k_{sp} x$, where x is the displacement from the rest length. We can write down an equivalent formulation for the force in z-direction $F_z = nk_z$, where the factor n counts the number of attached springs, which is 2 in this case but can easily be generalized. The aim is now to express k in terms of k_{sp} , z and a. We can assume that $x, z \ll a$ since membrane fluctuations are small compared to the length of the spectrin filaments. Further, the connection point is assumed to be in equilibrium along the x-direction, so that horizontal forces cancel out and we can focus on the z component of the spring force $F_{sp,z} = F_{sp} \sin\alpha$.

After expanding the left hand side of the relation $\sqrt{z^2/a^2+1} = 1 + x/a$ to find that $x \approx \frac{z^2}{2a}$ and noticing the first order approximation of $\sin\alpha$ to be z/a , we obtain the final expression

$$F_z = nk_{sp}\frac{z^2}{2a^2}z. \tag{C.4}$$

In this expression we can identify $k = k_{sp}\frac{z^2}{2a^2}$ and notice that the motion in z-direction does not follow a linear spring but the spring constant increases with z^2 for small displacements.

Appendix D

Details on Cytoskeletal Model

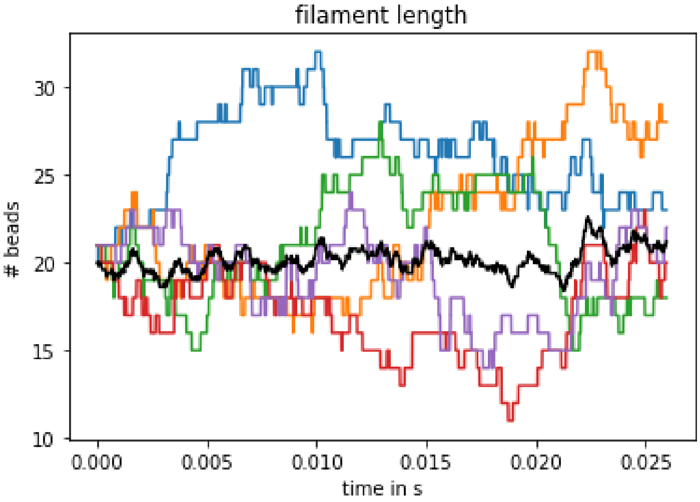

Figure D.1: The length evolution of five different filaments is plotted with their average length indicated by the black line.

D.1 Experimental Rate Constants

In Table D.1 rate constants from literature for the attachment and detachment at the actin barbed and pointed ends are summarized. There are two studies on Mg-ATP actin, three studies on Mg-ADP actin and one set of rates from an analytical calculation.

D.2 Rates Used in Models

In Table D.2 the actin polymerization rates from different simulation studies are compared. Firstly, probability distributions are used to describe the system, secondly, a Master equation approach is applied, thirdly, the actin monomers are treated in a Brownian dynamics study, fourthly, the Gillespie algorithm is applied and finally, an analytic calculation is done. References are shown in the table.

D.3 Length Fluctuations at Treadmilling Concentration

Five filaments were set up in a simulation box with a number of free monomers that match the treadmilling concentration. No monomers were added or taken out of the simulation box. In Figure D.1 we see that the average filament length, i.e. the total number of bound actin monomers stays approximately constant (black line). At the same time the individual filament lengths fluctuate a lot. The reason is, that only the overall bound monomer number is controlled by the concentration.

D.4 KAHRP Cluster Positioning

In Figure D.2 the fractional positioning of KAHRP clusters compared for the four different interaction cases (from top to bottom). Each column shows the time evolution for a specific interaction energy ϵ ($\epsilon = 0.1\ \mathrm{k_B T}$, $\epsilon = 1.5\ \mathrm{k_B T}$, $\epsilon = 5.0\ \mathrm{k_B T}$ and $\epsilon = 20.0\ \mathrm{k_B T}$ from left to right).

D.5 Cluster Sizes Using 500 KAHRP Particles

Figure D.3 shows similar graphs to the main text but with a larger number of KAHRP particles in the simulation box; the number was increased from 200 to 500. The plots show the average cluster size as a function of the interaction energy ϵ. The different colors in the plot show various time points as indicated in the legend.

Study	attachment rate constant ($\mu M^{-1} s^{-1}$)		detachment rate (s^{-1})		critical conc. ($\mu M/l$)	
	barbed	pointed	barbed	pointed	barbed	pointed
Mg-ATP-actin [246]	11.6	1.3	1.4	0.8	0.12	0.62
Mg-ATP-actin [108]	7.4 ± 0.5	0.56 ± 0.10	0.8 ± 0.8	0.44 ± 0.17	0.11 ± 0.12	0.8 ± 0.4
Mg-ADP-actin [246]	3.8	0.16	7.2	0.27	1.89	1.69
Mg-ADP-actin [108]			1.37 ± 2.87	0.16 ± 2.05		
Mg-ADP-actin [158]	2.9 ± 0.21	0.134 ± 0.03	5.4 ± 0.14	0.25 ± 0.04	1.8 ± 0.14	
Calculation [247]	11.6		1.41		0.12	

Table D.1: Rate constants collected from different experimental studies.

Model	ATP attachment rate constant ($\mu M^{-1} s^{-1}$)		ATP detachment rate (s^{-1})		ADP attachment rate constant ($\mu M^{-1} s^{-1}$)		ADP detachment rate (s^{-1})	
	barbed	pointed	barbed	pointed	barbed	pointed	barbed	pointed
Prob. dist. [109]	11.6		1.4				7.2	
master eq. [110]	11.6	1.3	1.4	0.8			7.2	0.27
BD [112]	11.6	1.3	1.4	0.16			5.4	0.25
Gillespie [248]	11.6	1.3	1.4	0.8	2.9	0.09	5.8	0.25
Analytic [249]	11.6	1.3	1.4	0.8	3.8	0.16	7.2	0.3

Model	ADP-P attachment rate constant ($\mu M^{-1} s^{-1}$)		ADP-P detachment rate (s^{-1})		hydrolysis rate (s^{-1})	P-release rate (s^{-1})
	barbed	pointed	barbed	pointed		
Prob. dist. [109]			1.1		0.3	0.004
master eq. [110]					0.3	
BD [112]			0.2	0.02	0.3	0.003
Gillespie [248]	3.4	0.11	0.16	0.02	0.3	0.0068
Analytic [249]	11.6	1.3	1.4	0.8	0.3	0.0026

Table D.2: Rate constants collected form different theory studies.

all equal

$\epsilon_{k-k} = \epsilon$
$\epsilon_{k-sp} = \epsilon_{k-k}$
$\epsilon_{k-a} = \epsilon_{k-k}$

weak self-association

$\epsilon_{k-k} = \epsilon$
$\epsilon_{k-sp} = 2\epsilon_{k-k}$
$\epsilon_{k-a} = 2\epsilon_{k-k}$

strong self-association

$\epsilon_{k-k} = \epsilon$
$\epsilon_{k-sp} = 0.5\epsilon_{k-k}$
$\epsilon_{k-a} = 0.5\epsilon_{k-k}$

strong actin-association

$\epsilon_{k-k} = \epsilon$
$\epsilon_{k-a} = 2\epsilon_{k-k}$
$\epsilon_{k-sp} = \epsilon_{k-k}$

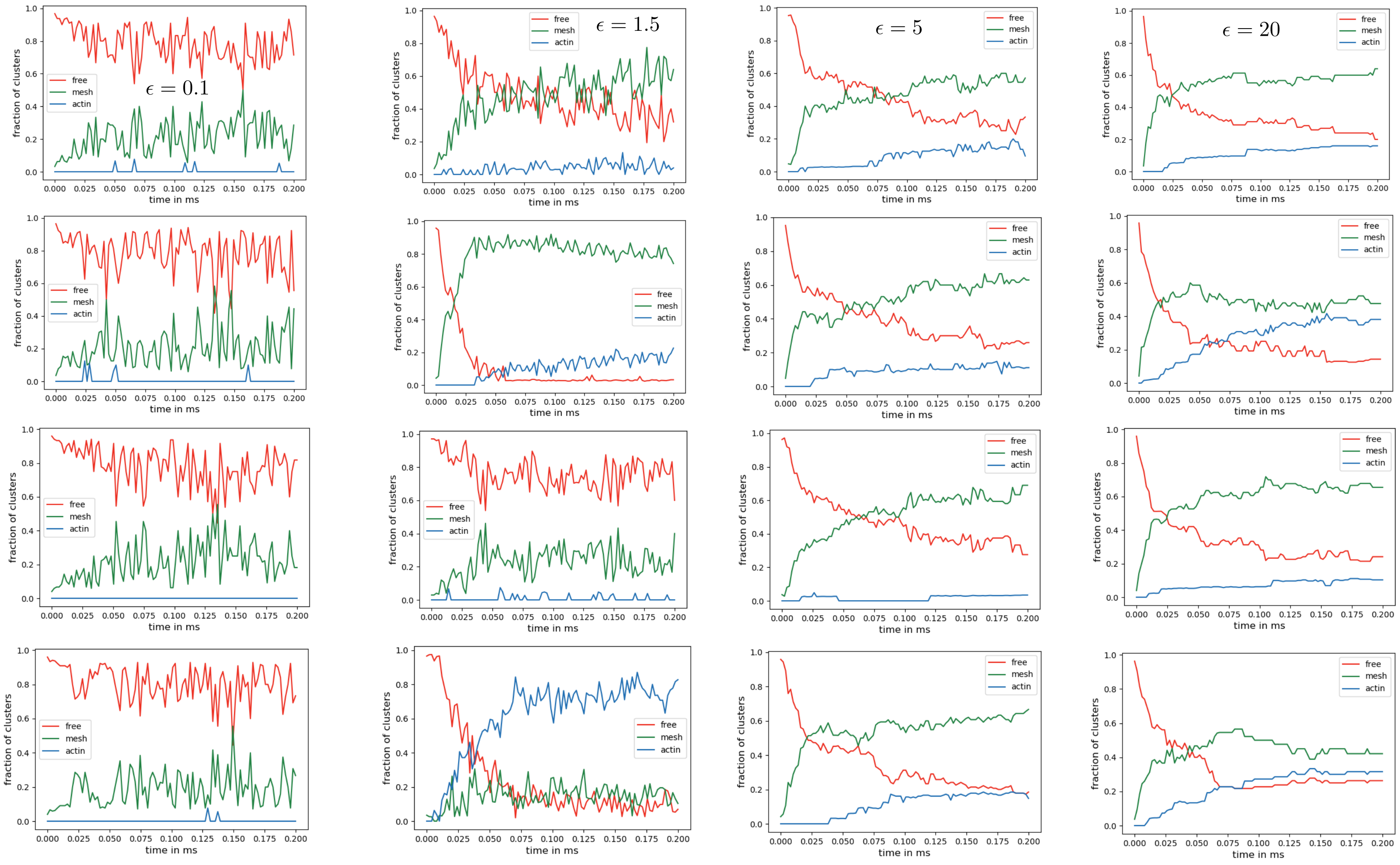

Figure D.2: The positioning of KAHRP clusters is compared for the four interaction cases (all equal, weak self-association, strong self-association and strong actin association from top to bottom). The graphs show the temporal evolution of the fractions for a specific ϵ ($\epsilon = 0.1$ k$_\mathrm{B}$T, $\epsilon = 1.5$ k$_\mathrm{B}$T, $\epsilon = 5.0$ k$_\mathrm{B}$T and $\epsilon = 20.0$ k$_\mathrm{B}$T from left to right).

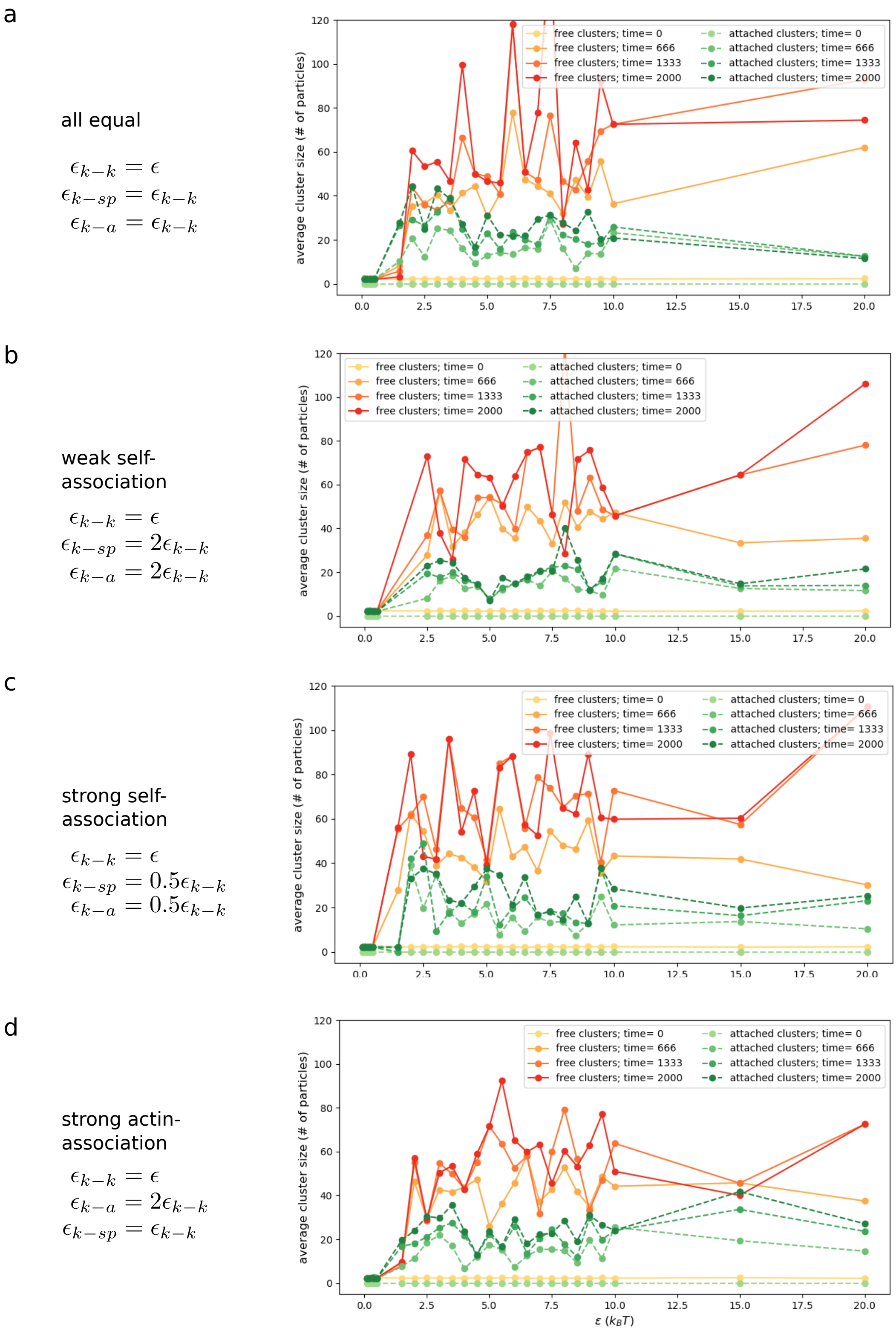

Figure D.3: The average cluster size in simulations with 500 KAHRP particles is displayed as a function of the potential depth ϵ. Free and attached clusters are considered separately as indicated in the legend. a to d) show the four interaction cases (all equal in a, weak self-association in b, strong self-association in c and strong actin association in d).

Bibliography

[1] F. Brochard and J. F. Lennon. Frequency spectrum of the flicker phenomenon in erythrocytes. *Journal de Physique*, 36(11):1035–1047, 1975.

[2] Gerald Lim H. W, Michael Wortis, and Ranjan Mukhopadhyay. Stomatocytediscocyteechinocyte sequence of the human red blood cell: Evidence for the bilayer couple hypothesis from membrane mechanics. *PNAS*, 99(26):16766–16769, December 2002.

[3] Bruce Alberts, Alexander Johnson, Julian Lewis, Martin Raff, Keith Roberts, and Peter Walter. Molecular Biology of the Cell (Garland Science, New York, 2002). *There is no corresponding record for this reference*, 1997.

[4] N. Gov, A. G. Zilman, and S. Safran. Cytoskeleton confinement and tension of red blood cell membranes. *Physical review letters*, 90(22):228101, 2003.

[5] Lawrence C. L. Lin, Jay T. Groves, and Frank L. H. Brown. Analysis of Shape, Fluctuations, and Dynamics in Intermembrane Junctions. *Biophysical Journal*, 91(10):3600–3606, November 2006.

[6] Timo Betz and Ccile Sykes. Time resolved membrane fluctuation spectroscopy. *Soft Matter*, 8(19):5317–5326, 2012.

[7] H. Turlier, D. A. Fedosov, B. Audoly, T. Auth, N. S. Gov, C. Sykes, J.-F. Joanny, G. Gompper, and T. Betz. Equilibrium physics breakdown reveals the active nature of red blood cell flickering. *Nature Physics*, 2016.

[8] Anil K. Dasanna, Dmitry A. Fedosov, Gerhard Gompper, and Ulrich S. Schwarz. State diagram for wall adhesion of red blood cells in shear flow: from crawling to flipping. *Soft Matter*, 15(27):5511–5520, July 2019.

[9] Udo Seifert. Morphology and dynamics of vesicles. *Current Opinion in Colloid & Interface Science*, 1(3):350–357, June 1996.

[10] David Abreu, Michael Levant, Victor Steinberg, and Udo Seifert. Fluid Vesicles in Flow. *Advances in Colloid and Interface Science*, 208:129–141, June 2014. arXiv: 1311.7341.

[11] Hui Shi, Zhuo Liu, Ang Li, Jing Yin, Alvin GL Chong, Kevin SW Tan, Yong Zhang, and Chwee Teck Lim. Life cycle-dependent cytoskeletal modifications in Plasmodium falciparum infected erythrocytes. *PLoS One*, 8(4):e61170, 2013.

[12] Jan D. Warncke, Ioannis Vakonakis, and Hans-Peter Beck. Plasmodium Helical Interspersed Subtelomeric (PHIST) proteins, at the center of host cell remodeling. *Microbiology and Molecular Biology Reviews*, 80(4):905–927, 2016.

[13] Manuel Thry, Anne Ppin, Emilie Dressaire, Yong Chen, and Michel Bornens. Cell distribution of stress fibres in response to the geometry of the adhesive environment. *Cell Motil. Cytoskeleton*, 63(6):341–355, June 2006.

[14] Philipp J. Albert and Ulrich S. Schwarz. Dynamics of cell shape and forces on micropatterned substrates predicted by a cellular Potts model. *Biophysical journal*, 106(11):2340–2352, 2014.

[15] Erich Sackmann and Rudolf Merkel. *Lehrbuch der Biophysik*. Wiley-VCH, 2010.

[16] WHO | World malaria report 2019. Library Catalog: www.who.int Publisher: World Health Organization.

[17] Jan D. Warncke and Hans-Peter Beck. Host Cytoskeleton Remodeling throughout the Blood Stages of Plasmodium falciparum. *Microbiology and Molecular Biology Reviews*, 83(4):e00013–19, November 2019.

[18] Yao Zhang, Changjin Huang, Sangtae Kim, Mahdi Golkaram, Matthew WA Dixon, Leann Tilley, Ju Li, Sulin Zhang, and Subra Suresh. Multiple stiffening effects of nanoscale knobs on human red blood cells infected with Plasmodium falciparum malaria parasite. *Proceedings of the National Academy of Sciences*, 112(19):6068–6073, 2015.

[19] Mailin Waldecker, Anil K. Dasanna, Christine Lansche, Marco Linke, Sirikamol Srismith, Marek Cyrklaff, Cecilia P. Sanchez, Ulrich S. Schwarz, and Michael Lanzer. Differential time-dependent volumetric and surface area changes and delayed induction of new permeation pathways in P. falciparum-infected hemoglobinopathic erythrocytes. *Cellular Microbiology*, 2016.

[20] Jude M. Przyborski, Britta Nyboer, and Michael Lanzer. Ticket to ride: export of proteins to the Plasmodium falciparum-infected erythrocyte. *Molecular microbiology*, 101(1):1–11, 2016.

[21] Michael Lanzer, Hannes Wickert, Georg Krohne, Laetitia Vincensini, and Catherine Braun Breton. Maurer's clefts: a novel multi-functional organelle in the cytoplasm of Plasmodium falciparum-infected erythrocytes. *International journal for parasitology*, 36(1):23–36, 2006.

[22] Tobili Y. Sam-Yellowe. The role of the Maurer's clefts in protein transport in Plasmodium falciparum. *Trends in parasitology*, 25(6):277–284, 2009.

[23] Marek Cyrklaff, Cecilia P. Sanchez, Nicole Kilian, Cyrille Bisseye, Jacques Simpore, Friedrich Frischknecht, and Michael Lanzer. Hemoglobins S and C interfere with actin remodeling in Plasmodium falciparuminfected erythrocytes. *Science*, 334(6060):1283–1286, 2011.

[24] Alexander G. Maier, Brian M. Cooke, Alan F. Cowman, and Leann Tilley. Malaria parasite proteins that remodel the host erythrocyte. *Nature Reviews Microbiology*, 7(5):341–354, 2009.

[25] Manouk Abkarian, Gladys Massiera, Laurence Berry, Magali Roques, and Catherine Braun-Breton. A novel mechanism for egress of malarial parasites from red blood cells. *Blood*, 117(15):4118–4124, 2011.

[26] Timm Krger. Introduction to the physics of red blood cells and hemorheology. In Timm Krger, editor, *Computer Simulation Study of Collective Phenomena in Dense Suspensions of Red Blood Cells under Shear*, pages 11–14. Vieweg+Teubner Verlag, Wiesbaden, 2012.

[27] Michael F. Hagan. Modeling Viral Capsid Assembly. *Advances in chemical physics*, 155:1–68, 2014.

[28] Seigo Nonaka, Honda Naoki, and Shin Ishii. A multiphysical model of cell migration integrating reactiondiffusion, membrane and cytoskeleton. *Neural Networks*, 24(9):979–989, November 2011.

[29] Elena Kassianidou, Dimitri Probst, Julia Jaeger, Stacey Lee, Anne-Lou Roguet, Ulrich Sebastian Schwarz, and Sanjay Kumar. Extracellular Matrix Geometry and Initial Adhesive Position Determine Stress Fiber Network Organization during Cell Spreading. *Cell Reports*, 27(6):1897–1909.e4, May 2019.

[30] Celeste M. Nelson, Ronald P. Jean, John L. Tan, Wendy F. Liu, Nathan J. Sniadecki, Alexander A. Spector, and Christopher S. Chen. Emergent patterns of growth controlled by multicellular form and mechanics. *Proceedings of the National Academy of Sciences of the United States of America*, 102(33):11594–11599, August 2005.

[31] Carina M. Edwards and Ulrich S. Schwarz. Force Localization in Contracting Cell Layers. *Physical Review Letters*, 107(12):128101, September 2011. Publisher: American Physical Society.

[32] Jrme RD Soin, Christoph A. Brand, Jonathan Stricker, Patrick W. Oakes, Margaret L. Gardel, and Ulrich S. Schwarz. Model-based traction force microscopy reveals differential tension in cellular actin bundles. *PLoS Comput Biol*, 11(3):e1004076, 2015.

[33] N. Gov and S. A. Safran. Pinning of fluid membranes by periodic harmonic potentials. *Physical Review E*, 69(1):011101, 2004.

[34] Lawrence C.-L. Lin and Frank LH Brown. Simulating membrane dynamics in nonhomogeneous hydrodynamic environments. *Journal of chemical theory and computation*, 2(3):472–483, 2006.

[35] Rolf-Jrgen Merath and Udo Seifert. Nonmonotonic fluctuation spectra of membranes pinned or tethered discretely to a substrate. *Physical Review E*, 73(1):010401, 2006.

[36] Wonjune Choi, Juyeon Yi, and Yong Woon Kim. Fluctuations of red blood cell membranes: The role of the cytoskeleton. *Physical Review E*, 92(1):012717, 2015.

[37] Benjamin Froehlich, Julia Jaeger, Christine Lansche, Cecilia P. Sanchez, Marek Cyrklaff, Bernd Buchholz, Serge Theophile Soubeiga, Jacque Simpore, Hiroaki Ito, Ulrich S. Schwarz, Michael Lanzer, and Motomu Tanaka. Hemoglobin S and C affect biomechanical membrane properties of P. falciparum -infected erythrocytes. *Communications Biology*, 2(1):1–11, August 2019. Number: 1 Publisher: Nature Publishing Group.

[38] P. B. Canham. The minimum energy of bending as a possible explanation of the biconcave shape of the human red blood cell. *Journal of Theoretical Biology*, 26(1):61–81, January 1970.

[39] W. Helfrich. Elastic Properties of Lipid Bilayers: Theory and Possible Experiments. *Zeitschrift fr Naturforschung C*, 28(11-12):693–703, December 1973. Publisher: De Gruyter Section: Zeitschrift fr Naturforschung C.

[40] U. Seifert. The concept of effective tension for fluctuating vesicles. *Zeitschrift fr Physik B Condensed Matter*, 97(2):299–309, 1995.

[41] U. Seifert, L. Miao, H.-G. Dbereiner, and M. Wortis. Budding Transition for Bilayer Fluid Vesicles with Area-Difference Elasticity. In Reinhard Lipowsky, Dieter Richter, and Kurt Kremer, editors, *The Structure and Conformation of Amphiphilic Membranes*, Springer Proceedings in Physics, pages 93–96, Berlin, Heidelberg, 1992. Springer.

[42] W. Wiese, W. Harbich, and W. Helfrich. Budding of lipid bilayer vesicles and flat membranes. *Journal of Physics: Condensed Matter*, 4(7):1647–1657, February 1992. Publisher: IOP Publishing.

[43] B Bozic, S Svetina, B Zeks, and R E Waugh. Role of lamellar membrane structure in tether formation from bilayer vesicles. *Biophysical Journal*, 61(4):963–973, April 1992.

[44] Ou-Yang Zhong-can and Wolfgang Helfrich. Bending energy of vesicle membranes: General expressions for the first, second, and third variation of the shape energy and applications to spheres and cylinders. *Phys. Rev. A*, 39(10):5280–5288, 1989.

[45] Mark A. Peterson. Shape dynamics of nearly spherical membrane bounded fluid cells. *Molecular Crystals and Liquid Crystals*, 127(1):257–272, 1985.

[46] Scott T. Milner and S. A. Safran. Dynamical fluctuations of droplet microemulsions and vesicles. *Physical Review A*, 36(9):4371, 1987.

[47] Jacques Pcraux, H.-G. Dbereiner, Jacques Prost, J.-F. Joanny, and Patricia Bassereau. Refined contour analysis of giant unilamellar vesicles. *The European Physical Journal E*, 13(3):277–290, 2004.

[48] S. B. Rochal, V. L. Lorman, and G. Mennessier. Viscoelastic dynamics of spherical composite vesicles. *Physical Review E*, 71(2):021905, 2005.

[49] Hans-Gnther Dbereiner, Gerhard Gompper, Christopher K. Haluska, Daniel M. Kroll, Peter G. Petrov, and Karin A. Riske. Advanced flicker spectroscopy of fluid membranes. *Physical review letters*, 91(4):048301, 2003.

[50] S. A. Safran. statistical thermodynamics of surfaces - Google Scholar. 1994.

[51] W. Helfrich. Steric Interaction of Fluid Membranes. *Berichte der Bunsengesellschaft fr physikalische Chemie*, 82(9):927–927, 1978. _eprint: https://onlinelibrary.wiley.com/doi/pdf/10.1002/bbpc.19780820941.

[52] G. Gompper and D. M. Kroll. Steric Interactions in Multimembrane Systems: A Monte Carlo Study. *Europhysics Letters (EPL)*, 9(1):59–64, May 1989. Publisher: IOP Publishing.

[53] R.-J. Merath and Udo Seifert. Fluctuation spectra of free and supported membrane pairs. *The European Physical Journal E*, 23(1):103, 2007.

[54] Thorsten Auth, S. A. Safran, and Nir S. Gov. Fluctuations of coupled fluid and solid membranes with application to red blood cells. *Physical Review E*, 76(5):051910, 2007.

[55] Cyril Dubus and J.-B. Fournier. A Gaussian model for the membrane of red blood cells with cytoskeletal defects. *EPL (Europhysics Letters)*, 75(1):181, 2006.

[56] Lawrence C.-L. Lin and Frank L. H. Brown. Brownian Dynamics in Fourier Space: Membrane Simulations over Long Length and Time Scales. *Physical Review Letters*, 93(25):256001, December 2004.

[57] L. D. Landau and E. M. Lifshitz. *Fluid Mechanics: Landau and Lifshitz: Course of Theoretical Physics, Volume 6*. Elsevier, September 2013. Google-Books-ID: eOBbAwAAQBAJ.

[58] M. B. Schneider, J. T. Jenkins, and W. W. Webb. Thermal fluctuations of large quasi-spherical bimolecular phospholipid vesicles. *Journal de Physique*, 45(9):1457–1472, 1984.

[59] N. Gov, A. G. Zilman, and S. Safran. Hydrodynamics of confined membranes. *Phys. Rev. E*, 70(1):011104, July 2004.

[60] Yoshihisa Kaizuka and Jay T. Groves. Hydrodynamic damping of membrane thermal fluctuations near surfaces imaged by fluorescence interference microscopy. *Physical review letters*, 96(11):118101, 2006.

[61] Arthur A. Evans, Basanta Bhaduri, Gabriel Popescu, and Alex J. Levine. Geometric localization of thermal fluctuations in red blood cells. *Proceedings of the National Academy of Sciences*, 114(11):2865–2870, 2017.

[62] J.-B. Manneville, P. Bassereau, D. Levy, and J. Prost. Activity of transmembrane proteins induces magnification of shape fluctuations of lipid membranes. *Physical review letters*, 82(21):4356, 1999.

[63] J. Prost and R. Bruinsma. Shape fluctuations of active membranes. *EPL (Europhysics Letters)*, 33(4):321, February 1996.

[64] J. Prost, J.-B. Manneville, and R. Bruinsma. Fluctuation-magnification of non-equilibrium membranes near a wall. *The European Physical Journal B - Condensed Matter and Complex Systems*, 1(4):465–480, March 1998.

[65] Sriram Ramaswamy, John Toner, and Jacques Prost. Nonequilibrium noise and instabilities in membranes with active pumps. *Pramana*, 53(1):237–242, 1999.

[66] Sriram Ramaswamy, John Toner, and Jacques Prost. Nonequilibrium fluctuations, traveling waves, and instabilities in active membranes. *Physical review letters*, 84(15):3494, 2000.

[67] N. S. Gov and S. A. Safran. Red blood cell membrane fluctuations and shape controlled by ATP-induced cytoskeletal defects. *Biophysical journal*, 88(3):1859–1874, 2005.

[68] Lawrence C.-L. Lin, Nir Gov, and Frank L. H. Brown. Nonequilibrium membrane fluctuations driven by active proteins. *The Journal of Chemical Physics*, 124(7):074903, February 2006.

[69] Bastien Loubet, Udo Seifert, and Michael Andersen Lomholt. Effective tension and fluctuations in active membranes. *Physical Review E*, 85(3):031913, March 2012. Publisher: American Physical Society.

[70] Ruddi Rodrguez-Garca, Ivn Lpez-Montero, Michael Mell, Gustavo Egea, Nir S. Gov, and Francisco Monroy. Direct cytoskeleton forces cause membrane softening in red blood cells. *Biophysical journal*, 108(12):2794–2806, 2015.

[71] Rui Zhang and Frank L. H. Brown. Cytoskeleton mediated effective elastic properties of model red blood cell membranes. *The Journal of Chemical Physics*, 129(6):065101, August 2008.

[72] A. M. Gennaro, A. Luquita, and M. Rasia. Comparison between internal microviscosity of low-density erythrocytes and the microviscosity of hemoglobin solutions: an electron paramagnetic resonance study. *Biophysical Journal*, 71(1):389–393, July 1996.

[73] Lawrence C.-L. Lin and Frank LH Brown. Dynamics of pinned membranes with application to protein diffusion on the surface of red blood cells. *Biophysical journal*, 86(2):764–780, 2004.

[74] Lawrence C.-L. Lin and Frank LH Brown. Dynamic simulations of membranes with cytoskeletal interactions. *Physical Review E*, 72(1):011910, 2005.

[75] Neil W. Ashcroft and N. David Mermin. *Solid State Physics.* Holt, Rinehart and Winston, 1976. Google-Books-ID: 1C9HAQAAIAAJ.

[76] Peter Atkins, Peter William Atkins, and Julio de Paula. *Atkins' Physical Chemistry.* OUP Oxford, March 2014. Google-Books-ID: sWTYAwAAQBAJ.

[77] Andrea Nans, Narla Mohandas, and David L. Stokes. Native ultrastructure of the red cell cytoskeleton by cryo-electron tomography. *Biophysical journal*, 101(10):2341–2350, 2011.

[78] David Boal and David H. Boal. *Mechanics of the Cell.* Cambridge University Press, 2012.

[79] Lipeng Lai, Xiaofeng Xu, Chwee Teck Lim, and Jianshu Cao. Stiffening of Red Blood Cells Induced by Cytoskeleton Disorders: A Joint Theory-Experiment Study. *Biophysical journal*, 109(11):2287–2294, 2015.

[80] Narla Mohandas and Patrick G. Gallagher. Red cell membrane: past, present, and future. *Blood*, 112(10):3939–3948, November 2008.

[81] Samuel E. Lux. Anatomy of the red cell membrane skeleton: unanswered questions. *Blood*, pages blood–2014, 2015.

[82] Rui Zhang, ChenYu Zhang, Qi Zhao, and DongHai Li. Spectrin: Structure, function and disease. *Science China Life Sciences*, 56(12):1076–1085, December 2013.

[83] Jeffrey W. Brown, Esther Bullitt, Sira Sriswasdi, Sandra Harper, David W. Speicher, and C. James McKnight. The Physiological Molecular Shape of Spectrin: A Compact Supercoil Resembling a Chinese Finger Trap. *PLOS Computational Biology*, 11(6):e1004302, June 2015.

[84] T J Byers and D Branton. Visualization of the protein associations in the erythrocyte membrane skeleton. *Proceedings of the National Academy of Sciences of the United States of America*, 82(18):6153–6157, September 1985.

[85] Jeanine A. Ursitti, David W. Pumplin, James B. Wade, and Robert J. Bloch. Ultrastructure of the human erythrocyte cytoskeleton and its attachment to the membrane. *Cell Motility*, 19(4):227–243, 1991.

[86] Jeanine A. Ursitti and James B. Wade. Ultrastructure and immunocytochemistry of the isolated human erythrocyte membrane skeleton. *Cell Motility*, 25(1):30–42, 1993.

[87] A. H. Swihart, J. M. Mikrut, J. B. Ketterson, and R. C. Macdonald. Atomic force microscopy of the erythrocyte membrane skeleton. *Journal of Microscopy*, 204(3):212–225, 2001.

[88] S Ohno. An ultrastructural study of the cytoplasmic aspects of erythrocyte membranes by a quick-freezing and deep-etching method. *Journal of Anatomy*, 180(Pt 2):315–320, April 1992.

[89] Valerie L Grum, Dongning Li, Ruby I MacDonald, and Alfonso Mondragn. Structures of Two Repeats of Spectrin Suggest Models of Flexibility. *Cell*, 98(4):523–535, August 1999.

[90] A. M. McGough and R. Josephs. On the structure of erythrocyte spectrin in partially expanded membrane skeletons. *Proceedings of the National Academy of Sciences of the United States of America*, 87(13):5208–5212, July 1990.

[91] B. T. Stokke, A. Mikkelsen, and A. Elgsaeter. Spectrin, human erythrocyte shapes, and mechanochemical properties. *Biophysical Journal*, 49(1):319–327, January 1986.

[92] D. H. Boal. Computer simulation of a model network for the erythrocyte cytoskeleton. *Biophysical Journal*, 67(2):521–529, August 1994.

[93] Catherine Picart, Paul Dalhaimer, and Dennis E. Discher. Actin Protofilament Orientation in Deformation of the Erythrocyte Membrane Skeleton. *Biophysical Journal*, 79(6):2987–3000, December 2000. Publisher: Elsevier.

[94] V. Heinrich, K. Ritchie, N. Mohandas, and E. Evans. Elastic thickness compressibilty of the red cell membrane. *Biophysical Journal*, 81(3):1452–1463, September 2001.

[95] Matthias Rief, Jaime Pascual, Matti Saraste, and Hermann E Gaub. Single molecule force spectroscopy of spectrin repeats: low unfolding forces in helix bundles11Edited by W. Baumeister. *Journal of Molecular Biology*, 286(2):553–561, February 1999.

[96] P. Dimitrakopoulos. Analysis of the variation in the determination of the shear modulus of the erythrocyte membrane: Effects of the constitutive law and membrane modeling. *Physical Review E*, 85(4):041917, April 2012.

[97] James C-M. Lee and Dennis E. Discher. Deformation-Enhanced Fluctuations in the Red Cell Skeleton with Theoretical Relations to Elasticity, Connectivity, and Spectrin Unfolding. *Biophysical Journal*, 81(6):3178–3192, December 2001.

[98] R. Waugh and E. A. Evans. Thermoelasticity of red blood cell membrane. *Biophysical Journal*, 26(1):115–131, April 1979.

[99] Leiting Pan, Rui Yan, Wan Li, and Ke Xu. Super-Resolution Microscopy Reveals the Native Ultrastructure of the Erythrocyte Cytoskeleton. *Cell Reports*, 22(5):1151–1158, January 2018.

[100] Marek Cyrklaff, Cecilia P. Sanchez, Friedrich Frischknecht, and Michael Lanzer. Host actin remodeling and protection from malaria by hemoglobinopathies. *Trends in parasitology*, 28(11):479–485, 2012.

[101] David S. Gokhin, Roberta B. Nowak, Joseph A. Khoory, Alfonso de la Piedra, Ionita C. Ghiran, and Velia M. Fowler. Dynamic actin filaments control the mechanical behavior of the human red blood cell membrane. *Molecular Biology of the Cell*, 26(9):1699–1710, May 2015.

[102] David S. Gokhin and Velia M. Fowler. Feisty filaments: actin dynamics in the red blood cell membrane skeleton. *Current opinion in hematology*, 23(3):206–214, 2016.

[103] Laurent Blanchoin and Thomas D. Pollard. Hydrolysis of ATP by polymerized actin depends on the bound divalent cation but not profilin. *Biochemistry*, 41(2):597–602, 2002.

[104] M. F. Carlier and Do Pantaloni. Direct evidence for ADP-inorganic phosphate-F-actin as the major intermediate in ATP-actin polymerization. Rate of dissociation of inorganic phosphate from actin filaments. *Biochemistry*, 25(24):7789–7792, 1986.

[105] Thekla Ohm and Albrecht Wegner. Mechanism of ATP hydrolysis by polymeric actin. *Biochimica et Biophysica Acta (BBA)-Protein Structure and Molecular Enzymology*, 1208(1):8–14, 1994.

[106] Ulrike Pieper and Albrecht Wegner. The End of a Polymerizing Actin Filament Contains Numerous ATP- Subunit Segments That Are Disconnected by ADP- Subunits Resulting from ATP Hydrolysis. *Biochemistry*, 35(14):4396–4402, 1996.

[107] T. D. Pollard and M. S. Mooseker. Direct measurement of actin polymerization rate constants by electron microscopy of actin filaments nucleated by isolated microvillus cores. *The Journal of Cell Biology*, 88(3):654–659, March 1981.

[108] Jeffrey R. Kuhn and Thomas D. Pollard. Real-time measurements of actin filament polymerization by total internal reflection fluorescence microscopy. *Biophysical journal*, 88(2):1387–1402, 2005.

[109] Dimitrios Vavylonis, Qingbo Yang, and Ben O'Shaughnessy. Actin polymerization kinetics, cap structure, and fluctuations. *Proceedings of the National Academy of Sciences*, 102(24):8543–8548, 2005.

[110] Evgeny B. Stukalin and Anatoly B. Kolomeisky. ATP Hydrolysis Stimulates Large Length Fluctuations in Single Actin Filaments. *Biophysical Journal*, 90(8):2673–2685, April 2006.

[111] Kunkun Guo, Julian Shillcock, and Reinhard Lipowsky. Self-assembly of actin monomers into long filaments: Brownian dynamics simulations. *The Journal of Chemical Physics*, 131(1):015102, July 2009.

[112] Kunkun Guo, Julian Shillcock, and Reinhard Lipowsky. Treadmilling of actin filaments via Brownian dynamics simulations. *The Journal of chemical physics*, 133(15):10B613, 2010.

[113] Kunkun Guo, Wenjia Xiao, and Dong Qiu. Polymerization of actin filaments coupled with adenosine triphosphate hydrolysis: Brownian dynamics and theoretical analysis. *The Journal of Chemical Physics*, 135(10):105101, September 2011.

[114] V. M. Fowler. Tropomodulin: a cytoskeletal protein that binds to the end of erythrocyte tropomyosin and inhibits tropomyosin binding to actin. *The Journal of Cell Biology*, 111(2):471–481, August 1990.

[115] Annemarie Weber, Cynthia R. Pennise, and Velia M. Fowler. Tropomodulin Increases the Critical Concentration of Barbed End-capped Actin Filaments by Converting ADPPi-actin to ADP-actin at All Pointed Filament Ends. *Journal of Biological Chemistry*, 274(49):34637–34645, March 1999.

[116] Kevin Gardner and Vann Bennett. Modulation of spectrinactin assembly by erythrocyte adducin. *Nature*, 328(6128):359, 1987.

[117] Xiaolin Li, Yoichiro Matsuoka, and Vann Bennett. Adducin Preferentially Recruits Spectrin to the Fast Growing Ends of Actin Filaments in a Complex Requiring the MARCKS-related Domain and a Newly Defined Oligomerization Domain. *Journal of Biological Chemistry*, 273(30):19329–19338, July 1998.

[118] Rick M. Fairhurst, Cameron D. Bess, and Michael A. Krause. Abnormal PfEMP1/knob display on Plasmodium falciparum-infected erythrocytes containing hemoglobin variants: fresh insights into malaria pathogenesis and protection. *Microbes and Infection*, 14(10):851–862, August 2012.

[119] Cathleen Magowan, Wataru Nunomura, Karena L. Waller, Jackson Yeung, Joy Liang, Heidi Van Dort, Philip S. Low, Ross L. Coppel, and Narla Mohandas. Plasmodium falciparum histidine-rich protein 1 associates with the band 3 binding domain of ankyrin in the infected red cell membrane. *Biochimica et Biophysica Acta (BBA)-Molecular Basis of Disease*, 1502(3):461–470, 2000.

[120] Melanie Rug, Stuart W. Prescott, Kate M. Fernandez, Brian M. Cooke, and Alan F. Cowman. The role of KAHRP domains in knob formation and cytoadherence of P falciparum-infected human erythrocytes. *Blood*, 108(1):370–378, 2006.

[121] Akshay Kumar Ganguly, Priyatosh Ranjan, Ashutosh Kumar, and Neel Sarovar Bhavesh. Dynamic association of PfEMP1 and KAHRP in knobs mediates cytoadherence during Plasmodium invasion. *Scientific Reports*, 5:8617, March 2015.

[122] B. S. Crabb, B. M. Cooke, J. C. Reeder, R. F. Waller, S. R. Caruana, K. M. Davern, M. E. Wickham, G. V. Brown, R. L. Coppel, and A. F. Cowman. Targeted gene disruption shows that knobs enable malaria-infected red cells to cytoadhere under physiological shear stress. *Cell*, 89(2):287–296, April 1997.

[123] S. Steven Oh, Sabine Voigt, Derek Fisher, J. Yi Scott, Patrick J. LeRoy, Laura H. Derick, Shih-Chun Liu, and Athar H. Chishti. Plasmodium falciparum erythrocyte membrane protein 1 is anchored to the actinspectrin junction and knob-associated histidine-rich protein in the erythrocyte skeleton. *Molecular and biochemical parasitology*, 108(2):237–247, 2000.

[124] Araxie Kilejian, Mohammad A. Rashid, Masamichi Aikawa, Toshiki Aji, and Yong-Fan Yang. Selective association of a fragment of the knob protein with spectrin, actin and the red cell membrane. *Molecular and Biochemical Parasitology*, 44(2):175–181, February 1991.

[125] Xinhong Pei, Xiuli An, Xinhua Guo, Michal Tarnawski, Ross Coppel, and Narla Mohandas. Structural and functional studies of interaction between Plasmodium falciparum knob-associated histidine-rich protein (KAHRP) and erythrocyte spectrin. *Journal of Biological Chemistry*, 2005.

[126] Haibo Weng, Xinhua Guo, Julien Papoin, Jie Wang, Ross Coppel, Narla Mohandas, and Xiuli An. Interaction of Plasmodium falciparum knob-associated histidine-rich protein (KAHRP) with erythrocyte ankyrin R is required for its attachment to the erythrocyte membrane. *Biochimica et biophysica acta*, 1838(1 0 0):185–192, January 2014.

[127] Erin E. Cutts, Niklas Laasch, Dirk M. Reiter, Raphael Trenker, Leanne M. Slater, Phillip J. Stansfeld, and Ioannis Vakonakis. Structural analysis of P. falciparum KAHRP and PfEMP1 complexes with host erythrocyte spectrin suggests a model for cytoadherent knob protrusions. *PLOS Pathogens*, 13(8):e1006552, August 2017.

[128] Vasken Ohanian, Lawrence C. Wolfe, Kathryn M. John, Jennifer C. Pinder, Samuel E. Lux, and Walter B. Gratzer. Analysis of the ternary interaction of the red cell membrane skeletal proteins, spectrin, actin, and 4.1. *Biochemistry*, 23(19):4416–4420, September 1984. Publisher: American Chemical Society.

[129] J. M. Tyler, B. N. Reinhardt, and D. Branton. Associations of erythrocyte membrane proteins. Binding of purified bands 2.1 and 4.1 to spectrin. *The Journal of Biological Chemistry*, 255(14):7034–7039, July 1980.

[130] A. Podgrski and D. Elbaum. Properties of red cell membrane proteins: mechanism of spectrin and band 4.1 interaction. *Biochemistry*, 24(27):7871–7876, December 1985.

[131] Paul S. Eder, Chu Jing Soong, and Mariano Tao. Phosphorylation reduces the affinity of protein 4.1 for spectrin. *Biochemistry*, 25(7):1764–1770, April 1986. Publisher: American Chemical Society.

[132] He Li and George Lykotrafitis. Erythrocyte membrane model with explicit description of the lipid bilayer and the spectrin network. *Biophysical journal*, 107(3):642–653, 2014.

[133] V. Bennett and P. J. Stenbuck. Association between ankyrin and the cytoplasmic domain of band 3 isolated from the human erythrocyte membrane. *The Journal of Biological Chemistry*, 255(13):6424–6432, July 1980.

[134] B. J. Thevenin and P. S. Low. Kinetics and regulation of the ankyrin-band 3 interaction of the human red blood cell membrane. *The Journal of Biological Chemistry*, 265(27):16166–16172, September 1990.

[135] V. M. Fowler and V. Bennett. Erythrocyte membrane tropomyosin. Purification and properties. *Journal of Biological Chemistry*, 259(9):5978–5989, October 1984.

[136] Karena L. Waller, Brian M. Cooke, Wataru Nunomura, Narla Mohandas, and Ross L. Coppel. Mapping the binding domains involved in the interaction between the plasmodium falciparum knob-associated histidine-rich protein (KAHRP) and the cytoadherence ligand P. FalciparumErythrocyte membrane protein 1 (PfEMP1). *Journal of Biological Chemistry*, 274(34):23808–23813, 1999.

[137] David E. Arnot and Anja T. R. Jensen. Antigenic Variation and the Genetics and Epigenetics of the PfEMP1 Erythrocyte Surface Antigens in Plasmodium falciparum Malaria. *Advances in Applied Microbiology*, 74:77–96, 2011.

[138] Christina Mayer, Leanne Slater, Michele C. Erat, Robert Konrat, and Ioannis Vakonakis. Structural analysis of the Plasmodium falciparum erythrocyte membrane protein 1 (PfEMP1) intracellular domain reveals a conserved interaction epitope. *The Journal of Biological Chemistry*, 287(10):7182–7189, March 2012.

[139] Neline Kriek, Leann Tilley, Paul Horrocks, Robert Pinches, Barry C. Elford, David JP Ferguson, Klaus Lingelbach, and Chris I. Newbold. Characterization of the pathway for transport of the cytoadherence-mediating protein, PfEMP1, to the host cell surface in malaria parasite-infected erythrocytes. *Molecular microbiology*, 50(4):1215–1227, 2003.

[140] Q. Chen, A. Heddini, A. Barragan, V. Fernandez, S. F. Pearce, and M. Wahlgren. The semiconserved head structure of Plasmodium falciparum erythrocyte membrane protein 1 mediates binding to multiple independent host receptors. *The Journal of Experimental Medicine*, 192(1):1–10, July 2000.

[141] B. M. Cooke, N. Mohandas, and R. L. Coppel. The malaria-infected red blood cell: structural and functional changes. *Advances in Parasitology*, 50:1–86, 2001.

[142] Rachna Hora, Daniel J. Bridges, Alister Craig, and Amit Sharma. Erythrocytic casein kinase II regulates cytoadherence of Plasmodium falciparum-infected red blood cells. *The Journal of Biological Chemistry*, 284(10):6260–6269, March 2009.

[143] Melanie Rug, Marek Cyrklaff, Antti Mikkonen, Leandro Lemgruber, Simone Kuelzer, Cecilia P. Sanchez, Jennifer Thompson, Eric Hanssen, Matthew ONeill, Christine Langer, Michael Lanzer, Friedrich Frischknecht, Alexander G. Maier, and Alan F. Cowman. Export of virulence proteins by malaria-infected erythrocytes involves remodeling of host actin cytoskeleton. *Blood*, 124(23):3459–3468, November 2014.

[144] Marianne C. Murray and Margaret E. Perkins. Phosphorylation of erythrocyte membrane and cytoskeleton proteins in cells infected with Plasmodium falciparum. *Molecular and Biochemical Parasitology*, 34(3):229–236, May 1989.

[145] Marta C. Nunes, J. P. Dean Goldring, Christian Doerig, and Artur Scherf. A novel protein kinase family in Plasmodium falciparum is differentially transcribed and secreted to various cellular compartments of the host cell. *Molecular Microbiology*, 63(2):391–403, 2007. _eprint: https://onlinelibrary.wiley.com/doi/pdf/10.1111/j.1365-2958.2006.05521.x.

[146] C. Magowan, J. Liang, J. Yeung, Y. Takakuwa, R. L. Coppel, and N. Mohandas. Plasmodium falciparum: influence of malarial and host erythrocyte skeletal protein interactions on phosphorylation in infected erythrocytes. *Experimental Parasitology*, 89(1):40–49, May 1998.

[147] Brian M. Cooke, Narla Mohandas, and Ross L. Coppel. Malaria and the red blood cell membrane. In *Seminars in hematology*, volume 41, pages 173–188. Elsevier, 2004.

[148] Joseph M. Rifkind, Enika Nagababu, Somasundaram Ramasamy, and Luke Babu Ravi. Hemoglobin redox reactions and oxidative stress. *Redox Report*, 8(5):234–237, October 2003.

[149] Martin Olivier, Kristin Van Den Ham, Marina Tiemi Shio, Fikregabrail Aberra Kassa, and Sophie Fougeray. Malarial Pigment Hemozoin and the Innate Inflammatory Response. *Frontiers in Immunology*, 5, February 2014.

[150] Johannes Schneberg, Alexander Ullrich, and Frank No. Simulation tools for particle-based reaction-diffusion dynamics in continuous space. *BMC Biophysics*, 7(1):11, October 2014.

[151] Thomas R. Sokolowski and Pieter Rein ten Wolde. Spatial-Stochastic Simulation of Reaction-Diffusion Systems. *arXiv:1705.08669 [cond-mat, q-bio]*, May 2017.

[152] Philipp OJ Scherer and Sighart F. Fischer. *Theoretical molecular biophysics*. Springer, 2010.

[153] Ju Li, George Lykotrafitis, Ming Dao, and Subra Suresh. Cytoskeletal dynamics of human erythrocyte. *Proceedings of the National Academy of Sciences*, 104(12):4937–4942, March 2007.

[154] Hung-Yu Chang, Xuejin Li, He Li, and George Em Karniadakis. MD/DPD multiscale framework for predicting morphology and stresses of red blood cells in health and disease. *PLoS computational biology*, 12(10):e1005173, 2016.

[155] Qiang Zhu, Carlos Vera, Robert J. Asaro, Paul Sche, and L. Amy Sung. A hybrid model for erythrocyte membrane: a single unit of protein network coupled with lipid bilayer. *Biophysical journal*, 93(2):386–400, 2007.

[156] Dmitry A. Fedosov, Bruce Caswell, and George Em Karniadakis. A Multiscale Red Blood Cell Model with Accurate Mechanics, Rheology, and Dynamics. *Biophysical Journal*, 98(10):2215–2225, May 2010.

[157] Christine Lansche, Anil K. Dasanna, Katharina Quadt, Benjamin Frhlich, Dimitris Missirlis, Marilou Ttard, Benoit Gamain, Bernd Buchholz, Cecilia P. Sanchez, Motomu Tanaka, Ulrich S. Schwarz, and Michael Lanzer. The sickle cell trait affects contact dynamics and endothelial cell activation in Plasmodium falciparum -infected erythrocytes. *Communications Biology*, 1(1):211, November 2018.

[158] Ikuko Fujiwara, Dimitrios Vavylonis, and Thomas D. Pollard. Polymerization kinetics of ADP-and ADP-Pi-actin determined by fluorescence microscopy. *Proceedings of the National Academy of Sciences*, 104(21):8827–8832, 2007.

[159] Michio Tomishige, Yasushi Sako, and Akihiro Kusumi. Regulation mechanism of the lateral diffusion of band 3 in erythrocyte membranes by the membrane skeleton. *The Journal of cell biology*, 142(4):989–1000, 1998.

[160] F Lanni and B R Ware. Detection and characterization of actin monomers, oligomers, and filaments in solution by measurement of fluorescence photobleaching recovery. *Biophysical Journal*, 46(1):97–110, July 1984.

[161] Christine A. Hughes and Vann Bennett. Adducin: a Physical Model with Implications for Function in Assembly of Spectrin-Actin Complexes. *Journal of Biological Chemistry*, 270(32):18990–18996, November 1995.

[162] Lishibanya Mohapatra, Thibaut J. Lagny, David Harbage, Predrag R. Jelenkovic, and Jane Kondev. The Limiting-Pool Mechanism Fails to Control the Size of Multiple Organelles. *Cell Systems*, 4(5):559–567.e14, May 2017.

[163] Nathan W. Goehring and Anthony A. Hyman. Organelle growth control through limiting pools of cytoplasmic components. *Current biology: CB*, 22(9):R330–339, May 2012.

[164] Cecilia P. Sanchez, Christos Karathanasis, Rodrigo Sanchez, Marek Cyrklaff, Julia Jaeger, Bernd Buchholz, Ulrich S. Schwarz, Mike Heilemann, and Michael Lanzer. Single-molecule imaging and quantification of the immune-variant adhesin VAR2CSA on knobs of Plasmodium falciparum -infected erythrocytes. *Communications Biology*, 2(1):1–9, May 2019. Number: 1 Publisher: Nature Publishing Group.

[165] P. Gaehtgens, C. Dhrssen, and K. H. Albrecht. Motion, deformation, and interaction of blood cells and plasma during flow through narrow capillary tubes. *Blood Cells*, 6(4):799–817, 1980.

[166] M. M. Guest, T. P. Bond, R. G. Cooper, and J. R. Derrick. RED BLOOD CELLS: CHANGE IN SHAPE IN CAPILLARIES. *Science (New York, N.Y.)*, 142(3597):1319–1321, December 1963.

[167] R. Skalak and P. I. Branemark. Deformation of red blood cells in capillaries. *Science (New York, N.Y.)*, 164(3880):717–719, May 1969.

[168] A. R. Pries, K. Ley, M. Claassen, and P. Gaehtgens. Red cell distribution at microvascular bifurcations. *Microvascular Research*, 38(1):81–101, July 1989.

[169] A. R. Pries, T. W. Secomb, P. Gaehtgens, and J. F. Gross. Blood flow in microvascular networks. Experiments and simulation. *Circulation Research*, 67(4):826–834, October 1990.

[170] O. Otto, P. Rosendahl, S. Golfier, A. Mietke, M. Herbig, A. Jacobi, N. Topfner, C. Herold, D. Klaue, S. Girardo, M. Winzi, E. Fischer-Friedrich, and J. Guck. Real-time deformability cytometry as a label-free indicator of cell function. *Conference proceedings: ... Annual International Conference of the IEEE Engineering in Medicine and Biology Society. IEEE Engineering in Medicine and Biology Society. Annual Conference*, 2015:1861–1864, 2015.

[171] Alexander Mietke, Oliver Otto, Salvatore Girardo, Philipp Rosendahl, Anna Taubenberger, Stefan Golfier, Elke Ulbricht, Sebastian Aland, Jochen Guck, and Elisabeth Fischer-Friedrich. Extracting Cell Stiffness from Real-Time Deformability Cytometry: Theory and Experiment. *Biophysical Journal*, 109(10):2023–2036, November 2015.

[172] Nicole Toepfner, Christoph Herold, Oliver Otto, Philipp Rosendahl, Angela Jacobi, Martin Krter, Julia Stchele, Leonhard Menschner, Maik Herbig, Laura Ciuffreda, Lisa Ranford-Cartwright, Michal Grzybek, nal Coskun, Elisabeth Reithuber, Genevive Garriss, Peter Mellroth, Birgitta Henriques-Normark, Nicola Tregay, Meinolf Suttorp, Martin Bornhuser, Edwin R. Chilvers, Reinhard Berner, and Jochen Guck. Detection of human disease conditions by single-cell morpho-rheological phenotyping of blood. *eLife*, 7, 2018.

[173] Hiroaki Ito, Ryo Murakami, Shinya Sakuma, Chia-Hung Dylan Tsai, Thomas Gutsmann, Klaus Brandenburg, Johannes M. B. Pschl, Fumihito Arai, Makoto Kaneko, and Motomu Tanaka. Mechanical diagnosis of human erythrocytes by ultra-high speed manipulation unraveled critical time window for global cytoskeletal remodeling. *Scientific Reports*, 7, February 2017.

[174] Dmitry A. Fedosov, Bruce Caswell, and George Em Karniadakis. Systematic coarse-graining of spectrin-level red blood cell models. *Computer Methods in Applied Mechanics and Engineering*, 199(29):1937–1948, June 2010.

[175] Hiroshi Noguchi and Gerhard Gompper. Fluid vesicles with viscous membranes in shear flow. *Physical Review Letters*, 93(25):258102, December 2004.

[176] Udo Seifert. Adhesion of vesicles in two dimensions. *Physical Review. A, Atomic, Molecular, and Optical Physics*, 43(12):6803–6814, June 1991.

[177] Timothy W. Secomb, Beata Styp-Rekowska, and Axel R. Pries. Two-dimensional simulation of red blood cell deformation and lateral migration in microvessels. *Annals of Biomedical Engineering*, 35(5):755–765, May 2007.

[178] E. M. Purcell. Life at low Reynolds number. *American Journal of Physics*, 45(1):3–11, January 1977. Publisher: American Association of Physics Teachers.

[179] Maciej Lisicki. Four approaches to hydrodynamic Green's functionsthe Oseen tensors. *arXiv preprint arXiv:1312.6231*, 2013.

[180] Martini, Pierach, and Scheryer. Die Stroemung des Blutes in engen Gefaessen. Eine Abweichung vom Poiseuille'schen Gesetz. *Deutsches Archiv fuer klinische Medizin*, 1(169):212–222, 1930.

[181] H. L. Goldsmith. Red cell motions and wall interactions in tube flow. *Federation Proceedings*, 30(5):1578–1590, October 1971.

[182] Mats G. Larson and Fredrik Bengzon. *The Finite Element Method: Theory, Implementation, and Applications*. Texts in Computational Science and Engineering. Springer-Verlag, Berlin Heidelberg, 2013.

[183] D. N. Arnold, F. Brezzi, and M. Fortin. A stable finite element for the stokes equations. *CALCOLO*, 21(4):337–344, December 1984.

[184] Luigi Morino and Renzo Piva, editors. *Boundary Integral Methods: Theory and Applications*. Springer-Verlag, Berlin Heidelberg, 1991.

[185] Charles S Peskin. Flow patterns around heart valves: A numerical method. *Journal of Computational Physics*, 10(2):252–271, October 1972.

[186] Charles S. Peskin. The immersed boundary method. *Acta Numerica*, 11:479–517, January 2002. Publisher: Cambridge University Press.

[187] Guy R. McNamara and Gianluigi Zanetti. Use of the Boltzmann Equation to Simulate Lattice-Gas Automata. *Physical Review Letters*, 61(20):2332–2335, November 1988. Publisher: American Physical Society.

[188] S. Succi. *The Lattice Boltzmann Equation: For Fluid Dynamics and Beyond*. Clarendon Press, June 2001. Google-Books-ID: OC0Sj_xgnhAC.

[189] Xiaoyi He and Li-Shi Luo. Theory of the lattice Boltzmann method: From the Boltzmann equation to the lattice Boltzmann equation. *Physical Review E*, 56(6):6811–6817, December 1997. Publisher: American Physical Society.

[190] Ripoll, M. Simulation Methods in a Nutshell. In *49th IFF Spring School 2018 Physics of Life Lecture Notes*, volume 158. Forschungszentrum Juelich GmbH, 2018.

[191] P. J. Hoogerbrugge and J. M. V. A. Koelman. Simulating Microscopic Hydrodynamic Phenomena with Dissipative Particle Dynamics. *Europhysics Letters (EPL)*, 19(3):155–160, June 1992. Publisher: IOP Publishing.

[192] Anatoly Malevanets and Raymond Kapral. Mesoscopic model for solvent dynamics. *The Journal of Chemical Physics*, 110(17):8605–8613, April 1999. Publisher: American Institute of Physics.

[193] Anatoly Malevanets and Raymond Kapral. Solute molecular dynamics in a mesoscale solvent. *The Journal of Chemical Physics*, 112(16):7260–7269, April 2000. Publisher: American Institute of Physics.

[194] Hiroshi Noguchi and Gerhard Gompper. Shape transitions of fluid vesicles and red blood cells in capillary flows. *Proceedings of the National Academy of Sciences of the United States of America*, 102(40):14159–14164, October 2005.

[195] Hiroshi Noguchi. Dynamic modes of red blood cells in oscillatory shear flow. *Physical Review E*, 81(6):061920, June 2010. Publisher: American Physical Society.

[196] Igor V. Pivkin and George Em Karniadakis. Accurate coarse-grained modeling of red blood cells. *Physical Review Letters*, 101(11):118105, September 2008.

[197] Prosenjit Bagchi. Mesoscale simulation of blood flow in small vessels. *Biophysical Journal*, 92(6):1858–1877, March 2007.

[198] Chenghai Sun and Lance L. Munn. Particulate Nature of Blood Determines Macroscopic Rheology: A 2-D Lattice Boltzmann Analysis. *Biophysical Journal*, 88(3):1635–1645, March 2005.

[199] Badr Kaoui, Jens Harting, and Chaouqi Misbah. Two-dimensional vesicle dynamics under shear flow: Effect of confinement. *Physical Review E*, 83(6):066319, June 2011. Publisher: American Physical Society.

[200] Sebastian Melinger, Benjamin Schmidt, Hiroshi Noguchi, and Gerhard Gompper. Dynamical regimes and hydrodynamic lift of viscous vesicles under shear. *Physical Review E*, 80(1):011901, July 2009. Publisher: American Physical Society.

[201] Martin Alns, Jan Blechta, Johan Hake, August Johansson, Benjamin Kehlet, Anders Logg, Chris Richardson, Johannes Ring, Marie E. Rognes, and Garth N. Wells. The FEniCS Project Version 1.5. *Archive of Numerical Software*, 3(100), December 2015. Number: 100.

[202] Jared O. Barber, Jonathan P. Alberding, Juan M. Restrepo, and Timothy W. Secomb. Simulated Two-dimensional Red Blood Cell Motion, Deformation, and Partitioning in Microvessel Bifurcations. *Annals of Biomedical Engineering*, 36(10):1690–1698, October 2008.

[203] Daniel S. Hariprasad and Timothy W. Secomb. Two-dimensional simulation of red blood cell motion near a wall under a lateral force. *Physical Review E*, 90(5):053014, November 2014.

[204] Daniel S. Hariprasad and Timothy W. Secomb. Prediction of noninertial focusing of red blood cells in Poiseuille flow. *Physical Review E*, 92(3):033008, September 2015. Publisher: American Physical Society.

[205] Klaus-Jrgen Bathe. *Finite Element Procedures*. Klaus-Jurgen Bathe, 2006. Google-Books-ID: rWvefGICfO8C.

[206] Javier Bonet and Richard D. Wood. Nonlinear Continuum Mechanics for Finite Element Analysis, March 2008. ISBN: 9780521838702 9780511755446 Library Catalog: www.cambridge.org Publisher: Cambridge University Press.

[207] Daniele Boffi, Franco Brezzi, and Michel Fortin. *Mixed Finite Element Methods and Applications*. Springer Science & Business Media, July 2013. Google-Books-ID: mRhAAAAAQBAJ.

[208] Franois Graner and James A. Glazier. Simulation of biological cell sorting using a two-dimensional extended Potts model. *Physical Review Letters*, 69(13):2013–2016, September 1992.

[209] Andrs Szab and Roeland M. H. Merks. Cellular Potts Modeling of Tumor Growth, Tumor Invasion, and Tumor Evolution. *Frontiers in Oncology*, 3, 2013.

[210] Ren F. M. van Oers, Elisabeth G. Rens, Danielle J. LaValley, Cynthia A. Reinhart-King, and Roeland M. H. Merks. Mechanical cell-matrix feedback explains pairwise and collective endothelial cell behavior in vitro. *PLoS computational biology*, 10(8):e1003774, August 2014.

[211] Elisabeth G. Rens and Roeland M. H. Merks. Cell Shape and Durotaxis Follow from Mechanical Cell-Substrate Reciprocity and Focal Adhesion Dynamics: A Unifying Mathematical Model. *arXiv:1906.08962 [cond-mat, physics:physics, q-bio]*, June 2019. arXiv: 1906.08962.

[212] Athanasius F. M. Mare, Alexandra Jilkine, Adriana Dawes, Vernica A. Grieneisen, and Leah Edelstein-Keshet. Polarization and Movement of Keratocytes: A Multiscale Modelling Approach. *Bulletin of Mathematical Biology*, 68(5):1169–1211, July 2006.

[213] Yoichiro Mori, Alexandra Jilkine, and Leah Edelstein-Keshet. Wave-pinning and cell polarity from a bistable reaction-diffusion system. *Biophysical Journal*, 94(9):3684–3697, May 2008.

[214] Danying Shao, Wouter-Jan Rappel, and Herbert Levine. Computational Model for Cell Morphodynamics. *Physical Review Letters*, 105(10):108104, September 2010.

[215] Florian Throff, Andriy Goychuk, Matthias Reiter, and Erwin Frey. Bridging the gap between single-cell migration and collective dynamics. *eLife*, 8, 2019.

[216] Ilka B. Bischofs, Franziska Klein, Dirk Lehnert, Martin Bastmeyer, and Ulrich S. Schwarz. Filamentous network mechanics and active contractility determine cell and tissue shape. *Biophysical journal*, 95(7):3488–3496, 2008.

[217] Laurent Blanchoin, Rajaa Boujemaa-Paterski, Ccile Sykes, and Julie Plastino. Actin Dynamics, Architecture, and Mechanics in Cell Motility. *Physiological Reviews*, 94(1):235–263, January 2014. Publisher: American Physiological Society.

[218] Drazen Raucher and Michael P. Sheetz. Cell Spreading and Lamellipodial Extension Rate Is Regulated by Membrane Tension. *Journal of Cell Biology*, 148(1):127–136, January 2000. Publisher: The Rockefeller University Press.

[219] Bruno Pontes, Pascale Monzo, and Nils C. Gauthier. Membrane tension: A challenging but universal physical parameter in cell biology. *Seminars in Cell & Developmental Biology*, 71:30–41, 2017.

[220] L. M. Machesky and R. H. Insall. Scar1 and the related Wiskott-Aldrich syndrome protein, WASP, regulate the actin cytoskeleton through the Arp2/3 complex. *Current biology: CB*, 8(25):1347–1356, December 1998.

[221] L. M. Machesky, R. D. Mullins, H. N. Higgs, D. A. Kaiser, L. Blanchoin, R. C. May, M. E. Hall, and T. D. Pollard. Scar, a WASp-related protein, activates nucleation of actin filaments by the Arp2/3 complex. *Proceedings of the National Academy of Sciences of the United States of America*, 96(7):3739–3744, March 1999.

[222] Noa Ofer, Alexander Mogilner, and Kinneret Keren. Actin disassembly clock determines shape and speed of lamellipodial fragments. *Proceedings of the National Academy of Sciences of the United States of America*, 108(51):20394–20399, December 2011.

[223] Cyrus A. Wilson, Mark A. Tsuchida, Greg M. Allen, Erin L. Barnhart, Kathryn T. Applegate, Patricia T. Yam, Lin Ji, Kinneret Keren, Gaudenz Danuser, and Julie A. Theriot. Myosin II contributes to cell-scale actin network treadmilling through network disassembly. *Nature*, 465(7296):373–377, May 2010.

[224] Antonina Y. Alexandrova, Katya Arnold, Sbastien Schaub, Jury M. Vasiliev, Jean-Jacques Meister, Alexander D. Bershadsky, and Alexander B. Verkhovsky. Comparative Dynamics of Retrograde Actin Flow and Focal Adhesions: Formation of Nascent Adhesions Triggers Transition from Fast to Slow Flow. *PLOS ONE*, 3(9):e3234, September 2008. Publisher: Public Library of Science.

[225] Nathalie Q. Balaban, Ulrich S. Schwarz, Daniel Riveline, Polina Goichberg, Gila Tzur, Ilana Sabanay, Diana Mahalu, Sam Safran, Alexander Bershadsky, Lia Addadi, and Benjamin Geiger. Force and focal adhesion assembly: a close relationship studied using elastic micropatterned substrates. *Nature Cell Biology*, 3(5):466–472, May 2001.

[226] Benjamin Geiger, Joachim P. Spatz, and Alexander D. Bershadsky. Environmental sensing through focal adhesions. *Nature Reviews Molecular Cell Biology*, 10(1):21–33, January 2009. Number: 1 Publisher: Nature Publishing Group.

[227] Alexandre R. Gingras, Klaus-Peter Vogel, Heinz-Jrgen Steinhoff, Wolfgang H. Ziegler, Bipin Patel, Jonas Emsley, David R. Critchley, Gordon C. K. Roberts, and Igor L. Barsukov. Structural and Dynamic Characterization of a Vinculin Binding Site in the Talin Rod,. *Biochemistry*, 45(6):1805–1817, February 2006. Publisher: American Chemical Society.

[228] Evangelos Papagrigoriou, Alexandre R Gingras, Igor L Barsukov, Neil Bate, Ian J Fillingham, Bipin Patel, Ronald Frank, Wolfgang H Ziegler, Gordon CK Roberts, David R Critchley, and Jonas Emsley. Activation of a vinculin-binding site in the talin rod involves rearrangement of a five-helix bundle. *The EMBO Journal*, 23(15):2942–2951, August 2004.

[229] Colin K. Choi, Miguel Vicente-Manzanares, Jessica Zareno, Leanna A. Whitmore, Alex Mogilner, and Alan Rick Horwitz. Actin and alpha-actinin orchestrate the assembly and maturation of nascent adhesions in a myosin II motor-independent manner. *Nature Cell Biology*, 10(9):1039–1050, September 2008.

[230] Manuel Salmern-Snchez and Matthew J. Dalby. Synergistic growth factor microenvironments. *Chemical Communications*, 52(91):13327–13336, November 2016. Publisher: The Royal Society of Chemistry.

[231] Elena Kassianidou and Sanjay Kumar. A biomechanical perspective on stress fiber structure and function. *Biochimica Et Biophysica Acta*, 1853(11 Pt B):3065–3074, November 2015.

[232] Dylan T. Burnette, Suliana Manley, Prabuddha Sengupta, Rachid Sougrat, Michael W. Davidson, Bechara Kachar, and Jennifer Lippincott-Schwartz. A role for actin arcs in the leading-edge advance of migrating cells. *Nature cell biology*, 13(4):371–382, 2011. Publisher: Nature Publishing Group.

[233] Tianchi Chen, Andrew Callan-Jones, Eduard Fedorov, Andrea Ravasio, Agust Brugus, Hui Ting Ong, Yusuke Toyama, Boon Chuan Low, Xavier Trepat, Tom Shemesh, Raphal Voituriez, and Benot Ladoux. Large-scale curvature sensing by directional actin flow drives cellular migration mode switching. *Nature Physics*, 15(4):393, April 2019.

[234] Sanjay Kumar, Iva Z. Maxwell, Alexander Heisterkamp, Thomas R. Polte, Tanmay P. Lele, Matthew Salanga, Eric Mazur, and Donald E. Ingber. Viscoelastic Retraction of Single Living Stress Fibers and Its Impact on Cell

Shape, Cytoskeletal Organization, and Extracellular Matrix Mechanics. *Biophysical Journal*, 90(10):3762–3773, May 2006.

[235] Elena Kassianidou, Christoph A. Brand, Ulrich S. Schwarz, and Sanjay Kumar. Geometry and network connectivity govern the mechanics of stress fibers. *Proceedings of the National Academy of Sciences*, page 201606649, 2017.

[236] David P. Landau and Kurt Binder. *A Guide to Monte Carlo Simulations in Statistical Physics*. Cambridge University Press, November 2014.

[237] Ilka B. Bischofs, Sebastian S. Schmidt, and Ulrich S. Schwarz. Effect of adhesion geometry and rigidity on cellular force distributions. *Physical review letters*, 103(4):048101, 2009.

[238] Aaron F. Mertz, Shiladitya Banerjee, Yonglu Che, Guy K. German, Ye Xu, Callen Hyland, M. Cristina Marchetti, Valerie Horsley, and Eric R. Dufresne. Scaling of Traction Forces with the Size of Cohesive Cell Colonies. *Physical Review Letters*, 108(19), May 2012.

[239] Miriam Cohen, Derk Joester, Benjamin Geiger, and Lia Addadi. Spatial and temporal sequence of events in cell adhesion: from molecular recognition to focal adhesion assembly. *Chembiochem*, 5(10):1393–1399, 2004.

[240] Fuchang Gao and Lixing Han. Implementing the Nelder-Mead simplex algorithm withadaptive parameters. *Computational Optimization and Applications*, 51(1):259–277, January 2012.

[241] Philipp J. Albert and Ulrich S. Schwarz. Modeling cell shape and dynamics on micropatterns. *Cell adhesion & migration*, 10(5):516–528, 2016.

[242] Tom Shemesh, Alexander D. Bershadsky, and Michael M. Kozlov. Physical model for self-organization of actin cytoskeleton and adhesion complexes at the cell front. *Biophysical journal*, 102(8):1746–1756, 2012.

[243] W. Hckl, U. Seifert, and E. Sackmann. Effects of fully and partially solubilized amphiphiles on bilayer bending stiffness and temperature dependence of the effective tension of giant vesicles. *Journal de Physique II*, 7(8):1141–1157, 1997.

[244] H. P. Duwe, J. Kaes, and E. Sackmann. Bending elastic moduli of lipid bilayers: modulation by solutes. *Journal de Physique*, 51(10):945–961, 1990.

[245] Young-Zoon Yoon, Ha Hong, Aidan Brown, Dong Chung Kim, Dae Joon Kang, Virgilio L. Lew, and Pietro Cicuta. Flickering analysis of erythrocyte mechanical properties: dependence on oxygenation level, cell shape, and hydration level. *Biophysical journal*, 97(6):1606–1615, 2009.

[246] T. D. Pollard. Rate constants for the reactions of ATP- and ADP-actin with the ends of actin filaments. *The Journal of Cell Biology*, 103(6):2747–2754, December 1986.

[247] David Sept and J. Andrew McCammon. Thermodynamics and Kinetics of Actin Filament Nucleation. *Biophysical Journal*, 81(2):667–674, August 2001.

[248] C. Erlenkmper and K. Kruse. Treadmilling and length distributions of active polar filaments. *The Journal of Chemical Physics*, 139(16):164907, October 2013.

[249] M. Bindschadler, E. A. Osborn, C. F. Dewey Jr, and J. L. McGrath. A mechanistic model of the actin cycle. *Biophysical journal*, 86(5):2720–2739, 2004.

List of Manuscripts

Elena Kassianidou, Dimitri Probst, **Julia Jäger**, Stacey Lee, Anne-Lou Roguet, Ulrich Sebastian Schwarz and Sanjay Kumar **Extracellular Matrix Geometry and Initial Adhesive Position Determine Stress Fiber Network Organization during Cell Spreading** *Cell Reports, 27 1897-1909 (May 2019)*	Chapter 5
Cecilia P. Sanchez, Christos Karathanasis, Rodrigo Sanchez, Marek Cyrklaff, **Julia Jäger**, Bernd Buchholz, Ulrich S. Schwarz, Mike Heilemann and Michael Lanzer **Single-molecule imaging and quantification of the immune-variant adhesin VAR2CSA on knobs of Plasmodium falciparum-infected erythrocytes** *Communications Biology, 2 172 (May 2019)*	Chapter 2
Benjamin Fröhlich, **Julia Jäger**, Christine Lansche, Cecilia P. Sanchez, Marek Cyrklaff, Bernd Buchholz, Serge Theophile Soubeiga, Jacque Simpore, Hiroaki Ito, Ulrich S. Schwarz, Michael Lanzer and Motomu Tanaka **Hemoglobin S and C affect biomechanical membrane properties of P. falciparum-infected erythrocytes** *Communications Biology, 2 311 (August 2019)*	Chapter 2

Danksagung

Zuallererst möchte ich mich bei Ulrich Schwarz für die Betreuung meiner Arbeit bedanken. Ohne seine Unterstützung wäre diese nicht möglich gewesen. Ich bin über die Zeit in seiner Arbeitsgruppe sehr dankbar und blicke auf hilfreiche Diskussionen bezüglich der Biophysik zurück. Außerdem hat er mir ermöglicht, mich auf zahlreichen Konferenzen weiterzubilden und wissenschaftlich auszutauschen.

Ich möchte mich weiterhin bei Prof. Frauke Gräter für ihr Interesse an meiner Arbeit bedanken, für die sie zweite Gutachterin ist. Vielen Dank auch für die hilfreichen Kommentare wärend meiner TAC meetings.

Ein besonders Dank gilt der HGS MathComp, die mich für mein Pormotionsvorhaben mit einem Stipendium gefördert hat. Neben der finanziellen Unterstützung habe ich auch von vielen Angeboten der Graduiertenschule profitiert; es gab regelmäßig Seminare, Kurse und einen regen Austausch unter den Mitgliedern bei den jährlichen Kolloquien. Obwohl ich kein direktes Mitglied war, habe ich auch sehr vom SFB 1129 profitiert. Im Rahmen dieses Sonderforschungsbereiches fanden monatliche Malaria-Treffen statt, in denen zahriche Informationen ausgetauscht und Anregungen gegeben wurden. In diesem Rahmen einen besonderen Dank auch an Prof. Lanzer, der Mitglied meines TAC Committees war und für alle biologischen Fragen bezüglich des Malaria-Parasieten der richtige Ansprechpartner war.

Vielen Dank an alle Mitglieder der Arbeitsgruppe Schwarz. Obwohl wir teilweise räumlich getrennt waren, konnten wir uns doch bei den wöchentlichen Gruppentreffen sehr gut austauschen. Ich habe gerne mit euch gearbeitet und über physikalische Themen diskutiert. Dieser Dank geht an folgende Personen: Marco Linke, Nils Klughammer, Dimitri Probst, Anil Kumar Dasanna, Nikolas Schnellbächer, Felix Frey, Tom Kaufmann, Falko Ziebert, Pintu Patra, Justin Grewe, Dennis Wörthmüller, Patrick Binder, Johannes Blumberg, Rabea Link, Robert Chojowski, Oliver Drozdowski und Timothy Herbst. Ein besonderer Dank geht an Niko und Nils, durch die ich mich zu Beginn der Arbeit besonders schnell eingelebt habe und an Pintu und Anil, mit denen ich viel über die Biophysik des Malaria-Parasiten diskutiert habe. Vielen Dank weiterhin an alle meine Kollaborationspartner: Benjamin Fröhlich, Prof. Tanaka, Cecilia Sanchez, Marek Cyrklaff, Elena Kassianidou, Prof. Kumar und Dimitri. Durch die interdisziplinären Diskussionen habe ich sehr viel gelernt.

Als nächstes möchte ich mich herzlich bei all meinen Freunden bedanken, die bei der Korrektur meiner Arbeit geholfen haben. Eure Kommentare haben grundlegend dazu beigetragen diese Arbeit verständlicher zu machen. Hierbei geht es sowohl um meine Physiker- und Mathematiker-Freunde; Markus Griedel, TobiAss Heldt, Marcus Held, Marie Westermann, Saerah Homer, Pintu Patra und Alastair

Stewart, der mich außerdem durch mein gesamtes Physikstudium in Edinburgh begleitet hat, als auch um meine sprachlich begabten Freunde Hannah Rothermel und Ute Gradmann. Ohne Eure Unterstützung und zusätzliche Motivation wäre diese Arbeit nicht so zustande gekommen, wie sie jetzt ist.

Vielen Dank an Markus, Hannah und Hendrik für die ausdauernde Unterstützung während des Schreibens der Arbeit. Durch sportliche Pausen mit Euch und zahlreiche Verpflegungsangebote hatte ich genügend Zeit und Kraft die Arbeit rechtzeitig zu vollenden. Außerdem möchte ich mich bei allen Neckarkrokodilen, unter denen ich viele gute Freunde gefunden habe, für die Zeit auf dem Wasser und am Bootshaus bedanken. Dies war immer ein guter Ausgleich zur langen Arbeit am Schreibtisch und der sehr hohe Anteil an Physikern im Kanupolo-Sport Heidelberg überrascht mich immer noch positiv.

Als letztes möchte ich mich noch besonders bei meiner Familie für die andauernde Unterstützung bedanken. Ihr habt es mir ermöglicht Physik zu studieren und ohne Euch wäre ich jetzt nicht in dieser Position diese Arbeit abzugeben. Vielen Dank dafür!